ENHANCING THE CORROSION RESISTANCE OF API 5L X70 PIPELINE STEEL THROUGH THERMOMECHANICALLY CONTROLLED PROCESSING

A Thesis Submitted to the
College of Graduate and Postdoctoral Studies
In Partial Fulfillment of the Requirements
For the Degree of Doctor of Philosophy
In the Department of Mechanical Engineering
University of Saskatchewan
Saskatoon

By

Enyinnaya George Ohaeri

PERMISSION TO USE

In presenting this thesis, in partial fulfillment of the requirements for a degree of Doctor of Philosophy from the University of Saskatchewan, I agree that the Libraries of this University may make it freely available for inspection. I further agree that permission for copying this thesis in any manner, in whole or in part, for scholarly purposes may be granted by Professor Jerzy Szpunar, who supervised my thesis work or, in his absence, by the Head of the Department or the Dean of the College in which my thesis work was done. It is understood that any copying or publication or use of this thesis, or parts thereof, for financial gain shall not be allowed without my written permission. It is also understood that due recognition shall be given to me and to the University of Saskatchewan in any scholarly use which may be made of any material in my thesis.

Requests for permission to copy or to make other use of material in this thesis in whole or in part should be addressed to:

Head of the Department of Mechanical Engineering
University of Saskatchewan
57 Campus Drive
Saskatoon, Saskatchewan S7N 5A9
Canada

OR

Dean
College of Graduate and Postdoctoral Studies
University of Saskatchewan
116 Thorvaldson Building, 110 Science Place
Saskatoon, Saskatchewan S7N 5C9
Canada

ABSTRACT

Pipelines are widely used for transportation of oil and gas because they can carry large volume of these products at lower cost compared to rail cars and trucks. However, they are prone to environmentally assisted degradation. Different methods of optimizing pipeline steels such as micro-alloying, desulfurization, microstructure design, and inclusion morphology control have been used to improve their performance in different service environments. This study presents the use microstructure and texture control to improve the reliability of API 5L X70 pipeline steel.

The properties of API 5L X70 steel was manipulated through thermomechanical processing. Pipeline steel plates were produced using different processing schedules. The final microstructure and texture of processed steels were determined. Also, electrochemical corrosion studies were performed on selected steels in hydrogen producing and non-hydrogen producing electrolyte solutions. In addition, samples from each steel was investigated for hydrogen induced cracking (HIC) with and without the application of tensile stress. Further annealing heat treatments were conducted on the steel with improved HIC behavior before assessing hydrogen embrittlement characteristics. All the tests were performed at room temperature.

Generally, the lowest corrosion rate was measured in the hydrogen producing electrolyte due to the rapid formation of a corrosion protective film on the pipeline substrate. It was found that variations in the processing conditions affects corrosion and cracking behavior of steels. The least corrosion resistant steels experienced more intense surface deterioration after polarization. Subsequently, such steels were damaged by hydrogen attack. The steel with improved corrosion resistance displayed no visible cracking after probing in corrosive mediums and charging with hydrogen. Despite weak texture noticed in all the steels, (111) crystal planes showed better electrochemical corrosion resistance compared to (110) and (100). Moreover, microstructural features such as non-metallic inclusions/precipitates, grain characteristics, phase distribution, and local average misorientations were analyzed in relation crack initiation and propagation. Evidence suggests that cracking occurred mainly through deformed regions in the mid-thickness section. Early onset of crack formations was characterized by stepwise discontinuities. It was demonstrated that during in-situ tensile deformation and hydrogen charging, sudden failure takes place in the elastic zone. The obtained results indicate that cracks propagated through segregations of iron

carbide around high angle grain boundaries. Also, multi-component inclusion particles comprising of angular (Ti-Nb) N precipitates, spherical Al-Mg-Ca oxides, and some traces of Mo-Mn-S influenced susceptibility to HIC. It was observed that hydrogen embrittlement susceptibility was lowered after annealing in two consecutive cycles compared to single annealing treatment. The double step heat treatment resulted in a dual-phase (ferrite and tempered martensite) microstructure with greater ductility than in original steels. Finally, the pipeline steel that was hot rolled (880 – 820 °C) and rapidly cooled (755 – 615 °C) at the rate of 25 °C/s has shown improved resistance to corrosion.

ACKNOWLEDGEMENTS

My sincere appreciation goes to the University of Saskatchewan for this great opportunity. I am endlessly grateful to Prof. Jerzy A. Szpunar for his astounding supervision. Your guidance, understanding, and fatherly advice during my studies remained resolute. I always marvel at the amount of confidence you have in my abilities. You considered me worthy of an opportunity many would have denied me. Your good will towards me has made me perpetually thankful to you. The words of advice from Prof. Ikechukwuka N. Oguocha and Prof. Akindele G. Odeshi contributed greatly towards the success of my studies. I would never forget other members of my advisory committee, Prof. Duncan Cree and Prof. Richard Evitts. I would not have been where I am today without the support from each of you.

The generosity of Natural Sciences and Engineering Research Council of Canada (NSERC Strategic Grant 470033) towards funding this project is recognized. Special thanks to the University of Saskatchewan for offering me the devolved scholarship. I also appreciate the support of EVRAZ North America, CANMET Natural Resources, Ontario, Canada, and the Saskatchewan Structural Sciences Center (SSSC). The comradeship shown to me by all members of the Advanced Materials and Renewable Energy (AMRE) research group at the University of Saskatchewan will never be forgotten. My exceptional thanks go to Dr. Ubong Eduok, and Dr. Ahmed Tiamiyu for their helpful suggestions and immense encouragement. Many thanks to Garry & Eleanor Mckay, and Gerry & Shirley Falk for always being there to pray for me. To my family and friends, I cannot acknowledge you enough for patiently standing by me throughout this period. It would have been impossible to attain this height without the early teachings of my late father Mr. Ajaraonye C. Ohaeri. You planted a tree, but never sat under its shade. Instead, you left an indelible mark for humanity. My eternal respect goes to my mother Mrs Ngozi V. Ohaeri and all my siblings for always believing in me. I must say you all are the best family anyone can have. I thank you all for understanding and tolerating me through these years. I cannot thank Godswill Enyinnaya-Ohaeri enough for ensuring that my sanity remained intact during this program.

Finally, I am nothing without the grace of the almighty God in whom I trust.

DEDICATION

To many who had lofty dreams, but never got the opportunity to actualize them.

TABLE OF CONTENTS

LIST OF TABLES

LIST OF FIGURES

LIST OF ABBREVIATIONS

AC	Alternating current
AFM	Atomic Force Microscopy
AIDE	Adsorption Induced Dislocation Emission
API	American Petroleum Institute
Ar3	Austenite-ferrite transformation temperature
ATR-IR	Attenuated Total Reflection-Infrared
BAE	Biologically active environment
BCC	Body centered cubic
CAPEX	Capital expenditure
COMPASS	Condensed-phase Optimized Molecular Potentials for Atomistic Simulation Studies
CP	Cathodic protection
CSL	Coincidence site lattice
DC	Direct current
DS method	*Devanathan–Stachurski* method
EBSD	Electron backscatter diffraction
ECCI	Electron channeling contrast imaging
EDTA	Ethylenediaminetetraacetic acid
EDX or EDS	Energy Dispersive X-ray
EFM	Electrochemical frequency modulation
EIS	Electrochemical impedance spectroscopy
EN	Electrochemical noise
EPS	Extracellular polymeric substances
FTIR	Fourier transform infrared
HAGB	High angle grain boundary
HALP	Hydrogen-Affected Localized Plasticity
HAZ	Heat affected zone
HDPE	High density polyethylene
HE	Hydrogen embrittlement
HEDE	Hydrogen Enhanced Decohesion

HELP	Hydrogen Enhanced Localized Plasticity
HIBC	Hydrogen induced blister crack
HIC	Hydrogen induced cracking
HMT	Hydrogen microprint technique
HAS	Hemi-spherical analyzer
HSLA	High strength low alloy steel
LAGB	Low angle grain boundary
LEIS	Localized electrochemical impedance spectroscopy
LPR	Linear polarization resistance
MIC	Microbiologically influenced corrosion
MPI	Magnetic particle inspection
NACE	National Association of Corrosion Engineers
ND	Normal direction
NDT	Non-destructive testing
NRB	Nitrate reducing bacteria
OLAC	On-line accelerated cooling
OPEX	Operational expenditure
PDP	Potentiodynamic polarization
RD	Rolling direction
Redox	Reduction-oxidation
SCC	Stress corrosion cracking
SEM	Scanning electron microscopy
SMA	Spherical mirror analyzer
SOHIC	Stress-oriented hydrogen induced cracking
SRB	Sulphate-reducing bacteria
SSCC	Sulfide stress corrosion cracking
TD	Transverse direction
TDS	Thermal desorption spectrometry
TEM	Transmission electron microscopy
TMCP	Thermomechanical controlled processing
Tnr	Non-recrystallization temperature

TRIP	Transformation induced plasticity steel
TWIP	Twinning-induced plasticity
UV–vis	Ultraviolet–visible spectroscopy
WQ	Water quenching
WR	Warm rolled
XPS	X-ray Photoelectron Spectroscopy
XRD	X-ray Diffraction
j_{corr}	Corrosion current density
E_{corr}	Corrosion potential
E_{oc}	Open circuit potential
α-Fe	Alpha iron
Σ	Sigma
σ	Stress
σ_{app}	Applied stress
σ_{coh}	Cohesive stress
σ_0	Yield strength
σ_i	Lattice frictional stress
D_{eff}	Effective diffusivity
$J_\infty L$	Permeability
C_{app}	Apparent solubility

CHAPTER 1 : INTRODUCTION

1.1 Overview

This chapter provides a brief background of the development of modern-day pipeline steel. The common processing techniques deployed in the production of high strength pipeline steels are also introduced. Next, the problems associated with utilizing current pipeline steel for application in severe operating environments are highlighted, which leads to the objectives of this research. At the end of the chapter, an outline of the entire thesis is presented.

1.2 Background

Steel is the most common material used in the fabrication of numerous strength demanding structures, such as buildings, ship hulls, offshore platforms, pipelines, automobiles, industrial storage tanks, bridges, earth-moving equipment, penstocks (pipes used in hydroelectric power stations), and so on [1,2]. Among these engineering structures, pipelines are believed to be very critical, because of their strategic role in the transportation of fluids. The continuously increasing demand for energy has necessitated the use of pipeline infrastructure in the supply of oil and gas through severely corrosive environments under high temperatures and pressures. Although many corrosion resistant alloys such as duplex stainless steel have been developed, a few challenges still abound. Most of the difficulties associated with the usage of these alloys are associated with cost effectiveness and problems with welding. The notable high cost of purchase/installation related to some of these materials and the potential for unpredictably welds are concerns. Carbon-manganese steels offer the best option for a variety of low corrosion risk applications. Additionally, technological advancements in steel processing has made it possible for industries to efficiently control microstructure evolution and improve mechanical properties without relying solely on traditional heat treatments (i.e. quenching, normalizing and tempering) and micro-alloying approaches. This achievement was made possible by optimizing steel structure through the combination of controlled rolling followed by water cooling in a process known as '*thermomechanically controlled processing'* (TMCP) [3]. The effects of the different processing parameters on the TMCP technique has been investigated experimentally and mathematically modeled by Yoshie *et al*. [4]. In their study, they established a correlation between the changes in microstructure during processing and the mechanical properties of steel plates. Similarly, Nishioka

and Ichikawa [1] reviewed the commercial implications of TMCP. With the aid of thermomechanical treatments, steel plates that have excellent balance between strength, toughness, and weldability have been produced for pipeline construction. However, the pipelines produced through this method are by no means perfect. Sometimes, pipelines fail while in service and result in serious environmental devastation. These incidents have created many doubts about the future application of such important means of conveying fluids.

In general, the processing route adopted in steel production affects behavior in the service environment. There are insinuations that failure of pipelines either in the form of leakage or rupture may be due to material susceptibility (composition, microstructure), service environment (fluid composition, temperature, flow rate), and applied stress [5]. Therefore, controlling the microstructure development is necessary to minimize the vulnerability of pipeline steel to develop fractures. Most of the pipelines rupture through crack related mechanisms. The two main failure modes reported in the pipeline industry are stress corrosion cracking (SCC) and hydrogen embrittlement (HE). Amongst these damage types, the most critical is the HE mechanism, which comprises of hydrogen induced cracking (HIC) and sulfide stress cracking (SSC). Pipeline steel embrittlement is strongly linked to the presence of hydrogen sulfide (sour gas) in the vicinity of the operation. Some sour service pipelines encounter H_2S partial pressure levels above 0.3 kPa [6]. The process of HE can either manifest internally due to already existing hydrogen inside the steel structure or as a result of external migration of hydrogen from the environment [7]. Although many pieces of literature [8–10] exist on the hydrogen degradation of steel, it is important to identify common ways by which hydrogen is made available for entry into pipeline steel while in service. The different sources are broadly categorized as gaseous hydrogen entry and corrosion process (i.e. electrochemical hydrogen evolution). Hydrogen can be given off as the by-product of the cathodic half-cell reaction during electrochemical processes [11]. Numerous studies [12–15] have adopted these methods of introducing atomic hydrogen into steel for experimental studies. Perng and Wu [16] documented that the electrolytic technique gained more attention as a means of hydrogen charging due to its ability to maintain hydrogen gas supply to the metal surface at relatively high pressure. They further concluded that the amount of dissolved hydrogen in a metal subjected to gaseous phase charging is proportional to the square root of the pressure, $P_{H_2}^{\frac{1}{2}}(atm^{\frac{1}{2}})$ at which hydrogen is supplied. On the other hand, the same authors stated that the quantity of

dissolved hydrogen in metals exposed to electrochemical charging is proportional to the applied cathodic current density $i^{\frac{1}{2}}$ $(\mathrm{Amp/m^2})^{\frac{1}{2}}$. It is typical to generate hydrogen by excessively applying cathodic potential to protect pipeline steel from corrosion [17]. Such severe conditions will promote the migration of hydrogen atoms into the steels thereby causing catastrophic failure by cracking.

1.3 Historical perspective on pipeline steel development

Over the past 50-60 years, many advancements in the steel making process have resulted in better quality materials for pipeline applications. Prior to this time, molten steel was poured into an ingot where it was reheated and rolled to make the final products. Before the 1960's, pipeline steel manufacturing was limited to the semi-killing process (i.e. incompletely removing oxygen from the melt), which gave rise to the preliminary grades described in Table 1.1. During this period, only pipeline steel grades specified as A25, A, B, X42, X46, and X52 were made. These different classes of early pipelines were sold irrespective of their poor mechanical properties and high susceptibility to failure in severe service conditions. As time passed beyond the 1960's, there was a need to improve strength to the higher grades. The only option was to adopt processing techniques that permits the development of stronger microstructures. Consequently, better understanding of the relationship between processing temperature and mechanical properties led to the creation of grades such as X56 and X60 [18]. During the 1980's, more strength was developed for pipeline steel. This was the beginning of a drastic reduction in the addition of alloying elements, which gave rise to an increase in mechanical properties. These advancements could not have been possible without the introduction of techniques such as full-killing, continuous casting, controlled rolling, and accelerated cooling. Continuously cast steels undergo constant stirring during processing. The reason is to minimize the agglomeration of elements and/or non-metallic inclusions along the plate's mid-thickness. Moreover, making steel through a continuous process allows for easier control of the temperature throughout the entire sequence of activities. The primary aim of this system is to achieve the complete removal of oxygen by extensive killing thereby allowing the incorporation of additional elements which then forms micro-alloyed steel. Generally, the basic steel grades possess larger grains compared to the contemporary ones. It became imperative to further reduce grain size in order to achieve even greater strength. The TMCP technique is an advanced form of continuous casting which effectively harnesses the

advantages offered by micro-alloying, while applying different degrees of rolling reductions to impart grain refinement [19]. As such, recent steel production employs a careful alteration of different rolling parameters as a means of controlling microstructure evolution during processing. The outcome of combining these procedures was an increase in strength up to the X65, X70, X80, X90, X100, and X120 grades. Each of these high strength steels are manufactured with a remarkable proportion of refined grains and enhanced properties.

Table 1.1 Pipeline steel grades and their strength requirements [7]

API 5L Grade*	Min YS (MPa/ Ksi)	Max YS (MPa/Ksi)	Min TS (MPa/Ksi)	Max TS (MPa/Ksi)	Min elongation (%) for 0.2 sqin sample
A25	172/20	-	310/45	-	-
A	207/30	-	331/48	-	-
B	241/35	448/65	413/60	758/110	22.5
X42	289/42	496/72	413/60	758/110	22.5
X46	317/46	524/76	434/63	758/110	21.5
X52	358/52	531/77	455/66	758/110	21.0
X56	386/56	544/79	489/71	758/110	19.5
X60	413/60	565/82	517/75	758/110	18.5
X65	448/65	600/87	530/77	758/110	18.0
X70	482/70	621/90	565/82	758/110	17.0
X80	551/80	690/100	620/90	827/120	15.5

*American Petroleum Institute (grading system where the identification number for each steel corresponds to the minimum yield strength measured in Ksi); YS – yield strength; TS – tensile strength

The illustration in Fig. 1.1 presents different stages in the development of pipeline steel. In the early days of pipeline manufacturing, high strength, low alloy steels were used [19]. Then, hot rolling and normalizing were considered as the major means of processing pipeline steel. The addition of alloying elements was minimal, except for carbon, which determined the bulk strengthening. As time progressed towards the 1980's and 1990's, the carbon content continued to diminish in steel, while other alloying elements began to feature more prominently. The introduction of precipitation strengthening, as well as TMCP, led to significant increases in strength and toughness. Grain refinement also contributed to improving the mechanical properties of higher-grade steels. Modifications such as accelerated cooling/quenching were applied in processing recent steels to lower the proportion of pearlite phase that is formed. Consequently, more ferrite with other phases such as bainite, retained austenite, and martensite may be formed.

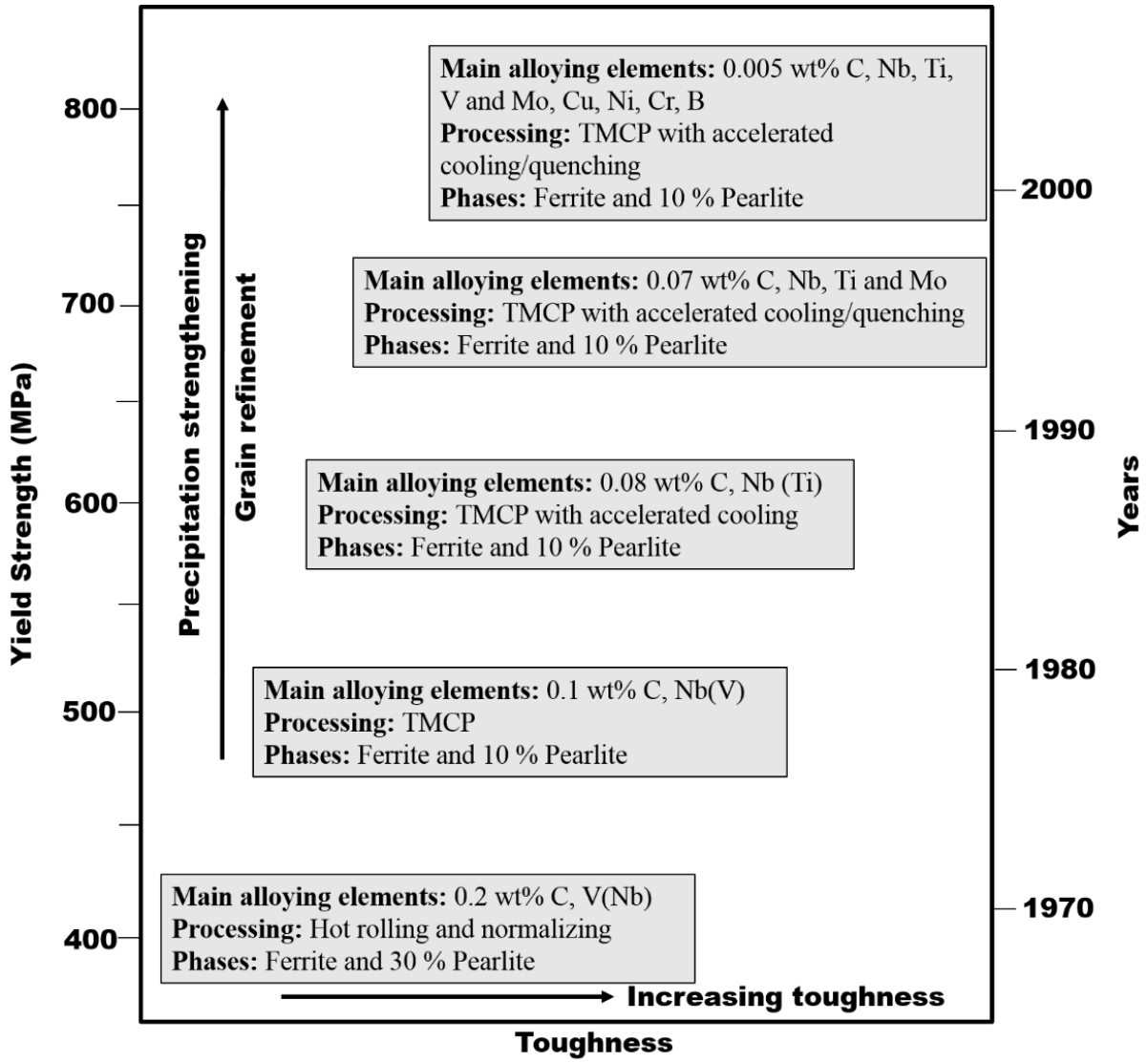

Fig. 1.1 An illustration of the different stages in pipeline steel development (adapted from Ref. [27])

1.4 Thermomechanically controlled processing (i.e. hot rolling)

This is a systematic approach for producing pipeline steel with improved mechanical properties. High-strength pipeline steel production leverages on this method to control austenite grain growth, recrystallization, dislocation density, precipitation strengthening, and microstructural phase formation [20,21]. In general terms, steels produced through this route are controlled rolled and accelerated cooled. The TMCP method comprises of a sequence of activities involving careful control of the temperature, while executing various degrees of rolling deformations. The extent of

hot plastic deformation (i.e. rolling) imparted during this thermomechanical treatment is estimated in terms of reduction ratio. Also, the temperatures chosen for finishing rolling, cooling, and coiling are critical in determining the end properties of the final steel plate. This procedure effectively manages structure formation through deformation at appropriate conditions and cooling at a suitable rate. Eventually, manipulating these steps properly will improve mechanical properties and crack behavior of pipeline steel. Findley *et al*. [22] proposed a model for crack initiation and propagation in steel. They are of the opinion that the hydrogen embrittlement susceptibility increases with the tensile strength. However, it is unrealistic to lower the mechanical properties of pipeline steel. Instead, thermomechanical treatment should be used to determine microstructural features in steel. Similarly, another study [17] established that an uncontrolled increase in strength can adversely affect the susceptibility of steel to develop crack-related failures. So, carefully manipulating the rolling and cooling processes can potentially help to manage inclusions and reduce hard segregated bands, which will indirectly improve the HE resistance of pipeline steels [23,24]. Also, the final microstructure in pipeline steels mostly consist of pearlite, various morphologies of ferrite (such as acicular, granular, polygonal, quasi-polygonal ferrite), bainite, and some micro-constituents (e.g. micro-alloying precipitates and austenite/martensite islands) [25,26]. All these phases contribute by either increasing the resistance of pipelines to embrittlement or predisposing them to easy failure.

Steel plates can be made with a reasonable amount of grain refinement. A study noted that controlled rolling is preferably performed at relatively low temperatures (non-recrystallization range) of around 900℃ [2]. They further proposed that deforming steel at such temperatures increases the dislocation density as well as promotes the formation of in-grain/grain boundary nucleation sites. The reason being that deformation at austenitic temperatures increases the chances of grain growth, even as the steel plate continues to cool down. Nevertheless, the unwanted manifestation of large sized grains is minimized by applying further rolling to limit the grain growth and/or break down already grown grains. According to the Hall-Petch relation in Eqn. 1.1, an inverse relationship exists between strength and grain size of steel alloys [27]. Therefore, there is a need to establish an ideal grain size in order to ensure excellent properties. It is important to state that the conventional controlled rolling process can only support the production of pipeline

steel up to grade X65. Attempts to use this procedure for higher strength grades will ultimately result in poor mechanical properties and weldability.

$$\sigma_0 = \sigma_i + {}^{k}/_{\sqrt{D}} \tag{1.1}$$

where σ_0 = Yield strength, σ_i = Lattice frictional stress, k = constant (measures the amount of local stress required for yielding to occur across grain boundaries), and D = grain size.

Cooling pipeline steel plate rapidly after plastic deformation (i.e. controlled rolling) promotes the development of microstructures useful for higher strength applications. Indirectly, this cooling method reduces the cost incurred in adopting micro-alloying as a means of strengthening steel [28]. It was evident in their report that air cooling after controlled rolling proceeds in the two-phase region (austenite-ferrite), whereas accelerated cooling is performed in the single-phase (austenite) through the two-phase region typically at a rate of 10 to 30 ℃/s. For pipeline steel grades X70 and X80, they noticed mainly ferrite, bainite, and residual martensite-austenite phases after accelerated cooling. This highlights the limitation of controlled rolling alone as a technique that improves strength mainly by grain refinement, whereas accelerated cooling goes a step further by enhancing toughness through microstructural transformation [19]. The schematic diagram in Fig. 1.2 indicates a possible microstructure evolution form from either accelerated or controlled cooling. At the initial stage of the TMCP process, the steel slab is reheated up to 1100 – 1200 ℃ to generate austenite grains with diameters of approximately 100 – 200 μm. According to Vervynckt *et al.* [19], an exponential relationship exists between the grain size and the reheating temperature. Thus, an optimum temperature that guarantees micro-alloying elements going into solution should be chosen for reheating. The next operation after reheating is roughing. During this process, preliminary rolling reduction is carried out above the non-recrystallization temperature (T_{nr}) to reduce the recrystallized austenite grain size to about 30 – 40 μm. Thereafter, finishing rolling is performed in the non-recrystallized temperature range (i.e. below T_{nr}) down to the austenite-ferrite phase transformation region (A_{r3}) depending on the desired microstructure. It is clear in Fig. 1.2 that the controlled cooling route ultimately results in larger grains (4 – 8 μm) of ferrite and pearlite within the steel structure. Comparatively, an accelerated cooling method manifests relatively smaller sized grains (0.5 – 2 μm), which are basically ferrite and bainite. The occurrence of pearlite in the controlled rolled structure is mainly attributed to the ease at which

carbon diffuses from one place to another under high transformation temperature [1]. Then, air cooling after the process keeps the steel plate at a high temperature for a reasonable amount of time to allow the accumulation of carbon around the mid-thickness region. Contrarily, it is less likely for carbon segregation to occur in accelerated cooled steels, since temperature reduction occurs at a faster rate during this process. One can see in Fig. 1.2 that the accelerated cooling approach led to a sharp drop from ferritic into the bainitic zone, hence forming a ferrite–bainite microstructure. However, direct quenching after the rolling process will give rise to a purely martensitic microstructure, which is undesirable for pipeline applications. This implies that significant progress can be made in modern day pipeline manufacturing by considering the structure-property relationship in steel.

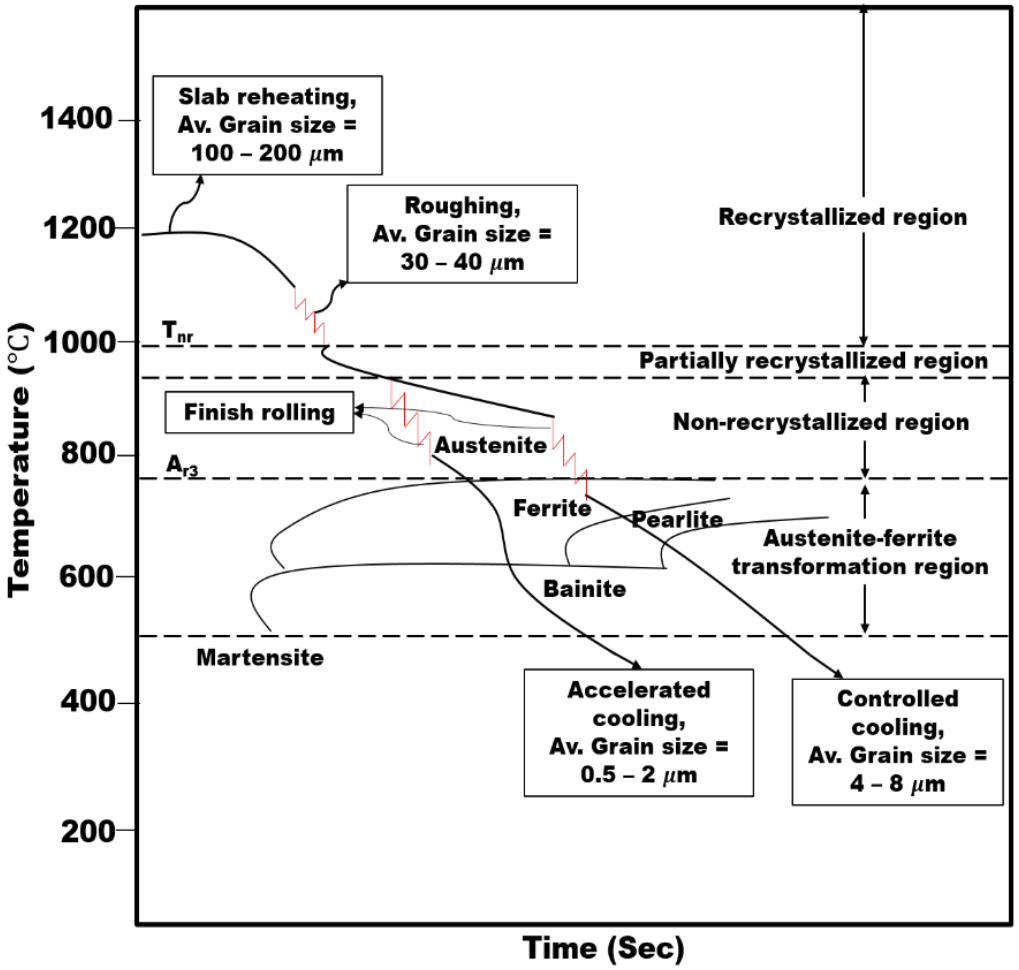

Fig. 1.2 Schematic representation of TMCP and the resultant microstructures from different processing routes (adapted from Refs. [27,47])

1.5 Motivation

Pipelines made of carbon steel are exposed to higher risks of failure when operating in severely corrosive environments. Some of these harsh environments contain hydrogen sulphide (H_2S) gas, chloride, and other forms of acids. It is highly probable that cracking will lead to catastrophic failure under such extreme service conditions, especially in H_2S (sour service) environments. A recent assessment established an estimate of $2,505 billion as the global cost of corrosion [29]. The report was based on details obtained from available information on type of failure. Such high cost accounts for 3.4% of the global GDP. Although it was mentioned that 15 – 35% of this cost can be reduced using current corrosion control strategies, such expenditure remains unsustainable for the world economy. In addition, most corrosion induced pipeline failures result in fatalities, economic losses, and environmental degradation. Thus, reducing corrosion in pipelines will boost the viability of many industries that transport fluids in one form or the other. For instance, some sectors of the world economy that can prosper through a robust pipeline operation include agriculture (food processing), mining/quarrying (natural gas, petroleum, and mining of other minerals), manufacturing (chemicals, petroleum refining, beverages, and pharmaceuticals), power (gas distribution and power generation), water supply, sewage transportation, waste management, and many others. With improvement in the quality of pipelines, all these industries can benefit from reduced operational costs and capital expenditures [30]. The implication is that pipeline steel processing must adapt towards the use of materials with enhanced corrosion resistance, thereby reducing the cost of corrosion indirectly.

In the pipeline market, preference is given to steel grades with excellent toughness, strength, and weldability. Due consideration should be given to the service environment when developing pipeline steel. The consequence of giving priority to strength without much regards to the potential operating surroundings of pipelines is that failure might be accelerated by environmental factors. Moreover, there is a disagreement between excessive improvement in mechanical properties and cracking in corrosive conditions. It has been established that high strength pipeline steels are prone to cracking in sour service [17]. This makes it insufficient to use tensile behavior alone to judge pipelines. Other criteria should be ensuring that characteristics of pipeline steel are favorable for their intended use in any specified situation. Also, some links have been noticed between cracking and other microstructural features like crystallographic texture and grain boundary characteristics

[15,31–34]. It is worth mentioning that controlling pipeline processing temperatures and including micro-alloying elements with precision has led to the creation of steel grades with outstanding properties [35,36]. The current study is expected to leverage on the correlation between the evolution of microstructure, texture, and deformation from the TMCP process to optimize pipeline properties. The goal is to propose necessary modifications in the thermomechanical treatment conditions for pipeline steel by experimentally investigating hydrogen assisted corrosion patterns with respect to structure. In addition, offering better understanding on the damaging effect of hydrogen on pipelines is the driving force behind this study. Therefore, the overall objective is to establish the damaging effects of hydrogen on pipeline steel, as well as to highlight the role of processing in limiting this problem. Considering the catastrophic failure that often occurs because of HE, the center of attention in this work is mainly on pipeline steel. However, other types of steels are occasionally mentioned in the literature review section. Despite numerous researches on this topic, many inconsistencies still exist. The crux of this research is to introduce a clearer view of HE in pipeline steel and offer a robust foundation towards the development of pipelines in the future.

1.6 Research objectives

The overall aim of this research is to experimentally investigate the behavior of pipeline steel produced using different thermomechanical processing routes. Variations in processing parameters will be applied with the intention of changing the structure of pipeline steels used for this study. To achieve this aim, the following specific objectives are undertaken.

1. Establish the role of microstructure and grain orientation on the electrochemical corrosion response of pipeline steel.

2. Determine the effect of different microstructural features on the hydrogen induced cracking behavior of pipeline steel.

3. Establish the effect of post-thermomechanical processing heat treatments on microstructure and hydrogen embrittlement behaviour of pipeline steel.

1.7 Research contributions

The findings from this research make novel contributions to knowledge. This investigation has further advanced the understanding of the hydrogen related failure mechanism in pipeline steel. Some of the key submissions from this study include:

1. Pipeline steel material with improved resistance to electrochemical corrosion and cracking in hydrogen environment has been produced.
2. Clearer understanding has been put forward on the role of microstructure and texture in improving hydrogen assisted degradation in pipeline steel. It is established that the interaction energy between selected iron crystals and corrosive species in hydrogen producing and non-hydrogen producing electrolytes is lowest on the (111) surface compared to (110) and (100).
3. A new post-processing annealing approach has been deployed in the development of dual-phase (ferrite and martensite) microstructure in pipeline steel. It is also established that susceptibility to hydrogen attack is reduced due to ferrite grain refinement within tempered martensite network. The significant increase in ductility at the expense of tensile strength was found in the dual-phase steel.
4. The research gaps identified during the literature survey presented in Chapter 2, as well as the initial research questions specified in the objectives, has been addressed by the findings presented in this work.
5. The results obtained from this study, including a detailed review of already existing knowledge in this field, has been published in several academic journals and presented in two international conferences. Each published article is duly cited as a footnote at the beginning of the chapter, but a list of publications is presented as Appendix A, as well.
6. Above all, the current research confirms that the service environment is of paramount importance during the production, grading, and marketing of pipelines. Also, microstructure, grain orientation, tensile properties, grain boundary distribution, grain morphology, inclusions, and precipitates are necessary considerations for assessing the suitability of pipelines for hydrogen related service environments. The results have shown that it is possible to enhance pipeline resistance to failure through processing.

1.8 Thesis outline

This thesis discusses the effects of various thermomechanical processing treatments on the electrochemical corrosion and hydrogen induced cracking behavior of API 5L X70 pipeline steel under static condition and tensile loading. The outline of this thesis is as follows:

1. In Chapter 2, a detailed review of important studies carried out in the field of hydrogen assisted failure of pipeline steel is presented. Information was also collected on the mechanisms associated with different forms of environmental assisted cracking and other causes of hydrogen related damages in steel. Finally, some experimental techniques for assessing the effect of hydrogen in steels were also explored. This chapter has been published by *International Journal of Hydrogen Energy*.
2. Chapter 3 presents the pipeline steel materials and the experimental procedures adopted for this study. These include the chemical composition of pipeline steel, and various thermomechanical and annealing treatment conditions applied during processing. The techniques used for characterizing test materials are also discussed.
3. The focus in Chapter 4 is on the influence of thermomechanical processing and crystallographic orientation on the corrosion behavior of API 5l X70 pipeline steel. This chapter specifically addresses Objective #1 and has been published in *Metallurgical and Materials Transactions: A.*
4. In Chapter 5, the results obtained from investigating the effect of warm rolling parameters on microstructure development and electrochemical corrosion response of API 5l X70 pipeline steel are reported. These are additional results related to Objective #1, which has now been publication in *Metallurgical and Materials Transactions: A.*
5. Chapter 6 addressed the influence of thermomechanical controlled processing on microstructure and hydrogen induced cracking susceptibility of API 5l X70 pipeline steel. Results from this evaluation satisfies Objective #2 and has been published in *Journal of Materials Engineering and Performance.*
6. More results obtained on hydrogen induced cracking susceptibility of API 5L X70 pipeline steel in relation to microstructure and crystallographic texture developed after different thermomechanical treatments are discussed in Chapter 7. These findings are also related to Objective #2 and have been published in *Materials Characterization.*

7. The development of microstructure and texture for improved resistance to hydrogen embrittlement in API 5L X70 pipeline steel was reported in Chapter 8. This chapter addresses objective #3 by applying changes to pipeline steel structure through post-processing annealing treatments. The results are now published in *Materials Characterization*.
8. Finally, the overall conclusions from this study and the recommendations are provided in Chapter 9. Also, some future perspectives on hydrogen embrittlement mechanisms and related issues in steels are mentioned.

CHAPTER 2 : LITERATURE REVIEW

2.1 Hydrogen related degradation in pipeline steel: a review [1]

2.2 Overview

The objective of this chapter is to evaluate previous research works that have been done on this subject to date. Some updates have been made to this section to include more recent literatures that are not featured in the original manuscript. The following are major changes that where made:

a) The section containing future perspectives and opinions on hydrogen embrittlement mechanism and related issues is now shown as part of Chapter 9.
b) Table 2.2, 2.5 and section 2.12.1 within this thesis are not part of the published manuscript.
c) Also, Fig. 2.12 is not part of the published manuscript, but has been reproduced with permission from Elsevier (Appendix C).

To support our increasing demand for energy, steel pipelines are deployed in transporting oil and natural gas resources for long distances. Numerous steel structures experience catastrophic failure due to hydrogen emanating from absorption of varying amounts of hydrogen in their service environments by corrosion reactions or cathodic protection. This process results in deleterious effect on the mechanical strength of these ferrous steel structures and their principal components. The major sources of hydrogen in offshore/subsea pipeline installations are moisture as well as molecular water reduction resulting from cathodic protection. Hydrogen-induced cracking comes into effect as a synergy of hydrogen concentration and stress level on susceptible steel materials, leading to severe hydrogen embrittlement (HE) scenarios. This often manifest in the form of induced-crack episodes, e.g., hydrogen induced cracking (HIC), stress-oriented hydrogen induced cracking (SOHIC) and sulfide stress corrosion cracking (SSCC). In this work, we have outlined sources of hydrogen attack as well as their induced failure mechanisms. Several past and recent studies supporting them have also been highlighted in line with understanding of the effect of

[1] This chapter has already been published, but was used with permission from *Elsevier* (Appendix B): E. Ohaeri, U. Eduok, J. Szpunar, 'Hydrogen related degradation in pipeline steel: A review', *International Journal of Hydrogen Energy*, 2018, Vol. 43, No 31, pp. 14584-14617

The PhD candidate E. Ohaeri compiled the information preseneted in this review, as well as finalised the manuscript after revision.

hydrogen on pipeline steel failure. Different experimental techniques such as *Devanathan–Stachurski* method, thermal desorption spectrometry, hydrogen microprint technique, electrochemical impedance spectroscopy, electrochemical noise, and X-ray tomography have proven to be useful in investigating hydrogen damage in pipeline steels. This challenge has necessitated our coverage of relatively comprehensive assessments of hydrogen effects on contemporary high strength pipeline steel processed by thermomechanical controlled rolling. The effect of HE on cleavage planes and/or grain boundaries has prompted in depth crystallographic texture analysis within this work as a very important parameter influencing the corrosion behavior of pipeline steels. More information regarding the roles of microstructure and grain boundary interaction have been presented in relation to the mechanisms of crack propagation. Since hydrogen degradation is accompanied by other corrosion-related causes, this review also addresses key corrosion causes affecting both onshore and offshore pipeline structures fabricated from steel. We have also enlisted and extensively discussed several recent corrosion mitigation trials and performance tests in various media at different thermal and pressure conditions.

2.3 Background

The continuous exposure of pipelines to severe conditions results in many unprecedented failures, due to hydrogen-induced damage. Diffused hydrogen can cause different forms of crack-related pipeline failures. In order to avoid these problems, steel plates used for pipeline production are subjected to critical processes during thermomechanical controlled processing (TMCP) [3]. Various processing parameters are optimized to enhance pipeline steel capabilities during steel manufacturing. The most important parameters that are often controlled during steel processing are rolling temperature, cooling temperature, and precise addition of micro alloying elements [35]. Changes in these process conditions combined with appropriate chemical composition has led to the development of pipeline steel grades bearing outstanding mechanical properties, while conforming to API 5L specifications [36]. However, improving mechanical properties of pipeline steel results in a knock-on effect on corrosion properties and susceptibility to cracking. Therefore, it may not be enough to categorize pipeline steel based on their strength, toughness and weldability alone. Additional criteria should be to ensure that the properties of pipeline steel are favorable for intended use within defined service environments.

The need to understand the deteriorating effect of hydrogen and develop pipeline steel with superior resistance to hydrogen embrittlement (HE) is the driving force behind this review. The focus of this research covers the application of TMCP as a means of microstructure control, crystallographic texture evolution and engineering grain boundaries to impact crack resistance. The overall aim is to make the reader aware of damaging effect of hydrogen on steels. Considering the catastrophic failure that often occurs because of HE, our center of attention is mainly on pipeline steel. However, other types of steels are occasionally mentioned. First, this work will discuss the general idea of corrosion, pipeline integrity management and different forms of hydrogen related degradation. The mechanisms and various factors that influence hydrogen attack will be surveyed. Then, insights will be provided on the experimental techniques for detecting hydrogen and evaluating susceptibility of steel to crack. Other potential causes of hydrogen degradation such as different kinds of microbial induced corrosion will later be introduced. Despite numerous researches on this topic, many inconsistencies still exist. The crux of this review is to introduce a clearer view of HE in pipeline steel as part of a robust foundation in the design and production of crack resistant pipelines in the future.

2.4 Concept of pipeline corrosion

Before delving into discussing hydrogen degradation, it is important to understand the overall principles of corrosion in pipelines. In general, corrosion is defined as material degradation because of environmental influences. In more specific terms, it refers to an electrochemical process involving electron release due to metal dissolution at an anodic site and subsequent electron transfer to cathodic sites where oxygenated water is reduced to hydroxyl ions (OH^-). Hydrogen ions (H^+) may also be chemically converted to gaseous hydrogen [11]. The important reduction-oxidation (redox) processes involved in the corrosion process are represented by two half-cells and overall reactions as presented in Eqs. 2.1-2.5.

Anodic reaction:

$$Fe \rightarrow Fe^{2+} + 2e^- \text{ (Iron dissolution)} \quad (2.1)$$

Cathodic reactions:

$$2H^+ + 2e \rightarrow H_2 \text{ (Hydrogen reduction)} \quad (2.2)$$

$$O_2 + 2H_2O + 4e^- \rightarrow 4OH^- \text{ (Oxygen reduction in neutral and alkalis media)} \quad (2.3)$$

$$O_2 + 4H+ + 4e^- \rightarrow 2H_2O \text{ (Oxygen reduction in acidic media)} \quad (2.4)$$

Overall corrosion reaction:

$$Fe + 2H^+ \rightarrow Fe^{2+} + H_2 \quad (2.5)$$

The two electrodes (cathode and anode) are often located on the pipeline surface, and an electrolyte is necessary for any corrosion process to proceed successfully. The electrolytes complete the electric circuit in a corrosion cell by providing a transport medium for ions. Oil and gas transmission pipelines carry fluids mixed with corrosive agents like hydrogen sulfide (H_2S), carbon dioxide (CO_2), sand, microbes and other organic compounds. A different form of material loss known as sweet corrosion, manifest in CO_2 containing pipelines, while sour corrosion proceeds in the presence of H_2S in pipelines. For this review, our focal point will be limited to the form of corrosion often witnessed in sour environments. When the electrolyte (i.e. pipeline fluid) is contaminated with poisonous species, corrosion degradation tends to advance more rapidly. From H_2S, which is a weak acid, hydrogen ions are potentially produced, while iron sulfide (FeS) formation can be promoted within the corrosive media as shown in Eq. 2.6. The sulfide corrosion product passivates pipeline steel at low temperatures, provided chloride ions and oxygen are absent; otherwise, it may form a galvanic couple with the pipeline steel to exacerbate localized corrosion damage [37].

$$Fe + H_2S \rightarrow FeS_{(s)} + H_2 \quad (2.6)$$

The atomic hydrogen released during the corrosion process described in Eqs. 1-5 will either recombine to form molecules (Eqs. 2.7 and 2.8) on the pipeline steel surface before diffusing away or migrate into the structure where they recombine at defects [38,39]. The favorable hydrogen recombination spots within pipeline steel microstructure are referred to as *hydrogen trap sites*, which will be addressed in subsequent sections of this review. In an event of hydrogen entry into pipeline steel embrittlement and/or blistering might set in, followed by sudden failure.

$$H^+ + e^- \rightarrow H_{ads} \text{ (hydrogen atom)} \quad (2.7)$$

$$H_{ads} + H_{ads} \rightarrow H_2 \text{ (hydrogen molecule)} \quad (2.8)$$

Pipeline operators carefully adopt formulated management strategies aimed at controlling material loss in form of corrosion and sudden failure. These management procedures help to ensure the all-round integrity of in-service pipelines, not only against hydrogen related degradation. It is also a means of ensuring safe operations and profitability.

2.5 Pipeline integrity management

Pipeline infrastructures are key to providing the much-needed fuel for economic growth. This makes it imperative that integrity of pipeline structure and all related operational processes should be paramount. An important way of maintaining optimum output from in-service pipelines is by implementing suitable pipeline integrity management program [40–43]. Series of activities involved in a typical pipeline integrity management process are outlined on the flowchart depicted in Fig. 2.1. It is important to assess the corrosion risks of the pipelines through regular in-line inspections and external corrosion assessment to achieve an effective integrity management plan. Some common external corrosion monitoring techniques involve the use of ultrasonic probes, test coupons, electrical resistance probes, and linear polarization probes [44]. In-line inspection technologies (e.g. magnetic flux leakage tool, ultrasonic tool, and other smart tools) are cautiously used to identify locations of defects along the pipeline. A non-destructive testing (NDT) technique such as magnetic particle inspection (MPI) can then be applied to further asses any identified defect onsite [45].

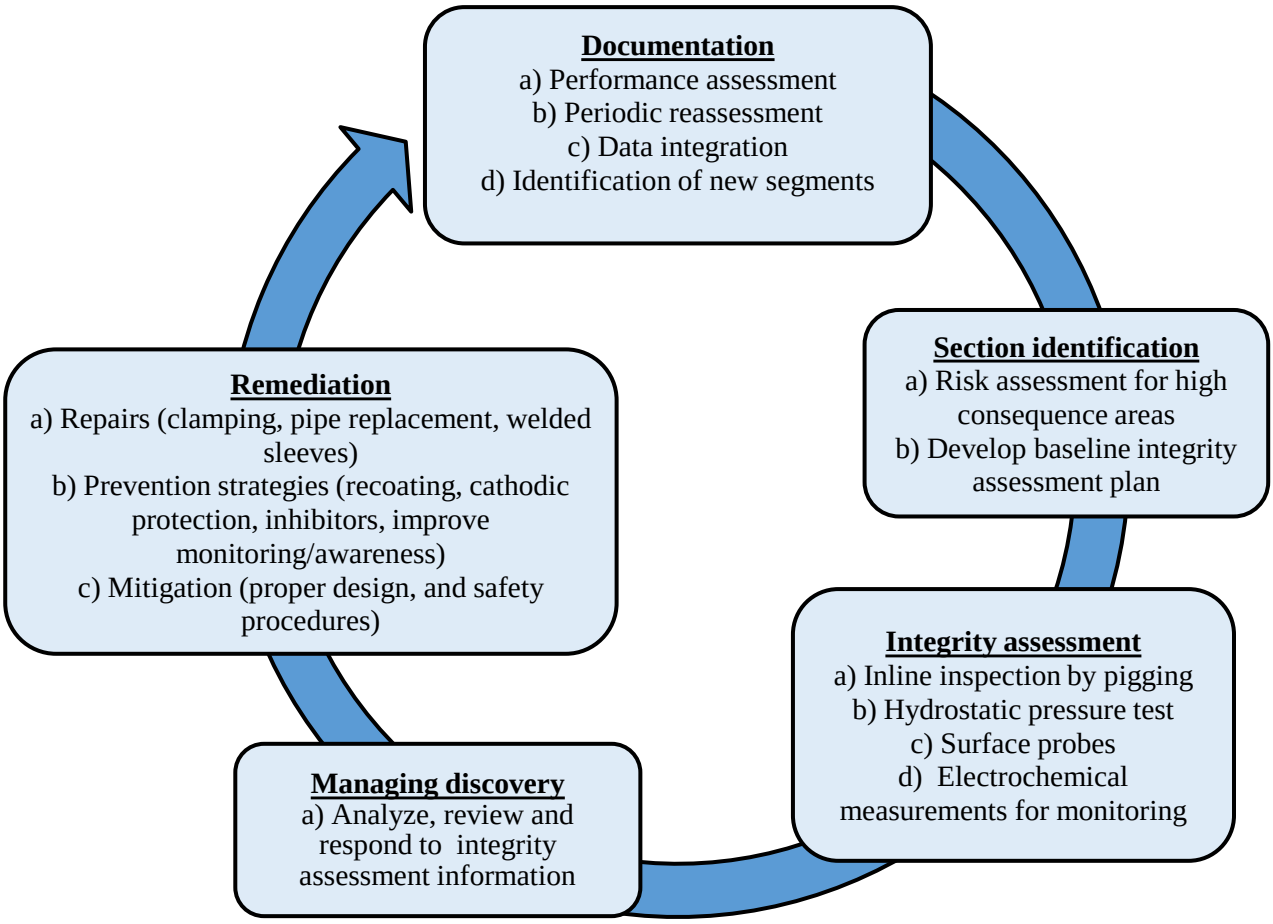

Fig. 2.1 Integrity management process (adapted from Refs. [40,46])

Integrity management also involves selecting appropriate pipeline material for every application. Ossai *et al.* [30] opined that during material selection a fair balance should be made between operational expenditure (OPEX) for pipeline operation and capital expenditure (CAPEX) required for pipeline construction. Their argument was that choosing materials which are less suitable for intended service conditions will cost less, but integrity management becomes too expensive in the long run. This is opposed to the fact that investing in more suitable material may cost more at the onset but will become cheaper afterwards due to minimal maintenance cost over time. However, it is difficult to achieve a good compromise between CAPEX and OPEX for pipelines operating in hydrogen damage prone environments. Some expensive corrosion resistant alloys may fail due to cracking under the influence of hydrogen, hence the need to investigate pipelines for

susceptibility to hydrogen degradation before they are selected for use. Nevertheless, operation cost may drastically decrease if the right type of material is chosen for pipeline construction.

Different monitoring techniques are employed to ensure protection of pipelines from hydrogen degradation. These procedures include regular in-line inspection to identify cracks before they reach critical levels, intermittent surveillance (ground and aerial) [42,43], coating and cathodic protection surveys, monitoring soil overburden and land slide around pipelines [46,47]. Some pipeline operators have resorted to combining different integrity assessment techniques to limit unwarranted failures. However, a more pre-emptive approach is to develop pipeline steel that are less prone to hydrogen degradation. Achieving this goal entails changing the steel structure and subsequently testing to ascertain the extent of resistance to hydrogen environment. The most important change will involve engineering steel materials to eliminate factors that support hydrogen attack. This requires adopting measures to limit hydrogen entry and developing pipeline steels with crack resistant structure [48]. Further tests should be carried out to determine the extent of diffusion and desorption of hydrogen within these materials. Also, different electrochemical measurement techniques have been proposed in the past for determining susceptibility of materials to hydrogen degradation [49,50].

2.6 Pipeline corrosion mitigation strategies

Various strategies can be applied in mitigating corrosion based on the risk level and/or extent of degradation. When choosing a mitigation strategy, due consideration must be given to the fact that the mechanisms associated with different forms of corrosion are not the same. A single strategy may not be the only required approach to guarantee the integrity of a pipeline. Also, a mitigation technique that offers protection against a form of corrosion can increase the risk of another; therefore, a detailed risk assessment would typically consider the practicality, suitability and cost effectiveness of any mitigation strategy before adopting it. The most familiar corrosion mitigation methods involve the application of external coatings, cathodic protection, internal lining, chemical treatment, operation control, changing the chemistry of electrolyte, suitable welding technique and appropriate material selection/design [44,51]. A brief summary of these mitigation methods is provided in Table 2.1.

Table 2.1 Summary of different strategies for pipeline corrosion mitigation

Corrosion mitigation strategy	Examples	Ref
External coating and cladding	a) First generation: asphalt, coal tar enamel, bitumen, heat shrink sleeves, wrapping tapes, single- and double-layer polyethylene, polyurethanes b) Second generation: multi-component liquids and single layer fusion bonded epoxy c) Third generation: Double layer fusion bonded epoxy, three-layer polyethylene, and three-layer polypropylene	[44,52–55]
Cathodic protection	Impressed current and sacrificial anode systems	[44,56,57]
Material selection	a) Use of reinforced composite and non-metallic pipelines (where applicable) b) Use of corrosion resistant alloys	[44,58,59]
Pipeline design	Application of corrosion risk-based design, which ensures additional allowance on wall thickness, easy operation, adequate maintenance, accessibility and efficient isolation (when out of service)	[44,60]
Operation control	Monitoring all relevant process parameter that influence corrosion (temperature, pH, fluid chemistry, flow rate, operating pressure, oxygen content, sand content)	
Internal lining	Internal coating of pipeline with polymeric material such as nylon	[44]
Chemical treatment	Addition of oxygen scavengers, biocides, corrosion inhibitors	[37,44,61]

2.7 Hydrogen degradation in pipeline steel

In general, the processing route adopted in the production of pipeline steel affects behavior in the service environment. There are insinuations that failure of pipelines either in the form of leakage or rupture may be due to material susceptibility (composition, microstructure), service environment (fluid composition, temperature, flow rate), and applied stress [5]. Fracture incidents in pipelines often occur due to ingress of atomic hydrogen into interstitial spaces. The following are some established means through which hydrogen migrate into steel structure [62]:

1. Absorption of molecular hydrogen from the atmosphere around the pipeline surface into the pipeline steel lattice.
2. Production and fabrication processes which introduce hydrogen into steel, and eventually cause embrittlement under favorable conditions (e.g. welding and heat treatment).

3. Presence of hydrogen-producing species, electrochemical reactions such as corrosion and/or precipitation of hydrides in hydride-producing elements.

For pipelines operating in H_2S-containing environments, the risk of cracking is very high. This is because it is highly probable that H_2S will poison hydrogen recombination process near the pipeline, leading to hydrogen attack. Eventually, the pipeline can experience leakage or rupture. The outcome is usually considerable economic losses to the pipeline operator and environmental degradation [63]. It is therefore necessary that pipeline steel be capable of withstanding severe environmental conditions. In most cases, cracking usually precede sulfide corrosion in high strength pipeline steel [64]; meaning that the mechanisms associated with various forms of hydrogen degradation are related. Nevertheless, the amount of microscopic defects formed while processing steel plates and the welding technique deployed in pipeline production are critical in ensuring that hydrogen atoms do not cause problems during service [5]. Some commonly reported forms of hydrogen related degradation in steels are discussed in the following chapters.

2.8 Forms of hydrogen related degradation

2.8.1 Hydrogen induced cracking (HIC)

To support our increasing demand for energy, steel pipelines are deployed in transporting oil and natural gas resources for long distances, but these pressing requirements have also forced steel deployments in harsh service environments. Pipeline failure mainly occur in two distinct modes: stress corrosion cracking (SCC) and hydrogen induced cracking (HIC). In as much as the former has been extensively reported in the literature [65–67], the insufficient coverage of the later calls for more studies of pipeline steel. In recent times, pipeline operators have recorded several catastrophic incidents because of HIC [68]. The major sources of hydrogen in offshore pipeline installations are moisture as well as molecular water reduction resulting from cathodic protection (CP). Cracking comes into effect as a synergy of hydrogen concentration and stress level on susceptible steel materials, leading to severe HE scenarios. The effect of migration of interstitial atoms (e.g. H, C, N etc.) on the physicochemical and mechanical properties of materials has been widely reported as time-dependent change [69]. The extent of atomic-lattice interactions of these atoms within materials depends on exposure period, ambient temperature as well as factors relating to the atomic size. Within the α-Fe lattice, H tends to become less soluble compared to N. Since the small atomic radius of H supports its mobility [70]. Steel-based material failures involving C

and N are associated with aging (followed by decreased ductility and hardness), while the presence of H could simultaneously soften as well as harden materials based on yield and tensile strengths [7,71–75]. These anomalies and others make it difficult to properly understand the degrading effects of H. This subject has become ambiguous even in recent times. There might be numerous studies related to hydrogen induced degradation, but in all, this subject is a complicated field with reports based on interpretations from small data sets and at times contradictory scientific views. Steel embrittlement is generally recognized as the effect of H-induced failure due to its deleterious consequence on ductility. Since the sensitivity to HE increases with increasing strength levels in steel alloys, the effect on their strength and microstructures is significant upon prolonged exposure. A few studies [76–78] have also revealed a correlation between HE susceptibility and microstructural constituents (pearlite, martensite, ferrite, bainite, etc.) as well as with other microstructural features (precipitates, grain boundaries, dislocations, incisions). These factors detect the mobility and distribution patterns of H within steel; since its atomic form is capable of existing between trap and lattice sites [79–81]. Rosenberg and Sinaiova [69] have recently studied the effect of hydrogen induced damage on some grade of steel using various techniques.

There are also situations where SCC may occur in the absence of hydrogen on pipelines. In such cases, passive film dissolution is considered responsible for crack propagation. Some commentators describe the combination of HIC and SCC as hydrogen-assisted stress corrosion cracking. Javidi *et al.* [82] revealed that anodic dissolution is paramount to stress corrosion cracking in near neutral pH environment, whereas a mix of hydrogen-based mechanisms becomes prominent at high pH. Also, crack propagation mode is often trans-granular in near-neutral pH conditions, but becomes intergranular at high pH [5]. For pipeline steel that is cathodically protected with highly negative applied potential, the susceptibility to hydrogen degradation is aggravated. Even pipeline coatings are not spared from hydrogen blistering attack, especially when cathodic potential is not properly controlled. This process known as *cathodic disbondment*, is fostered by interactions between pipeline coating and OH^- produced during water reduction [83]. At high cathodic potential, coatings experience accelerated water permeation at the edges, which culminates into pockets of hydrogen blisters and sites for localized hydrogen attack on steel [84]. There are also indications that high resistivity of coatings prevent permeation of cathodic current towards pipeline steel in the form of cathodic protection shielding, thereby increasing the chances of SCC [85]. A comparison between the cathodic shielding behavior of high density polyethylene

and fusion-bonded epoxy coatings on pipelines showed that high density polyethylene (HDPE) coating shielded cathodic protection current from reaching pipeline surface [86]. Therefore, pipelines coated with HDPE could experience hydrogen degradation under the coating. Fusion-bonded epoxy-coated pipeline steel allowed permeation of CP current. So, they offer better protection against corrosion compared to HDPE.

2.8.2 Sulfide stress corrosion cracking (SSCC)

HIC and SSC are the common failure routes that lead to HE in wet H_2S media containing steel oil and gas well lines [87]. Understanding SSC mechanism has led to the identification of a synergy of its key sources: susceptible microstructure, corrosive environment and tensile stresses. Since the microstructure of steels reveals their susceptibility to HE cracks, microstructural features play important roles in crack propagation [88]. It has been widely reported that bainite/martensite region with lower ductility are prone to SSC when compared with tempered martensite. This anomaly could be linked with a combination of strength and toughness factors in the presence of H_2S [89,90]. The martensite structures developed after subsequent quenching/tempering operations are refined and homogeneous, and these modification techniques can be controlled to produce martensitic steel materials with enhanced SSC resistance. The presence of some alloying elements (e.g. Nb, V, Mo and Ti) induces SSC resistance in steels at grain boundaries, and upon tempering, the precipitates formed by these elements limit diffusion and reduce the susceptibility of steel to SSC. Therefore, the hydrogen atoms generated at the surface of the steel substrates during cathodic reactions diffuse within the steel material, while the presence of H_2S and sulfide ions (HS^-) influence the combination of diffused atoms [91–93]. Diffused H atoms reside in reversible (e.g. lattice sites) or irreversible (e.g. inclusions) traps, though escape from the latter is possible at ambient thermal conditions. Liu *et al*. [94] have attempted to demonstrate the impacts of SSC on grain boundaries and dislocations of casing steel. Their results show that dislocations influenced SSC behavior much more than grain boundaries.

2.8.3 Stress-oriented hydrogen induced cracking (SOHIC)

Like HIC, sulfide stress cracking (SSC) occurs due to embrittlement associated with hydrogen trapping upon corrosion of pipeline steel by hydrogen sulfide (H_2S) [64,95,96]. There are two classes of SSC (Type I and II) [64]. When the formation of a hydrogen induced blister crack

(HIBC) formation aligns with the direction of applied stress, SSC could be classified as stress-oriented hydrogen induced cracking (SOHIC) or Type I. Its failure pattern may be in dual stages depending on the direction of crack propagation (parallel or perpendicularly) with respect to the applied stress. In the other form of SSC (Type II), cracking is propagated from typical HE. Even when the application of stress is the key distinction between HIBC (stress is applied) and HIC (propagated by internal crack; does not often require any external loading), they both resemble each other in some way: (a) their formation mechanism is better understood from internal pressure theory [9]; and (b) after crack nucleation, they are both propagated along the rolling direction of the steel material. This might not be all together advantageous. Even when HIC resistant steel grade materials have been considered as a solution to SOHIC, there is still no better understanding between HIC and SSC resistances in the SOHIC mode [97]. In fact, Cayard *et al*. [98] have also demonstrated that most HIC-resistant steel alloys may be more prone to SOHIC than some conventional ones; this further complicates the selection criteria for SOHIC resistant steel grades. Kim *et al.* [64] has detailed a correlation between HIC and Type I SSC in high-strength pipeline steel. In their work, the authors compared the resistance to SSC under applied stress condition with hydrogen charging.

2.9 Mechanisms of hydrogen related degradation

Hydrogen induced pipeline degradation is strongly dependent on the trapping behavior of the steel lattice structure. Various microstructures often found in pipeline steel consist of features which serve as potential traps for hydrogen. These trap sites include dislocations, grain boundaries, alloying elements, defects and interfaces as schematically presented in Fig. 2.2. Migration of hydrogen atoms into steel structure and consequent attraction towards crystal imperfections (grain boundaries, dislocations, vacancies, inclusions, precipitates) constitute the basis of hydrogen related degradation. Hydrogen and its isotope are among the smallest elements that are attracting a lot of research attention [9]. In view of the complexities associated with hydrogen related degradation mechanisms, it is important to understand the mode of transport and accumulation of atomic hydrogen to form molecules at defects. Locations within the crystal lattice where hydrogen atoms are less likely to pass through without being strongly trapped are regarded as irreversible trap sites (e.g. inclusions interfaces) [48]. This relates to the high potential energy barrier of these sites, which must be overcome to allow escape of hydrogen atoms. Strongly irreversible hydrogen

traps like martensite interface and mixed dislocation core usually possess binding energy in the range of 61.3 – 62.2 kJ/mol [99]. Even higher hydrogen trap binding energy of up to 89.1 – 89.9 kJ/mol were measured by the same authors at grain boundaries with high misorientation and undissolved carbides. Therefore, the belief is that hydrogen atoms trapped irreversibly are excluded from those diffusing through the steel. On the contrary, atomic hydrogen trapped at sites requiring relatively lower potential energy barrier to permit escape are considered reversible trap sites. For instance, the activation energy for hydrogen trapping at dislocations and grain boundaries are below the 61.3 kJ/mol threshold. The indication is that both features are reversible trap sites. Table 2.2 presents a summary of important hydrogen traps often recorded in steel. Strong presence of reversible traps has been noticed in cold rolled pipeline steel [100,101]. Enough plastic strain is impacted in cold rolled steel to cause multiplication of dislocation, hence increase in reversible traps. Meanwhile, detection of hydrogen atoms during their interactions with the steel structure is complicated. Some available characterization techniques are grossly limited in their abilities to analyze hydrogen because of its low atomic number. For instance, diffraction by electrons and X-rays are best suited for heavier atoms, which produce strong scattering compared to the lighter atoms like hydrogen. However, neutron diffraction has shown significant promise in the study of hydrogen interactions with metallic compounds [102,103]. The main challenges associated with neutron sources include cost of generation, accessibility to users, and controlling beam penetration.

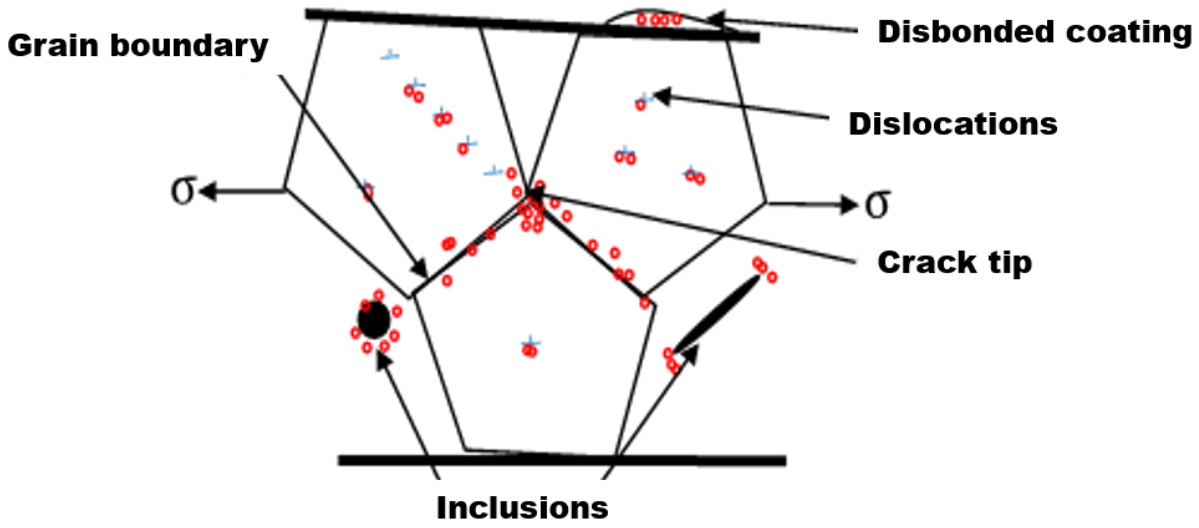

Fig. 2.2 Schematic representation of hydrogen trapping at various sites in pipeline steel (adapted from Ref. [107])

Table 2.2 Summary of different microstructural features and their hydrogen trapping properties

Microstructural features	Trap type		Activation energy (kJ/mol)	Ref
	Reversible (diffusible)	Irreversible (non-diffusible)		
Structural defects				
Dislocation	yes		26.8 (for pure iron)	[104,105]
1) Dislocation (elastic field)	yes		0 ~ 20.2	[106]
2) Screw dislocation (core)	yes		20 ~ 30	[106]
3) Mixed dislocation (core)			58.6	[106]
Vacancies			44	[106,107]
Grain boundaries	yes		17.2 (for pure iron)	[104,105]
Micro-voids		yes	35	[104]
Microstructural phases				
Retained austenite	-	yes	54	[104]
Ferrite-cementite interfaces	yes	-		[104]
Carbide interface			67 - 94	[108]
Cementite	yes		18 – 18.35	[104,108]
Austenite-ferrite interfaces		yes	52	[108]
Non-metallic inclusions/precipitates				
TiC	-	yes	87	[104,108]
MnS	-	yes	72	[104,108]
FeO, Fe_2O_3	-	yes	47	[104,108]
Al_2O_3			78.96	[108]

Among all the potential trap sites, grain boundaries are the most efficient interface for trapping hydrogen in steels [62]. The number of traps that are present within the microstructure in each steel grade and their role in hydrogen damage remain controversial within the scientific community. There are claims that high presence of strong (irreversible) hydrogen traps will increase the amount of hydrogen present within steel, but will also reduce diffusible hydrogen within the lattice [48,109–111]. The suggestion is that this situation starves the steel lattice of the much-needed hydrogen for crack initiation and propagation. Therefore, trapped hydrogen atoms

are regarded as less likely to cause degradation. The proposed idea suggests that recombination of atomic hydrogen within irreversible traps produce less offensive hydrogen molecules and impede their diffusion through interstitial spacing towards crack susceptible regions. It is also believed that widely distributed irreversible trap site could potentially diminish hydrogen from reversible traps; hence lower the chances of HE [22]. Whereas, reversible traps with low binding energy allow more hydrogen permeation through steel, thereby increasing crack susceptibility [112]. Interestingly, Dadfarnia *et al*. [113] used numerical simulation to establish that higher density of a particular type of trap can lower effective diffusion, but it does not necessarily affect amount of hydrogen diffusing through normal interstitial lattice sites or other kinds of traps. Although it is generally believed that accumulation of hydrogen in traps could result in internal pressurization and crack initiation at high stress concentration zones [114], many hydrogen trapping and embrittlement mechanisms that are proposed are still at variance. There are a lot of doubts about multiplying irreversible traps as a way of minimizing reversible hydrogen trapping.

Leading to HE, cracks initiate in a susceptible material from a combination of defined amounts of hydrogen and critical stress levels. This notion may be widely accepted, but to date, the exact HE mechanism is still a subject of intense debate [115]. Earlier suggestions indicate possibilities of restricted or promoted dislocation motion under the influence of hydrogen within interstitial spaces in steel. This view is supported by reports on decreased cohesion between cleavage planes and/or grain boundaries due to hydrogen [116]. In line with this, several theories and models have been brought forward, and two of them have been ranked as hypotheses with certain advanced level of acceptability for the case of HIC-led degradation of steel. The first is the Hydrogen Enhanced Decohesion (HEDE) model, which proposes that bond strength (i.e. the energy to fracture) is reduced by interstitial atomic hydrogen [65–67,117]. The second model proposes that occurrence of localized plastic deformation is due to hydrogen-induced dislocation processes. This is the Hydrogen-Affected Localized Plasticity (HALP) models, pioneered by Beachem [118], with two more modified variations in recent times: Hydrogen Enhanced Localized Plasticity (HELP) [119,120] and Adsorption Induced Dislocation Emission (AIDE) [116,121]. Currently, it is proposed that no one mechanism comprehensively explains the phenomena associated with HE; different systems are being explained by different theories or a combination of several of them depending of which fits a case. With recent advancements in fractographic analysis, the role of

hydrogen in localized mobility of dislocations around crack tip have been elucidated under the following principal mechanisms for hydrogen-related degradation [14,116,122–124].

2.9.1 Hydrogen enhanced decohesion (HEDE) model

Hydrogen-induced weakening of metal-metal bonds leads to decohesion instead of slip. This mechanism is described as Hydrogen Enhanced Decohesion (HEDE) and it is characterised by smooth brittle fracture surfaces with limited plasticity. HEDE model is one of the most frequently proposed mechanisms of steel HE. Decohesion as a factor of HE links material failure with reduction in atomic bond strength because of hydrogen segregation at defined interface (e.g. grain boundary). When applied stress (σ_{app}) is in a magnitude greater than the cohesive strength (σ_{coh}) along interfaces, the presence of impurities reduces the gross cohesive strength resulting in the initiation/propagation of interfacial cracks [125]. According to Birnbaum [126], concentration of atomic hydrogen decohesion events could manifest at a few locations: (a) at crack tips as adsorbed species, (b) at particle-matrix pivots ahead of cracks, especially where dislocation shielding effects leads to the utmost tensile stress, and (c) at locations of utmost hydrostatic stress. Compared to HELP, HEDE has few recorded experimental evidences especially in sub-grain boundaries and trans-granular fracture of micro-alloyed steel according to Katzarov and Paxton [125]. The authors also investigated HEDE within bcc α-Fe (111) crystal planes.

2.9.2 Hydrogen enhanced localized plasticity (HELP) model

HELP is the second most-referred to mechanism, which manifests as crack propagation via coalescence of micro voids in a localized manner, hence the name Hydrogen Enhanced Localized Plasticity (HELP). It proposes that within defined temperatures and strain rates, atomic hydrogen inside the structure of materials decrease dislocation motion restraints, leading to increasing deformation at localized regions [119]. With these sites close to fracture surfaces, the damage process is not an embrittlement but rather a localized plastic-type fracture [127,128]. Both HEDE and HELP are seemingly unrelated, just like the theories associated with them. For HEDE, there must be decohesion for cracking to exist. The plasticity of steel might be affected due to hydrogen, causing minimized obstructions and enhanced dislocation velocity. As dislocations continue to interact, they begin to pile-up at microstructural defects, and this may contribute to material failure

[129]. Katzarov *et al*. [125] have provided detailed studies of HE analysis via hydrogen enhanced localized plasticity; they have also outlined the effect of hydrogen on the velocity of screw dislocations in α-Fe. A few questions remain unanswered when considering the effect of hydrogen-induced crack enlargement. For instance, what is the role of hydrogen in plasticity enhancement as well as fracture (knowing that plasticity is linked with toughness via tip blunting)?

2.10 Factors that affect hydrogen embrittlement

Many conditions influence susceptibility of pipeline steel to hydrogen related degradation. These factors can be broadly classified into corrosive environment, material characteristics and tensile stress. In this section, details about some of these conditions were reviewed with specific attention on material requirements for pipeline steel.

2.10.1 Microstructure

Thermomechanical processing leads to a wide range of microstructures and anisotropy of mechanical properties in high strength pipeline steels. These steels are often comprised of ferritic pearlite, polygonal ferrite, quasi-polygonal ferrites, Widmanstätten ferrite, acicular ferrite, bainitic ferrite, bainite and martensitic microstructures [26,130]. The formation of each or a mixture of these microstructures is dependent on steel processing parameters, especially the cooling rate applied after hot rolling [131,132]. Fast cooling rates and low transformation temperatures produces bainitic ferrite, followed by acicular ferrites in decreasing order. Retained austenite and/or martensite-austenite islands are commonly found dispersed within acicular ferrite and bainitic ferrite microstructures. On the other hand, higher transformation temperatures and slower cooling rates often generate polygonal ferrite microstructure. A study [133] documented resistance to hydrogen damage in pipeline steel containing bainitic and/or acicular ferrite microstructures; this aspect was correlated to the presence of retained austenite and microstructural homogeneity of the pipeline steel. It was further highlighted that retained austenite was most preferable for HIC resistance compared to cementite-containing microstructures. In contemporary high grade TMCP pipeline steels, lower bainite is usually dominant [134,135]. Thermomechanical processing routes that involve starting cooling at relatively low temperature can improve the chances of obtaining high fraction of ferritic phase and excellent deformability in X80 pipeline steel [136]. In addition, lower ‘end cooling temperature’ produced more bainitic lathes with enhanced mechanical

properties in X120 pipeline steel, while higher ‘end cooling temperature’ generated a granular banite microstructure in the same pipeline steel. The authors attribute the excellent toughness in X90 – X100 pipeline grades to dominance of bainitic lathes and presence of alloying elements like molybdenum and boron that restrain ferrite nucleation. Typical microstructures corresponding to these pipeline steel grades are presented in Fig. 2.3.

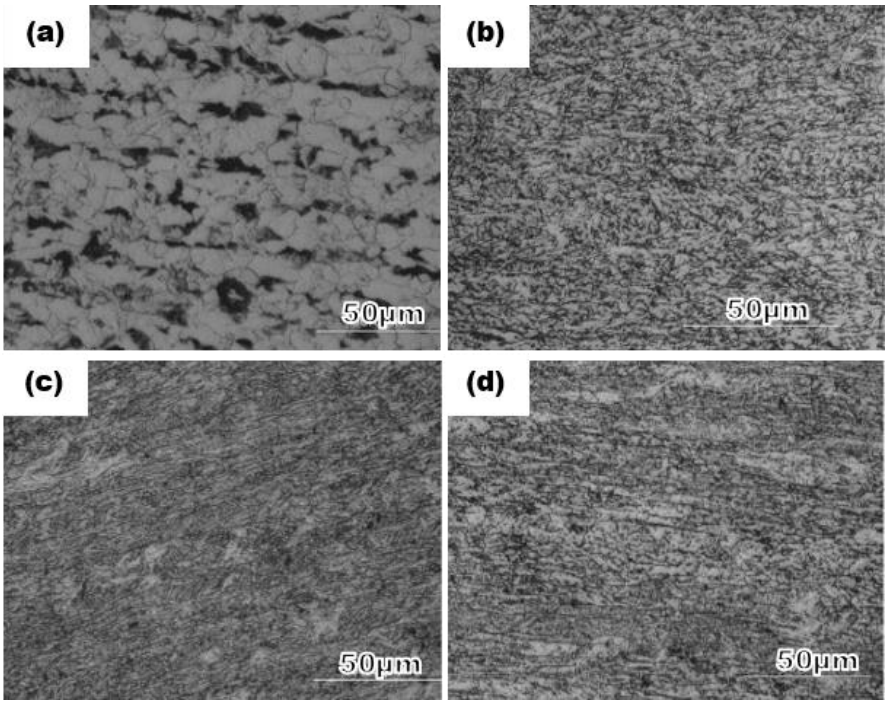

Fig. 2.3 Optical micrographs of pipeline steel grades showing (a) ferrite-pearlite microstructure in X65 (b) ferrite-bainite microstructure in X80 (c) mainly bainitic microstructure in X90-X100 and (d) uniform bainitic microstructure in X120 [139]

It is noticeable in Fig. 2.3a that the microstructure of X65 pipeline grade stands out from the rest. This is obviously a result of the processing conditions which gives rise to the ferrite-pearlite microstructure. Such kinds of banded microstructural phases are common features in lower grade pipeline steels like X52, X60 and X65. Studies have shown that microstructural banding comprising of ferrite-pearlite phases heighten susceptibility to hydrogen blistering [137]. However, the same authors claimed that supplementary thermomechanical processing resulted in different microstructures ranging from equiaxed ferritic pearlites, ferritic granular bainite and banitic ferrite. They noticed that the newly developed microstructures drastically reduced the blistering effect of hydrogen. Other examples of such ferrite-pearlite banded microstructure has

been reported in the literature [138]. Fig. 2.4a and 2.4b presents more pronounced pearlite bands uniformly distributed across the microstructure of X52 pipeline steel in comparison to X60, which is slightly of higher strength. Similar microstructural segregation have also been observed in other pipeline steels [114,139]. It is common to witness HIC along these banded regions. An example is shown in Fig. 2.4c where a crack is seen to have propagated along the ferrite-pearlite banded zone of X60 pipeline steel. One main reason for this phenomenon is higher hardness around the pearlite band, which is responsible for stabilizing crack propagation within the region. Remirez *et al.* [140] evaluated the role of different microstructures, mainly ferrite, bainitic-ferrite and martensite, on susceptibility of pipeline steel to hydrogen degradation. They observed that the presence of martensitic phase in pipeline steel increased susceptibility to hydrogen damage. Their finding explains the fact that martensitic microstructures are highly strained with a lot of interstitial carbon trapped within its lattice; thus, hydrogen attack is promoted. Secondly, the distribution of austenite and carbide within the martensitic lathes enhanced hydrogen diffusion in steel. So, it was concluded that segregation of carbon along the grain boundaries plus high energy stored in martensite will predispose pipeline steel to hydrogen attack.

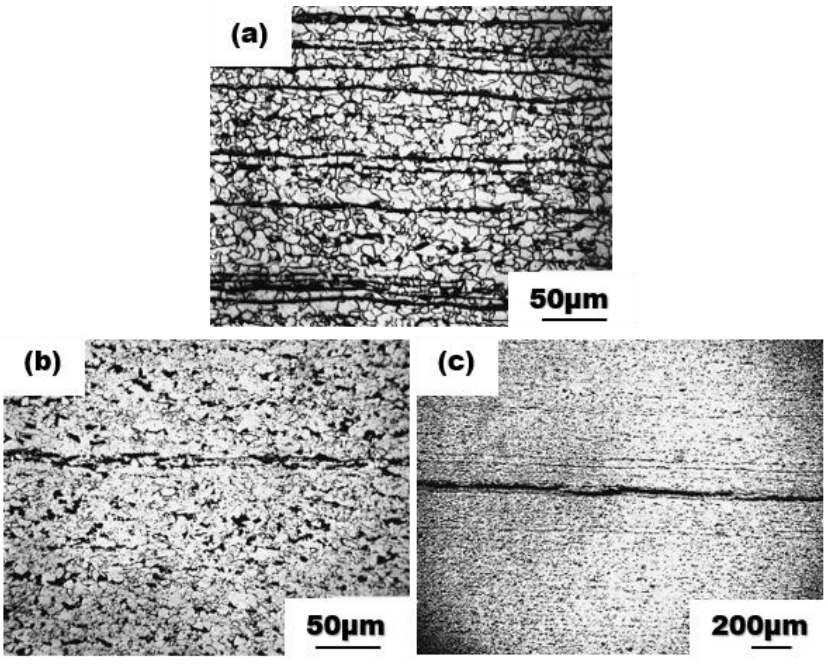

Fig. 2.4 Optical micrographs of pipeline steel showing (a) uniform distribution of pearlitic bands across X52 (b) segregation of pearlitic bands in X60 (c) crack at the ferrite-pearlite banding in X60 [141]

2.10.2 Mechanical properties

To achieve the desired mechanical properties for designated service environment, certain microstructures are more preferred than others. It has already been established that high presence of acicular and bainitic ferrite in the microstructure is beneficial in terms of grain refinement, strengthening and increasing dislocation density [141]. These microstructural features are favorable for excellent toughness in high grade pipeline steel. However, one should mention that higher strength often compromise resistance to HE. Pipeline steel with a bainitic microstructure will typically have good mechanical properties, but at the expense of its resistance to hydrogen degradation [17]. Hydrogen related degradation is manifested in the form of ductility loss and can be measured in terms of area reduction after tensile test. This phenomenon has been clarified in X60, X80 and X100 pipeline steel grades [142]. Results of this study, which is shown in Fig. 2.5, indicate similarity in the embrittlement pattern of the three pipeline steels when tested with hydrogen charging current density below 0.1 mA/mm^2. However, higher hydrogen charging current density of 0.66 mA/mm^2 caused more embrittlement in the stronger pipeline steels compared to the others. This is evident in relatively lower reduction in area values measured for X100 and X80 pipeline grades at 0.66 mA/mm^2 charging current respectively.

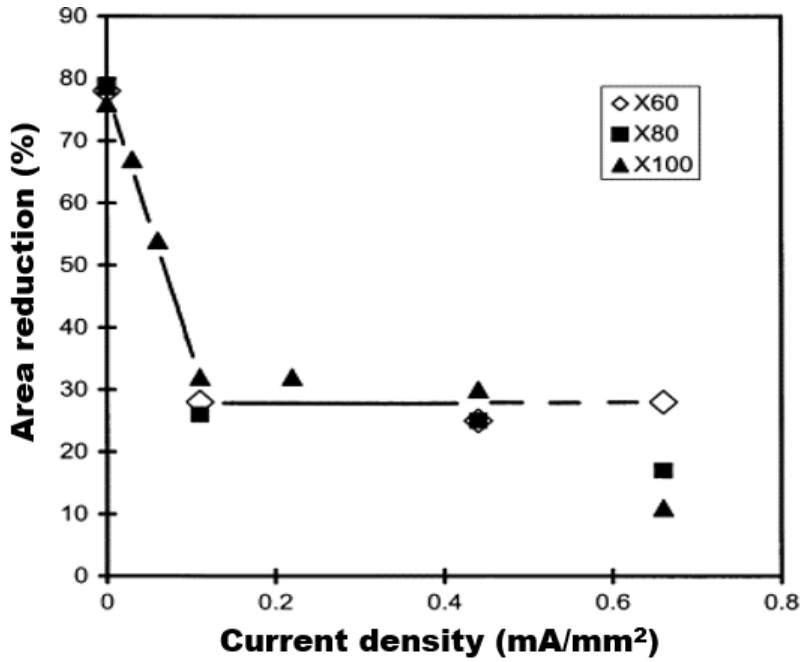

Fig. 2.5 Variation pattern of area reduction with hydrogen charging current density in pipeline steels [145]

Another comparative study on ferritic-bainite steel, dual-phase steel, high strength low alloy (HSLA) steel and transformation induced plasticity (TRIP) steel also showed similar hydrogen embrittlement-strength relationship [143]. The embrittlement index for the TRIP steel was the highest compared to other steels after hydrogen charging. An explanation put forward by the same authors was pronounced structure-related hydrogen solubility in the TRIP steel. Considering the ease of embrittlement in materials with face centered cubic (FCC) structure compared to those with body centered cubic (BCC) structure, it was not surprising that the TRIP steel showed higher degree of hydrogen related degradation. The difference in hydrogen diffusion pattern in different types of steel during tensile loading also affects their failure pattern. It is noticed that significant increase in hydrogen diffusion occur at the elastic deformation stage prior to plastic deformation [144,145]. The reason is that passive film formed on the steel surface at the elastic loading stage is highly unstable. Therefore, hydrogen permeation is highest before the plastic deformation stage is reached. There could even be more intense hydrogen diffusion at the early stages of tensile deformation depending on microstructural features (grain morphology, grain boundary, phase distribution, grain orientation etc.) that are present within the steel structure.

2.10.3 Grain boundary character

The distribution of grain boundaries is a major concern for pipeline steel designated for hydrogen prone environment. Considering that there is a tendency for hydrogen atoms to accumulate at grain boundaries, it is of interest to engineer grain boundaries that limit hydrogen attack on pipelines. Thermomechanical treatments are often designed to increase the amount of low angle grain boundaries (LAGB) and special coincidence site lattice (CSL) boundaries in steels [146]. These boundaries have low energy and are less susceptible to hydrogen attack. Therefore, risk of HIC becomes significantly reduced in pipeline steels with higher fraction of LAGB and CSL. It is reported elsewhere that more high angle grain boundaries (HAGB) was observed at the surface of X65 pipeline steel, but their number decreased towards the mid-thickness region where LAGB and CSL boundaries were dominant [147]. This result is clearly depicted statistically by the fractions of various types of grain boundaries measured at four (4) different locations from pipeline outer surface towards mid-thickness (Fig. 2.6a). Strikingly, the same study found that intergranular stress corrosion cracking got arrested at some special CSL boundaries with sigma-values below Σ13b. Their conclusion was based on high volume fraction of mainly Σ13b, Σ11 and Σ3

CSL grain boundaries found around the crack tips as shown in Fig. 2.6b and 2.6c. Further analysis to determine crack propagation pattern along grain boundaries confirmed that HAGB having angle of misorientation (θ) greater than 15º promoted crack propagation and branching; whereas, situations where crack encountered triple junctions consisting of LAGB and HAGB, deflection of crack propagation path tends towards the HAGB as indicated in Fig. 2.6d. Furthermore, Arafin and Szpunar noticed some deviations from the identified crack propagation pattern at certain grains where the crack path became discontinuous. Such behaviors were attributed to crack propagation beneath or above the grains (the so-called 3-dimensional effect), essentially causing the disappearance of the crack on the 2-dimensional surface being studied.

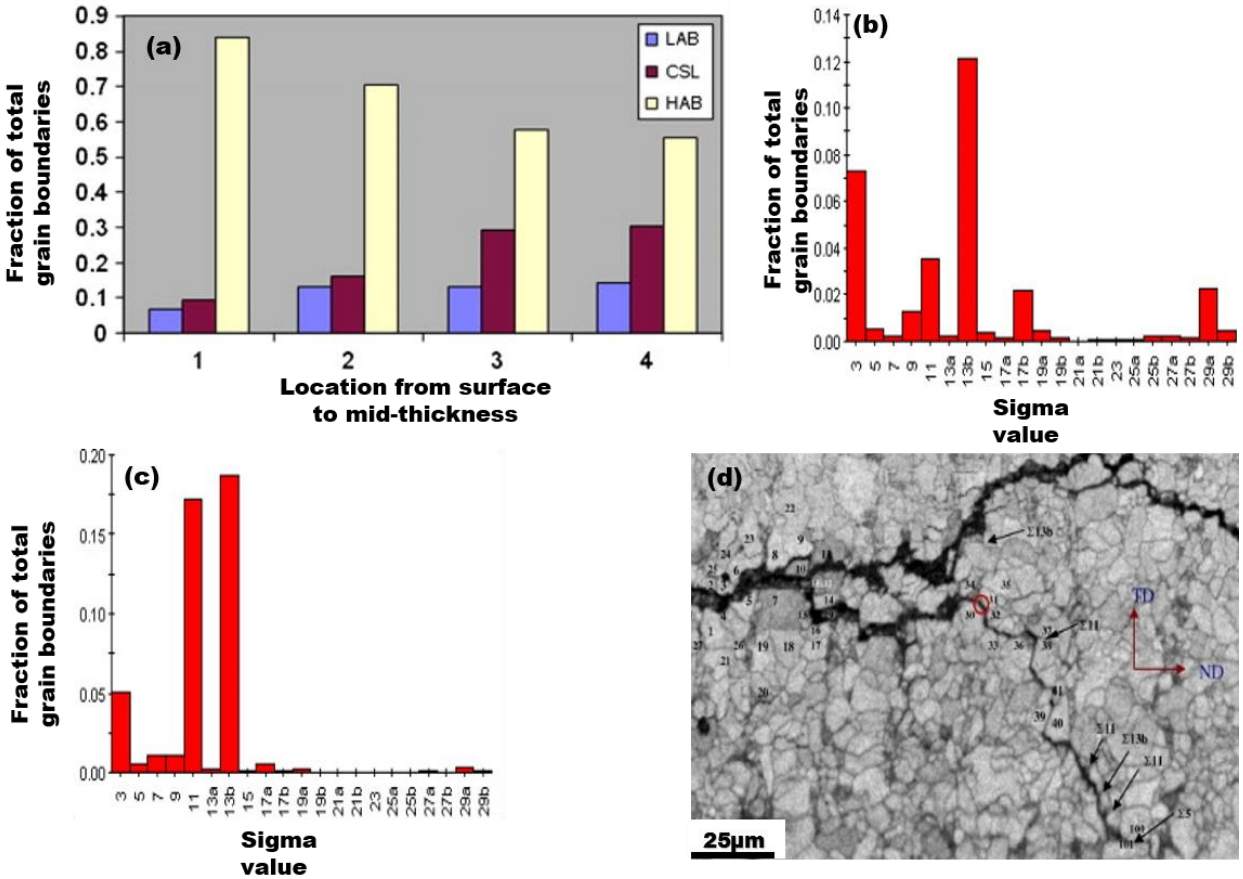

Fig. 2.6 (a) Grain boundary distribution from surface (location 1) to mid-thickness (location 4), (b-c) shows distribution of CSL boundaries at crack-tips, and (d) EBSD IQ map showing crack pattern along grain boundaries [150]

It is worth mentioning that the fraction of CSL boundaries found in pipeline steel is often low due to reduced stacking fault energy. Also, formation of these special boundaries is associated with twinning, which is difficult to achieve in pipeline steel [148]. The contributions of both low energy grain boundaries (LAGB and CSL) in lowering HIC has continued to feature prominently in literature [34,149–151]. Apart from the low energy of LAGB and CSL, another feature observed by Saleh *et al.* [151] was that these boundaries constitute reversible hydrogen trap sites; they do not allow the buildup of atomic hydrogen up to critical levels where cracks begin to initiate. Instead, they promote uniform hydrogen distribution across the pipeline steel structure and subsequently allow desorption to occur without increasing probability of cracking. Some researchers [34] have proposed warm (ferritic) rolling as a means of generating higher fraction of crack resistant LAGB in pipeline steel. Others researchers [150] have traced the crack resistance of $\Sigma 11$ type CSL boundaries to the fact that they are present around grains having $< 110 >$ oriented planes. Notably, Wright and Field [152] earlier suggested that a combination of crystallographic texture and grain boundary modification has prospects of impacting corrosion resistance in polycrystalline materials. A recent study [153] reported a relationship between electrochemical corrosion response of pipeline steel and different microstructural features such as crystallographic orientation and grain boundaries character developed from different TMCP routes.

The use of modern imaging techniques provides additional proof on the influence of hydrogen on crack initiation and propagation through grain boundaries. Several studies have used transmission electron microscopy (TEM), electron backscatter diffraction (EBSD) and electron channeling contrast imaging (ECCI) to probe the interactions of hydrogen with dislocation pile-ups at grain boundaries in steels [154]. An interesting work by Koyama *et al.* [155] clarified the role of grain boundaries on hydrogen-assisted degradation mechanism in twinning-induced plasticity (TWIP) steel using some of the earlier mentioned techniques. Their results showed clearly that HIC initiated and propagated at grain boundaries. Fig. 2.7a shows crack initiating at a triple junction before propagating along grain boundaries. Moreover, these authors found majority of micro cracks along HAGB as indicated in the EBSD inverse pole figure (IPF) maps obtained from both ND-TD (Fig. 2.7b) and RD-TD (Fig. 2.7c) planes respectively.

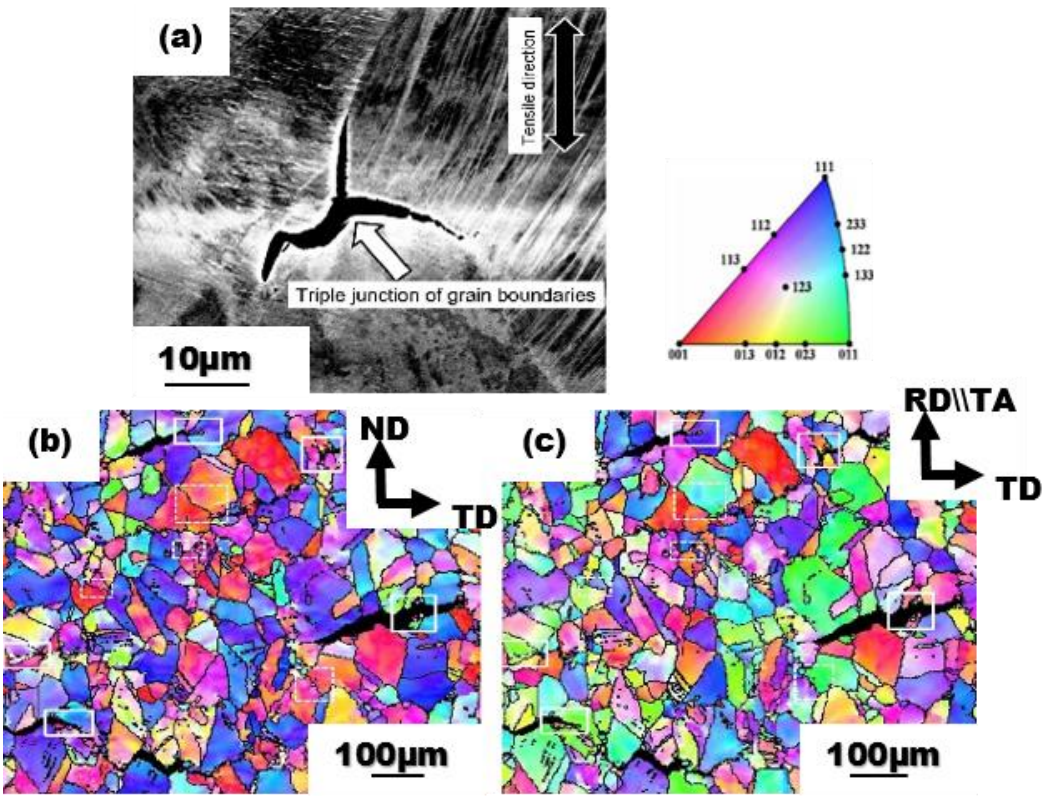

Fig. 2.7 HIC stricken TWIP steel (a) intergranular crack at a triple junction (b-c) IPF maps of fractured tensile specimen for ND-TD and RD-TD planes [157] (ND: normal direction, TD: transverse direction RD: rolling direction TA: tensile axis)

2.10.4 Crystallographic texture

Preferred orientation of grains, also known as texture, is an important factor that influence hydrogen related failures in pipeline steels. The process of thermomechanical treatment on pipeline steel results in extensive deformation, recrystallization, phase transformation and changes in grain size and shape [156]. All these processes alter the structure and affect performance of pipeline steel in various service conditions. For instance, grain size control and increase in dislocation density offer potential in for strengthening of pipeline steel. Also, inhomogeneity of grain characteristics coupled with through-wall texture variations can influence crack initiation and propagation in pipelines [157]. In spite of non-uniformity in the texture after hot rolling, it has been discovered that boundaries between grains containing $\langle 110 \rangle$ and $\langle 111 \rangle$ planes oriented parallel to the pipeline steel surface, are more resistant to hydrogen related degradation [150,158]. Lavigne *et al.* [157,159] demonstrated this using reconstructed three-dimensional crack images

obtained from cracked X65 pipeline steel using X-ray microtomography. They noticed that cracks started off perpendicular to the pipe outer surface but deviated out of its path on approaching the mid-thickness region (Fig. 2.8a-2.8c). Similarly, Arafin and Szpunar [147] discovered that texture was responsible for changes in intergranular SCC crack propagation pattern of X65 pipeline steel. They noticed some cracks were arrested at regions containing HAGB, which contradicts the belief that such boundaries promote crack propagation. Remarkably, texture analysis at different cracks and the corresponding regions around their crack-tips revealed the following new understanding. The cracks propagated through mainly grains with {100}||RP (rolling plane), as was determined from texture measurements performed at the cracked region (Figs. 2.8d and 2.8e), However, texture analysis at crack tip region indicate mostly the presence of {110}||RP oriented grains (Figs. 2.8f and 2.8g). Based on their observation, it was concluded that cracks were arrested at grains with {110}||RP texture. The results collected by the same authors also highlighted the idea that grains bounded by crack resistant CSL boundaries (e.g. Σ13b and Σ11) were predominantly {110}||RP and {111}||RP oriented grains. Although they claimed to have studied a total of 18 different cracked zones and the corresponding crack-tips, more studies will be necessary to clearly establish this finding in other pipeline steel grades. Apart from intergranular SCC, it will also be interesting to understand the role of crystallographic texture in either promoting or reducing other forms of crack related failure mechanisms. In all, these findings emphasize the possibility of optimizing {111} planes parallel to pipeline steel surface as a means of reducing susceptibility to cracking.

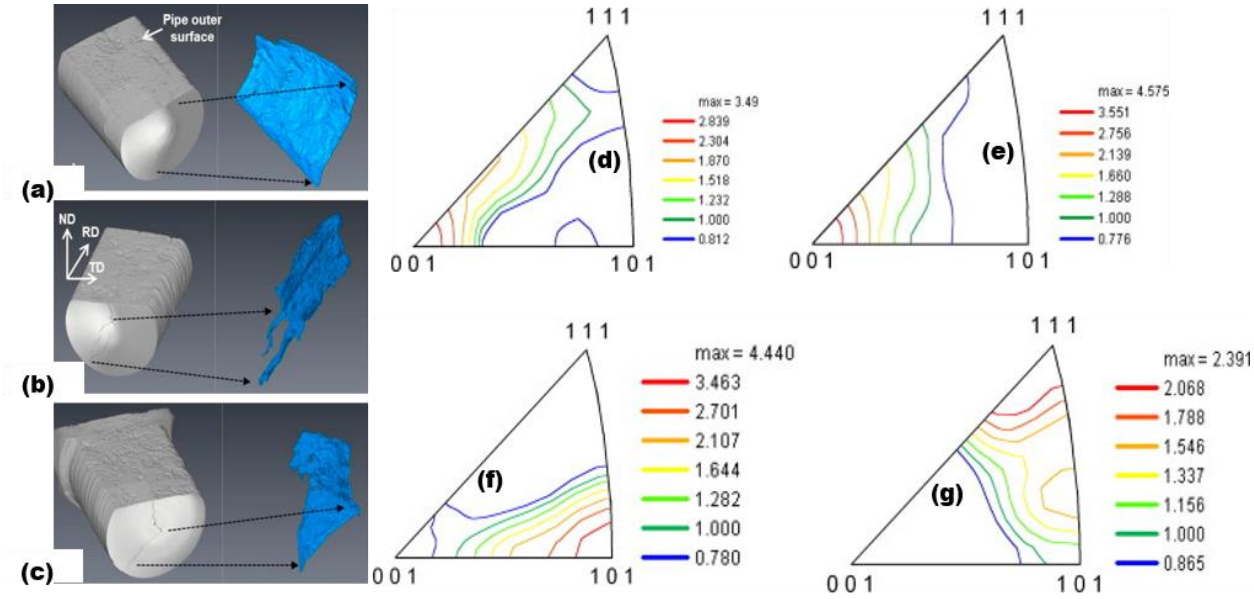

Fig. 2.8 (a-c) X-ray microtomography images showing deflected cracks and volumetric segments of cracked area [161], (d, e) IPF of cracked regions, and (f, g) IPF of region ahead of crack tips [150]

Some researchers have investigated the role of texture and grain boundary character on hydrogen-assisted degradation in pipeline steel. Masoumi *et al.* [160] reported preferential HIC propagation along regions dominated by small grains within X70 pipeline steel microstructure. Such regions were identified to contain more dislocations and grain boundaries, which constituted critical hydrogen trap sites and zones for HIC initiation and propagation in the steel structure as shown in Figs. 2.9a, 2.9b and 2.9c. The reason being that the high stored energy associated with small grains tend to promote cracking through such regions. However, there are opinions in the literature suggesting the possibility of cracks propagating along boundaries of ⟨111⟩||ND and ⟨011⟩||ND oriented grains contrary to the belief that these orientations offer resistance to cracking [114,147]. The understanding is that grain boundaries of crack resistant grains could be susceptible to cracking depending on their energies. An example is shown in Fig. 2.9d where HIC initiated at ⟨001⟩||ND oriented grain (red grain) but propagated through the boundaries of other grains with ⟨111⟩||ND and ⟨011⟩||ND orientation. The explanation offered in this case was that grain boundaries through which the crack propagated were mainly HAGB. Despite the crack resistant orientation of some grains, the crack continued to propagate because of the high stored energy associated with their boundaries.

Most pipeline steel currently in use are randomly textured with non-homogeneous grain morphology. Therefore, the results obtained from texture measurement vary significantly depending on the process history of the pipeline. Limited amount of data is generally collected through microstructural characterization. This makes it even more challenging to understand crack propagation mechanism in pipeline steel based on measurements performed on a small area. Nevertheless, many studies have correlated HIC to crystallographic texture in pipeline steel using EBSD technique [114,151,160]. The consensus is that a link exist between cracking/blistering and the microstructure inherent in TMCP pipeline steel [137,151]. Evidence for this was obtained from different X70 pipeline steel samples with microstructures ranging from equiaxed ferrite-pearlite (Fig. 2.9g), banded ferrite-pearlite (Fig. 2.9e), ferritic-granular bainite (Fig. 2.9f), and bainitic-ferrite (Fig. 2.9h). The authors observed that trans-granular cracks propagated in all steels except the one with bainitic-ferrite microstructure. However, the most sever cracking occurred in the pipeline steel with banded ferritic-pearlite microstructure. Hindrance to crack propagation was noticed at CSL and LAGB, but no dominance of a crystallographic orientation was seen on the crack path. What they saw was that cracks preferentially propagated through the best aligned slip planes, which corresponds to $\{110\}, \{123\}, \{112\}$ planes, as well as $\{100\}$ cleavage plane. Consequently, it was concluded that cracking was controlled by dominantly slip-based mechanism and less of cleavage. The absence of any prominent orientation along HIC propagation path has earlier been documented for X46 pipeline steel by Venegas *et al.* [149]. An interesting observation in their results is that the cracks aligned towards radial direction of pipeline in somewhat 'S' shape, which is considered an indication of crack connection. Also, pipelines experience hoop stress along its radial direction during service, which means that strain fields near cracks could potentially cause convergence of smaller cracks into larger ones.

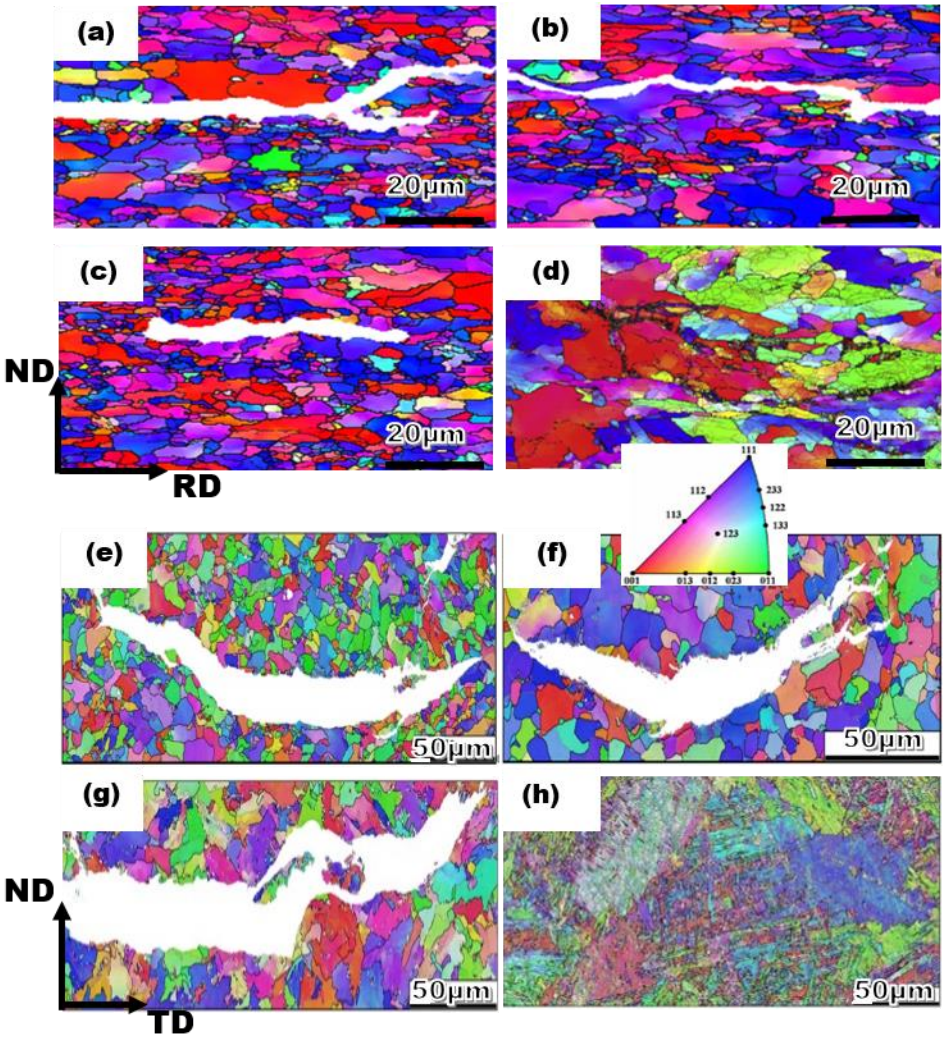

Fig. 2.9 EBSD IPF maps of X70 showing (a-c) cracks at areas having small grains [162], (d) cracks along boundaries of {100} grains [114], (e) banded ferritic-pearlite (f) ferritic-granular bainite (g) equiaxed ferritic-pearlite (h) bainitic-ferrite [154]

2.10.5 Inclusions and precipitates

It is difficult to fully understand the role of microscopic inclusions in crack initiation and propagation, because there are limited techniques available for studying HIC nucleation around them. However, it is established that non-metallic inclusions and precipitates aid hydrogen attack on pipeline steel by providing sites for accumulation of atomic hydrogen [32,161,162]. Inclusions are usually harder than the pipeline structure. As such they often create incoherent interface with pipeline steel matrix, which increase hydrogen trapping and cause failure by cracking [161]. The assumption is that inclusions having more coherent interface with pipeline matrix will tend to resist

crack initiation and propagation more than the incoherent ones. Particles which are either coherent or semi-coherent with the steel matrix often have lower binding energy compared to those that are incoherent [22,99]. An example is incoherent TiC precipitates, which traps hydrogen depending on temperature and volume of particles [163]. The authors attributed increased hydrogen trapping within incoherent TiC particle to high concentration of octahedral carbon vacancies in the semi-coherent particles with lower carbon vacancies. They also noticed an increase in the activation energy of hydrogen trapping at TiC interface with reduction in the coherency. Considering that pipelines operate under changing temperature, more research is required to fully establish how this affects the capacity of inclusions and precipitates to either function as reversible or irreversible trap sites. The schematic diagram in Fig. 2.2 clearly illustrates this phenomenon by depicting atomic hydrogen surrounding spherical and elongated inclusion. Consequently, voids which are created at inclusion/pipeline steel interface become trap sites for hydrogen. For elongated inclusions, hydrogen atoms tend to congregate more at the edges where stress concentration is usually higher. A widely accepted crack initiation mechanism around inclusions in pipeline steel is based on hydrogen migration into interfacial voids and pressurizing them under high strain conditions to form cracks [164]. Colonies of various kinds of metallic inclusions were observed along HIC propagation path in pipeline steel [165], and characterization of these inclusions showed that they contained mainly carbonitride precipitates of titanium (Ti), carbon (C), sulfur (S), nitrogen (N) and vanadium (V). In the same study, elongated manganese sulfide precipitates (MnS) were identified and were often responsible for crack initiation. A separate study [32] recognized three main inclusion types in X70 pipeline steel namely; carbonitride precipitates, sulfides and oxides. The authors argued that inclusion of oxides formed by aluminum (Al), calcium (Ca), manganese (Mn) and magnesium (Mg), which constituted 70 % of the total amount of inclusions, did not produce hydrogen related damage. Instead, they only gave rise to decrease in fracture toughness. The basis of their argument is that spherically shaped inclusions lack the ability to cause cracks according to the stress concentration theory. On the contrary, Jin *et al.* [164] concluded that spherical oxide inclusions of Al and Si were responsible for HIC as any other oxides of Ca-S-Al-O type and MnS found in X100 pipeline steel. Although this finding contradicts the strongly held opinion that spherical inclusions do not cause cracks, more studies have taken the same stance by associating oxide inclusions of Ca and Al with HIC in X70 pipeline steel [151,166]. Figs. 2.11a and 2.11b shows mainly MnS and aluminum oxide types of inclusions surrounded by porous voids

at the pipeline steel matrix/inclusion interface [167]. Both images indicate that crack nucleated at the cavities formed by poor adhesion of pipeline steel matrix and inclusion. In addition, Fig. 2.11e indicates HIC nucleating from oxide inclusions of Al and Ca, as well as carbonitride precipitates of Ti, Nb and V (Figs. 2.10c and 2.10d). It is evident from these findings that HIC is capable of nucleating and propagating across a majority of inclusion types, but there are still many disparities. Additional investigations will be helpful in explaining in-depth the interactions between inclusions and atomic hydrogen. Furthermore, the combined role of inclusions and other microstructural parameters in promoting crack propagation still requires further attention.

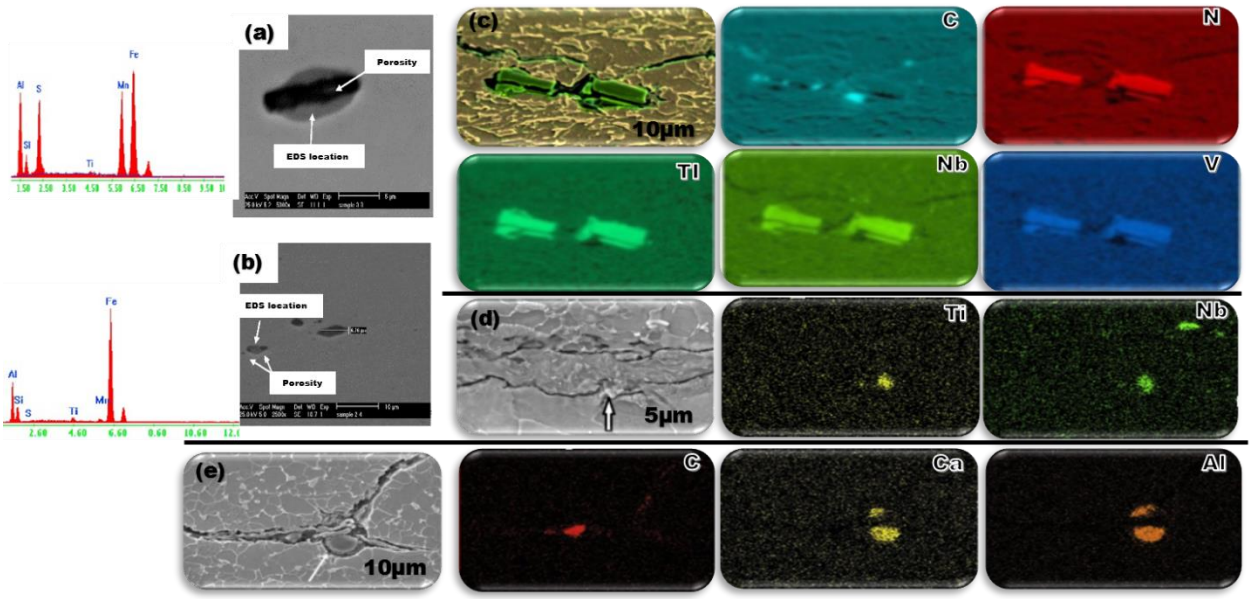

Fig. 2.10 EDS analysis on inclusions in X70 pipeline steel (a, b) point analysis at inclusions [169], (c) maps showing HIC nucleating at Ti-Nb-V enriched carbonitrides [124], and (d, e) Al-Ca-C enriched oxide inclusions [154]

It is important to mention at this point that quantity, shape, size and chemical composition of inclusions also affect hydrogen assisted damage in steels [168]. The major consideration when it comes to fracture toughness of pipeline steel is precipitate size, because of its contribution to strengthening. For instance, large sized Ti precipitates are less effective in pinning down austenite grain growth, hence this depletes fracture toughness [169]. Therefore, changes in composition and morphology of inclusions has been advocated for increasing toughness and resistance to HIC in pipeline steel. This is mainly because MnS inclusions easily become sites for hydrogen attack,

especially after being elongated by thermomechanical processing. Domizzi *et al.* [138] observed mainly elongated sulfide and alumina stringers as the dominant inclusions present within the microstructure of pipelines and pressure vessel steel plates as shown in Tables 2.3. According to their findings, less sulfide was present in the pressure vessel steel compared to the pipeline steel. No doubt, this is justified by the amount of sulfur used in micro alloying each steel plate (Table 2.3, column 7). Judging from the total length of inclusions per unit area, the X60 grades contain less sulfide than the X52 grades among the pipeline steel category, while the pressure vessel plates had generally lower length of inclusion. In the same vein, the longest alumina stringers were featured in the X52 grades. The interesting conclusion made from their work was that lower number of long inclusions will offer the same level of HIC resistance compared to larger number of short inclusions. The authors went further to suggest that increase in average length of inclusion (sulfide and alumina) increased susceptibility to HIC for each pipeline grade.

Alloying pipeline steel with Ca or rare earth elements is a way of forming calcium sulfide (CaS) precipitates, which is preferable than MnS. It can help in controlling the shape of inclusions and limit hydrogen attack. Globular inclusions in pipeline steel have been shown to be less susceptible to HIC compared to elongated MnS inclusions. This is because edges in the elongated inclusion often provide stress concentration zones for crack initiation [23]. Therefore, the overall aim of calcium treatment in pipeline steel is to develop more globular inclusions instead of the elongated ones [170,171]. The belief is that calcium captures sulfur during steel solidification and prevents precipitation of MnS inclusions. An investigation into the transformation mechanism of MnS inclusion in X80 pipeline steel found that Ti also plays a role in this process [172]. Ti does not only improve strength of pipeline steel through precipitation strengthening, it also helps in transforming MnS into less damaging titanium sulfide (TiS) and titanium carbosulfide ($Ti_4C_2S_2$) precipitates. Diminishing MnS precipitation will indirectly improve resistance of pipeline steel to hydrogen attack. The summary in Table 2.4 shows different inclusion types and their role in hydrogen assisted cracking.

Table 2.3 Sulfide and alumina inclusion analysis in different pipeline and pressure vessel steel plates [141][2]

Steel specification	Sulfide inclusion						Alumina stringers	
	Mid-thickness	Near surface	Average in thickness					
	LM^m (μm)	LM^s (μm)	LM (μm)	LA (mm/mm^2)	NA ($1/mm^2$)	Sulfur (wt. %)	LM (μm)	LA (mm/mm^2)
Pipeline steel plates								
API 5L X60			32.4±14.0	0.34±0.07	11.2±2.9	0.007	39.6±16.9	0.05±0.03
API 5L X60			16.7±4.3	0.21±0.05	12.7±0.1	0.007	23.0±15.4	0.06±0.05
API 5L X52	39.0±12	22.5±4.6	29.5±8.3	1.36±0.03	48.8±14.5	0.15	133.8±56.8	0.08±0.06
API 5L X52	18.1±5.7	18.2±3.7	18.7±4.2	1.12±0.07	61.1±10.6	0.15	155.4±108.9	0.08±0.06
Pressure vessel steel plates								
ASTM 516G70	31.5±4.1	30.5±6.7	31.8±1.8	0.19±0.04	5.9±1.3	0.005	0	0
F	20.0±2.1	12.8±1.1	15.9±1.4	0.14±0.02	9.0±1.6	0.009	19.7±16.3	0.06±0.07
G	14.1±1.5	10.9±1.0	12.2±0.9	0.50±0.08	41.6±6.9	0.010	0	0
H	10.7±2.8	8.9±1.7	9.8±2.3	0.48±0.07	52.2±18.5	0.010	0	0

[2] LM: average length of inclusion, LA: total length per unit area, NA: total number of particles per unit area, LM^m: average length of sulfide inclusion at mid-thickness, LM^s: average length of inclusion near surface

Table 2.4 Summary on inclusion types and their contributions towards hydrogen degradation in pipeline steel

S/No	Pipeline steel	Inclusion analysis technique	Inclusion types found	Findings	Ref
1	X70	SEM and EDX analysis after slow strain rate tensile test in acidic soil solution	Al and Si enriched inclusions	For cracks to initiate at inclusions, their morphology and composition should be such that encourage hydrogen trapping and pressure build up at interface. Si-enriched inclusions were quite coherent with pipeline steel matrix and did not initiate cracks, but cracks initiated at Al-enriched inclusion due to incoherency with pipeline matrix.	[173]
2	X100	SEM, EDX and localized electrochemical impedance spectroscopy (LEIS) techniques before and after immersion in NS4 solution (neutral pH bicarbonate solution)	Si-O enriched, Al-Si-S-Ca-O enriched, Mg-Al-Ca-O enriched, and Al-Si-Ca-O inclusions	Inclusions of Si-O type were coherent with steel matrix and did not result in any obvious localized corrosion. Whereas, other inclusions containing relatively less Si-O experienced localized corrosion attack after complete dissolution or fall-out of inclusions with increasing immersion time.	[174]
3	X100	Hydrogen charging with 0.1 M H_2SO_4 solution at different current densities in the absence of stress and inclusion analysis by SEM and EDX	Mixture of Ca-Al-O-S, MnS, and oxides of Al and Si inclusions	HIC occurred at critical hydrogen charging concentration of 3.24 ppm at mainly Si and Al oxide enriched inclusions instead of elongated MnS and Ca-Al-O-S inclusion. The reason being higher degree of non-cohesiveness between Si and Al inclusions.	[164]
4	X80	Electrochemical hydrogen permeation test in 0.5M H_2SO_4 and polarization measurement with SEM and EDX inclusion characterization.	Mainly Si and Al-Si enriched inclusions	The high presence of irreversible hydrogen traps (inclusions) at the weld heat affected zone predisposed pipeline steel to preferential anodic dissolution. Inclusion analysis showed that hydrogen related localized corrosion occurred mainly around those enriched with Si and Al-Si.	[175]
5	X120	HIC susceptibility measurement according to NACE TM0284-2003 and hydrogen permeation test.	Primarily Al_2O_3 or MnS inclusions	Microstructure and inclusions were significant in influencing HIC. Variations in amount of inclusions (irreversible trap sites) resulted in differences in HIC susceptibility for different X120 pipeline steel	[176]

		Microstructure and inclusion studies were performed with SEM and EDX respectively.		specimens (with varying alloying composition) as a result of changes in hydrogen diffusion pattern.	
6	X70	Electrochemical hydrogen charging with 0.5mol/L H_2SO_4 and AS_2O_3 p hydrogen permeation studies	Oxides of Ca and Al with nitrides of Ti and Nb	Uniform distribution of NbN and TiN was observed, but cracks were mainly associated with oxides of Ca-Mn-Al. Nitrides and carbide precipitates of Ti and Nb contributed to precipitation strengthening of pipeline steels. Also, observed precipitates are smaller than oxides or oxysulfides of Ca and can accommodate more hydrogen beside them to cause HIC.	[166]

2.10.6 Micro-alloying composition

Micro alloying is described as the process of adding smaller quantity of different elements into steels to achieve desired properties. Grain refinement in micro-alloyed steels is accomplished by grain growth control during recrystallization and austenite-ferrite transformation. Alloying elements such as Nb, Ti and V are added to pin down microstructural grain boundaries and restrict excessive grain growth in pipeline steel [177,178]. These elements also assist in eliminating other elements like C, N, S and P from solid solution during hot rolling process. The absence of Ti in solid solution limits carbide precipitation and diminish resistance to hydrogen degradation in steels [179,180]. Steels containing relatively high proportion of Nb in addition to minimal amount of Mn and P have shown significant improvement in mechanical properties [181,182]. Nitride and carbide forming elements such as Mo, V, Nb, Cr and Ti tend to lower the diffusion of hydrogen in steel lattice due to formation of precipitates that trap hydrogen, as well as enhance mechanical properties of steel [183]. Alloying with Ni can unfavorably impact on the resistance of steel to cracking in sulfide service environment [184]. This behavior is related to the ability of Ni to influence phase transformation in favor of martensite formation and increase susceptibility to HIC.

Significant progress could not have been made towards present-day pipeline steel development, while neglecting contributions from alloying elements. Advances in research trends include different alterations in the chemical composition of steel as shown in Table 2.5. Micro-alloying elements such as Nb, Ti and V are primarily added to form strain induced precipitates of nitrides and carbides (e.g. TiN, TiC, NbC, NbN, VC, VN), which pin down grain growth [185]. In addition, these elements enhance mechanical properties by combining to form complex compounds known as carbonitrides and/or carbosulphides such as (Ti-Nb-V)N,C and $Ti_4C_2S_2$ [186]. Although carbonitride nano-precipitates enhance tensile deformation resistance, they can also become initiation sites for cracking when formed in large sizes [187]. However, calcium is added to control the morphology of inclusions that may be responsible for the formation of crack-prone hardened zones within the steel structure [188]. Also, lower levels of sulfur are recommended to improve strength and toughness in pipeline steel. Despite the role of carbon as the main alloying element in steel, it has been considerably reduced to as low as 0.05 % in latest pipeline steel grades such as X80 – X120. Based on the consistent lowering of carbon content, newer pipeline steels are becoming more deformable and weldable.

Table 2.5 Typical composition of micro-alloying elements in each pipeline steel grades and their effect on thermomechanical processing

Micro-alloying element	Composition (wt. %)	Influence on TMCP	Ref
Nb	X65: 0.018 – 0.06 X70: 0.051 – 0.092 X80: 0.038 – 0.090 X100: 0.043 – 0.089 X120: 0.048 – 0.1	a) Grain refining and precipitation strengthening agent b) Prevents growth of austenite grains, while impeding continued recrystallization and recovery	[1,186, 189–191]
Ti	X65: 0.002 – 0.01 X70: 0.009 – 0.03 X80: 0.007 – 0.024 X100: 0.011 – 0.02 X120: < 0.015	a) Mainly refines grains b) Contributes towards ferrite strengthening	[19,191 ,192]
V	X65: 0.042 – 0.21 X70: 0.001 – 0.095 X80: 0.002 – 0.1 X100: 0.003 – 0.07 X120: < 0.025	Ferrite strengthening agent	[19,193]
Cr	X65: 0.02 – 0.157 X70: 0.007 – 0.266 X80: 0.015 – 0.12 X100: 0.016 – 0.42 X120: 0.22 – 0.42	a) Increases hardenability by delaying ferrite-pearlite transformation; thus, promoting formation of bainite and martensite/austenite constituents. b) Improves corrosion resistance c) Reduce susceptibility to hydrogen assisted cracking by impeding absorption of atomic hydrogen	[10,187 ,191]
Cu	X65: 0.02 – 0.31 X70: 0.006 – 0.27 X80: 0.015 – 0.20 X100: 0.25 – 0.46 X120: 0.010 – 0.015	a) Act as ferrite strengthener, by producing Cu-rich precipitates which act as strengthening agents. b) Improves corrosion and crack resistance by forming a thin protective layer of Cu at steel surface.	[10,19, 191]
Mo	X65: 0.005 – 0.14 X70: 0.01 – 0.3 X80: 0.05 – 0.3 X100: 0.19 – 0.43 X120: 0.01 – 0.40	a) Strengthens ferrite and stimulates formation bainite b) Promotes the formation carbides, which lowers coarsening of M_4C_3 (where M stands for Ti, V, Nb and Mo atoms). c) Enhances hardenability	[19,191 ,194]
S	X65: 0.0002 – 0.03 X70: 0.001 – 0.015 X80: 0.001 – 0.009 X100: 0.001 – 0.0024 X120: 0.010 – 0.015	a) Possess relative stability within precipitates during rolling at high temperatures, hence it restricts austenite grain growth b) Segregated Mn can recombine with S to form MnS inclusion, which aggravates HIC	[10,165 ,191]

C	X65: 0.041 – 0.17 X70: 0.037 – 0.125 X80: 0.028 – 0.142 X100: 0.025 – 0.1 X120: 0.027 – 0.05	a) Mainly controls strengthening mechanisms b) High tendency to segregate at high content to form hard bainitc and martensitic phases c) Formation of carbides which are potential hydrogen traps d) Reduced proportions improved weldability	[10,19, 191,194]
Mn	X65: 0.30 – 1.68 X70: 1.4 – 1.76 X80: 1.52 – 1.90 X100: 1.56 – 2.0 X120: 0.54 – 2.14	a) Solid solution strengthening agent b) Lowers the temperature at which ductile to brittle transition occurs c) Slows the rate at which austenite decompose during accelerated cooling d) Show strong segregation tendencies which increases the risks of HIC e) Eliminates hot cracking while forging f) Lower proportions help reduce segregation	[19,191 ,194]
Mn	X65: 0.30 – 1.68 X70: 1.4 – 1.76 X80: 1.52 – 1.90 X100: 1.56 – 2.0 X120: 0.54 – 2.14	g) Solid solution strengthening agent h) Lowers the temperature at which ductile to brittle transition occurs i) Slows the rate at which austenite decompose during accelerated cooling j) Show strong segregation tendencies which increases the risks of HIC	[19,191]
N		Promotes formation of nitride precipitates	[19]
Ni	X65: 0.005 – 0.8 X70: 0.02 – 0.23 X80: 0.02 – 0.75 X100: 0.13 – 0.54 X120: 0.017 – 1.35	Improves fracture toughness	[19]
Si	X65: 0.02 – 1.39 X70: 0.14 – 0.44 X80: 0.17 – 0.31 X100: 0.1 – 0.25 X120: 0.08 – 0.31	a) Removes oxygen from molten steel b) Aids in solid solution strengthening	[19]

Summation of Nb, Ti and V must not be more than 0.15%

For the pipeline steel designed to operate in mild H_2S service environment, alloying with Cu was found to lower the hydrogen diffusion as well as corrosion rate [195]. The authors reported that co-precipitation of iron sulfide (from dissolved ferrous ions) and copper sulfide films (from dissolved copper ions) formed on the steel surface was responsible for such behavior. Other authors [196] claimed that Cu addition produced good strength in X120 pipeline steel, because of Cu-rich precipitates found in its microstructure. These nano-sized precipitates were also beneficial as irreversible hydrogen trap sites, because they restrict hydrogen diffusion. This should indirectly reduce the risk of degradation. Other alloying elements have also indicated similar relationship

with hydrogen permeation in pipeline steel. Haq *et al.* [197] shown that low quantity of Mn gave rise to a more refined microstructure with lower hydrogen diffusivity in X70 pipeline steel; whereas, increasing the amount of Mn resulted in coarse grains and increased hydrogen diffusion. It is obvious that there is a delicate balance in determining the amount of micro alloying required to obtain the desired resistance to corrosion and cracking. More details about the effects of various micro-alloying elements in hydrogen degradation are featured in Table 2.6. Another approach to improving properties of pipelines in service environment could be to alter the microstructure using the thermomechanical treatment during manufacturing.

Table 2.6 Influence of increasing amount of specific pipeline micro alloying elements on properties associated with hydrogen degradation

Micro alloying elements	Hydrogen trapping	Hydrogen diffusion	Precipitation strengthening	Ref
Aluminum (Al)		Decrease		[183]
Molybdenum (Mo)	Increase		Increase	[183]
Manganese (Mn)		Increase		[197]
Copper (Cu)		Decrease		[183,195,196]
Niobium (Nb)	Increase	Increase	Increase	[179,180]
Chromium (Cr)	Increase	Decrease	Increase	[183]
Carbon (C)		Increase		[183]
Nickel (Ni)		Decrease		[183,184]
Titanium (Ti)	Increase		Increase	[179,180,183]
Silicon (Si)		Decrease		[183]
Vanadium (V)	Increase		Increase	[183]
Sulphur (S)		Increase		[183]
Phosphorous (P)		Increase		[183]

2.10.7 Temperature

The tendency for pipeline steel to undergo hydrogen damage during service is related to temperature. This behavior is attributed to the following reasons [183]*:*

1. Low mobility of atomic hydrogen within steel lattice at low temperature and
2. High mobility of atomic hydrogen with temperature rise. This is usually accompanied by reduced possibility of hydrogen recombination at defects.

Studies [198,199] have shown that increasing temperature around the pipeline results in decreased susceptibility to SCC. For pipelines operating in H_2S environment, resistance to degradation is believed to be optimum at temperatures ranging from 20º - 50ºC, because of the formation of

protective FeS film [200]. Above the identified range, spalling of passivation film may occur, leading to hydrogen ingress and subsequent increase in probability of failure.

2.11 Experimental methods for detecting and evaluating hydrogen degradation in steel

Investigation of pipeline failure mechanism requires experimental methods for measuring interactions of diffused hydrogen with pipeline steel under applied stress. Also, better understanding of hydrogen adsorption at defects within the pipeline steel microstructure is necessary. There are well established standards that are adopted for the experimental evaluation of different forms of hydrogen damage in metals. The common testing standards are NACE TM-0284 [201] for evaluating HIC susceptibility in pressure vessel and pipeline steels, NACE TM-0177 [202] for SCC assessment on metals in H_2S service environment, then NACE TM0198 [203], which is used to screen corrosion resistant alloys for SCC in sulfide containing oils fields. NACE standards specify the use of H_2S gas to simulate sour corrosion environment during test. Nevertheless, many researchers apply electrochemical hydrogen charging in place of gaseous hydrogen charging (with H_2S), because of safety concerns. However, reasonably good correlation has been established between results obtained for these techniques [204]. Most importantly, there must be a way of matching the results obtained from laboratory HIC assessment and real service conditions experienced by pipelines. The HIC propagation pattern can be predicted from experimental data using fracture mechanics [22]. Since hydrogen has a small atomic size, migration within the pipeline steel lattice is possible; hence there is a need for using sensitive measurement techniques in detecting hydrogen present inside steel. Some of these procedures are as follows:

2.11.1 Hydrogen microprint (silver decoration) technique

A commonly used method for detecting hydrogen at the microscopic level in steel is the hydrogen microprint technique (HMT) [205]. The uniqueness of HMT in comparison to other hydrogen visualization technique lies in its ability to show local distribution of atomic hydrogen. This technique involves the reduction of the silver ions (Ag^+) in silver bromide (AgBr) by absorbed hydrogen in order to produce chunks of metallic silver (Ag^0), which indicates hydrogen sites. This process is expressed by Eqs. 2.9 – 2.10.

$$AgBr + \frac{1}{2}H_2 = Ag^0 + H^+ + Br^- \quad (2.9)$$

$$Ag^{+} + H^{0} \rightarrow Ag^{0} + H^{+} \quad (2.10)$$

After the reduction of AgBr, a fixing solution comprising of 1.4 mol/l sodium nitrate ($NaNO_2$) and 0.6 mol/l of sodium thiosulfate ($Na_2S_2O_3$) is used to wash off unreduced crystals of AgBr form the steel surface in order to reveal only the reduced Ag^0 grains [206]. The grains of Ag^0 left on the steel surface after the reduction reaction are seen as markers of hydrogen exit at imperfections (e.g. areas of high strain concentration) on the microstructure of steel [107,207]. Also, the accumulation of more hydrogen at the grain boundaries shows higher trapping efficiency in comparison to other trapping sites found in iron. Areas through which hydrogen advance from steel specimens during this test are identified by white spherical grains of silver under a scanning electron microscope (SEM). HMT offers the flexibility of allowing changes in hydrogen degassing pattern to be studied with respect to time in steels with mainly reversible trap sites [208]. According to Ovejero-Garcia [209], who first developed this technique, the sensitivity of HMT helps to reveal the routes of escape of hydrogen from micro-cracks, grain boundaries, slip lines, twin boundaries, inclusions and other microstructural features. This tool is best suited for hydrogen diffusion studies in steel with coarse grains. In such steels, it is less difficult to identify and interpret differences in hydrogen accumulation pattern within the structure.

An interesting feature of this technique is that it provides a means of investigating the relationship between hydrogen degassing and grain boundary character. Koyama *et al.* [207] investigated hydrogen evolution from iron after different hydrogen charging times. Their results showed formation of silver grains on the hydrogen exit side after 90 mins of hydrogen charging, as illustrated in Fig. 2.11. An enlarged secondary electron image (Fig. 2.11b) of the highlighted portion in Fig. 2.11a clearly depict hydrogen discharge through grain boundaries after 90 min of charging. However, reduced charging time of 53 min resulted in minimal deposition of silver particles (Fig. 2.1c). With the help of EBSD, the authors identified grain boundary misorientation as a possible reason for the non-uniform distribution of silver grains on the steel surface after hydrogen charging. The grain boundaries having low misorientation angles ($0^{o} < \theta < 15^{o}$) are marked in Fig. 2.11d (black arrows). Further analysis performed by the authors showed that the low angle boundaries displayed lower number of silver grains than the high angle misorientation boundaries (Fig 2.11e). Since there is more misalignment and dislocations in high angle

boundaries, they are expected to saturate with hydrogen (allow greater hydrogen diffusion through them) compared to the low angle boundaries.

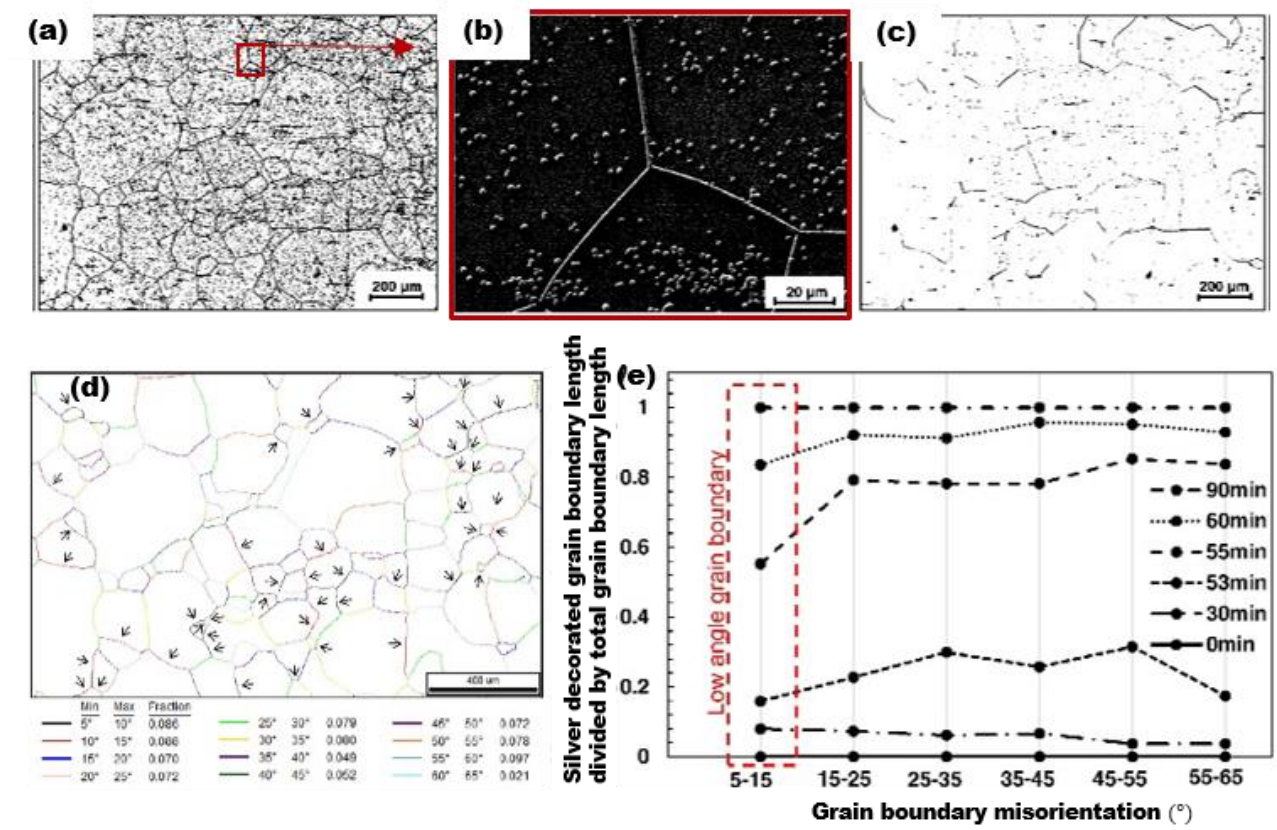

Fig. 2.11 SEM and optical images showing (a) more silver particles appearing after 90 mins of hydrogen charging (b) high resolution image of silver particles at selected hydrogen exit, and (c) few silver particles appearing after 53 mins of hydrogen charging (d) grain boundary distribution (e) misorientation – grain boundary plot [202]

2.11.1 Radiography-based approach

The use of radiography as a non-destructive characterization technique has numerous scientific applications. Until now one major limitation associated with microscopic approach to crack analysis is its inability to offer detailed understanding of the extent of damage experienced by test pieces in three-dimension. Interestingly, the tomography can reveal the interior of most engineering materials by providing both two and three-dimensional images of structures which cannot be examined only at the surface. Common electromagnetic radiations deployed in tomography studies are the X-rays [210]. Also, neutrons are used in tomographic measurements

[211]. Hydrogen assisted cracking (HAC) nucleate and propagate in three-dimensional manner. This means that a discontinuous crack noticed at the steel surface may have proceeded beneath the surface and may reappear at different locations. Alternatively, cracks can take turn inwards instead of appearing continuously at the surface. There are situations where cracks initiate inside the steel structure without propagating to the surfaced region. Griesche *et al.* [212,213] observed hydrogen induced blistering cracks (HIBC) and quantitatively analyzed the distribution of hydrogen in iron using neutron tomography. The authors reconstructed a three-dimensional model of the hydrogen charged specimen as presented in Fig. 2.12. Their findings show visible hydrogen blistering at the surface (Fig. 2.12a) with additional cracking inside the specimen (Fig. 2.12b), and hydrogen presence in the interior (Fig. 2.12c) of the charged steel specimens. Two-dimensional slices obtained from different planes (x-y, y-z, and x-z) of the three-dimensional model displayed in Figs. 2.12d-f confirm the presence of cracks including trapped hydrogen. The authors further authenticated the presence of hydrogen around cracked regions identified by the whitish coloring in Fig. 2.12g by annealing at 49.85 ℃ for two days. They found that image obtained after heat treatment revealed only cracks without the trapped hydrogen (Fig. 2.12h). The reason is that annealing the samples led to the escape of accumulated hydrogen. It is evident that high density of hydrogen atoms is featured at the vicinity of cracks in Fig. 2.12i. These findings indicate potentials for the use of tomography in hydrogen detection and assessment of the risk of failure.

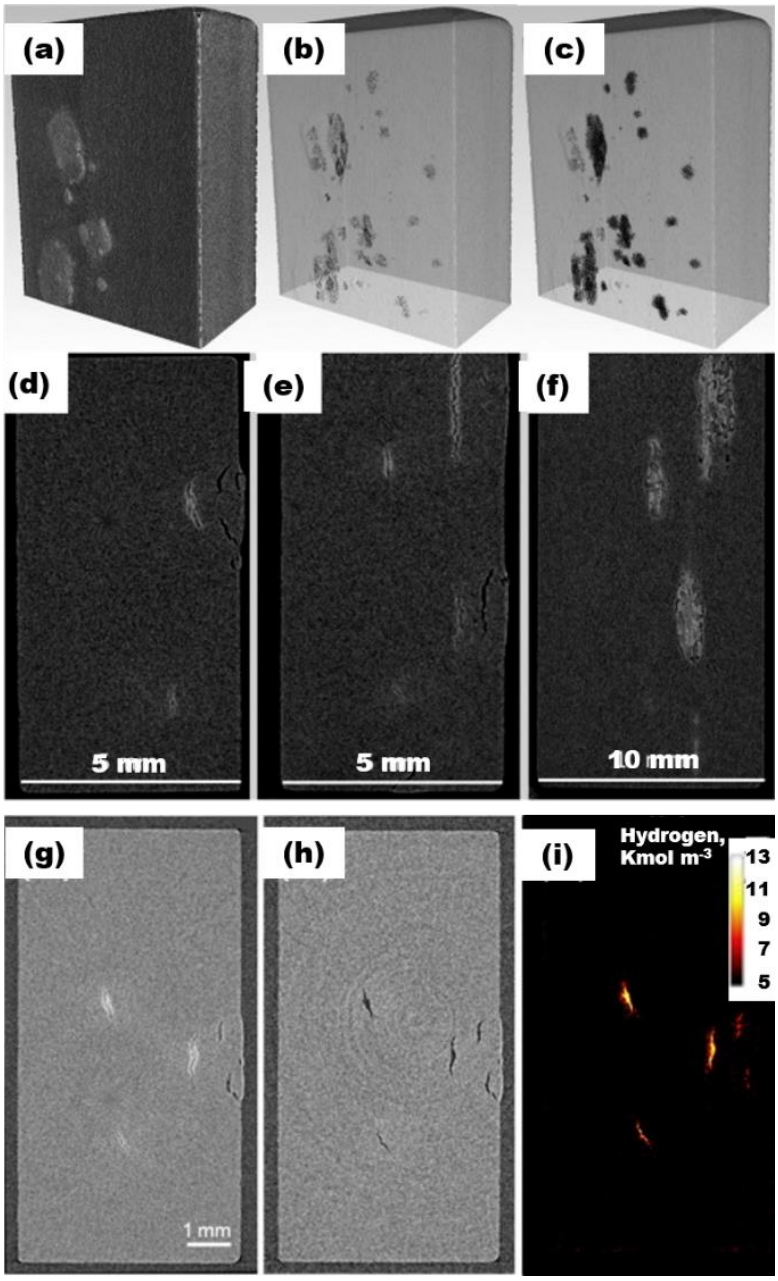

Fig. 2.12 (a-c) are typical reconstructed three-dimensional model of hydrogen charged specimen; (a) HIBC at the surface region, (b) cracking beneath the surface (c) shows the spread of hydrogen within the interior. (d-f) are slices obtained from the three-dimensional model with cracks and whitish patches of hydrogen; where (d) is the x-y plane, (e) is the y-z plane (f) is the x-z plane. (g-i) slices obtained from the x-y planes; where (g) is immediately after hydrogen charging (h) after hydrogen charging and annealing treatment (i) density of hydrogen after charging [212,213]

2.11.2 Thermal desorption spectrometry (TDS)

This method measures hydrogen desorption from various traps within the steel structure after saturation with hydrogen. The steel sample is either saturated with hydrogen gas inside an enclosure or electrochemically charged with hydrogen, before being placed in a tube furnace and heated at a controlled rate. A systematic application of this technique has proven that gaseous hydrogen charging softens low carbon steel, while electrochemical charging hardens it [214]. With the aid of a gas chromatograph attached to the furnace, hydrogen released from the steel can easily be detected and quantified. Data collected from TDS is analyzed using different models [48,215]. However, quality of the data analysis depends on the model used. Turnbull *et al.* [216] examined the available models with the intention of highlighting their respective limitations and proposing a more robust model. Several researchers [217,218] have found TDS is useful in the investigation of pipeline steel designated for sour service.

2.11.3 Devanathan-stachurski (DS) method

This technique involves using double-cell apparatus to study diffusion of hydrogen across a membrane. The steel sample, which is the permeation membrane is placed between both electrolytic cells. One cell (cathodic section) serves as the source of hydrogen adsorption on the sample, while hydrogen desorption occurs on the other side of the sample where oxidation takes place (anodic section). The signals from hydrogen oxidation is typically reduced by applying a thin palladium film on the hydrogen desorption side. The effective hydrogen diffusion coefficient obtained from DS experiment gives an idea of susceptibility to hydrogen damage [219]. The DS method is widely used because it provides information about hydrogen diffusion pattern, trap density and relates hydrogen flux to time [110,220]. Hydrogen trapping behavior and permeation properties of X60 and X60SS (sour service) pipeline steel were investigated using this procedure [221]. Based on the differences observed in hydrogen permeation coefficients and number of traps in investigated pipeline steel, X60 was confirmed to be more susceptible to HIC compared to X60SS. According to the authors, lower density of the reversible traps featured in X60SS made it less susceptible to hydrogen damage. A separate study used this method to compare hydrogen permeation characteristic of pipeline steel weld and parent metal [175]. The authors noticed that the weld heat affected zone (HAZ) experienced low hydrogen permeation with high trapping

efficiency compared to the pipeline substrate. This observation allowed the authors to conclude that the HAZ is more susceptible to hydrogen damage.

2.11.4 Electrochemical impedance spectroscopy (EIS)

EIS has found broad application in many aspects of electrochemical studies. It has been effectively applied in the evaluation of barrier properties of polymeric coatings [222,223], corrosion inhibitors [37], metal dissolution and corrosion rates [224]. This technique helps in understanding both kinetics and mechanisms of electrochemical reactions [225]. Macdonald [226] outlined the benefits of EIS as follows:

1. Ease of data validation using an integral transform method that does not depend on the physical processes associated with the experiment (Kramers-Kronig transform).
2. Straightforward interpretation of results based on Linear System Theory.
3. Extremely high experimental efficiency.

A key feature of EIS is the sensitivity of certain impedance equivalent circuit parameters to hydrogen content [227]. Also, they established a linear correlation between impedance parameters and HIC susceptibility in steels. Such findings could potentially form the basis for applying this technique in evaluating susceptibility of pipeline steel to hydrogen related failures.

2.11.5 Electrochemical noise (EN)

Electrochemical noise technique involves measuring resistance to noise based on deviations in current and voltage fluctuation pattern on two identical working electrodes (test samples) connected to the cell [228]. It is important that both working electrodes have similar open circuit potential to ensure accurate determination of noise resistance during experiments. In other to achieve this, the working electrodes are connected to a zero-resistance ammeter. The relationship between polarization resistance and noise resistance allows the estimation of the corrosion rates using the Stern-Geary equation. However, the major concern about using DC polarization methods for corrosion studies in H_2S environment is the disturbance this method causes on the mechanism of passive film formation [229]. Although this is not usually the case when using less interfering EN technique, Mansfeld [230] pointed out two other limitations of this technique that may affect data analysis and create artefacts in the final results. They include asymmetry of both electrodes used in the experiment (especially in cases of localized corrosion, low rates of corrosion and coated

materials), and drift or signal trend (constitute nuisance during analysis of results). Characteristics of the noise spectrum obtained from EN measurements are quantified statistically to provide details about mechanism of corrosion. Ricker *et al.* [231] suggested EN as a viable tool for investigating degradation mechanisms associated with hydrogen. These authors reported that the frequency spectra of EN is lower for general corrosion and increase in cases of hydrogen-related corrosion attack. They attributed these finding to alternating passivation and repassivation of metal surface during localized hydrogen degradation. Other researchers [232] used a combination of EN and Mott-Schottky measurements to establish variations in pitting corrosion pattern of different pipeline steel grades. In their study, they analyzed noise data obtained from measuring electrochemical voltage and/or currents with respect to time. Both time and frequency domain were considered in their calculations.

2.12 Other causes of hydrogen related degradation

In the field, hydrogen degradation could be initiated by several sources. In this section of the review, we will be addressing other hydrogen related corrosion causes affecting marine and offshore pipeline structures. As diffused gaseous hydrogen impacts the microstructure of metals, the embrittlement is accompanied by loss of ductility and higher mechanical strength. The sources of hydrogen are different, so are inherent atomic-scale mechanisms towards bulk embrittlement. Corrosion-induced failures have been the reason for several reviews focused on oil and gas facilities. It has contributed to significant economic losses in maintenance and inspection of materials. Offshore oil and gas facilities could be damaged by hydrogen due to chemical attack, shifting hydrodynamic regime and the presence of microorganisms [61]. We will also be enlisting some works that have investigated the degradation of pipeline materials by harmful hydrogen exposure from various sources.

2.12.1 Microbiologically influenced corrosion

Microbiologically influenced corrosion (MIC) involves the fouling of surfaces by microorganisms and subsequent creation of corrosive oxygen concentration cells. Adhering bacterial biofilms alter the kinetics of anodic and/or cathodic reactions at metal/solution interfaces, leading to accelerated corrosion and subsequent dissolution of the metallic materials [233]. MIC accounts for more than 20% pipeline systems failures [234]. Bacterial biofilms play significant roles in understanding the

causes and control of surface pitting on metal substrates in marine environments. Among the numerous MIC-led corrosion mechanisms reported in the literature, the majority involve the corrosive actions of sulphate-reducing bacteria (SRB) and nitrate reducing bacteria (NRB) on metal surfaces [235]. SRBs are anaerobic bacteria that reduce sulphur/sulphur compounds (e.g. SO_4^{-2}, SO_3^{-2}, $S_2O_3^{-2}$ and sulfur) to sulphide [235]. Upon attachment on metal surfaces, they grow into communities of SRBs, anchoring by means of extracellular polymeric substances (EPS) secreted by their biofilms [236]. Within this biomatrix, the production of H_2S is enhanced, favouring electrochemical reactions that lead to localized corrosion episodes [235,237]. However, due to the complexity of the bacterial biofilm, the exact source of hydrogen is very difficult to determine. This is also related to some external and internal factors surrounding the bacteria. SCC is linked with the presence of both molecular hydrogen and H_2S gas, and both gases are by-products of biochemical conversions within bacterial biofilms. Also, the association of H_2S with Fe generates hydrogen gas according to Eqs. 2.6-2.8. These reactions are catalyzed by anaerobic SRB activity.

Biezma [238] has investigated the role of hydrogen in SCC and MIC as well as the decatalyzing of hydrogen recombination reaction at metal surfaces. The H_2 gas alters inherent crack conditions leading to tensile stresses and embrittlement. This condition escalates as gaseous H_2 is trapped at sites of different strengths. The effects of bacterial activities and interactions at *'biologically active environment* (BAE)' on metal surfaces with changing local chemistries have been also investigated. In this case, it was noticed that BAE facilitates hydrogen diffusivity within metals in anaerobic conditions. Wu *et al.* [239] investigated the effect of SRB-induced SCC susceptibility of X80 steel under cathodic potential in solutions of neutral pH. The susceptibility of the metal to degradation increased at negative cathodic potential and SRB pre-incubation period. However, the synergistic effect of the existence of these factors was limited at low cathodic potentials. The same authors also established a correlation between plasticity loss and permeable hydrogen concentration in the medium under study at open circuit potential. Electrochemical and fractographic analysis of MIC-assisted SCC of carbon steel was also studied by Stipanicev *et al.* [240]. The impact of the microbially-enriched environments on the topography of the specimens tested in tensile experiments were revealed. No evidence of inter-granular/ trans-granular corrosion failure was found on tensile specimens. The summary of the recent findings for MIC-

assisted cracking in the presence of some selected microbes are presented on Table 2.7. These studies have proposed MIC-influenced hydrogen embrittlement on metals with bacterial microorganisms acting as sources of hydrogen that was derived from their metabolism.

2.12.2 Acid-induced corrosion

The elimination of chromates from anti-corrosive/anti-fouling industrial paints has stimulated renewed research interests in alternative coating additives. Since ship hauls are affected by MIC at the similar rate as other forms of corrosion, more effective corrosion inhibition treatments are needed. In seawater, metals treated by the usual chemical corrosion inhibitors still corrode on prolonged exposure to extreme conditions. In recent years, the rapid progress in oil exploration is accompanied by designs of offshore facilities (e.g. transportation pipeline, platforms, storage and drilling equipment) [61]. Both internal and external parts of oil facilities are susceptible to corrosion depending on the conditions of service. In most cases, structural degradation may lead to reduced mechanical integrity as well as complete failure [61]. To control corrosion, the rate of metal degradation needs to be reduced, and this has been achieved via new designs of alloying, more reliable corrosion inhibition strategies and prevention of access to corrosion environment [241]. Companies incur considerable expenses due to new constructions and replacements of corroded machine parts, maintenance and repairs, corrosion-related downtime, total material failures and cost of periodic corrosion inhibitor purchase. Upon acid treatments, oil wells are exposed to corrosive environments with enhanced strength that can cause bulk damage. At higher temperatures, these concentrated acids (e.g. hydrogen halides) penetrate the rock formations and open both inherent and new pores in equipment and pipelines. During such operating conditions, exposed metallic structures severely degrade [242,243]. Corrosion of metals in acidic media is accompanied by two important reactions (Eqs. 2.1 and 2.2); anodic iron dissolution and hydrogen ion reduction. The formation of molecular hydrogen as a product of corrosion-related reaction may contribute to embrittlement. Corrosion inhibitors are known to reduce the rate of these reactions when adsorbed on metal surfaces. The effectiveness of adsorbed inhibitor films depends on several factors (e.g. the chemistry of the interface, inhibitor concentration and mechanical properties of adsorbed film, etc.). Also, some other specific molecular properties of chemical inhibitors like aromaticity, planarity, chain length, solubility, electronic structure, functional group chemistry and steric factors are of importance because they improve their effectiveness.

Several researchers have investigated the anticorrosion potentials of both inorganic and organic corrosion inhibitor compounds, singularly and in the form of blends. For higher organics, metal-surface adsorption occurs at coordination sites (where heteroatoms in the functional groups bear the following atoms: S, O, P, N etc.) [244]. The adsorption process is fostered by the presence of lone electron pairs (and π-bonds) at the sites, and a few recent reports enlisting some of the corrosion inhibition systems for pipeline steels in various media are presented in Table 2.8. Obot *et al.* [245] investigated the corrosion resistance of X60 pipeline steel in the presence of 8-Hydroxyquinoline in 15% HCl. Authors observed that corrosion inhibition increased with hydroxyquinoline content, and it can be improved in the presence of potassium iodide (KI) additive within the same test medium. This was attributed to molecular adsorption on the metal surface leading to formation of the hydroxyquinoline-KI barrier film that protected against steel corrosion. Calderon *et al.* [246] observed a similar trend when studying the corrosion behavior of P-110 commercial carbon steel in EDTA/mercaptobenzimidazole medium. In this case, the authors linked corrosion inhibition to the formation of chemisorbed mercaptobenzimidazole films on the metal surface. In another work, Ngobiri *et al.* [247] used weight loss and some electrochemical (potentiodynamic polarization and EIS) techniques to study the degradation pattern of an unnamed pipeline steel in simulated pipeline water spiked with sulfadoxine–pyrimethamine blends. Corrosion of the steel substrate was observed to be reduced in the presence of the chemical inhibitor blends at relatively increased concentrations. The trend of potentiodynamic polarization results revealed that the absorption of the inhibitors affected both anodic and cathodic reactions (mixed-type inhibitor system). Sulfadoxine–pyrimethamine adsorption on metal surface led to the formation of barrier films.

Table 2.7 A summary of few recent findings on MIC-assisted SCC in the presence of some microbes

S/No.	Type of metal	Type of microbe	Culture medium	What was studied and key findings	Ref.
1.	X80 pipeline steel	*Desulfovibrio desulfuricans*	A meadow soil, collected at Shenyang, China in API RP-38 medium (composition in 1 L): 0.2 g $MgSO_4 7H_2O$, 0.5 g KH_2PO_4, 10 g NaCl, 1 g ascorbic acid, 4 g sodium lactate, 1 g yeast extract and 0.02 g $Fe(NH_4)_2(SO4)_2$ at pH 7.	Authors were investigating the pattern of hydrogen permeation within X80 pipeline in the presence of a SRB (*Desulfovibrio desulfuricans*) culture. The tests were conducted under superficial stress and cathodic protection. A measure of the superficial stress on the metal substrate followed by abrasion; this physical quantity was observed to increase the surface area ratio. A combination of SRB metabolic activities and cathodic potential accelerated hydrogen flux within the metal substrate exposed to the soil solution.	[239]
2.	X80 pipeline steel	*Desulfovibrio desulfuricans*	Same as Ref. [239]	Authors were studying SRB-induced MIC on stressed X80 steel in a Chinese (Shenyang) soil. MIC resulted in severe metal surface degradation. Synergistic SRB growth and yield stress increased the corrosion rate of steel, while its anodic dissolution and morphology were probed.	[248]
3.	API 5L X80 steel	Unnamed SRB strain	Same as Ref. [239]	The gross susceptibility of the metal to degradation increased at negative cathodic potential and pre-incubation period of SRB; however, the synergy of both factors was limited at low cathodic potentials.	[249]
4.	Carbon steel S235JR rods	*Desufovibrio desulfuricans, Desufovibrio. Alaskensis,* and *Geobacter sulfurreducens*.	Saline modified-VMNI medium	Electrochemical and fractographic analysis of MIC-assisted SCC of carbon steel was investigated. Fractographic analysis revealed significant impact of the enriched environments on the topography of tensile specimens after testing. No evidence of intergranular/ trans-granular corrosion failure was found on tensile specimens.	[240]

5.	Fire hydrant metal: Composition: Mg 3.7, Cu 62.9, Al 5.6, Fe 2.7, Zn 24.7, Sn 0.04, and Pb 0.10.	Nitrate reducing bacteria (NRB)	Water sample from stagnant vertical outlet of a firewater hydrant (pH 7.9 and total dissolved salt of 49,200 mg/L).	The cracking failures on firewater hydrants handling was investigated in seawater. Fracture examination outlined effects of two failure causes linked with SCC, intergranular corrosion and dezincification confirmed by (Energy dispersive spectroscopy) at fracture surface grains. Ammonia gas evolution is associated with the NRB metabolic process in seawater.	[250]
6.	X70 steel	*Desulfovibrio desulfuricans*	The medium for SRB culturing contained 0.5 g K_2HPO_4, 0.5 g $(NH_4)_2SO_4$, 5 g sodium citrate, 3.5 g sodium lactate and 1 L extracted soil solution.	MIC of pipeline steel under cathodic protection in an extracted soil in solution was investigated in the presence of *Desulfovibrio desulfuricans*. Cathodic protection did not inhibit bacterial growth but facilitated its attachment to the steel surface. However, a biofilm layer on the cathodically protected steel reduced corrosion protection.	[251]
7.	X52 pipeline steel sheet	SRB seeds (ATCC 13541)	A modified Baar's medium (g/L): 0.5 g K_2HPO_4, 0.5 g $(NH_4)_2SO_4$, 0.2 g $(NH_2)Fe(SO_4)_2$, 0.3 g $MgCl_2$, 5 g sodium citrate, 1 g yeast extract and 3.5 g sodium lactate (pH 7.2).	The MIC mechanism in X52 pipeline steel was investigated in SRB-enriched Regina clay soil. Steel's MIC rate increased with water content and the presence of CO_2 within the soil. These two conditions thickened the SRB biofilm on the steel, thereby accelerating corrosion.	[252]
8.	X70 pipeline steel	Unnamed SRB strain isolated from the soil	Culture: 0.5 g K_2HPO_4, 0.5 g Na_2SO_4, 1 g NH_4Cl, 0.1g $CaCl_2$, 2 g $MgSO_4 \cdot 7H_2O$, 1 g yeast, and 3 ml of sodium lactate in 500 g of pure water. Second culture: 0.1 g ascorbic acid, 0.1 g sodium hydrosulphite, and 0.1 g of $(NH_4)_2Fe(SO_4)_2 \cdot 6H_2O$.	SRB growth on steel lowered its equilibrium potential and was anodically polarized in the SRB-containing solution. Biofilm formation initiated sulphide deposition as well as increased the potential difference in the crevice. Hydrogenase secretion within the SRB biofilm increased the bacterial solution pH.	[253]

9.	X70 pipeline steel	Unnamed SRB strain isolated from water	CSBK medium: 1 L in volume containing 1.5 g NaCl, 0.05 g KH_2PO_4, 0.32 g NH_4Cl, 0.21 g $CaCl_2$, 0.54 g $MgCl_2 \cdot 6H_2O$ and 0.1 g KCl.	Fluid flow regime on biofilm formation and MIC of X70 metal in oilfield water was investigated. At 0.2 m/s, biofilm grew, and MIC initiated pitting. However, no growth was observed at increased flow rate (1.0 m/s), hence, MIC reduces.	[254]
10.	X80 pipeline-steel	*B. cereus* was isolated from the soil	Medium composition in 1 L volume: 10 g sucrose, 1 yeast extract, 13.9 g K_2HPO_3, 2.7 g KH_2PO_4, 1 g NaCl, 1 g $NaNO_3$, and 0.25 g $MgSO_4$.	MIC-induced degradation of X80 steel was investigated in the presence of *Bacillus cereus* growth in a soil. *B. cereus* accelerated X80 corrosion from impedance results. SEM analyses revealed pitting corrosion on X80 steel surfaces from *B. cereus* growth.	[255]

Table 2.8 A summary of few recent findings on corrosion inhibition in pipeline steel materials exposed to various media

S/No.	Type of metal substrate and corrosive medium	Inhibitor type (Classification of corrosion inhibitor)	Barrier performance evaluation techniques	Corrosion reduction is attributed to the following reasons.	Ref.
1.	X60 pipeline steel/0.5 M HCl	Pectin/nano CeO_2 (Mixed-type corrosion inhibitor)	EIS, potentiodynamic polarization and Weight loss techniques	Pectin combined with CeO_2, and the absorption of this hybrid composite led to protective films.	[244]
2.	API X60 pipeline steel/15% HCl	8-Hydroxyquinoline-KI (Mixed-type corrosion inhibitor)	Weight loss, potentiodynamic polarization, linear polarization (LPR), EIS, EFM, Scanning electron microscopy (SEM) with energy dispersive X-ray (EDX), and Fourier transforms infrared (FTIR) spectroscopy	Molecular adsorption on metal surface leading to formation of barrier film against steel corrosion.	[245]
3.	Pipeline steel (unnamed grade)/ pipeline water	Sulfadoxine–Pyrimethamine (Mixed-type corrosion inhibitor)	Weight loss, potentiodynamic polarization and EIS techniques	Molecular adsorption on metal surface leading to formation of barrier film against steel corrosion.	[247]
4.	API X120 pipeline steel/ 0.5 M HCl	Stearamidopropyl dimethylamine (Mixed-type corrosion inhibitor)	EIS, potentiodynamic polarization, SEM and optical profilometry techniques	Molecular adsorption on metal surface leading to formation of barrier film against steel corrosion.	[256]
5.	API 5L-X60 pipeline steel/ petrol–water mixtures	1-Aminoanthraquinone derivatives (Anodic-type corrosion inhibitor)	Weight loss, EIS, potentiodynamic polarization, SEM and Atomic Force Microscopy (AFM) techniques	Molecular adsorption on metal surface leading to formation of barrier film against steel corrosion.	[257]
6.	X80 pipeline steel/0.5 M HCl	Cytosine-*L*-alanine derivatives (Mixed-type corrosion inhibitor)	Weight loss, potentiodynamic polarization, EIS and SEM techniques	Molecular adsorption on metal surface leading to formation of barrier film against steel corrosion.	[258]

7.	X70 pipeline steel/ 5 M HCl	Methyl acrylate/ N-alkylpyridinium bromide (MPA) (Mixed-type corrosion inhibitor)	EIS, SEM, Weight loss and potentiodynamic polarization techniques	Molecular adsorption on metal surface leading to formation of barrier film against steel corrosion. Hydrophobic interaction between alkyl chains of MPA molecules further protect X70 steel.	[259]
8.	API 5L X70 pipeline alloy/ Acidified NaCl	Chitosanic hydrogel/ nano-CeO2 (Mixed-type corrosion inhibitor)	Potentiodynamic polarization, EIS, SEM and AFM techniques	Formation of compact films reduces the percolation of corrosive ions towards the metal by formation of adsorbed inhibitor double-layers.	[260]
9.	API N80 pipeline steel/ 1 M HCl	N-(3-(dimethyl hexadecyl ammonio)propyl) palmitamide Bromide (Mixed-type corrosion inhibitor)	Potentiodynamic polarization, EIS and EFM techniques	Quaternary nitrogen atom adsorbed at cathodic sites thereby decreasing hydrogen evolution while the counter ion adsorbed on the anodic sites to reduce the anodic dissolution.	[261]
10.	N80 carbon steel/CO_2 saturated NaCl in acetic acid	Imidazoline inhibitor (Mixed-type inhibitor but predominantly cathodic at 3 g/L)	Weight loss, potentiodynamic polarization, EIS, SEM and OCP techniques	Molecular adsorption on metal surface leading to formation of barrier film against steel corrosion.	[262]
11.	X80 pipeline steel/Oilfield acidizing solutions	3-(2-chloro-5,6-dihydrobenzo[b][1] benzazepin-11-yl)-N,N-dimethylpropan-1-amine (Mixed-type corrosion inhibitor)	Weight loss, EIS, potentiodynamic polarization FTIR, SEM and EDS techniques	Molecular adsorption on steel surface by physical and chemical interactive forces.	[263]
12.	N80 pipeline steel/ 15% HCl	1-(2-aminoethyl)-2-oleylimidazoline and 1-(2-oleylamidoethyl)-2-oleylimidazoline	Weight loss, potentiodynamic Polarization, EIS, FTIR spectra and SEM techniques	Molecular adsorption on metal surface leading to formation of barrier film against steel corrosion.	[264]

		(Mixed-type corrosion inhibitor)			
13.	X60 pipeline steel/ 0.5 M HCl	Pectin (Mixed-type corrosion inhibitor but predominantly cathodic)	Weight loss; potentiodynamic Polarization, EIS, SEM and Water contact angle techniques	Molecular adsorption on metal surface leading to formation of barrier film against steel corrosion.	[265]
14.	X60 pipeline steel/ 15% HCl	Polypropylene glycol (Mixed-type corrosion inhibitor)	Weight loss, EIS, EFM, LPR and potentiodynamic polarization (PDP) techniques; water contact angle measurements and SEM techniques	Molecular adsorption on metal surface leading to formation of protective film against steel corrosion	[266]
15.	X70 pipeline steel/HCl	Rare Earth Inhibitor: ($La(NO_3)_3$+Na_2MoO_4(LaN-M), $Ce(NO_3)_3$+Na_2MoO_4(CeN-M), $Pr(NO_3)_3$+Na_2MoO_4(PrN-M)). (Mixed-type corrosion inhibitor)	Weight loss, potentiodynamic polarization, XPS/XRD and SEM techniques	Formation of precipitation films on metal surface.	[267]
16.	X70 pipeline steel/HCl	Methyl acrylate and N-cetylpyridinium bromide in N-cetyl-3-(2-methoxycarbonylvinyl) pyridinium bromide (Mixed-type corrosion inhibitor)	OCP, potentiodynamic polarization, SEM-EDX and EIS techniques	Molecular adsorption on metal surface leading to formation of barrier film against steel corrosion.	[268]
17.	X70 pipeline steel/ acidic NaCl	Thioureido imidazoline and $NaNO_2$ (Mixed-type corrosion inhibitor)	XPS, SEM-EDX, potentiodynamic polarization and EIS techniques	Synergy of thioureido imidazoline and $NaNO_2$ absorption leads to multi-layer film formation.	[269]

Authors in these works were studying pipeline degradation in acidic media but were not necessarily investigating metallic corrosion as a cause of hydrogen related failures.

2.13 Summary

Corrosion in hydrogen environments remains a critical pipeline integrity challenge that can result in catastrophic failure through various forms such as material loss, hydrogen induced cracking, stress-oriented hydrogen induced cracking and sulfide stress corrosion cracking. Hydrogen induced corrosion initiates cracks when the steel has reached a critical stage represented by the presence of critical amounts of hydrogen and high stress level. The reasons behind the damage mechanism for most applications in different environments have been discussed in this review and related to mechanical properties. Also, several theories and models were outlined and have been considered as hypotheses with certain level of acceptability for the case of pure surface corrosion and HIC-led degradation of steel. The effect of HE on cleavage planes and grain boundaries has prompted in depth analysis of crystallographic texture within this work as a very important parameter influencing the corrosion behavior of pipeline steels. More information regarding microstructure and grain boundary interaction in steel have been presented to illustrate the mechanisms of crack interaction with microstructure.

Hydrogen related corrosion can occur in pipelines by any mechanism or a combination of different mechanisms including HELP, HEDE, AIDE and possibly others. Degradation of pipeline steel due to hydrogen ingress is affected by conditions of pipeline material, environment (temperature, Cl^- ions, H_2S gas) and tensile stress. Recorded failures for various applications have been enlisted and discussed, while the causal factors affecting hydrogen ingress like micro alloying, inclusions, grain orientation, grain boundary character, grain size and microstructure have also been mentioned. Although some studies on pure corrosion and HE on pipeline steels were reviewed; there are insufficient data on the application of TMCP as a means of improving failure resistance during service. Experimental techniques such as thermal desorption spectroscopy, hydrogen microprint technique, *Devanathan–Stachurski* method, electrochemical impedance spectroscopy and electrochemical noise measurements have proven to be useful in investigating hydrogen damage in pipeline steels. Since hydrogen degradation is accompanied by other corrosion-related problems, this review also addresses key corrosion causes affecting marine and offshore pipeline structures fabricated from steels. Several recent corrosion mitigation trials and performance tests in various media at different temperature and pressure conditions are also discussed.

CHAPTER 3 : MATERIALS AND METHODS

3.1 Overview

In this section, different thermomechanical treatment parameters applied in the development of pipeline steel materials are outlined. Computational details used for molecular dynamics simulation are provided, including the procedures for various experimental studies. Some of the characterization techniques adopted in this study are the potentiodynamic polarization, HIC test, hardness test, tensile test, X-Ray Diffraction (XRD) technique, Electron Backscatter Diffraction (EBSD) technique, Energy Dispersive X-ray Spectroscopy (EDS) technique, Optical Microscopy (OM) technique, and Scanning Electron Microscopy (SEM) technique.

3.2 Pipeline steel material

3.2.1 Chemical composition

All of the specimens contain the same chemical composition with weight percent's (wt. %) as follows: C: 0.047, Mn: 1.65, S: 0.0018, P: 0.009, Si: 0.18, Cu: 0.29, Ni: 0.07, Cr: 0.06, V: 0.001, Nb: 0.073, Mo: 0.247, Sn: 0.01, Al: 0.044, Ca: 0.0014, B: 0.0001, Ti: 0.022, N: 0.0099, O: 0.003, and the balance is Fe.

3.2.2 Thermomechanical treatment parameters

Pipeline steel blocks supplied by EVRAZ North America were thermomechanically processed at CanmetMATERIALS, Natural Resources, Canada by exposure to different conditions. The processed specimens were compared with commercially available API 5L X70 pipeline steel from EVRAZ, which is described as the reference material (Ref X70). The first set of two hot rolled X70 pipeline steel specimens are referred to as WE and WD respectively. It is worth stating that the labels given to these steels have no other meaning except for identification and batching purposes. Processing of both specimens started with reheating at 1250 ℃ and soaking for 8 h before roughing at a temperature range of 1200 – 1110 ℃. After this stage, an initial thickness of 203 mm was reduced to 23 mm in 9 passes. Detailed parameters for all the stages of the thermomechanical treatments are presented in Table 3.1. A final thickness of 9.6 mm was achieved in both specimens after finishing the hot rolling with 4 additional passes. Immediately after completing the rolling procedure, specimen WE was cooled in air for 10 s, while specimen WD

was cooled for 12 s. The subsequent online accelerated cooling proceeded at a rate of 42.75 ℃/s for WE and 51.5 ℃/s for WD, before both specimens were coiled at the same temperature of 580 ℃. Another pair of specimens were arbitrarily labelled WG and WH. Similar thickness measured in WE and WD was achieved after hot rolling these new set of steels. In this case, the thermomechanical treatment parameters were changed as indicated in Table 3.1. A transfer bar measuring 450 mm in length was cut-out and finished by rolling in multiple passes to achieve the final specimen thickness on WG and WH. The finishing rolling temperatures and cooling rates were varied for both specimens. Most especially, the rate of online accelerated cooling was much lower in these set of samples compared to the earlier ones (i.e. WE and WD). Specimens WG and WH then underwent an accelerated cooling at ≈ 25 ℃/ s.

Table 3.1 Thermomechanical processing parameters for pipeline steel specimens

Parameters (℃)	WE	WD	WG	WH
Reheating/soaking	1250 ℃/8 h	1250 ℃/8 h	1240 ℃/7 h	1240 ℃/7 h
Roughing	1200 – 1110	1200 – 1110	1150 – 1070	1150 – 1070
Hot shear	1110 – 850	1110 – 895	1060	1070
Finishing rolling	850 – 805	880 – 815	880 – 820	830 – 760
Air cooling	805 – 780	815 – 755	820 – 760	760 – 740
Online accelerated cooling (OLAC)	780 – 609	750 – 544	755 – 615	735 – 565
Final cooling	609 – 584	544 – 500	615 – 600	565 – 565
Coiling	580	580	580	580

3.2.3 Post-processing annealing treatments

After TMCP, specimen WG was selected for further annealing treatments as shown in Fig 3.1. The initial thermomechanical treatment for the starting material (i.e. specimen WG) is represented in section (a) of Fig 3.1. Later, different post-processing annealing treatments were performed on the rolled pipeline steel plate according to the procedures reported in literature [270]. At first, the steel sample was subjected to a one-step isothermal annealing treatment at an inter-critical temperature of 720 ℃ for 1 h before quenching in water as indicated in section (b) of Fig. 3.1. Again, the procedure described in section (c) of Fig. 3.1 was carried out as a two-step annealing treatment. The second treatment process involve preliminary annealing the initial TMCP sample at 780 ℃ for 1 h was followed by basic water quenching and another annealing at 720 ℃ for 15 mins before a final quenching in water.

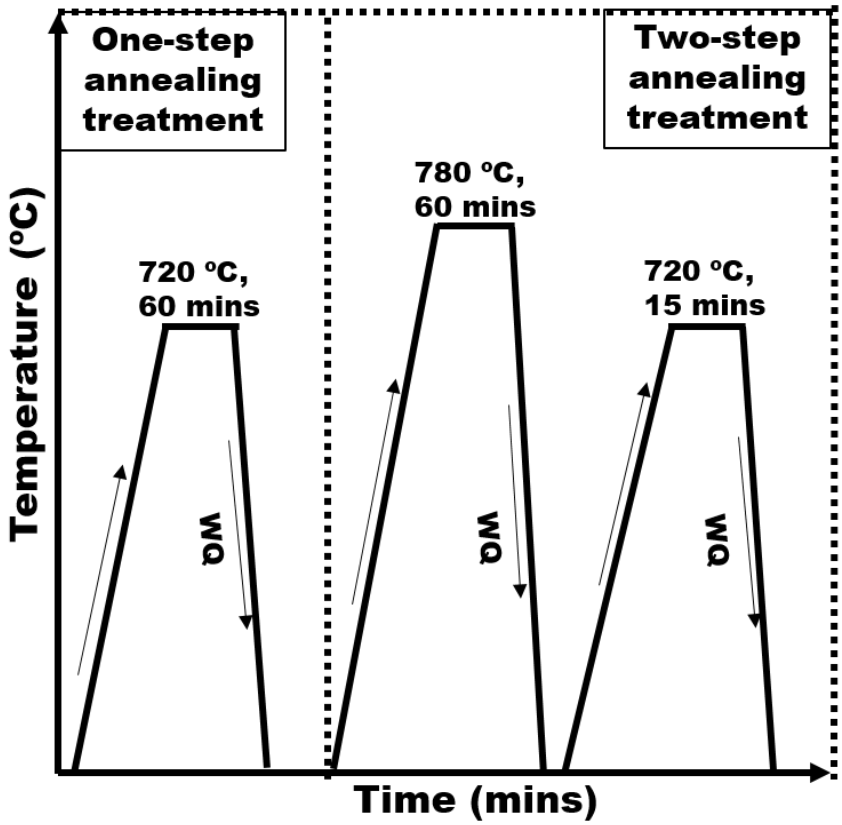

Fig. 3.1 Schematic representation of initial hot rolling process followed by the one-step and two-step annealing heat treatments (WQ: Water Quenching)

3.2.4 Warm rolling parameters

An alternative rolling procedure was also carried out on machined specimens with dimensions of 100 x 30 x 5 mm. Since the preceding thermomechanical treatments were performed at higher transformation temperatures, it was of interest to try some rolling at lower (ferritic) temperatures. Initially, samples were reheated up to 1050 ºC and soaked for 30 mins before air cooling down to different warm rolling temperatures, as indicated in Fig. 3.2. The targeted rolling temperatures of 700 ºC, 600 ºC, and 500 ºC were chosen so that deformation would be achieved in the ferritic region. Each of the three warm rolled steel plates experienced a degree of deformation amounting to a 40% reduction in two the different passes during processing. This resulted in a decrease in thickness from 5 – 3 mm on the rolled plate. Thereafter, the samples were cooled to room temperature in air.

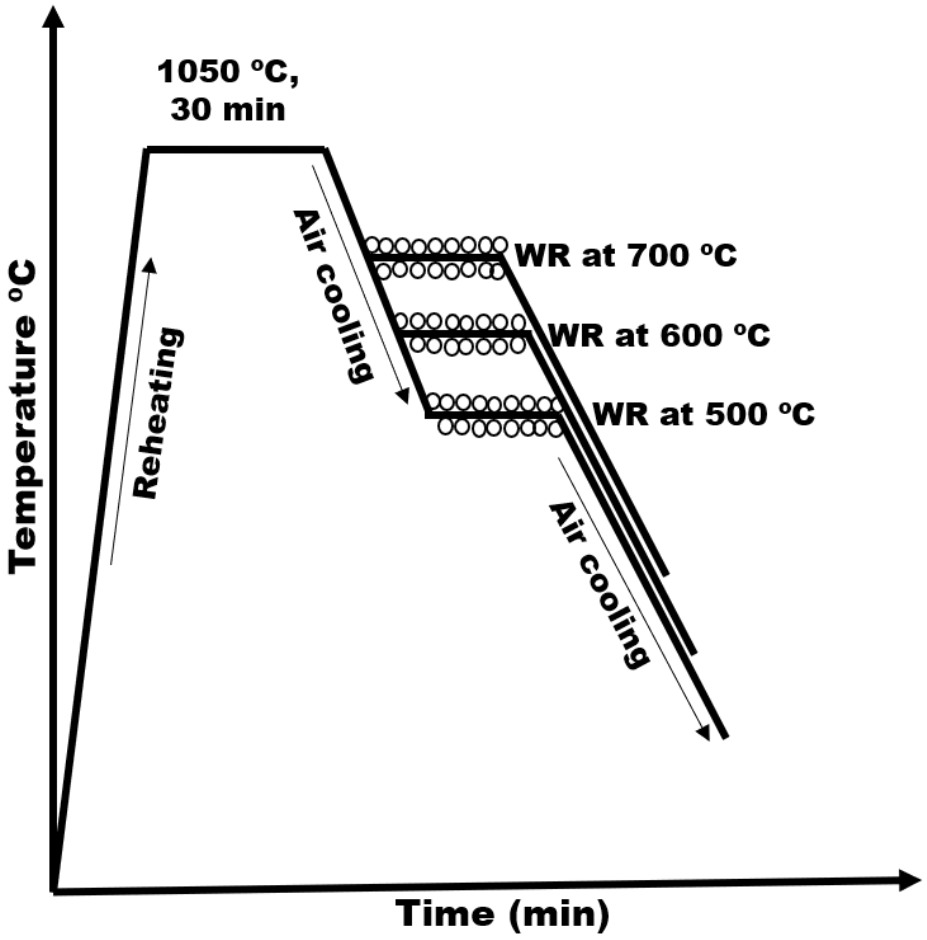

Fig. 3.2 Schematic diagrams indicating temperature histories for warm rolled (WR) samples

3.3 Methodology

3.3.1 Optical microscopy

Metallographic examination of each pipeline steel substrate was conducted after the thermomechanical treatment before proceeding with the various characterization and corrosion tests. A piece of sectioned sample from each pipeline steel was hot mounted in Bakelite and polished with various grades of silicon carbide paper ranging from 320, 500, 800, 1000, 1200, 2000, and 4000 grits, respectively. Further polishing was done in a 3 μm and a 1 μm diamond suspension media. The polished samples were etched in a 5 % nital solution before a microstructure evaluation under the Nikon MA 100L Inverted Materials Microscope pictured in Fig. 3.3. With the aid of a PAXcam digital microscope camera connected to a computer, micrographs were viewed and analysed using the PAX-it imaging software.

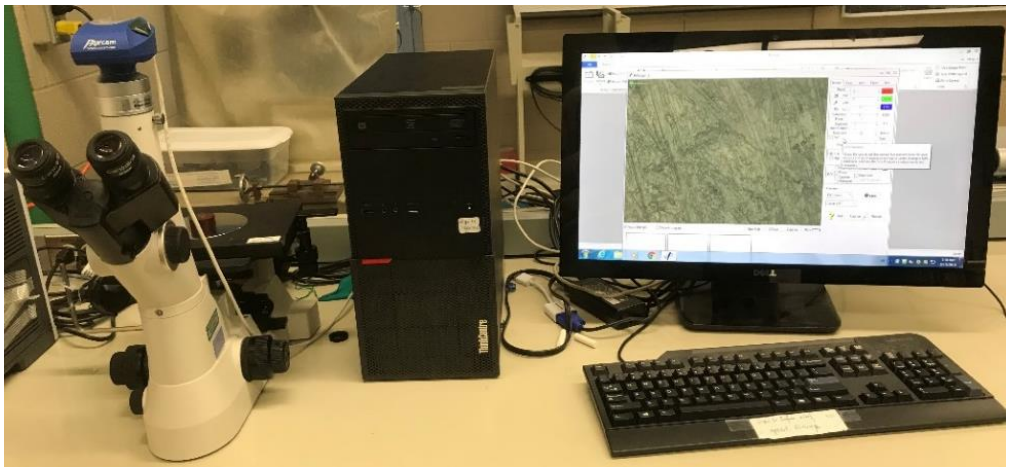

Fig. 3.3 Photograph of the Nikon MA 100L inverted optical microscope connected to a computer running the PAX-it software

3.3.2 SEM, EDS and EBSD analyses

Reconstructed maps from EBSD scans were used to characterize grain orientation in a specific volume fraction of pipeline steel samples. This method is commonly referred to as Orientation Imaging Microscopy (OIM) and it relies on the use of SEM/EBSD to evaluate the microstructure and the lattice orientations found in polycrystalline materials [271]. The EBSD approach facilitates micro-texture analysis, which means that it can be used to determine individual grain characteristics. Moreover, it quantitatively measures crystallographic texture, grain boundary distribution, grain size, and phase identification within the structure [272]. The results obtained from the OIM technique are diffraction patterns originating from each individual crystallite. When backscattered electrons interact with lattice planes around the material surface, diffraction is achieved in the form of cones. With the aid of a phosphor screen positioned on the detector, and a high-speed camera, the diffraction cones are intercepted and displayed as Kikuchi bands. Then, the orientation information from all the collected patterns is evaluated through a process of indexing. This involves identification of poles and bands within the generated patterns, as well as establishing links between these parameters and some chosen references. The results are data consisting of (a) principal coordinates, (b) Euler angles, (c) Phase details, and (d) pattern quality. These outputs are further transformed into crystallographic orientation and presented in the form of colour coded maps.

Operating the EBSD involves positioning the mirror-like polished sample surface on a tilted SEM stage inside the high vacuum chamber as shown in Fig. 3.4. Then, an incident electron beam accelerating at a voltage of 10 to 30 kV is diffracted by crystals of the specimen. This leads to the creation of an electron backscatter diffraction pattern. With the help of a detector, these patterns are captured and used to determine the lattice parameters of the specific crystals interfering with the beam. The system can match the identified crystallographic orientation with the suspected crystal phase chosen from a built-in database. An additional instrumentation feature attached to the SEM is the EDS detector. This analytical technique is based on the interaction between the X-rays from a source and the specimen. Using this procedure, qualitative maps corresponding to the elemental composition of inclusions, precipitates, and microstructural phases was obtained.

Pipeline steel specimens used for EBSD analysis were vibratory polished in a 0.04 μm silica solution for another 12 h after mechanical polishing. The Field Emission Hitachi SU6600 Scanning Electron Microscope pictured in Fig. 3.5 was used for this investigation under ultra-high vacuum conditions. All EBSD scans were taken with an accelerating voltage of 30 kV, a tilt angle of 70°, and a working distance of approximately 17 mm was maintained. Tilting the specimen ensures that more diffracted electrons are collected by the detector. Electron diffraction patterns were acquired on Oxford Instrument's AZTEC 2.0 software suite using a step size of 0.14 μm and a binning mode of 8 x 8 pixels. Post-processing was carried out on the raw data with the Oxford Instrument's Channel 5 software. The average size of grains in each specimen was determined as an estimate of the average diameter of all grains present within the scan area. Grain boundary distribution with a misorientation angle (θ) within the range of $5° < \theta < 15°$ was regarded as low angle grain boundary (LAGB), while $15° < \theta < 62.5°$ was a high angle grain boundary (HAGB). For recrystallization fraction studies, sub-grains are separated by misorientation angles (θ) ranging from $1° < \theta < 7.5°$ and grains are separated by $\theta > 7.5°$. Meanwhile, the kernel average misorientation (KAM) measurements covered a range of $\theta < 5°$. Then, coincident site lattice (CSL) grain boundaries were categorized within $3 \leq \Sigma \leq 33$ at a deviation of 15º according to the following expression: $\Delta\theta_{max} = {}^{15°}/_{\sqrt{\Sigma}}$ (Brandon criterion) [273]. The same microstructural characterization technique was repeated after testing each pipeline steel specimen for hydrogen induced cracking susceptibility.

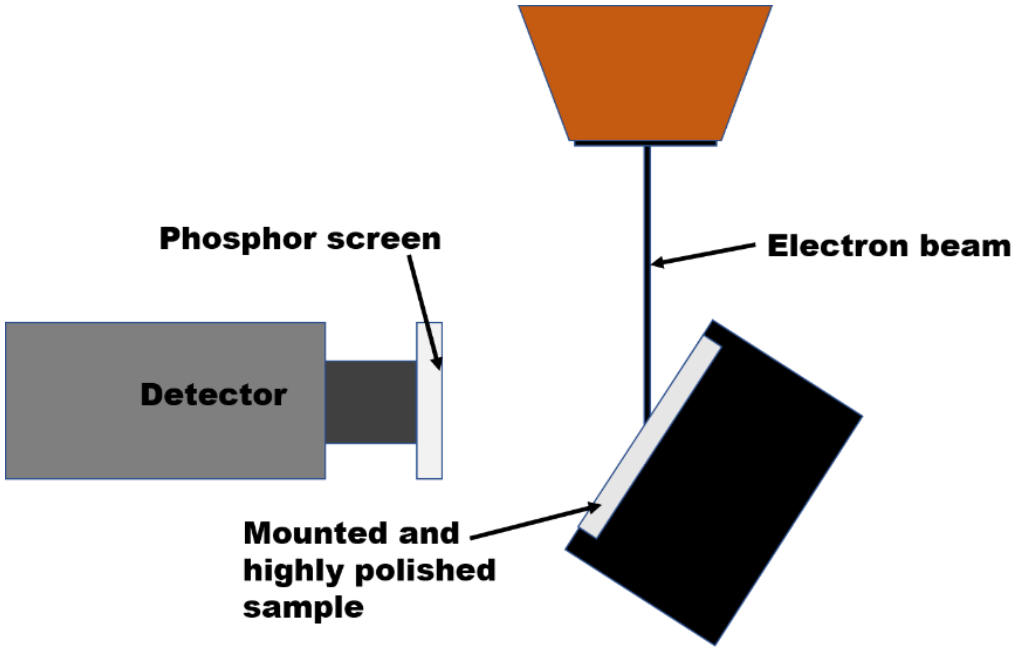

Fig. 3.4 Schematic representation of an SEM chamber showing positioned sample under an incident electron and an electron backscattered pattern detector

Fig. 3.5 Photograph of the field emission Hitachi SU6600 SEM/EBSD device connected to a computer running AZTEC 2.0 software

3.3.3 Micro-hardness testing

The micro-hardness of the test specimens was determined via indentations with the aid of an MVK-H1 Mitutoyo hardness tester shown in Fig. 3.6. The machine was set to a fixed load of 1 kg before taking measurements. During each test, the indenter contacts the specimen for about 10 sec. Thereafter, readings were taken based on the dimension of the indent. Up to ten different measurements were taken prior to reporting the average values in Vickers scale (HV).

Fig. 3.6 Photograph of the MVK-H1 Mitutoyo Vickers micro-hardness tester used for this study

3.3.4 XRD texture measurement

This method of analysis depends on X-ray diffraction by a crystal lattice. The diffraction patterns obtained were used to determine lattice parameters, crystallographic texture, and strain distribution. A beam of X-ray, which is incident on a rotary goniometer, releases secondary waves [274]. The waves are collected by a detector that can change its position by 2θ, if the goniometer is inclined at an angle θ. According to Bragg's law Eq. 3.1, this condition must be met for diffraction to be achieved. The diffracted beams acquired by the detector are used to generate a diffraction pattern.

$$n\lambda = 2dsin\theta \qquad 3.1$$

where θ = incident angle of X-ray, λ = wavelength of X-ray, d = spacing between crystallographic planes, and n = positive integer.

The Brunker D8 diffractometer with a Cr Kα radiation source which was used for the texture measurements is pictured in Fig. 3.7. Incomplete pole figures for (110) and (200) planes were first plotted from raw XRD data. Then, orientation distribution functions (ODF) were constructed from the incomplete pole figures with the help of Resmat – TexTools software.

Fig. 3.7 Photograph of the Brunker D8 X-ray diffractometer used for this study

3.3.5 Electrochemical corrosion studies

The electrochemical corrosion response of each pipeline steel sample was probed in different electrolyte solutions by means of potentiodynamic polarization using the Gamry Instrument's Interface 1000 Potentiostat/Galvanostat/ZRA, as shown in Fig. 3.8. For the specimens used for electrochemical corrosion tests, ultrasonic degreasing was performed in a solution of acetone for 30 mins. Each test coupon was polarized within a potential range of $\pm$250 mV at a scan rate of 1 mV/s according to the literature [275]. However, trial tests were performed using a scan rate of 0.5 mV/s. In order to avoid the destruction of the polished pipeline steel surface, all polarization scans commenced at the cathode before proceeding towards the anode. The results obtained using both scan rates did not show any significant variation. The experimental set-up consisted of a three-electrode system including some pipeline steel substrates as working electrodes measuring 20 mm (length) x 20 mm (width) x 2 mm (thickness), a saturated calomel electrode (SCE) as a reference electrode, and a graphite rod as counter electrode. Pure corrosion is often observed as metal loss

from the pipeline steel surface. Therefore, samples for this study were machined from the surface layer of the rolled plate as shown in Fig. 3.8. The three electrodes were connected in an electrochemical cell maintained at 25±1 °C. All polarization tests were performed after stabilizing the open circuit potential for 3600 sec. The PTC1 Kit electrochemical sample masks aided in defining a 1 cm^2 working area on every test sample (i.e. working electrode) within the cell. To avoid the occurrence of crevice corrosion, no space was allowed between the mask and steel coupon.

Two electrolytes deployed for this test were prepared in line with NACE TM 0284-2016 test solution A, which consist of H_2S, NaCl, and CH_3COOH dissolved in distilled water. However, H_2S did not feature in this study due to laboratory safety concerns. An addition of H_2SO_4 and NH_4SCN was used to simulate hydrogen production (sour service) within the test environment. As such, samples were polarized in a binary solution of 5 wt. % NaCl and 0.5 wt. % CH_3COOH at a pH of 4.5, which represented a non-hydrogen producing media. Later, the same test solution was modified with 1 wt. % H_2SO_4 to create the hydrogen producing media with drops of 3 g/l NH_4SCN acting as a hydrogen recombination poison within the medium at a pH of 1.5. The similar use of hydrogen promoting species for simulating corrosive conditions experienced by pipelines have already been established [204,276].

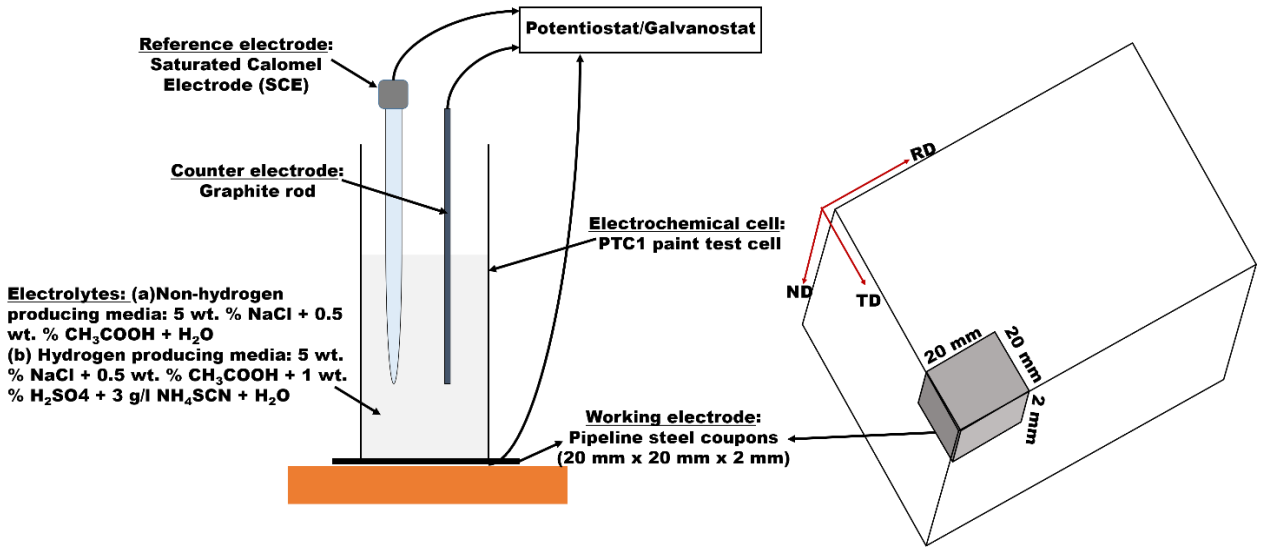

Fig. 3.8 Schematic diagram of the electrochemical corrosion test set-up and the region of the rolled plate from which test coupons where obtained (RD: rolling direction, TD: transverse direction, ND: normal direction)

3.3.6 Computational details

Molecular dynamics (MD) simulation was used to model the interplay between the corrosive environment and the iron (Fe) crystal surface. This procedure was implemented with the Forcite module which is embedded in the Materials Studio Software. Various molecular configurations were tried at low energy before identifying the minimum energy. The crystal planes of Fe corresponding to the (111), (110), and (100) surfaces were examined for the effect of both hydrogen producing and non-hydrogen producing media. For this study, a 8 x 8 x 1 supercell was deployed for each of the Fe surfaces and periodic boundaries were set on the x and y coordinates. Periodic plate surfaces having four atomic layers and a 25 Å thick vacuum plate were designed on top of each crystal planes (i.e. (111), (110) and (100)). All the calculations were done at 300K using a time step of 0.1 fs and a simulation period of 0.5 ps in an Anderson thermostat. In order to optimize the geometry of different structures, the Condensed-phase Optimized Molecular Potentials for Atomistic Simulation Studies (COMPASS) were applied. As an ab initio force field, the COMPASS is capable of predicting interaction and cohesive energies for a variety of organic and inorganic molecules [277]. The energies associated with the interactions ($E_{interection}$) between the molecules in each electrolyte and the Fe-crystal surfaces were estimated using the following expression (Eq. 3.2).

$$E_{interaction} = E_{total} - (E_{surface} + E_{molecule}) \quad (3.2)$$

The total system energy, which comprises of those from the combined molecules present in each corrosive media and Fe surface, is designated as E_{total}. In the absence of any adsorption molecule, the energy of the Fe-surface is given as $E_{surface}$, whereas $E_{molecule}$ defines the energy of a specific molecule.

3.3.7 Corroded surface analyses

Sequences of additional analyses were carried out to supplement the electrochemical studies on the pipeline specimens. First, the morphology of pre-cleaned corroded surfaces was studied by taking images with an SEM. The corrosion products formed on each coupon were further characterized by an X-ray Photoelectron Spectroscopy (XPS) technique. All XPS measurements were made using a Kratos (Manchester, UK) AXIS Supra system located at the Saskatchewan

Structural Sciences Centre (SSSC). It is a system equipped with a 500 mm Rowland circle monochromated Al K-α (1486.6 eV) source, a combined hemi-spherical analyzer (HSA), and a spherical mirror analyzer (SMA). Analysis was done with a spot size of hybrid slot (300 x 700 microns) and wide scans were collected in the binding energy range of -5 to 1200, in 1 eV steps and a pass energy of 160 eV. For high resolution scans, 0.1 eV steps and a pass energy of 20 eV was used. Throughout this analysis, the operating vacuum pressure was below $1x10^{-8}$ Torr, while the accelerating voltage and the emission current were fixed at 15 keV and 15 mA respectively. The XPS spectra of the respective adsorbed film/corrosion product aggregates were deconvoluted using a least squares algorithm with Gaussian–Lorentzian combination from CasaXPS software.

3.3.8 Hydrogen permeation test

Hydrogen permeation studies was conducted across the ND – TD plane of 20 mm x 20 mm x 2 mm (length x width x thickness) test pieces obtained from the mid-thickness section. For this test, the modified Devanathan-Stachurski electrochemical cell [278] was deployed in accordance with standard procedure described in ISO 17081: 2004 for hydrogen permeation in metals [279]. In order to increase accuracy of results obtained from oxidation current measurement, all specimens were polished on both sides up to 4000 grits silicon carbide paper and 1 μm diamond suspension to create a mirror-like surface before testing. The schematic diagram in Fig. 3.9 shows the two-compartment experimental set-up comprising of a charging cell with 0.1 M sulfuric acid (H_2SO_4) and 3 g/l ammonium thiocyanate (NH_4SCN) in 250 mls of distilled water on the hydrogen entry side, and 0.1 M sodium hydroxide (NaOH) in 250 mls of distilled water on the oxidation side. An area of approximately 100 mm^2 of the pipeline steel was chosen to serve as the permeation layer between the different cells. Both electrochemical cells (i.e. charging and hydrogen oxidation) consist of a graphite counter electrode. However, a SCE reference electrode was included in the oxidation cell. A constant charging current of 5 mA was maintained on the hydrogen entry side of the experimental set-up using an Instek DC power source, while current measurements were collected with a Gamry Interface 1000 Potentiostat/Galvanostat/ZRA. Before commencing hydrogen charging, current was stabilized at approximately 1 μA. After the initial polarization cycle, the DC power source was turned-off to allow easy discharge of charging current. The second polarization cycle proceeds immediately the baseline current is attained (i.e. 1 μA). Saturating all traps with hydrogen in the first round of charging allows only the reversible traps to discharge prior to the next charging. This implies that the irreversible traps are left permanently occupied by hydrogen, while the second charging cycle refills only the reversible traps. Thereafter, hydrogen permeation parameters were determined based on Eqs 3.3-3.5 and constants obtained from literature [114].

$$\text{Effective diffusivity } (D_{eff}) = \frac{L^2}{6t_1} \quad (3.3)$$

$$\text{Permeability } (J_\infty L) = \frac{I_\infty L}{FA} \quad (3.4)$$

$$\text{Apparent solubility } (C_{app}) = \frac{J_\infty L}{D_{eff}} \quad (3.5)$$

where; L (cm) = thickness of pipeline steel membrane, A (cm^2) = area of pipeline steel subjected to permeation test, F (C/mol) = Faraday constant (96,500 C/mol), $I_\infty(\mu A)$ = steady state current density, t_1 (s) = time lag (ie time at $0.63I_\infty$). To ensure reproducibility, the average values obtained from two separate measurements where determined.

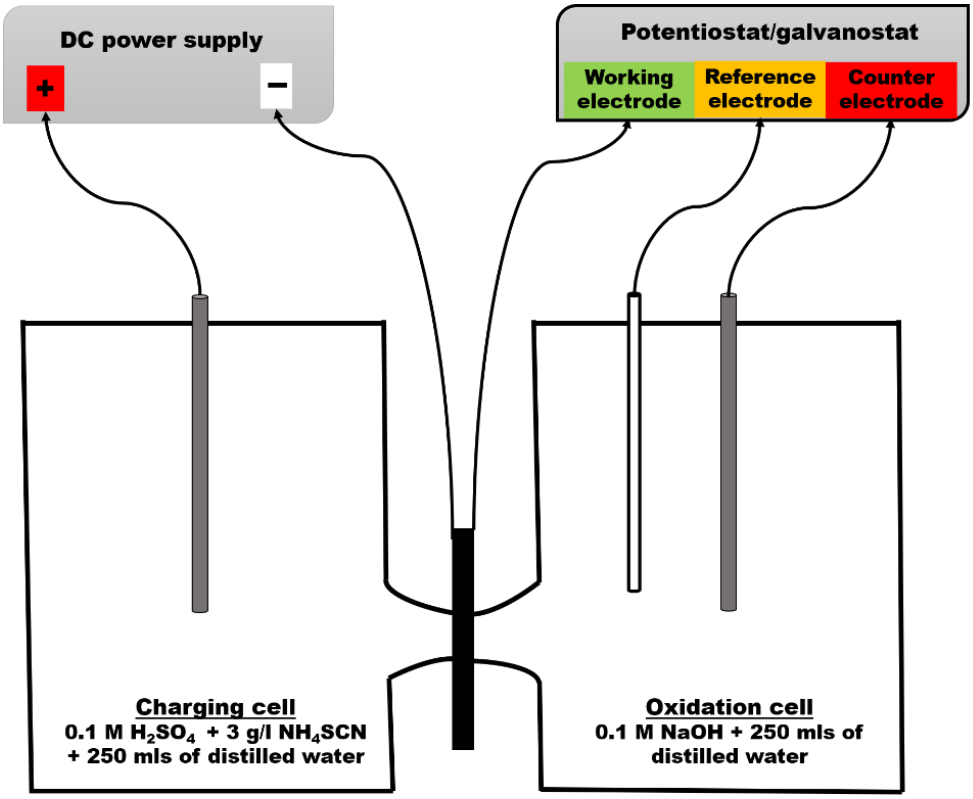

Fig. 3.9 Schematic representation of hydrogen permeation test set-up indicating the pipeline steel sample (working electrode) held between the charging and oxidation cells

3.3.9 Environmentally assisted cracking studies

Pipeline specimens were tested for HIC under the influence of tensile loading. For investigation under tensile stress condition, a slow strain rate tensile (SSRT) testing technique was used. The modified tensile testing machine used for this study was set at an elongation rate of 2.5×10^{-5} mm/s, which amounts to a strain rate of 10^{-6} s^{-1}. This setting was chosen to ensure adequate time for diffusion during hydrogen charging. Specimens were machined parallel to the rolling direction from the top surface and mid-thickness layers as represented schematically in Fig. 3.10. These two regions of each specimen were chosen to examine the contributions of different steel layers to HIC susceptibility. All dimensions of the 4 mm thick test specimens were determined based on ASTM E8/E8M-08 standard as shown in Fig. 3.10. First, baseline tensile properties of specimens were determined in air (without exposure to electrochemical hydrogen charging).

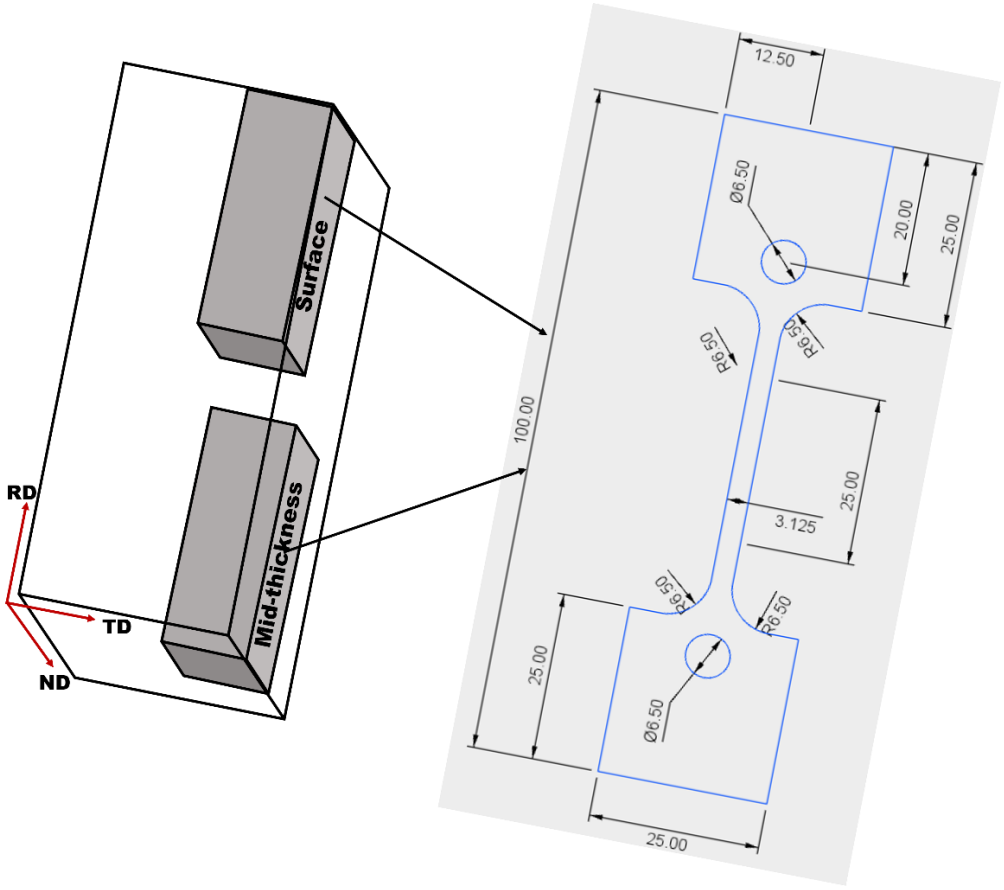

Fig. 3.10 A sketch of tensile specimen obtained from the mid-thickness portion or rolled plate along the rolling direction (all dimensions are in mm, RD: rolling direction, TD: transverse direction, ND: normal direction)

Second, the tests in hydrogen environment were conducted by setting up an electrochemical hydrogen charging cell around each mounted tensile specimen to provide hydrogen *in-situ* during tensile loading. The percentage elongation, tensile stress or failure stress (in case of test with hydrogen charging), and yield stress were measured for each tested specimen to determine the effects of hydrogen. There are two methods commonly used for investigating the effect of hydrogen in steels. It is either by gaseous (sour) hydrogen charging or electrochemical hydrogen charging. However, a similarity has been established between results obtained using both procedures [280]. For this study, the electrochemical charging method was adopted. This approach eliminates the possible uses of toxic H_2S gas. An electrolyte comprising of 0.2 M H_2SO_4 and 3 g/l NH_4SCN (to promote hydrogen ingress) dissolved in distilled water was used for hydrogen charging as previously reported in the literature [204,281].

Also, the tensile properties of pipeline steel specimens produced after post-processing annealing treatments were examined before and after pre-hydrogen charging. These mechanical tests were performed using a KAPPA 250 DS Zwick/Roell tensile testing machine at a straining rate of 10^{-3} s-1. Specimens were pre-charged with hydrogen for 12 h, and immediately tested for mechanical properties. In order to minimize desorption of hydrogen from the pre-charged steel, each specimen was quickly removed from the charging set-up and tested in an ex-situ tensile tester. The density of dimples present on the fractured surfaces of each processed steel was estimated using the ImageJ and adobe photoshop software. Three different tests were used to determine the average tensile parameters for each steel. In addition, the SEM fractographs obtained from the center of every failed specimen were analyzed to determine the average number of dimples.

Full thickness samples measuring 9.6 mm (ND), 100 mm (TD) long, and 20 mm (RD) wide were machined according to NACE TM 0284-2016 standard [201] for HIC evaluation without tensile loading. The schematic diagram of a typical HIC experimental set up is displayed in Fig. 3.11. For the preliminary studies on specimens WE and WD, electrochemical hydrogen charging was performed for 12 h and 16 h without any applied stress. Thereafter, a charging time of 12 h was fixed for the next set of specimens. During charging, the pipeline steel sample was made the cathode, while a platinum wire served as the anode. An Instek DC power supply was used to maintain a constant current density of 20 mA/cm^2 for the entire duration of every test. Also, the electrochemical cell was constantly monitored to ensure that the electrolyte was replenished as

soon as it started depleting and the tests were repeated two times to guarantee reproducibility. At the end of the charging duration, specimens were removed and cleaned. The charged specimens were cut to reveal the thickness cross-section, before crack examination with an SEM.

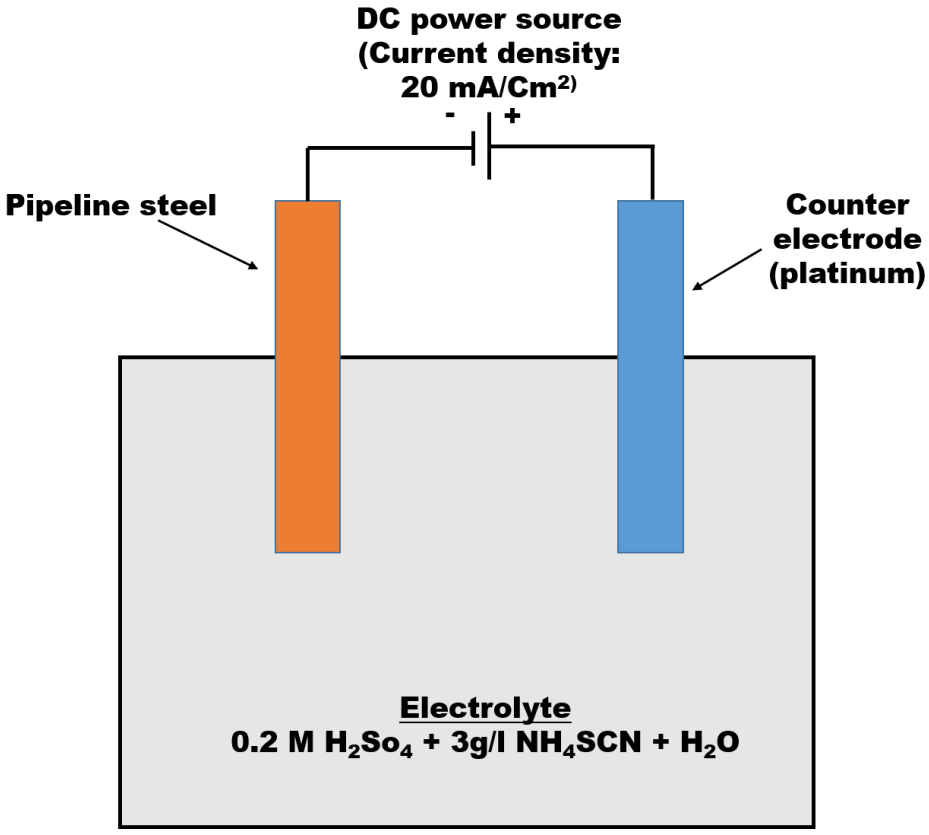

Fig. 3.11 Schematic representation of experimental set-up for electrochemical hydrogen charging,

CHAPTER 4 : EFFECT OF THERMOMECHANICAL PROCESSING AND CRYSTALLOGRAPHIC ORIENTATION ON THE CORROSION BEHAVIOUR OF API 5L X70 PIPELINE STEEL[3]

4.1 Overview

In this chapter, the influence of various thermomechanical treatment conditions on the electrochemical corrosion response of API X70 pipeline steel was discussed. The focus of this section is to address the first objective in this thesis, which is to correlate microstructural features in processed steels to their corrosion response. Some changes which differentiates this chapter from the originally published manuscript are as follows:

a) The materials and methodology section have been removed to avoid duplication, as this aspect is already described in chapter 3 of this thesis.
b) Additional results for other newly developed pipeline steel specimens (WG and WH) were merged with those initially published (WE and WD) in this article.
c) Results from all processed steel plates are compared with a commercially available X70 specimen, which is described as Ref X70 throughout this section.
d) All references in this manuscript are provided at the end of the thesis.

This work presents the electrochemical corrosion response of X70 pipeline steel substrates thermomechanically processed at different conditions and compared with a commercial sample labeled Ref X70. Corrosion tests were conducted by potentiodynamic polarization in hydrogen producing and non-hydrogen producing environments. Generally, a lower corrosion rate was measured in hydrogen producing media due to the rapid formation of a corrosion product film on pipeline substrate, but the Ref X70 and WE specimens emerged as the most susceptible to corrosion in both test situations. Variations in thermomechanical rolling conditions influenced

[3] Most of the results in this chapter are already published, but were used with permission from *Springer* (Appendix D): E. Ohaeri, J. Omale, U. Eduok, J. Szpunar, 'Effect of thermomechanical processing and crystallographic orientation on the corrosion behavior of API 5L X70 pipeline steel', *Metallurgical and Materials Transaction A*, 2018, Vol. 49, No 6, pp. 2269-2280

The PhD candidate E. Ohaeri designed all experiments, characterised microstructure, and surface morphology of specimens, compiled the report, as well as finalised the manuscript after revision by supervisor and peer-reviewers.

grain orientation, protective film properties, corrosion, and cracking behavior on all specimens. Cracks were seen in specimens WE, WD, and Ref X70 after the test in hydrogen producing scenario. The Ref X70 and WE specimens experienced the most intense deterioration of protective corrosion product film. Subsequently, these two specimens were stricken by hydrogen assisted cracks. A large part of specimen WD retained its protective corrosion product film after the polarization test, and sites where spalling occurred resulted in pitting with less cracking. Specimens WH and WG did not display any visible surface cracking after being probed in either test medium. Despite weak crystallographic texture noticed in specimens WD, WG, and WH they showed a higher intensity of ⟨111⟩||ND oriented grains relative to Ref X70 and WE with a more random distribution of ⟨111⟩||ND, ⟨011⟩||ND and ⟨001⟩||ND oriented grains.

4.2 Background

In recent years, more pipelines have been manufactured in order to meet the world's growing energy need. A key factor in maintaining an adequate energy supply through pipelines is improving the corrosion resistance of the steel plates, especially under severe service conditions. A report from the National Association of Corrosion Engineers (NACE), the internationally renowned authority in corrosion, placed the global cost of corrosion at a whopping 2.5 trillion USD, an equivalent of 3.4% of the entire world's GDP [282]. Such striking statistics shows the overwhelming impact of corrosion on our infrastructures. Corrosion is a means through which metals achieve thermodynamic stability after being transformed by processing [283]. With oxidation and reduction occurring on the steel during the corrosion process, water reduction reactions may result in the release of hydrogen gas. This is also similar during uncontrolled cathodic protection of pipelines, as the production of hydrogen becomes imminent at highly cathodic potentials [284,285]. In the case of pipelines, corrosion behavior becomes even more complex when exposed to service environments containing other hydrogen-producing species.

Corrosion in pipelines is closely related to various environmental factors. The presence of corrodents such as sulfides, chlorides, and carbonates highly influence the corrosion behavior of pipeline steel [286]. Some of these species interfere with the corrosion potential of carbon steel, while others destabilize passivation film and enhance anodic sensitivity [287,288]. However, the combined activities of acetic acid and sodium chloride within the vicinity of pipeline steel further

increase the corrosion rate [289]. Thus, it is important to properly understand the role of metallurgical variables in altering corrosion resistance of pipeline steel. Many corrosion studies have focused mainly on electrochemical testing of steels for different applications. Less consideration is given to the effect of hot rolling on the electrochemical response of steels. Interestingly, a recent study established that pitting corrosion resistance in 316LVM austenitic stainless steel was increased at ⟨111⟩ and ⟨011⟩ oriented planes compared to other planes of lower atomic density [290]. Also, crystallographic orientation of grains has been proposed as a major corrosion controlling factor for commercial grade titanium [291]. Since corrosion is a surface phenomenon, the effect of plane orientation at the steel surface remains an important aspect. The idea of creating a material with the dominance of a preferred orientation is simply referred to as crystallographic texture. Even though variations in texture are commonly seen across pipeline steel thickness, boundaries of ⟨111⟩ and ⟨011⟩ planes oriented parallel to the rolling plane offer more resistance to cracking [147]. These orientations can potentially enhance corrosion resistance, especially the ⟨111⟩ planes oriented parallel to the steel surface. Therefore, it is logical to hypothesize that improving the fraction of grains with a corrosion-resistant orientation on pipeline steel surface will reduce predisposition to corrosion. Thermomechanical controlled processing shows great promise in the development of pipeline steel bearing specific preferred orientation of grains. During this process, pipeline steel grains undergo intense plastic deformation, which directly affects mechanical properties. Changes in mechanical properties will have consequences on the corrosion behavior of pipeline steel. As such, understanding corrosion susceptibility with respect to crystallographic texture evolution during thermomechanical processing will assist in the development of pipeline steel with enhanced corrosion resistance.

This study lays the background for the suitable thermomechanical processing conditions to produce pipeline steels that can serve in extreme environments. The main objective of this study is to comparatively investigate the corrosion behavior of X70 pipeline steels with the same alloying compositions, after thermomechanical treatments at different temperature conditions.

4.3 Experimental procedure

Refer to sections 3.2, 3.3.1 – 3.3.4, and 3.3.5 – 3.3.6 for details about pipeline steel material, microstructural evaluation techniques, electrochemical corrosion test procedure, and corrosion surface analysis.

4.4 Result and discussions

4.4.1 Microstructure characterization

Thermomechanical processing conditions for these pipeline steel specimens are presented in Tables 3.1, and their microstructures as displayed in Fig. 4.1 are a direct consequence of the thermomechanical processing deployed. The presence of pearlite-enriched ferrite and acicular ferrite microstructure, as well as martensite-austenite constituents, are evident in pipeline steels. The rolling temperature at the austenite/ferrite region may have contributed to the observed grain morphology. However, rolling pipeline steel below recrystallization temperature enhances the formation of polygonal ferrite during austenite to ferrite transitions [160]. Microstructure is critical in terms of mechanical properties of high strength pipeline steel, because of its role in determining good combination of strength, toughness, and weldability. Typical microstructures often found in pipeline steel include acicular ferrite, polygonal ferrite, bainitic-ferrite, martensite, granular bainitic-ferrite, and Widmanstätten-ferrite [26,130,292]. The micrographs indicate predominance of ferrite microstructures in specimens of all pipeline steels. Nevertheless, significant manifestation of polygonal ferrite can be seen in the Ref X70 specimen (Figs. 4.1a-b). Abundant patches of perlite-enriched ferrite are evident in the whitish regions shown in Fig. 4.1b. In a like manner, sparse appearances of polygonal ferrite, some acicular ferrite, and minor traces bainitic-ferrite occurred in specimen WE (Fig. 4.1c-d). More significant evolution of acicular ferrite with some lath-like bundles of bainitic-ferrite are obvious in other specimens WD (Figs. 4.1e-f), WH (Figs. 4.1g-h) and WG (Figs. 4.1i-j). That notwithstanding, it is clear that the observed microstructural features in all steel specimens are consistent with those reported in literature for X70 pipeline steel [139,293–295].

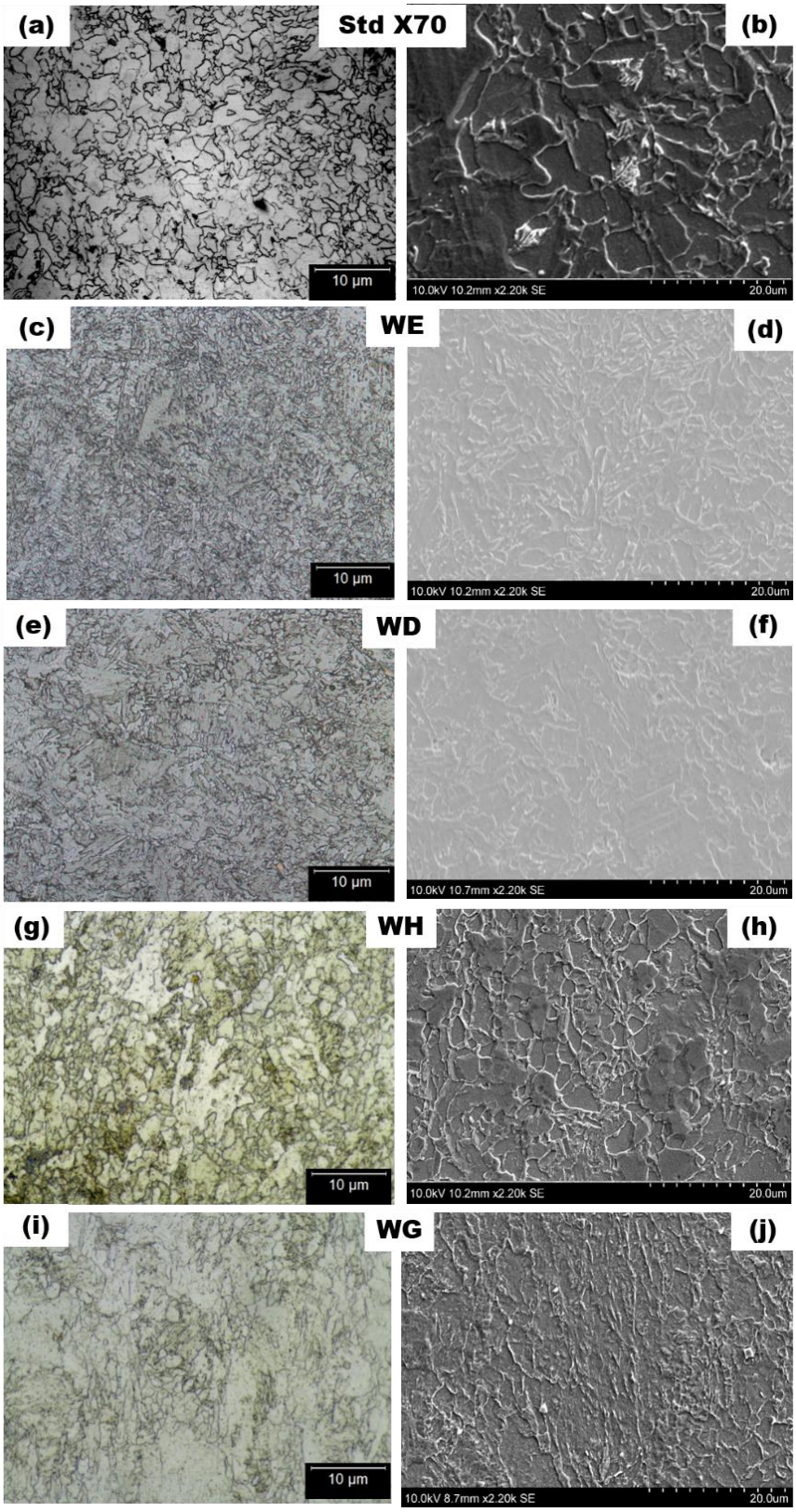

Fig. 4.1 Optical and SEM micrographs of pipeline steel specimens (a-b) Ref X70 (c-d) WE (e-f) WD (g-h) WH and (i-j) WG

Microstructure and grain properties play important roles in resistance to corrosion. Pipeline steel containing mainly acicular ferrite and granular bainite experience low electrochemical activity when compared to others with polygonal ferrite and acicular ferrite [141,296]. The authors attributed the toughness of acicular ferrite grains to their low effective grain size in comparison to those of the polygonal ferrite. Another explanation for this phenomenon is the reduction in misorientation angle between grains due to the lath-like appearance of acicular ferrite. Accumulation of immobile dislocations within small grains is responsible for optimum strength and toughness in acicular ferrite dominated pipeline steel, while a mixture of polygonal ferrite and acicular ferrite creates more susceptible grain boundaries, which aid in electrochemical activities [166].

4.4.2 EBSD analysis

Noticeable property changes impacted in pipeline steel during the hot rolling process, often includes texture evolution. This simply refers to preferred orientation of grains within the steel structure. Apart from deformation related changes in grain orientation, other factors, such as recrystallization, rolling temperatures, and phase transformation, also make significant contributions towards the surface texture [297]. A correlation between texture and corrosion in steels can be explained by the fact that dense planes with low surface energy dissolve slower than less dense planes with higher surface energy [156]. The same authors stated that crystallographic planes of lower atomic density (higher surface energy) offers water adsorption sites and promotes hydrogen evolution, while planes of high atomic density (low surface energy) present hydrogen reduction sites. Therefore, orientating crystals towards denser planes (lower surface energy) can reduce corrosion. Furthermore, low resistance to corrosion has been observed in cold rolled steel containing increasing volume fractions of $\langle 111\rangle||\mathrm{ND} < \langle 011\rangle||\mathrm{ND} < \langle 001\rangle||\mathrm{ND}$ texture fibers, compared with hot rolled steel containing $\langle 001\rangle||\mathrm{ND} < \langle 011\rangle||\mathrm{ND} < \langle 111\rangle||\mathrm{ND}$ texture distribution [298]. It was concluded that a higher corrosion rate in cold rolled samples was a result of variation in texture, grain refinement, and formation of inclusions within the steel microstructure. Another report attributed the anisotropy of corrosion behavior in hot-rolled carbon steel rods to variation in the dissolution rate of $\langle 011\rangle||\mathrm{ND}$ and of $\langle 001\rangle||\mathrm{ND}$ crystals [299]. Other grain properties also play significant roles in either increasing or reducing the extent of anodic dissolution during corrosion process.

Properties of pipeline steel are closely related to those of its grains. An important grain property is crystallographic orientation. Fig. 4.2 presents results obtained from EBSD microstructural analysis on all test specimens. A unique color-coding corresponds to each plane described in the legend for IPF orientation maps in Figs. 4.2a, d, g, j, and m. The contrast between grains bearing ⟨111⟩||ND, ⟨011⟩||ND and ⟨001⟩||ND orientations are shown in these maps. Grain orientation in the thermomechanically processed pipeline steel specimens (i.e. WE, WD, WH and WG) look quite similar except in the Ref X70 specimen, A possible explanation is the temperature applied during finishing rolling on the new steels. Although the treated specimens were finish rolled at close temperature ranges within the austenite-ferrite transformation region, they still displayed distinct structures. Additional microstructural characteristics showed some differences. For instance, variations in other grain properties may be attributed to wider finish rolling temperature range applied on WH: (830 – 760℃), WD: (880 – 815 ℃), and WG (880 – 830 ℃), while a relatively narrower rolling temperature range (850 – 805 ℃) was used for WE. It is evident that the three principal orientations (⟨111⟩||ND, ⟨011⟩||ND, and ⟨001⟩||ND) appear randomly on all specimens. In comparison, the presence of ⟨001⟩||ND oriented grains (red colored grains) are more dominant in the Ref X70 specimen (Fig 4.2a) than in the others. This means that specimens are not strongly textured. However, there is some intensity of ⟨111⟩||ND oriented grains (blue colored grains) in specimen WG (Fig. 4.2m). Yet, orientation maps alone are unable to show some specific differences in test specimens. Extra methods of analysis are required to specifically differentiate the structure of each specimen.

Recrystallization fraction analysis showed the area fraction of recrystallized, recovered, and deformed grains in Ref X70 as 13 %, 62 %, and 23 %; WD as 16 %, 55 %, and 28 %; WE as 5 %, 45 %, and 48 %; WH as 6 %, 53 %, and 40 %; and WG as 7 %, 44 % and 47 % respectively. As shown in Figs. 4.2, relatively higher fraction of recrystallization (blue colored grains) and recovery (yellow colored grains) in Ref X70 (Fig. 4.2b), WD (Fig. 4.2e), WH (Fig. 4.2k), and WG (Fig. 4.2n) suggest that the grains have less defected structure compared to specimen WE (Fig. 4.2e) The least fraction of recrystallized grains are displayed in the WE specimen. This implies that some fraction of elastic energy stored in deformed grains was released during recrystallization giving rise to a relatively lower fraction of deformed grains seen in Ref X70, WD, WH, and WG. There are suggestions in the literature that recrystallized grains have a lower susceptibility to

hydrogen attack, while deformed grains are often incoherent and prone to attack by hydrogen and other corrosive species [158]. This implies that lower fraction of recrystallized and recovered grains in WE specimen can adversely affect its resistance to environmental assisted attacks compared to other pipeline steel specimens.

The influence of phase distribution on corrosion patterns was also examined. Grade X70 pipeline steel typically consists of different phases as indicated in the phase maps shown in Figs. 4.2c, f, i, l, and o. The ferrite dominance (blue color) in all specimens corroborates our observations during the microstructural examination in Fig. 4.1. Nevertheless, other secondary phases were also identified. Cementite (yellow spots) and martensite (back spots) were seen dispersed within the ferritic phase. Considering the level of recrystallization and recovery in test specimens, it was not surprising that an insignificant amount of retained austenite (red spots) was featured in any of the specimens. From a thermodynamic standpoint, dominantly ferritic microstructure will tend to corrode easily compared to bainitic-ferrite microstructure, because anodic dissolution is lowered by the greater presence of harder phases such as bainite [300]. Therefore, the corrosion pattern of test specimens can be traced back to the microstructural phases developed after thermomechanical treatment. It can be noticed that more cementite (iron carbide) precipitates were found on the surface of WE (Fig. 4.2i) compared to the rest of the specimens. Such microstructural characteristics in specimen WE could potentially serve as a reason for an enhanced corrosive degradation rate. The possibility of intensified hydrogen trapping at interfaces between ferrite and cementite in low carbon steel has already been established [301]. However, the trapping efficiency at dislocations is usually higher compared to ferrite-cementite interfaces in steels [302]. With a higher presence of deformed grains at the surface of WE (Fig. 4.2h), and less deformed grains on other pipeline steel specimens, it is expected that dislocation density will also be higher in WE. The consequence will be the increased corrosion activities and the increased hydrogen damage in WE compared to the other specimens.

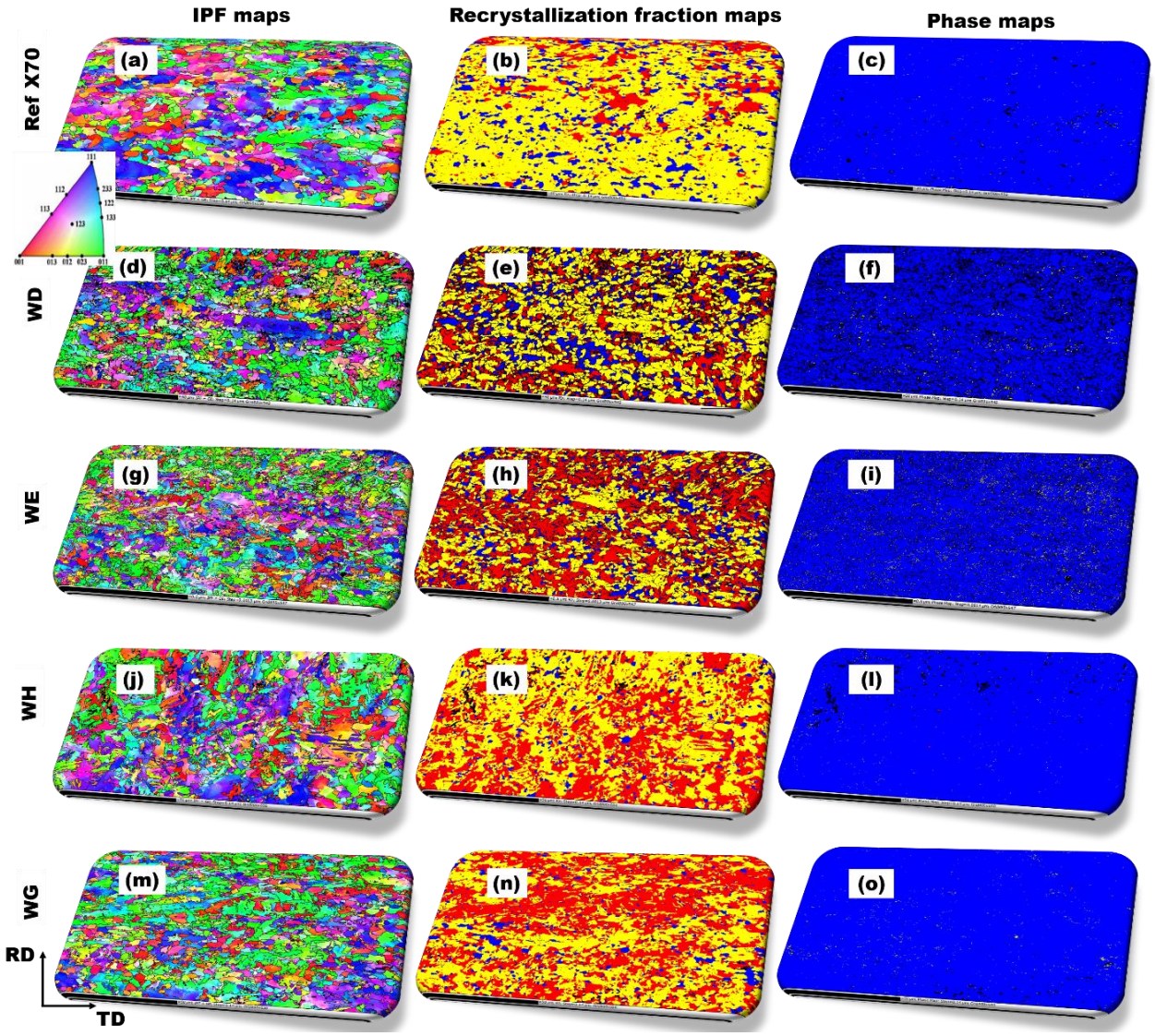

Fig. 4.2 EBSD maps for pipeline steel: Orientation maps (a) Ref X70 (d) WE (g) WE (j) WH (m) WG, Recrystallization fraction maps (b) Ref X70 (e) WD (h) WE (k) WH (n) WG, Phases maps (c) Ref X70 (f) WD (i) WE (l) WH (o) WG (For the recrystallization area fraction maps, the deformed regions are red, recovered regions are yellow, and recrystallized regions are blue. For the phase maps, ferrite is blue, cementite is yellow, while austenite is red)

Grain boundary character is of interest to corrosion behavior in pipeline steel. Thermomechanical processing alters the network of grain boundaries, especially high angle grain boundaries, and thus increases the relative frequency of special coincident site lattice (CSL) boundaries [303]. Increasing the fraction of these low energy CSL grain boundaries also reduces corrosion rate and

improves resistance to cracking [147,304]. Although high strength pipeline steel produced through TMCP does not show prominent twining, it is important to consider the contribution of CSL boundaries towards corrosion behavior in steel. Moreover, variations in processing parameters could affect the appearance of certain types of boundaries. Treatment procedures involving deformation and annealing have been identified as ways of increasing CSL boundary fractions in materials [305]. Thermomechanical treatment offers a means of reducing crack prone high energy boundaries by eliminating potential crack propagation path and enhancing the presence of low energy CSL boundaries [149]. For pipelines, typically, higher frequencies of CSL boundaries within the range of $3 \leq \Sigma \leq 33$ are often reported [306]. It is unclear what the role of other special CSL grain boundaries outside this range might be with respect to corrosion in pipeline steel. That notwithstanding, CSL boundaries possessed low energy which makes them less strained. However, the total fraction of these special boundaries was estimated to be approximately 7.3 %, 6.9 %, 11.7 %, 9.6 %, and 4.4 % for Ref X70, WD, WH, WG, and WE respectively. Again, the least fraction of CSL-type grain boundaries is recorded in specimen WE. Marked resistance to hydrogen induced cracking has been linked to the increased presence of $\Sigma 11$, $\Sigma 13b$, and $\Sigma 29a$ CSL boundaries, especially $\Sigma 13b$ [307]. The researchers found that large fraction of $\langle 111 \rangle || ND$ oriented grains were associated with the occurrence of $\Sigma 13b$ type CSL boundary. An explanation for this is the low misorientation angle between different $\langle 111 \rangle$ planes that define a $\Sigma 13b$ CSL boundary. Considering the low energy corresponding to an increased fraction of CSL boundaries, it can be suggested that WE, with the least fraction of CSL, may likely possess more energy for crack propagation in comparison to other steel samples.

To further analyze the micro-texture components of each steel specimen in line with the major crystallographic orientations, pole figures were generated as shown in Fig. 4.3. All test samples revealed weak texture, as indicated by their intensities. Nevertheless, WD had the highest intensity of 3.54, followed by WG at 2.93, and WH at 2.90. Meanwhile, specimens WE and Ref X70 attained the least texture intensity of 2.72 and 2.76 respectively. The most intense orientation in specimens WD and WG corresponds to a very close deviation towards $\langle 111 \rangle || ND$. In a like manner, specimen WH showed maxima that are also in the proximity of $\langle 111 \rangle || ND$. It can be deduced that TMCP treatment was more effective in promoting the evolution of $\langle 111 \rangle || ND$ orientation and lower energy CSL boundaries in WD and WG relative to other specimens.

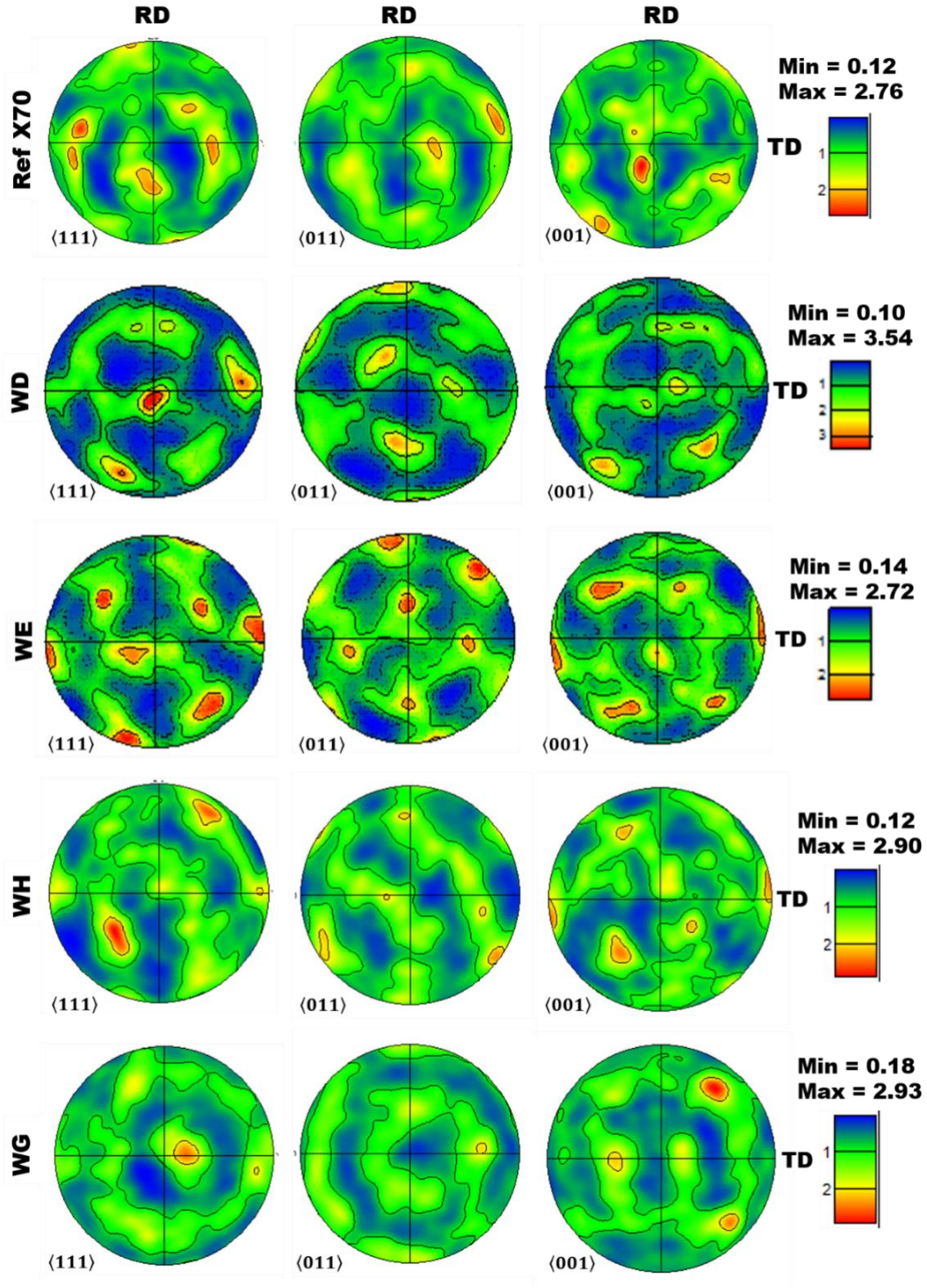

Fig. 4.3 Pole figures for each X70 pipeline steel substrate

4.4.3 Corrosion tests

Open circuit potential

The dependence of open circuit potential (E_{oc}) on time for metal substrates in the different corrosive media is presented in Fig. 4.4, with significant influence noticed in the hydrogen producing test environment (Fig. 4.4a). In the non-hydrogen producing system (Fig 4.4b), the magnitudes of E_{oc} for all the metals sharply decreased before gradually reaching a steady state. A shift to a negative value is observed for Ref X70 compared to WD, WE, WH, and WG. A similar trend is also recorded in the presence of sulfuric acid as the corrodent (i.e. hydrogen producing media). However, in Fig. 4.6 Ref X70, WH and WG specimens displayed curves with random patterns. The implication is that the test media experienced more disturbance due to the production of hydrogen. In addition, the process of passivation and re-passivation of the pipeline steel surface might have contributed to causing disorderliness within the test environment. In both media, OCP for WE and WD settled at more positive values in comparison to other specimens. Values of E_{oc} tend to more noble and positive values for the hydrogen producing electrolyte. The difference in E_{oc} between these two environments could be attributed to the formation of protective corrosion product film on one surface over the other. In corrosion systems with film-forming corrosion inhibitors, this phenomenon is further explained by monitoring the potential shifts up to ±85 mV [308]. An increase in corrosion potential with hydrogen production is observed for all samples, as they tend to stabilize at a higher accumulation period. The specimens exposed to a non-hydrogen producing electrolyte follow a similar trend. The difference in potential stabilization for hydrogen producing and non-hydrogen producing tested samples is less than 150 mV. As potential tends towards greater negative values, increased corrosion activities tend to occur [309]. This means that higher electrochemical activity occurred in tests performed under non-hydrogen producing conditions.

Potentiodynamic polarization measurements

These corrosion tests aim at assessing the corrosion behaviors of pipeline substrates when tested in both non-hydrogen producing and hydrogen producing corrosive environments at room temperature using electrochemical techniques. The Tafel parameters extrapolated from the DC curves in Figs. 4.4c-d are useful data in elucidating gross corrosion kinetics on each steel substrates

according to literature [310], and the former are presented in Table 4.1 as the magnitudes of corrosion potential (E_{corr}) and corrosion current density (j_{corr}). The Tafel slopes determined by extrapolating along the cathodic (β_c) and anodic (β_a) curves are also presented. These values are quite significant, especially for the specimens tested in hydrogen producing media. This can be attributed to the passive behaviour observed in Fig. 4.4c. Specimens WE and ref X70 were attacked the most by corrosion in comparison to other specimens when probed in both corrosive environments. All metal substrates corroded less in the hydrogen producing medium except the Ref X70 specimen. However, specimen WG corroded the least amongst all specimens. The improvement in its structure through TMCP might have warranted such reduction in electrochemical corrosion response. The j_{corr} value of 9.8 µA for WG can be considered as relatively drastic reduction in corrosive behavior. This indicates the higher propensity of WG to resist hydrogen related corrosive degradation, possibly by passivation and re-passivation.

Again, Table 4.1 and Fig. 4.4d shows that WG has the lowest j_{corr} value in the non-hydrogen producing condition. As an inference, a steady reduction in j_{corr} is consistent with reduced rates of anodic dissolution of metal substrates placed within the corrosive media [311]. Enhanced anodic sensitivity of corroding surfaces in non-hydrogen environment could be attributed to the corrosive action of the binary CH_3COOH/NaCl medium. On the other hand, the presence of sulfate ions contributed to hydrogen production, thus reducing the corrosion rate on specimens WH and WG significantly. Evidence of corrosion resistance for both WH and WG samples within the hydrogen producing medium is due to solid scale formed by the species in aqueous solution used for corrosion test. Also, stabilization of such films then becomes effective in enhancing the corrosion resistance of the metal samples as reflected on the Tafel curves at 0.00 V (passivation potential). Altogether, the rate of corrosion for WE and Ref X70 specimens are the highest relative to WD, WH and WG (Table 4.1) when tested in both non-hydrogen producing and hydrogen producing corrosive environments.

Table 4.1 Polarization parameters for pipeline samples in different corrosive environments

Specimens	Tafel parameters			
	β_a(V/decade)	β_c(V/decade)	j_{corr} (µA)	E_{corr} (V)
	Non-hydrogen producing media			
Ref X70	0.0426	0.135	98.3	-618
WE	0.0288	0.140	109.0	-596
WD	0.0565	0.125	92.4	-620
WG	0.169	0.179	75.1	-616
WH	0.0441	0.124	97.7	-625
	Hydrogen producing media			
Ref X70	0.0556	0.1343	123.0	-524
WE	0.042	0.1089	64.0	-525
WD	0.0904	0.1008	59.0	-504
WG	0.0567	0.0535	9.8	-498
WH	0.0441	0.0559	20.2	-505

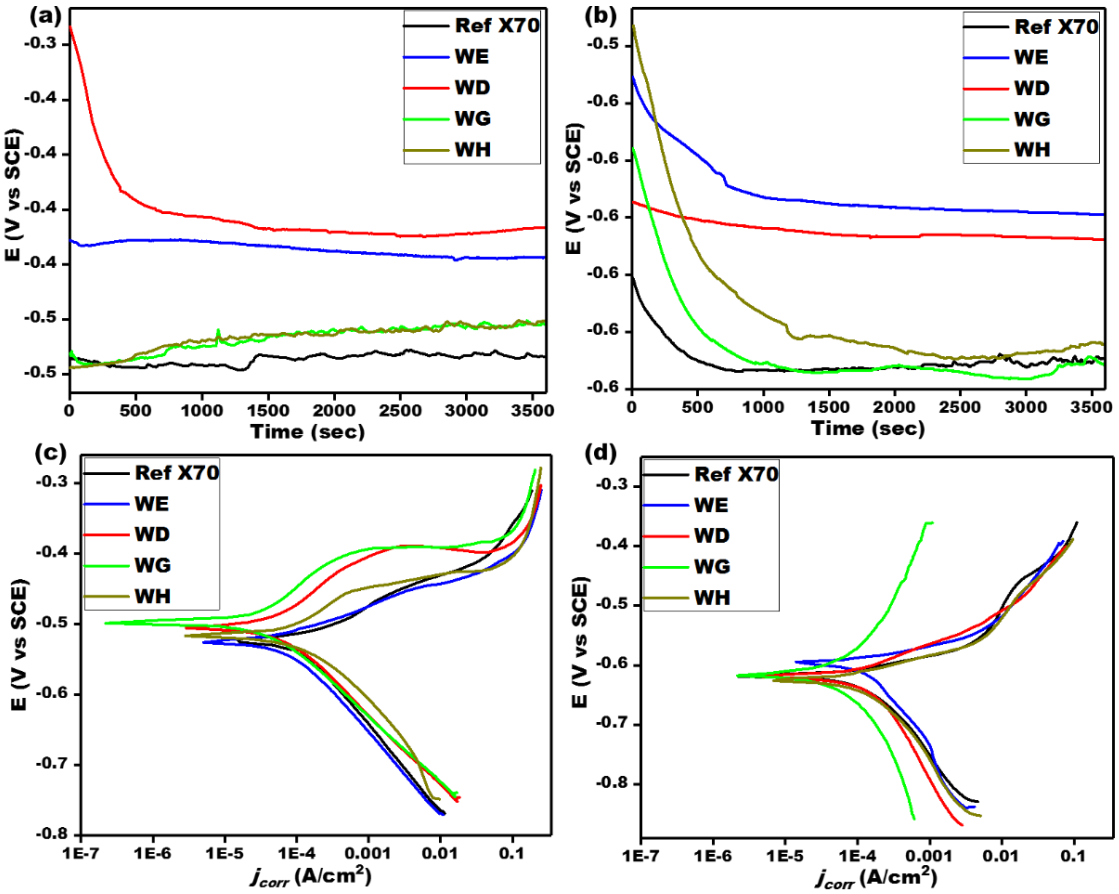

Fig. 4.4 Potential-time evolution for pipeline steel samples in (a) hydrogen producing corrosive (b) non-hydrogen producing corrosive environments; and potentiodynamic polarization curves in (c) hydrogen producing (d) non-hydrogen producing corrosive environments

The intensity of different crystallographic orientations at the surface of test specimens could have contributed to the increased electrochemical corrosion rate observed for sample WE. It is expected that specimens WD, WH, and WG having shown relatively higher presence of ⟨111⟩||ND oriented grains (Fig. 4.3) would corrode less. On the other hand, more corrosion would tend to occur on WE with higher intensity of ⟨100⟩||ND and ⟨110⟩||ND. In addition, the aggravated corrosion of WE relative to other specimens could also be attributed to its smaller grain size and abundant high energy grain boundaries. It is noteworthy to mention that the accelerated formation of protective corrosion products and reduced rate of galvanic couple at grain boundaries in specimens WD, WH, and WG must have been contributing factors to their lower electrochemical response, especially specimen WG when tested in hydrogen producing condition. Also, higher frequency of low energy CSL boundaries in every other specimen except WE might have influenced their reduced sensitivity to anodic dissolution, hence lowering their corrosion rate. All these behaviors are linked to the variations in TMCP parameters applied on the new steel specimens, especially the finishing rolling temperatures and cooling rates. A different study correlated the inhibition of magnesium corrosion to grain structures and the creation of protective films as well as precipitates within them [312]. It was concluded that grain refinement improved corrosion resistance, particularly in samples containing ultrafine-grained microstructure. It is possible that higher presence of bainite and acicular ferrite in specimens WD, WH, and WG created a refined microstructure, which offered better resistance to electrochemical corrosion compared to specimens WE and Ref X70.

4.4.4 Corrosion product analysis

Formation of corrosion products

Corrosion reaction on steels involve the following reactions:

Cathodic reactions

$$2H^{+} + 2e \rightarrow H_2 \text{ (Hydrogen reduction)} \quad (4.1)$$

$$O_2 + 2H_2O + 4e^{-} \rightarrow 4OH \text{ (water reduction)} \quad (4.2)$$

Anodic reaction

$$Fe \rightarrow Fe^{2+} + 2e^{-} \text{ (anodic dissolution)} \quad (4.3)$$

However, Fe^{2+} produced at the anode reacts with OH^{-} and O_2 in the solution to produce oxides and oxy-hydroxide, which are the primary products of corrosion reaction in steels as shown in Eqs. 4.4

– 4.6. The presence of anionic species like Cl^- and SO_4^{2-} within the corrosive environment support anodic dissolution to form unstable chlorides and sulfates. These compounds eventually oxidized to iron oxy-hydroxide resulting in the release of Cl^- and SO_4^{2-} for subsequent cycles of the same reactions in Eqs 4.7 – 4.10 [313].

$$Fe^{2+} + 2OH^- \rightarrow Fe(OH)_2 \quad (4.4)$$

$$2Fe(OH)_2 + O_2 + H_2O \rightarrow 2Fe(OH)_3 \quad (4.5)$$

$$Fe(OH)^3 \rightarrow FeOOH + H_2O \quad (4.6)$$

Considering the addition of Cl^- and SO_4^2

$$Fe + 2Cl^- \rightarrow FeCl_2 + 2e^- \quad (4.7)$$

$$4FeCl_2 + 8OH^- + O_2 \rightarrow 4FeOOH + 8Cl^- + 2H_2O \quad (4.8)$$

$$2Fe + SO_4^{2-} \rightarrow FeSO_4 + 2e^- \quad (4.9)$$

$$4Fe\ SO_4 + 8OH^- + O_2 \rightarrow 4FeOOH + 4SO_4^{2-} + 2H_2O \quad (4.10)$$

There is also a possibility of sulfide formation given the presence of NH_4SCN in the hydrogen producing test media [314,315]. Sulfide formation may have contributed to the creation of a protective film observed during polarization within hydrogen producing test environment. Oxidation of sulfides leads to the formation of reduced sulfur, which is adsorbed on the surface after reacting with steel. Furthermore, disproportionation of thiocyanate produces sulfur according to Eq. 4.11. As corrosion reaction proceeds, Fe^{2+} reacts with adsorbed sulfur to produce protective iron sulfide film on steel surface as shown in Eq. 4.12 [316,317].

$$SCN^- \rightarrow CN^- + S \quad (4.11)$$

$$Fe^{2+} + S \rightarrow FeS \quad (4.12)$$

Although iron sulfide protective film slows down the corrosion rate, it is conductive and often supports cathodic reaction in establishing galvanic couple with anodic steel surface. Also, chances of a localized attack becomes imminent if there is a flaw in the protective layer such as delamination or crack [288]. This implies that instability of protective corrosion products may have resulted in increased localized attack on pipeline steel specimens. It is believed that progressive hydrogen production inside the test environment creates flaws on these protective

films consequently allowing hydrogen entry into steel in areas that are most susceptible to hydrogen diffusion thereby resulting in degradation and/or cracking.

EDS analysis on corroded surfaces

The surface of the most corroded of all newly processed pipeline steel substrates was probed further with the EDS technique after polarization tests in both hydrogen producing and non-hydrogen producing media. The results obtained from this analysis are presented in Fig. 4.5. Significant chunks of corrosion products in the form of Oxygen (O) deposited on the surface of iron (Fe) can be seen on the surface of specimen WE after the test in the non-hydrogen producing media (Fig. 4.5a). Such deposits are indicative of oxide and hydroxides, which might have been formed according to chemical reactions described in Eqs. 4.3–4.7. The specimens tested in hydrogen producing media contain an accumulation of corrosion products and hydrogen inspired cracks (Figs. 4.5b-c). Mostly, cracks are embedded inside the layer of corrosion product film, which are also primarily O-based compounds. In addition, traces of carbon are evident near the crack in Fig. 4.5b-c, suggesting the presence of iron carbide in the region. Also, signs of other elements including Mg-Si-Al (Fig. 4.5b) and Mo-S-Ti (in Fig. 4.5c) are noticeable around the cracked section. Therefore, cracking might have been supported in specific zones by these precipitates or multi-component inclusions.

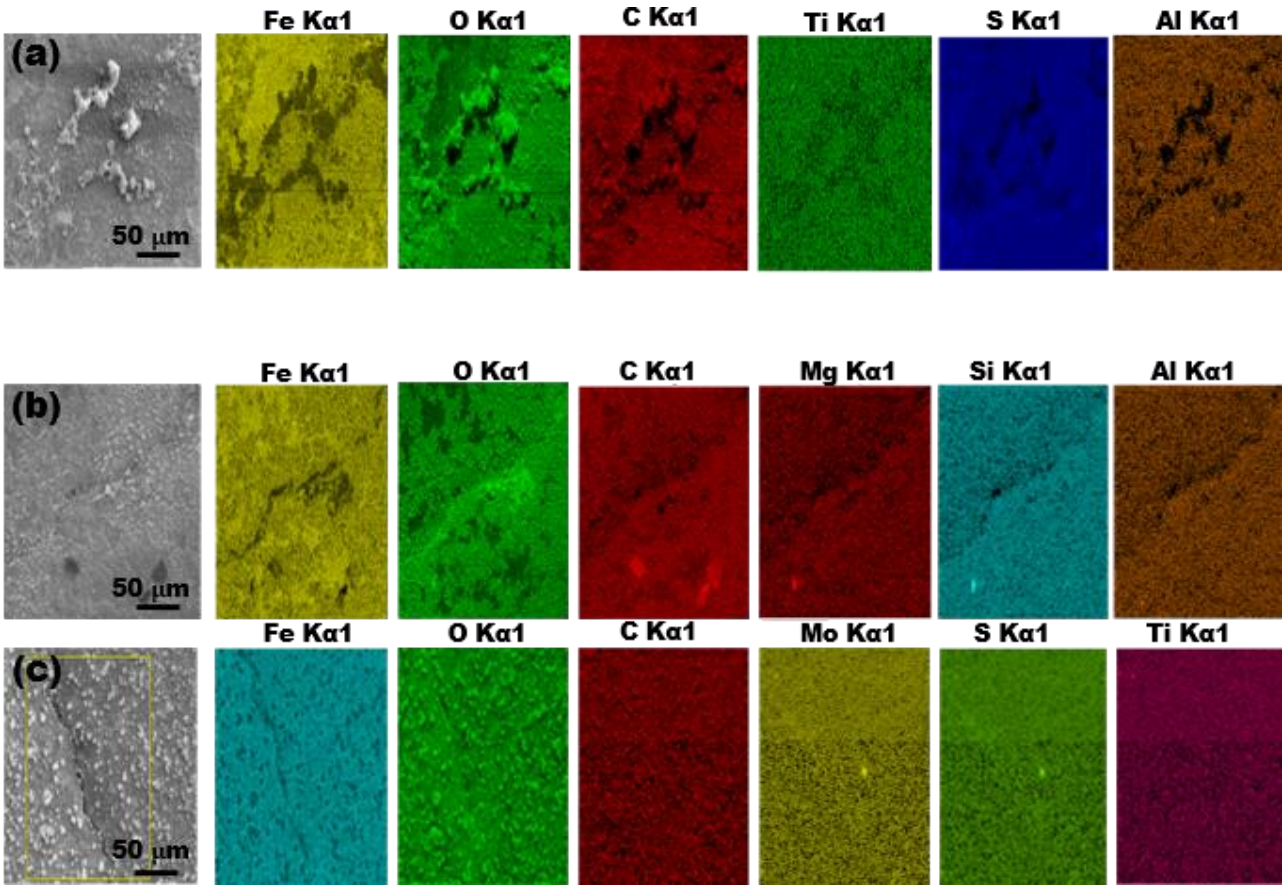

Fig. 4.5 Selected EDS maps obtained from the surface of pipeline steel specimen WE after polarization in (a) non-hydrogen producing and (b) hydrogen producing media

Corrosion surface morphology

Secondary electron images of the corroded surfaces of all pipeline steel substrates were collected after exposure to both corrosive environments and presented in Figs. 4.6 – 4.7. The results obtained from the all specimens were consistent with observations made during the electrochemical corrosion studies. Different sites were chosen from each specimen for evaluation. Yet, there are common features available across most parts. The corrosion product films are not uniform, but they are present in varying degrees on every specimen. In addition, cracks induced by hydrogen are clearly present on Ref X70 (Figs. 4.6a-b), WD (Figs. 4.6c-d), and WE (Figs. 4.6e-f) specimens. Spallation of the corrosion product layer occurred in specimen WH (Figs. 4.6g-h), without any significant cracks. Such evidence of micro-cracks on the adsorbed films could have led to further cracking and/or pitting of the substrate. A typical example is Fig. 4.6c which featured degrading films with intense pitting in selected parts of specimen WD followed by cracking in other regions

highlighted in Fig. 4.6d. In addition to the presence of cracks in specimen WE, the surface is heavily corroded due to episodes of localized under-film pitting (Fig. 4.6f). Interestingly, no remarkable cracks manifested in specimen WG. Only minimal spallation of protective corrosion product film can be seen in Figs. 4.6i-j. The morphology of the steels tested in non-hydrogen producing media showed relatively similar features. All specimen surfaces appeared to be uniformly corroded with visible aggregates of corrosion products, especially in Ref X70 (Figs. 4.7a-b), WD (Figs. 4.7c-d), and WE (Figs. 4.7e-f) and WH (Figs. 4.6g-h). The WG specimen experience the least surface damage compared to other specimens.

The nucleation of pits in WE and WD is largely related to the anodic behavior observed during the polarization test. Distribution of electric fields throughout the specimen surface may be affected by the presence of pits, thus increasing anodic sensitivity and corrosion rate [318]. There are possibilities that the uneven surface distribution of anodic sites is due to a localized galvanic couple created between pipeline steel specimens and protective layers at specific areas. The high internal stresses occurring during growth and formation of the protective layer often result in film fracture [317]. Moreover, hydrogen enhances the weakening of bonds to facilitate emission of dislocation from crack tips [319]. It can be implied that hydrogen migration into the pipeline steel structure aided crack propagation in some specimens. Also, the higher dislocation density caused by increased presence of deformed grains coupled with the precipitation of secondary phases promoted hydrogen trapping within the structure of test specimens. This observation is most prominent in Ref X70, WE, and WD where cracking occurred the most. Our observation highlights the limitations associated with the TMCP parameters used in processing the intensely cracked pipeline steel substrates. It is evident in these micrographs that treatment conditions resulted in structures that are more susceptible to both corrosion and cracking in all pipeline steels except WG. More crack sites in Ref X70 and WE specimens suggest relatively high propensity for crack propagation. In summary, the structure developed in WG can be said to have offered better passivation characteristics in hydrogen producing media thus limiting hydrogen ingress and subsequent cracking.

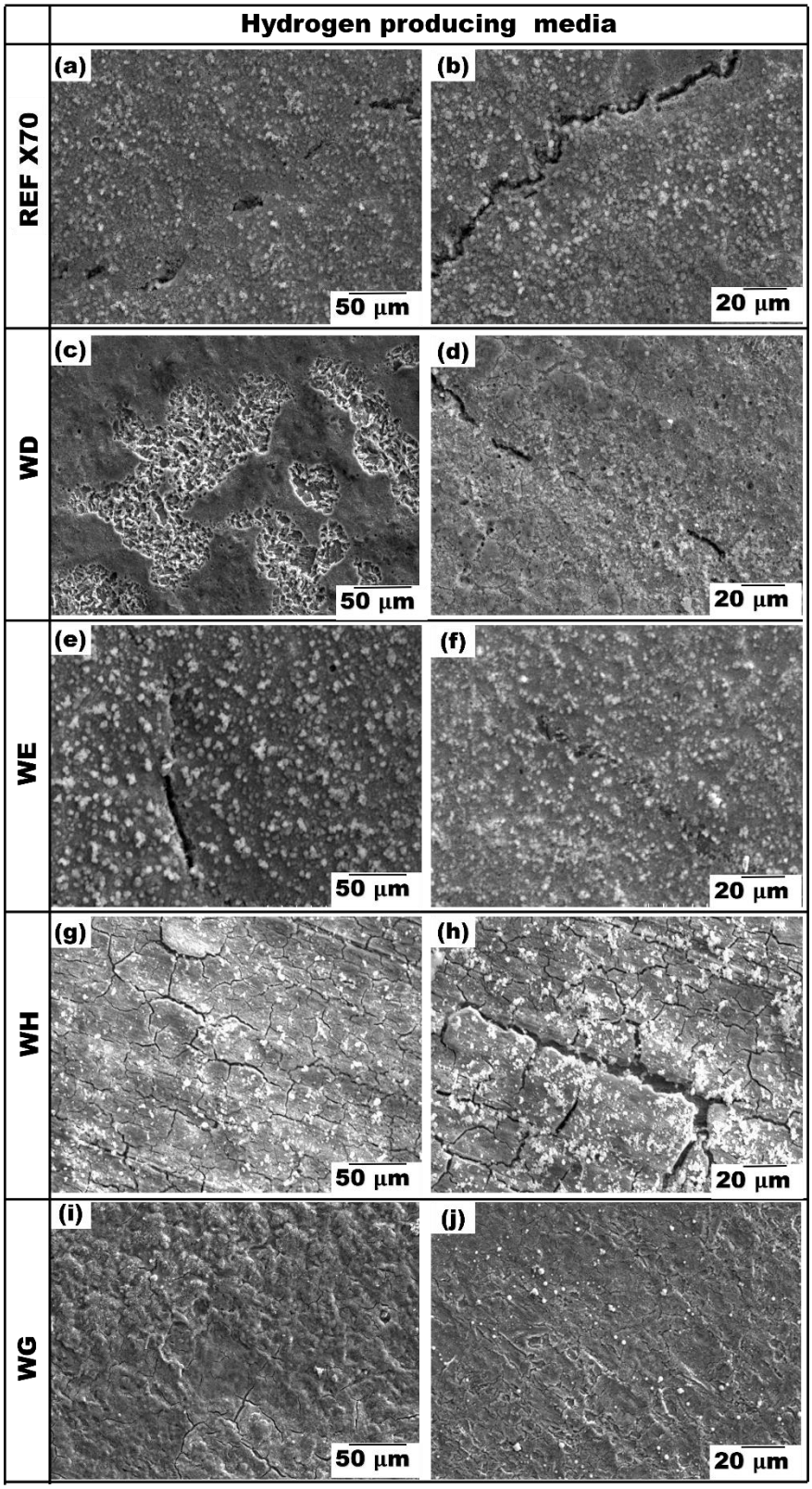

Fig. 4.6 SEM morphology of specimens exposed to hydrogen producing corrosive media (a, b) Ref X70 (c, d) WD (e, f) WE (g, h) WH (i, j) WG

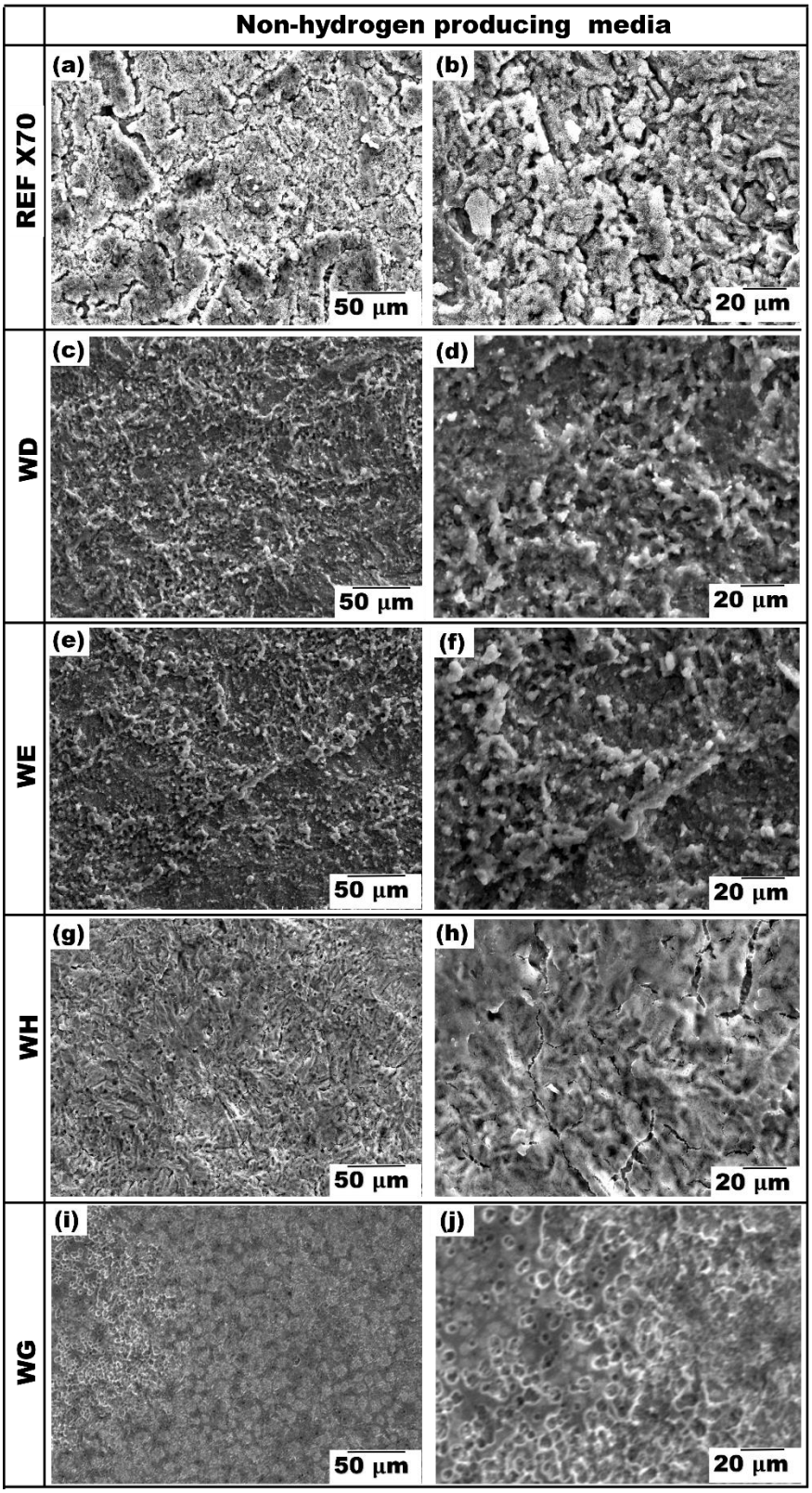

Fig. 4.7 SEM morphology of specimens exposed to hydrogen producing corrosive media (a, b) Ref X70 (c, d) WD (e, f) WE (g, h) WH (I, j) WG

4.5 Summary

In this article, the effect of two different thermomechanical processing routes on the corrosion behavior of API 5L X70 pipeline steel was experimentally determined. The role of the surface crystallographic texture of each pipeline steel specimen on electrochemical response in both hydrogen producing and non-hydrogen producing corrosive environments was established. The following are findings obtained from this study:

1. Thermomechanically controlled treatment enhanced the surface corrosion resistance of the WG sample more than the Ref X70, WD, WE, and WH samples in both non-hydrogen producing and hydrogen producing media.
2. Orientation and boundary character of surface grains were analyzed in relation to corrosion behavior. Although the texture was weak in all specimens, some intensity of $\langle 111 \rangle || ND$ orientation was seen in specimens WD, WH, and WG. The most corroded specimens (Ref X70 and WE) comprised of completely random grain orientation.
3. Open circuit corrosion potential measurement and polarization scans showed an increased corrosion behavior in non-hydrogen producing test environments, whereas the hydrogen producing environment passivated more.
4. Surface morphology examination confirmed greater presence of protective corrosion product films on specimens tested in hydrogen producing conditions. Pronounced hydrogen induced cracks manifested in specimens WE and Ref X70. However, specimen WD experienced a combination of cracking and pitting. All specimens subjected to non-hydrogen producing conditions were uniformly corroded.

CHAPTER 5 : EFFECT OF MICROSTRUCTURE AND TEXTURE EVOLUTION ON THE ELECTROCHEMICAL CORROSION BEHAVIOR OF WARM ROLLED API 5L X70 PIPELINE STEEL[4]

5.1 Overview

In this chapter, the corrosion behavior of warm rolled pipeline steels is presented. The results and discussions of this subject complements the previous chapter where electrochemical tests of corrosion are presented.

Thermomechanical treatments were used to improve the corrosion resistance of API 5L X70 pipeline steel materials. Successive warm rolling was performed at temperatures of 700 ℃, 600 ℃ and 500 ℃. The steel plates produced comprising of different ferrite grain sizes. However, the finest grain distribution was achieved at 700 ℃ rolling temperature. A combination of electron backscattered diffraction and x-ray diffraction techniques were used to determine weak texture (i.e. preferred grain orientation) across all specimens. Grain orientation showed deviation towards ⟨111⟩ direction at the surface of 700 ℃ rolled steel. After deformation at 600 ℃, mostly ⟨110⟩ grains oriented parallel to the normal direction were obtained. Rolling at 500 ℃ resulted in random orientation of grains. Corrosion test show that anodic dissolution increased as rolling temperature decreased in the order of 700 ℃ > 600 ℃ > 500 ℃ for hydrogen producing and non-hydrogen producing test media. Also, molecular dynamics simulation confirmed that the adsorption energy of corrosive species interacting with the iron surface increased in the order of $E_{interaction\ (111)} < E_{interaction\ (110)} < E_{interaction\ (100)}$ for the two types of electrolytes. The relationships between the molecular species interacting in each corrosive media and selected crystal planes (i.e. (111), (110) and (100)) were established. X-ray photoelectron spectroscopy

[4] The results in this chapter are already published, but was used with permission from *Springer* (Appendix E): E. Ohaeri, J. Omale, U. Eduok, J. Szpunar, M. Arafin, F. Fazeli 'Effect of warm rolling parameters on microstructure, texture evolution and electrochemical corrosion response of API 5l X70 pipeline steel', *Metallurgical and Materials Transaction A*, 2020, Vol. 51, pp. 2255-2275

The PhD candidate E. Ohaeri designed all experiments, characterised microstructures, and surface morphology of specimens, compiled the report, as well as finalised the manuscript after revision by supervisor and peer-reviewers.

confirmed that adsorbed corrosion films on all tested steels are Fe_2O_3 (Fe^{2+}) and hydrated ferric oxides such as FeOOH.

5.2 Background

Pipelines remain a convenient means of transporting oil and natural gas from one point to another. These assets play a crucial role in meeting the world's energy demand. Therefore, good quality steels are required for their construction. Steel classification place more emphasis on material strength, with little consideration towards corrosion dynamics within the operation environments. In sour service (i.e. H_2S-containing environment), pipelines often experience unforeseen damage due to cracking. Some reviews [8,320] have recommended that pipeline property enhancement is necessary for optimum reliability. However, this should be performed cautiously to avoid jeopardizing other inherent properties. Recent studies [15,321] are directed towards broadening the applications of steel through improvement in microstructure and crystallographic texture. There are correlations between corrosion in pipeline steel, and their inherent structure, especially when subjected to hydrogen environments [13,153,322]. Certain microstructural features such as inclusions, segregation and/or precipitates could serve as promoters of corrosion in steels through hydrogen embrittlement mechanisms (HE) [164,175]. For instance, the susceptibility to HE in X50 pipeline material varied from predominantly ferrite-pearlite to martensite after heat treatments [323]. The trans-granular cracks observed within the ferrite-pearlite microstructure initiated around non-metallic inclusion particles. Contrarily, the martensitic steels failed by intergranular cracking without significant contributions from inclusions. Also, hydrogen induced cracking (HIC) was previously identified at oxide inclusions of Al-Mg-Ca, precipitates of (Ti-Nb)N, and other elements such as Mo-Mn-S [12,13]. These multi-component inclusions were mostly found around segregations in the mid-thickness region of X70 pipeline steel. Consequently, embrittlement caused by the entry of hydrogen into steel may cause HIC. Numerous scenarios of pipeline failures across the world have been attributed to HE phenomenon, as well as other related corrosion causes [30,68,324]. It is therefore imperative to investigate processing methods that could potentially lead to the development of corrosion resistant steels with formidable texture.

The production of pipeline steel plates is done to achieve excellent properties at a minimal cost. However, contemporary steels are of higher quality compared with the older grades with large

amounts of impurities. This is primarily due to enhanced purification and processing methods offered by modern technology. Recent manufacturing activities are performed to accomplish structural refinement, as well as improve mechanical properties [325]. Thermomechanical treatments involve deforming the steel by rolling either within the austenitic (non-recrystallization region) or ferritic (austenite-ferrite transformation region) temperatures [326–328]. Despite the advantages of the later approach in terms of microstructure development and control, fewer studies have tried to explore it. The procedure of rolling at temperatures below 800 ºC is widely referred to as '*warm rolling'* [329]. Deforming steel at such reduced temperature range can result in the evolution of various types of microstructure and grain orientation. Applying warm rolling temperatures can minimize the enormous thermal energy required for steel processing. In addition, the extensive load needed to impact deformation during cold working can be lowered through warm rolling [330]. During processing, cast slabs must undergo reheating and roughing at high temperatures before they are cooled to warm rolling temperatures. There may be similarities in grain orientation after warm and cold rolling. Remarkably, the texture intensity is often higher for warm rolled (WR) steels [331]. The implication is that transformation from austenite to ferrite occur towards the end of warm rolling. This explains the routine presence of residual rolling textures, as well as poor through-thickness textures that regularly feature in WR steels [332]. Highly refined grains of approximately 300 – 400 nm was developed by warm rolling low carbon steel containing chromium [333,334]. The authors used a combination of dynamic recrystallization, ferrite nucleation and transformation to develop nano-scale grains. They eventually improved the mechanical properties of the examined steel. The mechanism of recrystallization in WR steels is usually discontinuous at the onset, then becomes continuous in the later part of the treatment process. On the other hand, cold rolled steels feature solely discontinuous recrystallization [335]. So, it is important to consider the role of recrystallization in determining the end structure of WR steels [336,337]. The warm rolling process is characterized by mainly dynamic recrystallization [338]. In an event of impeded recrystallization and recovery, multiplication of dislocations can aid the nucleation of new grains [339]. Nevertheless, such situations were reported to have occurred mostly at relatively low deformation strain rates.

Rolling low carbon steel at relatively low ferritic temperature is challenging due to the manifestation of Dynamic Strain Aging (DSA). Sanchez-Ariza *et al.* [340] attributed the DSA to

the influence of solute carbon atoms, which interfere with the motion of dislocation inside the steel. This phenomenon is supported by the frequent interactions (i.e. interlocking and disconnecting) of dislocations with substitutional and/or interstitial atoms present within the steel structure. Consequently, more load is required to release atoms that are pinned down by dislocations. However, they reported that addition of alloying elements such as Nb, B, Cr or Ti can lower the adverse effect of C in warm rolled steel. The following competing processes are typically observed during warm rolling [341];

a) Development of micro-bands and accumulation of solutes at sub-grain boundaries
b) Diffusion of solute atoms towards already formed shear bands
c) Formation of strain–induced carbide precipitates inside grains with micro-bands
d) DSA and Static Strain Aging (SSA) resulting from deformation and cooling, with subsequent creation of Cottrell atmosphere around dislocations during SSA
e) The precipitation of coarse carbides at sub-grain boundaries of both micro-bands and shear-bands

The same authors noted that incorporation of carbide-forming and borocarbide-forming alloying elements are reliable ways of eliminating carbon atoms present in solid solution. This is not the case in hot rolled steels, because the characteristic high entropy at such temperature range prevents the trapping of carbon atoms at defects. Another study [342] has identified strain rate sensitivity (i.e. variation in stress relative to a specific change in strain rate with temperature) as an important factor for texture evolution. It was established that low strain rate sensitivity resulted in the development of shear bands and grains with mainly $\{111\}\langle hkl\rangle$ texture. On the other hand, larger strain rate values generated $\langle 110\rangle||$RD texture fibers (where ||RD denotes that the specified family of directions are aligned parallel to the Rolling Direction). Their study also showed an increase in the appearance of ND (i.e. Normal Direction) fibers after warm rolling. They observed more $\langle 111\rangle||$ND recrystallization texture fibers at relatively lower rolling temperatures of 640 ℃ compared to 700 ℃. However, smaller grain size obtained at higher degrees of rolling reductions can produce better mechanical properties, and influence corrosion behaviour [343]. In a recent study, Wang and Yu [344] documented a correlation between processing parameters, grain size and surface corrosion pattern of low alloy steel in simulated oil and gas environment. They found that the steel with finer grains showed better corrosion resistance in comparison to the one with

coarser grains. Despite the important role of microstructural features on material degradation, few researchers have attempted to link corrosion to crystallographic orientation of grains.

It is evident that thermomechanical treatments at warm rolling temperatures can potentially improve the corrosion behavior of pipeline steel. In the present work, we have applied various warm rolling processing schedules with the aim of enhancing the resistance of API 5L X70 pipeline steel to corrosive degradation. First, the effect of microstructure and texture developed from the different processes were investigated. Then, an experimental approach was used to establish the electrochemical corrosion response of the steels in hydrogen producing and non-hydrogen producing environments. Finally, molecular dynamics simulation was used to determine the interaction between the molecules in each test medium and the (111), (110), and (100) iron (Fe) crystal planes.

5.3 Experimental procedure

Refer to sections 3.2, 3.3.1 – 3.3.4, and 3.3.5 – 3.3.7 for information about pipeline steel material, microstructural evaluation techniques, electrochemical corrosion test procedure, corrosion surface analysis and computational details.

5.4 Result and discussions

5.4.1 Microstructure evaluation

The optical micrographs of samples after warm rolling at three different temperatures are presented in Fig 5.1a-f. A dominantly ferritic structure is featured in the specimens after rolling. At comparatively higher temperature (700 ℃), numerous small grains which are consistent with acicular, and bainitic-ferrite structures are present. However, lower rolling temperatures of 500 ℃ and 600 ℃ resulted in mainly larger chunks of polygonal ferrite grains. The refined microstructure obtained at 700 ℃ can be explained as a product of ferrite recrystallization. Another possible reason for the observed feature could be the formation of new ferrite grains within the austenite (γ)/ferrite (α) transformation zone. For specimen processed at temperature closer to the soaking temperature in the austenitic range, its end microstructure will appear different from those deformed at lower temperatures. Remember that warm rolling was conducted in two passes. This implies that limited contact time with the roll will result in specimens with reasonably high exit

temperature. Also, many grain nucleation sites could have been formed in the rolling process; hence the formation of smaller-equiaxed grains at relatively higher rolling temperature of 700 ºC. Pandi and Yue [345] proposed that thermomechanically induced deformation in the dual phase region of ferrite and austenite concentrates straining on the softer ferrite grains. This will in turn lead to recrystallization of the highly deformed phase, and subsequent nucleation of smaller grains. Nonetheless, at lower temperatures below $\gamma \rightarrow \alpha$ transformation temperature, ferrite grains are dominant especially around the grain boundaries. Therefore, the resulting structure will be a combination of sizeable pancaked ferrite grains. Some strain-induced ferrite structures with finer sub-grains are observed at specific regions in the specimens that were rolled at reduced temperatures (i.e. 600 ℃ and 500 ℃). The increase in grain size with decrease in rolling temperature is an evidence of ferrite grain growth. In Figs. 5.1b, e, c, f, the pancaked ferrite grains with slight elongation towards the rolling direction are quite visible in contrast to Figs. 5.1a, d where grains are mostly refined. Another study reported a combination of granular bainite, ultrafine ferritic grains, including martensite and retained austenite constituents as the outcome of inter-critical annealing preceded by warm rolling in C-Mn steel [346]. Such variations in extent of grain growth for each WR pipeline steel specimen shows the effect of different processing conditions.

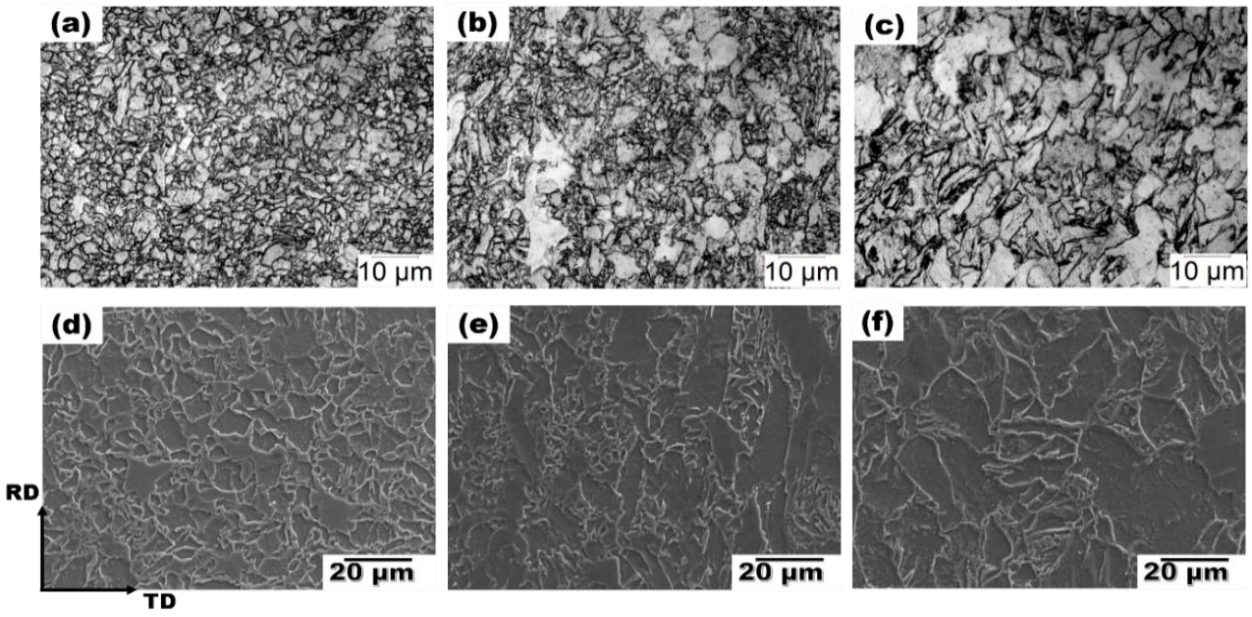

Fig. 5.1 Optical and SEM micrographs of pipeline steel specimens after warm rolling treatments at different temperatures (a,d) 700 ºC, (b,e) 600 ºC, and (c,f) 500 ºC

Judging from results presented in Fig. 5.1, the reasons for the observed microstructural development are not far-fetched. First, the lowest hardness value of 261 $\pm$ 6 HV was measured after warm rolling at 700 ºC, in contrast to 296 $\pm$ 14 HV and 338 $\pm$ 6 HV obtained from specimens rolled at 600 ºC and 500 ºC respectively. It is noteworthy that hardness of warm rolled materials often exceed what is obtained under normalized conditions [347]. This is clearly observable at the surface region compared to the inner core of the steel, where softness and toughness might be prevalent. A different study has shown that rolling at 600 ºC and 500 ºC resulted in extensively banded-deformed structure [348]. Other comparative studies on high Mn content twining–induced plasticity and transformation induced plasticity steels, each processed by hot and warm rolling, indicate significant rise in hardness after the later treatment [349,350]. These processing methods resulted in remarkable improvement in mechanical properties. They attributed the superior strength of warm rolled samples to dislocations and substructures (i.e. recovered grains) generated through work hardening. Therefore, insufficient time will be available for complete transformation of all austenite grains to ferrite at relatively higher warm rolling temperatures. In general, there is a consistent increase in hardness as rolling temperature decreases further in the ferrite region. A viable explanation would be that pipeline steel material work hardened more intensely at reduced rolling temperatures; hence dislocation multiplication may have led to the trend in the hardness results obtained.

The end microstructures obtained in the present study indicate that warm working led to noticeable formation of in-grain banding. These features manifested most in the darker regions of the maps in Fig. 5.2, particularly in specimens rolled at 500 ºC and 600 ºC respectively. Such banded microstructure indicates highly strained regions that resulted from DSA at low relatively lower rolling temperatures. Therefore, greater dislocation interactions resulted in clustering of defects at lower warm rolling temperatures. Serajzadeh [351] demonstrated that warm rolling at typically low temperatures could cause DSA; and subsequently lead to non-uniform spread of strain across the entire microstructure. In a separate study, [352] two-dimensional finite element modelling was used to predict the occurrence of DSA in warm rolled carbon steel. Although they reported that DSA may be unlikely to manifest based on their rolling schedule, SSA was evident after the rolling operation. So, they concluded that the final mechanical properties of warm rolled steel depend on SSA and the roller-speed employed in the processing mill to achieve desired reductions.

Ultimately, one would expect that the formability of steel will be affected after the aging process. It is notable that the rolling temperatures applied in the current study can be considered low enough to create dislocation entanglements within the steel structure. Moreover, poor EBSD indexing obtained from specimens rolled at relatively lower temperatures is suggestive of a strained structure.

Microstructural evolution in steel relates to critical temperature conditions that are set during thermomechanical treatments. These operations directly impact on phase transformation, especially the rate at which temperature reduces through the different stages of processing. In addition, tangled dislocations can be correlated to the area fraction of deformed, recovered and recrystallized regions within the steel microstructure. It has been shown that recrystallization process becomes retarded as warm rolling temperature decrease [321], and this could favor the evolution of certain textures in carbon steel [353]. Based on Figs. 5.2a-c, the volume fractions of recrystallized grains in specimens rolled at 700 ºC and 600 ºC are twice that of the 500 ºC rolled specimen. However, previous investigation [354] have shown that more recrystallization occurred at 700 ºC rolled steel compared to the one rolled at 600 ºC. The implication is that the incentive for recrystallization is diminished as warm rolling temperature reduces. Similar observations were also made in a comparative study on inter-critical annealed and warm rolled medium-manganese steel and ultra-purified Fe–17wt% Cr alloy steels [334,355]. Nevertheless, there is a notable increase in the amount of recovered grains observed after rolling at 600 ºC. This means that lowering rolling temperature to 600 ºC resulted in an increased formation of sub-structured grains. Such occurrence is often necessitated by the re-arrangement of defects inside the steel during plastic deformation. Since dislocations are the primary type of defects present in rolled steel plate, their repositioning in specific regions gave rise to the largely recovered portions seen in Fig. 5.2b. It can be said that the recovery process reduced the density of dislocations created by plastic deformation, which might have warranted the decreased quantity of deformed grains noticed in 600 ºC rolled specimen. The highest fraction of deformed region noticed in the specimen rolled at 500 ºC justifies its higher level of induced strain compared to the other WR pipeline steel samples. This is attributable to the combined effect of rolling and considerably low ferrite temperature. At such low temperature, the incentive for recovery is less and intense deformation will tend to generate high volume of dislocations. Notably, an indirect measure of dislocation density, known

as KAM, accounted for the least value of 0.7° for 600 ºC rolled specimen (Fig. 5.2e). The other specimens presented values of 0.9° and 1.0° for specimens rolled at 700 ºC (Fig. 5.2d) and 500 ºC (Fig. 5.2f) respectively. A clear correlation can be seen between the highest KAM value determined for the hardest and most deformed specimen rolled at 500 ºC.

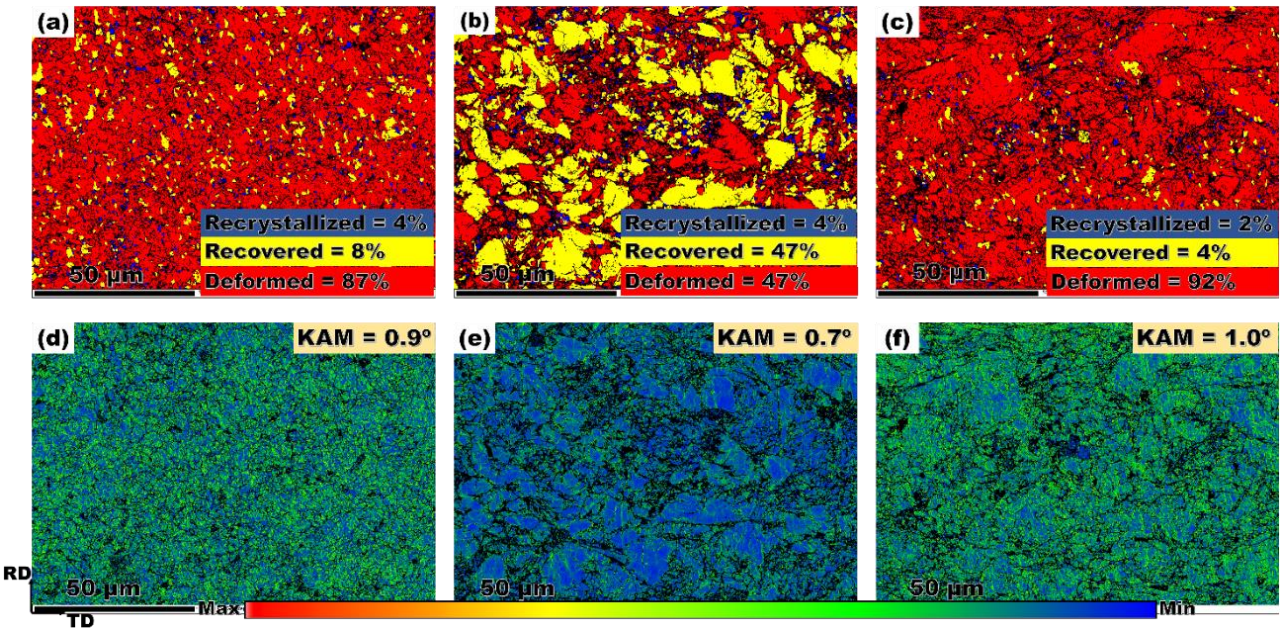

Fig. 5.2 EBSD maps showing recrystallized, recovered, and deformed area fractions for steel rolled at (a) 700 ºC, (b) 600 ºC, and (c) 500 ºC and the corresponding KAM maps for steels rolled at (d) 700 ºC, (e) 600 ºC, and (f) 500 ºC

An evaluation of grain boundary distribution is important for understanding the systematic development of microstructures at different warm rolling temperatures. The results in Table 5.1 show the estimated fractions of various grain boundary types that are present in the scanned region of each warm rolled steel. More grain boundaries are seen in the specimen rolled at 700 ºC compared to the others. This is a confirmation of grain refinement. Since grains became smaller after rolling at the highest temperatures, they are linked with each other through complex networks of boundaries. According to Handa *et al.* [336], primary recrystallization drives the formation of nuclei leading to subsequent grain growth. They are of the view that such occurrence is marked by the presence of HAGBs. Moreover, boundaries with high energy move alongside dislocations within the substructure. On the other hand, the absence of primary recrystallization supports the creation of LAGB, due to short range ordering of dislocations. In the current study, more

recrystallized fine grains featured at relatively higher rolling temperature, which translated to the dominance of HAGBs in specimens rolled at 700 ºC and 600 ºC respectively. However, the specimen rolled at 500 ºC possess the least fraction of both boundary types, owing to its constituent grains that are larger in size. Some form of relationship has been revealed in connection with the rate of corrosion and grains size in metals [356]. Also, high amount of grain boundaries are believed to promote effective distribution of impurities in polycrystals [357]. The consequence of developing finer grains after rolling at 700 ºC is the improvement in solute segregation. As such, the accumulation of impurities at grain boundaries is minimized along with susceptibility to corrosion.

In addition, the periodic behavior of HAGB ultimately results in the generation of coincident site lattice (CSL) boundaries. These boundaries possess low energy and can influence the behavior of steel in corrosive environment. The CSL grain boundaries are considered crack resistant like the LAGB, especially those with low sigma values [149]. This is because they do not have the adequate amount of energy required to drive crack propagation. It is of interest to point out that only CSL boundaries corresponding to $\sum 3$, $\sum 11$, $\sum 13b$, $\sum 39a$, $\sum 29b$, and $\sum 41c$ featured markedly in all WR specimens. Moreover, the specimen rolled at 500 ºC displayed the least fraction in comparison to 700 ºC and 600 ºC rolled specimen. The CSL is most prominent in 600 ºC rolled steel, where extensive recovery occurred. Some researchers [147,307] have documented relatively high proportions of $\sum 11$, $\sum 13b$, and $\sum 29b$ type CSL boundaries at regions where cracks got arrested in different grades of pipeline steel. Interestingly, the authors linked these boundaries to the crystallographic orientation of grains. For instance, they associated $\sum 13b$ with areas having relatively higher concentration of $\{110\}||ND$ oriented grains. However, there are contradicting views about the role of this category of boundaries in the corrosion of steel. It is simply unclear how some CSL boundaries affect crack related failures in pipeline steel, especially at boundaries with higher sigma values. Nonetheless, there are opinions in support of the idea that more LAGBs and low energy CSLs impede fracture propagation more than the HAGBs [358], but further investigations will be necessary to properly understand this subject.

Table 5.1 Distribution of grain boundaries across warm rolled steel samples

Samples	HAGB Fraction (%)	LAGB Fraction (%)	CSL (%)
WR at 700 ℃	9	6	6
WR at 600 ℃	9	1	9
WR at 500 ℃	4	3	3

5.4.2 Texture analysis

The results obtained from texture studies are matched with observations made earlier in terms of microstructural features. In Fig. 5.3, the EBSD orientation maps are displayed with their corresponding inverse pole figures (IPFs) for direction normal to the specimen surface. As can be seen, Figs. 5.3a-c are IPF orientation maps for specimens warm rolled at 700 ºC, 600 ºC, and 500 ºC respectively. The legend indicates the color coding for different grain orientations. One can notice that the intensity of texture is weak in all the specimens. However, it is clear in Fig. 5.3a and d that the specimen rolled at 700 ºC showed some intensity of grain orientation deviating significantly towards [111] direction. In the specimen rolled at 600 ºC both orientation map (Fig. 5.3b) and IPF (Fig. 5.3e) revealed greater intensity in the [110] direction. For rolling performed at 500 ºC, the steel sample exhibited the most random grain orientation according to Figs. 5.3c and f. Texture intensities in warm rolled extra low carbon steel has been found to be rolling temperature dependent [359]. Their result revealed dominant Goss $\{110\}\langle001\rangle$ texture at relatively lower rolling temperature; whereas elevated temperatures caused more grains to align towards the rolling direction. Most importantly, the authors found that texture fibers ranging from $\{001\}\langle110\rangle$ to $\{111\}\langle110\rangle$ were present in specimens processed at comparatively higher rolling temperatures at the expense of normal direction fibers and Goss texture components. Similar observations have been made elsewhere in annealed low carbon inter-critical ferritic (IF) steel [360]. A range of rolling direction texture fibers manifesting from $\{001\}\langle110\rangle$ to $\{112\}\langle110\rangle$, with insignificant amount of Goss components and fibers oriented parallel to normal direction was observed after rolling at 700 ºC. There are established effects of packing density and crystallographic orientation on corrosion reaction as well as passive film behavior of metals [361,362]. Specifically, anisotropic behavior has been noticed in the electrochemical corrosion response of steel rods containing $\langle110\rangle$ and $\langle100\rangle$ direction grains oriented along the rod axis [299]. This implies that improvements can be achieved in chemical reactivity and passivation/repassivation attributes of

steel having closely packed planes. The main reason being that the process of removing an atom from a loosely packed structure is easier compared to a densely packed structure.

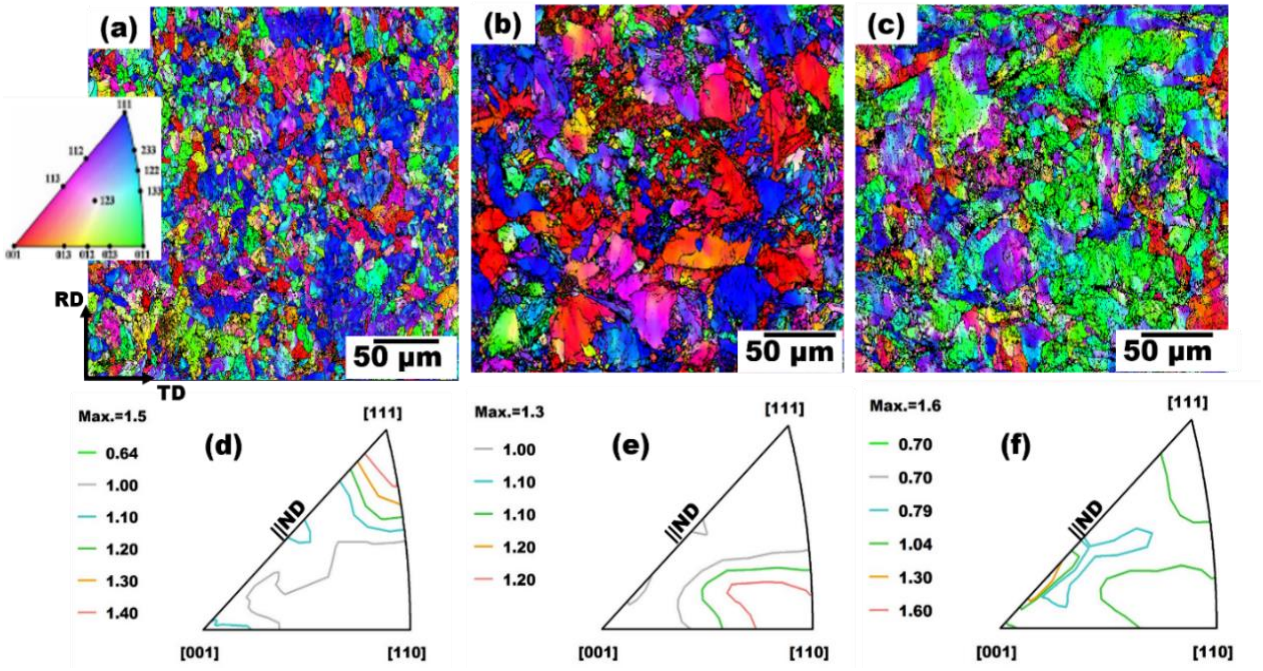

Fig. 5.3 EBSD orientation maps and corresponding IPFs of pipeline steel specimens warm rolled at (a, d) 700 ºC, (b, e) 600ºC, and (c, f) 500ºC

In order to represent the X-ray diffraction texture measurements of pipeline steel specimens, Orientation Distribution Functions (ODF) were calculated and presented as sections of φ_2 = 0º, 45º, and 65º in Fig. 5.4. The legend for ideal texture components corresponding to the selected ODF sections are available in the literature [363]. Also, the estimated volume fractions for some ideal and fiber texture constituents are shown in Tables 5.2 – 5.3 respectively. For the pipeline steel warm rolled at 700 ºC, some texture components that are featured in the ODF space include the R-Cube $\{001\}\langle110\rangle$, $\{100\}||ND$ (specifically the Cube $\{001\}\langle100\rangle$, and R-Cube textures) and the $\{111\}||ND$ fiber constituents occurred in relatively high proportion as marked in Figs. 5.4a-c. It can be seen in Tables 5.2 – 5.3 that the volume fractions of these identified texture components are highest in the 700 ºC rolled specimen. Also, an alignment of gamma (γ) fibers (i.e. $\{111\}||ND$ or $\{111\}\langle uvw\rangle$) is indicated by the dotted line in Fig. 5.4b, whereas the R-Cu $\{112\}\langle110\rangle$ texture intensity is signaled in Fig. 5.4c for the same specimen. The deformation texture shown in Figs. 5.4d-f for the specimen rolled at 600 ºC comprise of clearly identified alpha (α) fiber (i.e. $\{110\}||RD$ or $\{hkl\}\langle110\rangle$), Cu $\{112\}\langle111\rangle$ and $\{110\}||ND$ fibers (specifically the

Goss {110}⟨001⟩, and R-Goss {110}⟨110⟩ texture constituents). In addition, a spread around Y {111}⟨112⟩ and Z {111}⟨110⟩ components occurred at the middle of Fig. 5.4e. Table 5.2 indicates comparatively high fractions of Goss, Brass, S (i.e.{123}⟨634⟩) and Cu (i.e.{112}⟨111⟩) in the 600 ºC rolled specimen. On the other hand, 500 ºC rolling resulted in mainly α fibers, R-cube, Goss, and S texture components as recognized in Fig. 5.4g-i, as well as Tables 5.2 and 5.3. The significant manifestation of Goss and α fiber textures, at lower warm rolling temperatures of 600 ºC and 500 ºC in comparison to 700 ºC, is traceable to the intense strain hardening that might have occurred by reason of the TMCP schedule used. These textures could have evolved in the steel specimens deformed at 600 ºC and 500 ºC due to dense deformation bands, which could be likened to adiabatic shear bands (ASB). The creation of ASBs is facilitated by high strain rate ($> 10^3$ s^{-1}) from contact loading, and the consequent high reduced strains [364]. Materials subjected to deformation are often characterized by localized strain at areas of higher internal stresses. Therefore, the formation of ASBs increases the presence of deformed areas, which can increase susceptibility to cracking and/or fragmentation in steels [365]. Similar approach has been used to develop high proportion of Goss orientation in grain-oriented silicon steels. Lee and De Cooman [366] rolled 3 % Si steel at 50 – 300 ºC with post-annealing at 700 ºC for 100 sec. They observed significant presence of recrystallized Goss grains within the shear bands. The grains having intense shear banding typically consist of relatively high local misorientation and dislocation density [367]. Such banded areas in the microstructure of steel are considered favorable sites for recrystallized grains to nucleate; thus, promoting the evolution of {111}||ND textured grains. On the other hand, instability resulting from plastic deformation and subsequent formation of shear bands may lead to the preferential development of Goss oriented grains [368]. It is plausible that the structure generated from relatively lower warm rolling temperatures are more likely to have Goss grains as was noticed in the case of specimens rolled at 600 ºC and 500 ºC respectively. This observation agrees with previous findings presented in literature [348,367,369].

The development of texture through warm deformation shows the impact of friction during the rolling process. In steel sheet rolled within the ferritic region, coefficient of friction between the plate and rolls determine the dominant surface deformation texture [370]. Thus, indicating a connection between grain orientation and shear strains induced by warm rolling. A detailed review was documented by Barnett and Jonas [371] on the metallurgy of warm rolled steel. In their work,

they attributed the prevalent evolution of $\{110\}$ orientation at the surface of steel rolled at ferritic temperatures to stable shear strains impacted by intense frictional force during rolling. This can be considered as explanation for the appearance of α fibers in Fig. 5.4e and h coupled with the shift in pole intensity towards $[110]$ pole for 600 ºC rolling (Fig. 5.3e) and some random deviation towards the same pole after 500 ºC rolling (Fig. 5.3f). Conversely, lower degree of deformation occurred on the specimen rolled at 700 ºC. This might have warranted the intensity observed at the $[001]$ pole in Fig. 5.3d, and the occurrence of maxima corresponding to R-cube in Fig. 5.4a. Moreover, the Gamma (γ) texture fibers $\{111\}\langle uvw\rangle$ developed in relatively higher proportion after 700 ºC rolling validates the low level of strain induced in the specimen. It is often difficult to breakdown the formation of various textures into specific reasons for their appearance. There are controversial reasons ascribed to the dominance of normal direction fibers (such as γ fibers) at elevated warm rolling temperatures. Previous study [372] stated that an inverse relationship exist between Goss texture evolution and normal direction fibers. The reason is that the formation of such fibers typically occurs at the same regions where Goss texture nucleate. Therefore, when the formation of Goss nuclei gets restrained due to low shear band formation at relatively higher warm rolling temperatures, the evolution of normal direction fibers is favored. Although the present investigation did not include any proof of γ fiber formation at shear bands in specimen rolled at 700 ºC, there is an indirect evidence in the extent of recrystallization experienced by the specimen. Again, the fine grains present in specimen rolled at 700 ºC has been partly attributed to increased level of recrystallization. This could have been motivated by less severe shear banding and motion of dislocation in the mentioned specimen. In comparison, severe (high strain) shear banding result in grains that are rotated in relation to Goss, whereas shear bands with low strain lead to rotation towards the $\langle 111\rangle$ direction parallel to the plate surface [360]. Therefore, an optimum rolling temperature is needed to achieve the desired end texture in steel. These findings also emphasize the importance of dynamic recrystallization in the entire sequence of operations required for steel processing.

Table 5.2 Volume fractions of ideal texture component (in %)

	Cube	Goss	Brass	S	Cu	R-cube
WR at 700 ℃	2.0	2.0	3.2	7.3	3.32	2.9
WR at 600 ℃	1.8	3.5	4.6	9.0	4.0	2.5
WR at 500 ℃	1.9	3.4	4.1	6.7	2.6	2.9

Table 5.3 Volume fractions of texture fibers (in %)

	{111}||ND	{110}||ND	{110}||RD	{100}||ND
WR at 700 ℃	15.8	16.1	7.14	12.3
WR at 600 ℃	10.6	22.9	10.1	11.1
WR at 500 ℃	14.3	21.1	10.2	11.7

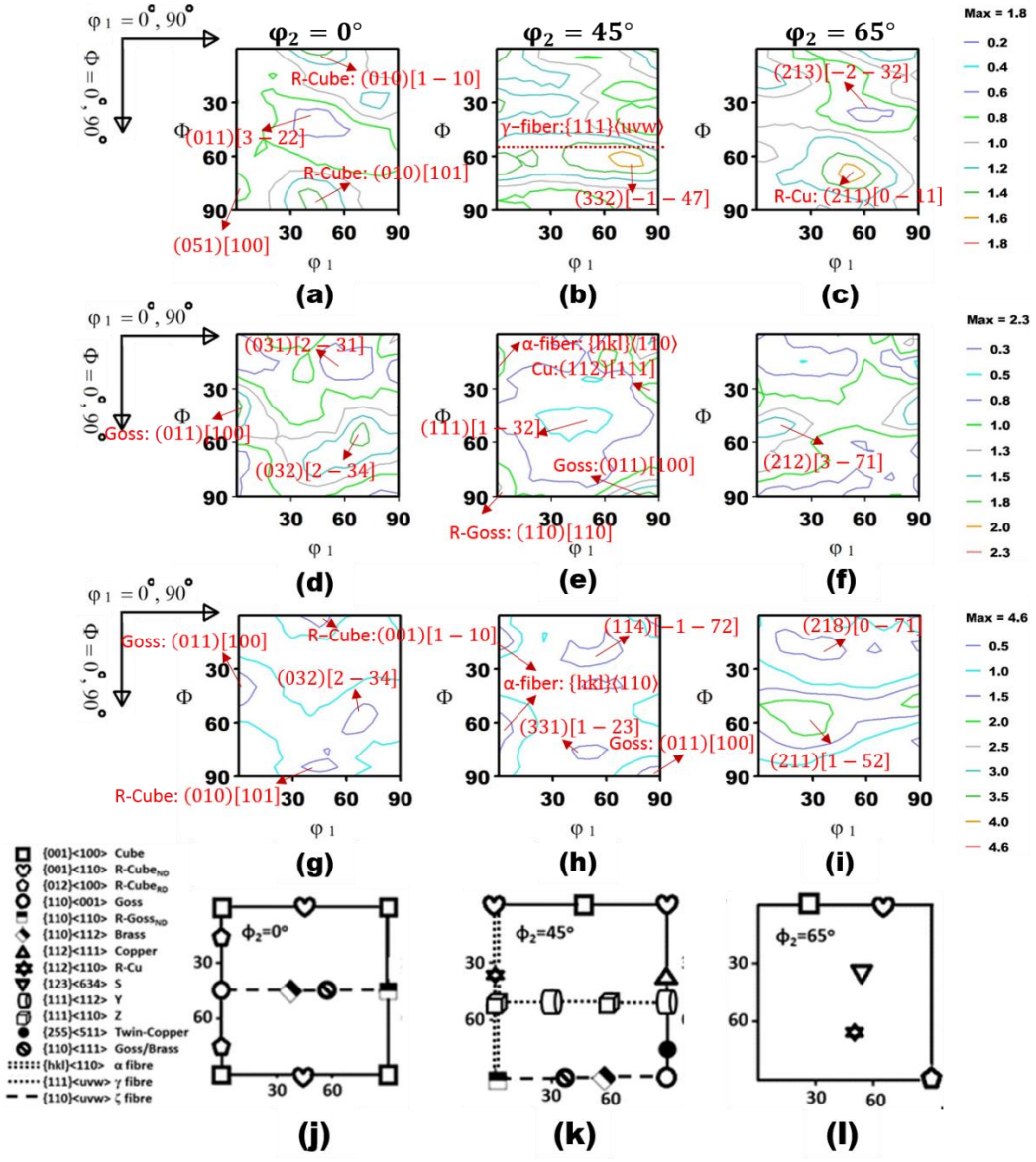

Fig. 5.4 Sections of ODF corresponding to φ_2 = 0º, 45º, and 65º for pipeline steel warm rolled at (a-c) 700 ºC, (d-f) 600 ºC, (g-i) 500ºC, and (j-l) legends for ideal texture components corresponding to selected ODF sections [363]

5.4.3 Electrochemical corrosion response

The behaviors of all warm rolled pipeline steel specimens were investigated by electrochemically probing them in various corrosive media. Initial changes in open circuit potential (E_{oc}) of steel substrates were monitored in the prescribed media for 3600 s. This duration was chosen since steady state could easily be attained within such period. The related plots of E_{oc} against time for these specimens in hydrogen and non-hydrogen producing solutions are presented in Figs.5.5a-b. As can be seen, there are limited fluctuations in the E_{oc} curve. This suggests the both corrosive media were adequately settled prior to polarization experiments. In hydrogen producing environment, the curves commenced at relatively more positive range of potentials (-0.48 to -0.51) as shown in Fig. 5.5a. In comparison, measurements made in non-hydrogen producing condition resulted in less positive potentials (-0.54 to -0.59) according to Fig. 5.5b. Overtime, the curve for each media stabilized in decreasing order of potential values according to reduction in warm rolling temperatures. Based upon this observation, we can deduce that more negative shifts in E_{oc} are achievable through warm rolling at even lower temperatures and steady state E_{oc} curves were attained within the duration of the test.

In order to properly understand the kinetics of cathodic and anodic corrosion reactions related to the microstructure inherent within each WR pipeline steel, potentiodynamic polarization measurements were conducted. The associated Tafel curves for the two different corrosive media are shown in Fig. 5.5c-d. Also, Tafel fittings were used to generate their respective electrochemical parameters: corrosion potential (E_{corr}), corrosion current density (I_{corr}), cathodic Tafel slope (β_c) and anodic Tafel slope (β_a). The variation in the values of these parameters are presented in Table 5.4. These values were determined by extrapolating β_c and β_a according to the Tafel equation presented in Eq. 5.1 [373]. The expression shows a logarithmic connection between current (I) and overpotential (η), where letters a and b are constants related to anodic and cathodic reactions respectively.

$$\eta = a \pm b \ln I \tag{5.1}$$

Tafel corrosion test can be employed to assess the electrochemical performance of alloys that experienced different heat treatment conditions [374]

In the current study, curve fitting for specific segments of the cathodic and anodic offshoots from the curve were chosen and projected linearly towards E_{corr} before measuring the corresponding values of I_{corr}. The reduction in warm rolling temperatures resulted in progressive increase in the values of I_{corr} obtained from test in both hydrogen producing and non-hydrogen producing environment. The value of I_{corr} in hydrogen producing solution is the least at 3.98 µA for specimen warm rolled at 700 ℃, then increased to 10.30 µA for specimens warm rolled at 600 ℃, and 35.30 µA after warm rolling at 500 ℃. This is suggestive of diminishing corrosive tendencies at relatively higher ferritic rolling temperatures. It could imply that adsorbed passive film/corrosion product aggregates were more effective in limiting anodic sensitivity at 700 ℃. On the other hand, polarizing the specimens in non-hydrogen producing media prompted similar trend of results. The increase in I_{corr} with reducing warm rolling temperatures represents improved resistance to corrosion in specimen warm rolled at relatively higher temperature.

Table 5.4 Tafel parameters for warm rolled pipeline steel in hydrogen producing and non-hydrogen producing media

Specimens	β_a (mV/dec)	β_c (mV/dec)	j_{corr} (µA)	E_{corr} (mV)	β_a (mV/dec)	β_c (mV/dec)	j_{corr} (µA)	E_{corr} (mV)
	Hydrogen producing media				Non-hydrogen producing media			
WR at 700 ℃	35.00	46.50	3.98	-468.00	79.70	173.90	11.70	-579.00
WR at 600 ℃	29.00	110.60	10.30	-440.00	70.70	89.40	42.10	-613.0
WR at 500 ℃	27.60	85.20	35.30	-430.00	88.50	112.10	87.70	-617.00

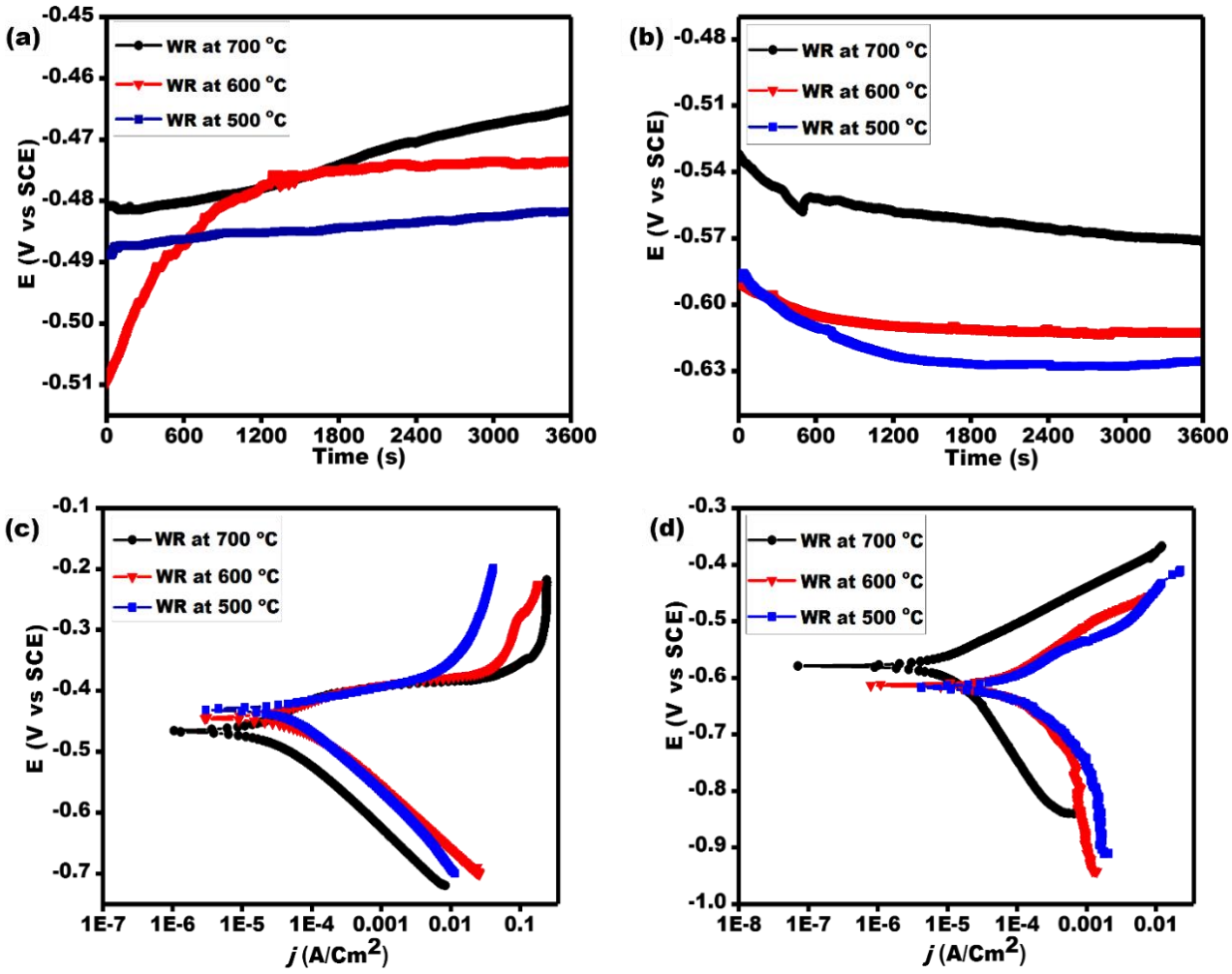

Fig. 5.5 Open circuit potential vs time plots for (a) hydrogen producing media and (b) non-hydrogen producing media; Tafel polarization plots for (c) hydrogen producing media and (d) non-hydrogen producing media for warm rolled pipeline steel specimens

5.4.4 Effect of microstructural characteristics on corrosion behavior

The corrosion responses observed at the surfaces are linked to the microstructure developed through warm rolling. Resistance to corrosive attack under hydrogen producing and non-hydrogen producing test conditions was enhanced in the specimen processed at 700 ℃**.** In all, one can relate the corrosion results to the microstructural differences generated at each rolling temperature. The medium that did not feature hydrogen producing molecules will likely experience delayed formation of protective corrosion products; thus, exposing pipeline steel substrates to mainly the corrosive action of Cl^- and CH_3COOH. The refined grain structure developed in 700 ℃ rolled

specimen is constituted by more boundaries, most of which possess high energy (Table 5.1). The sample also contain relatively higher fraction of other low energy boundaries (i.e. LAGB and CSL). It may be expected that the boundary energies will thermodynamically facilitate the onset of corrosion. Therefore, the role of microstructural characteristics in corrosion passivation cannot be ignored. Steel having ultrafine grain structure are more resistant corrosive degradation, owing to the formation of stable passivation film [375]. Another study [376] has established that anodic dissolution rates in excess of 10 μA/cm^2 on the surface of an ultrafine grain structured metallic alloy will ultimately lead to increased rate of corrosion. The criteria for achieving such low corrosion rate upon the presence and conduction rate of passive oxide film, which is indirectly linked to the density of grain boundaries at the material surface. Furthermore, the authors proposed a linear correlation between I_{corr} and grain size, where A is a constant representing the contributions of electrolyte, and B accounts for variations in material composition (Eq. 5.2)

$$I_{corr} = \text{(A) + (B) grain size}^{-0.5} \quad (5.2)$$

The consensus is that wide range of small grain distributions creates more boundaries across the steel surface, and facilitate easy passivation compared to larger grains. Hence, the density of grain boundaries determines corrosion resistance of fine grains. Corrosion rate is most likely to increase with grain boundary fraction in an event of intense surface reactivity, and the absence of passivating corrosion product films. In addition, the orientation of planes present at the steel surface affects corrosion response [299]. Many studies [12,377,378] have correlated hydrogen induced degradation to crystallographic texture in steels. The understanding is that increasing the fraction of $\{111\}$ and $\{110\}$ oriented grains diminishes the presence of $\{001\}$ grains, which eventually leads to a reduction in crack susceptibility. The increased presence of $\{111\}||ND$ fibers in WR 700 ℃ specimen and $\{hkl\}\langle 110\rangle$ fibers in WR 600 ℃ specimen can be considered as a reason for their enhanced corrosion resistance compared to WR 500 ℃ which showed a random type of grain orientation. However, sustaining the corrosion process at a rate depends on the reaction kinetics. Therefore, the structure created by rolling at 700 ℃ slowed the rate of anodic dissolution, whereas the steels deformed at relatively lower rolling temperatures exhibited a consistent increase in the rate of anodic dissolution.

5.4.5 Molecular interactions between Fe crystal and corrosive media

In order to further elucidate the connection between corrosion resistance (in terms of corrosion current) and texture, a theoretical approach was adopted. The mechanism that connects the observed microstructure and pure corrosion behavior is evaluated through the molecular interactions between pipeline steel material and the corrosive species in the two electrolytes considered during experimental work. The data outlined in Table 5.5 are the energy values determined from molecular dynamics simulation. A visual presentation of the optimized molecules attached to the surfaces of Fe (111), (110) and (100) crystals are shown in Fig. 5.6. The energies of interaction between the Fe crystals and molecular species in the electrolytes were found to increase in the order of $E_{interaction\ (111)} < E_{interaction\ (110)} < E_{interaction\ (100)}$ for both hydrogen producing and non-hydrogen producing media. Overall, there was an increase in energy for all crystal planes modelled with hydrogen producing molecules compared to those without hydrogen producing molecules. It is believed that the addition of hydrogen producing molecules increased the interaction activity at all crystal surfaces, thus resulting in relatively higher interaction energies. Also, both media showed slight energy increase from Fe (111) to (110) crystal planes as seen in Table 5.5. This suggest that both crystal planes respond similarly to the molecules present in the test environments. Therefore, the two planes are identified to be most favorable for corrosion resistance compared to (100) with relatively high molecular interaction energy across the test media. These theoretically derived results validate the experimental findings presented in Table 5.4 and Fig. 5.5. In addition, there are established effects of packing density and crystallographic orientation on corrosion reaction as well as passive film behavior of metals [361,362]. Particularly, anisotropic behavior has been noticed in the electrochemical corrosion response of steel rods containing $\langle 110 \rangle$ and $\langle 100 \rangle$ direction grains oriented along the rod axis [299]. This implies that improvements can be achieved in chemical reactivity and passivation/repassivation attributes of steel having closely packed planes.

Due to the proximity between surface atomic layers and the next, some researchers [379–381] have proposed that the (100) plane is more stable against electrochemical corrosion and passivates easily compared to the (111) and (110) plane. However, it is worth mentioning that their studies were conducted on either single or bi crystals. Also, most investigations on this subject are done using only simulations, which does not account for all material properties that can interfere with the

corrosion process. For instance, the microstructure of steels is often complex and inhomogeneous. This means that results from pure experimental studies may vary from those obtain by theoretical means. Moreover, the process of corrosion on pipeline steel involves anodic dissolution on a polycrystalline surface. The implication is that studies performed on a single crystal may not represent the effects of the microstructural factors involved in corrosion process. Instead, simulations can serve as a way of corroborating experimental findings. Aspects of crystallographic orientation in steel relates to atomic packing density within the structure. The closeness of atoms to one another has been established as an important consideration when determining the sensitivity of metals to corrosive degradation and/or passivation [362,382]. Therefore, (111) crystal plane with high atomic density tend to dissolve slower than the (110), while the (100) plane ranks as the lowest atomic density and the fastest corroding crystal plane. It is worth mentioning that their opinion agrees with the results of this current study, both experimentally and theoretically. Recall that the specimen rolled at 700 ℃ contained the highest volume fraction of {111}||ND fibers and finer grains. These are contributors to increased corrosion resistance. The importance of orientation on corrosion reaction have been a subject of many investigations and some outcomes from previous studies are compiled in Table 5.6. The summary is that (111) and (110) crystal planes are commonly considered as less prone to corrosion. Although there are contradicting results available in literature, the uniqueness of this study is that it has shown a correlation between experimental corrosion studies on pipeline steel and theoretical computation. This investigation has clearly shown that the implication of texture on corrosion resistance is apparent.

Table 5.5 Calculated energy values for molecular dynamics model components

Model Components	Energies (kcal/mol)
Electrolytes	
H_2O	-76.44
NaCl	-622.57
CH_3COOH	-229.11
H_2SO_4	-700.35
NH_3SCN	-548.25
Crystal planes	
Fe (111) surface	-88903.11
Fe (110) surface	-48373.23
Fe (100) surface	-95106.39
Interaction between crystal planes and non-hydrogen producing molecules	
Fe (111)	10617.99
Fe (110)	12494.87
Fe (100)	58997.26
Interaction between crystal planes and hydrogen producing molecules	
Fe (111)	26425.69
Fe (110)	27997.28
Fe (100)	141390.04

where 1 kcal/mol equals 4.184 kJ/mol

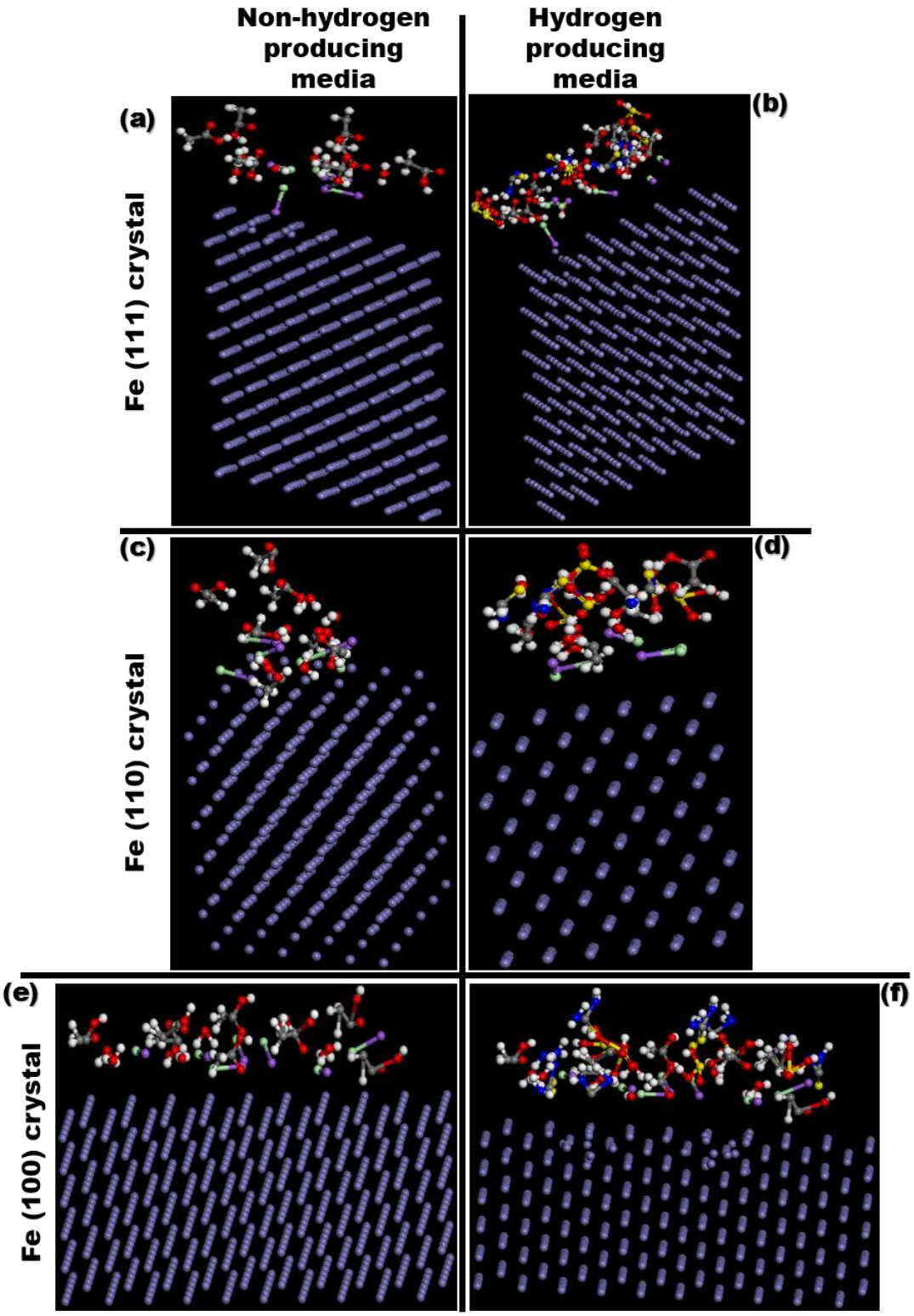

Fig. 5.6 Molecular dynamic model for adsorption of corrosive species on Fe (111), (110), and (100) crystal surfaces in (a, c, e) non-hydrogen producing and (b, d, f) hydrogen producing media

Table 5.6 Summary of anodic dissolution patterns as a function crystal orientation in iron exposed to various corrosive electrolytes

S/No	Electrode	Electrolyte	pH	Corrosion response versus crystal orientation	Ref
1	Polycrystalline iron	Polarized at -0.1 and 1.2 V versus standard hydrogen electrode respectively, in a borate solution with $Fe(CN)_6^{4-}$	8.4	$(100) > (111), (110)$: Thicker passive film formed on the iron (100) crystal plane compared to other planes	[379,383]
2	Single crystal iron	In-situ synchrotron X-ray diffraction in a borate buffer at 0.4 V versus mercurous sulfate electrode		Passive films on (001) face showed minimal defects compared to the (110) face.	[384]
3	Single crystal iron	Surfaces of the crystals were passivated potentiostatically in borate solution with and without immersion in $K_2Cr_2O_7$	8.4	$(110) > (100)$: Higher current requirement for passivation to occur on the (110) surface relative to (100) surface. Therefore, faster rate of repassivation was measured on the (100) surface.	[379–381]
4	Single crystal of Armco iron and steel	0.2 M Citric acid		$(321) > (100)$: The (321) crystal corroded rapidly compared to (100) crystal. Also, the (100) plane was identified as cathodic to the (321) face during potential measurement.	[379,385]
5	Polycrystalline iron rods of 99.998 wt % purity	Polarization in sulfuric acid	1.3	$(111) > (110), (100)$: Anodic dissolution was found to be higher on the (111) faces than on the(110) and (100) faces.	[379,386]
6	Bi-crystal iron	Cyclic voltammetry in acetate buffer solution	6.0	$(111) > (100)$: The (111) crystal displayed rapid corrosion relative to the (100)	[379]

5.4.6 Corroded surface analyses

Additionally, surface characterization techniques were used to probe the corrosion pattern after thermomechanical treatments at the different warm rolling temperatures. The SEM micrographs in Figs. 5.7-5.8 reveal the surface morphology of the pipeline steel substrates after exposure to both non-hydrogen producing and hydrogen producing media respectively. The surfaces of all tested specimens showed a significant degree of damage due to the combined action of aggressive chloride (Cl^-) in the non-hydrogen containing media, and sulfate (SO_4^{2+}) ions from the hydrogen containing test media. It is obvious that corrosion impact is conspicuous in the specimen processed at the least warm rolling temperature. Overall, the pattern of corrosion in the non-hydrogen producing medium can be said to be mostly uniform at the surface (Figs. 5.7a-f). An explanation could be the formation of protective iron oxide passive films, which physically impede the migration of corrosive species towards the steel surface [387–389].

The 500 ℃ rolled specimen experienced visible cracking when subjected to hydrogen media (Figs. 5.8e-f). Other specimens rolled at 700 ℃ (Figs. 5.8a-b) and 600 ℃ (Figs. 5.8c-d) featured mainly aggregates of corrosion products on their surfaces. Only a mild spread of corrosion product is seen in Figs. 5.8a-d. This indicates reduction in the extent of degradation on specimens rolled at relatively higher temperatures compared to the one rolled at the 500 ℃. A plausible reason for reduced corrosion current obtained for 700 ℃ rolled is the stronger barrier properties of the protective layer generated during its corrosion as seen in Figs. 5.7a-b and Figs. 5.8a-b. Conversely, the production of hydrogen within the test medium could have resulted in the continuous spalling and re-passivation of the shielding film, hence the disparity noticed in the electrochemical response of specimens. Considering that the 600 ℃ and 500 ℃ rolled specimens are the hardest with the highest deformed area fraction and KAM values recorded in 500 ℃ rolled specimen, they are expected to be more susceptible to cracking than the 700 ℃ rolled specimen. The micro-cracks on the specimen rolled at 600 ℃ (Fig. 5.8c-d) indicates potential cracking risks if exposed to further hydrogen. One can say that the aggressive corrosion attack on the 500 ℃ specimen resulted in the intense roughness noticed across the surface morphology of hydrogen and non-hydrogen tested steel. Consequently, the spike in corrosion current measured from the specimen in (Table 5.4) is justified. These findings clearly illustrate that the 500 ℃ rolled steel has relatively higher stored

energy within its structure, which might have been responsible for the facilitation of crack propagation.

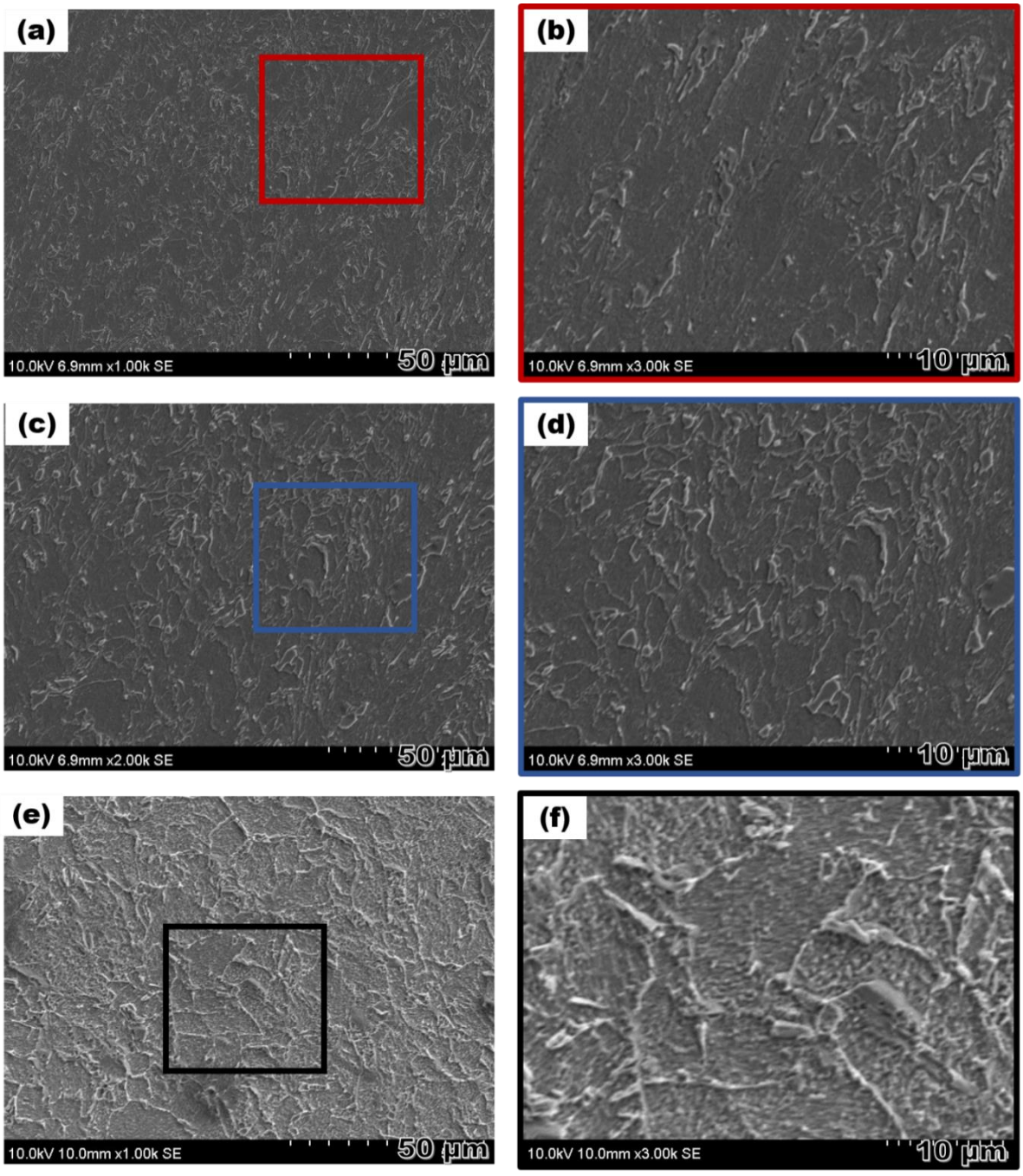

Fig. 5.7 SEM surface morphology after polarization in non-hydrogen producing media (a-b) 700, ºC (c-d) 600 ºC, and (e-f) 500 ºC

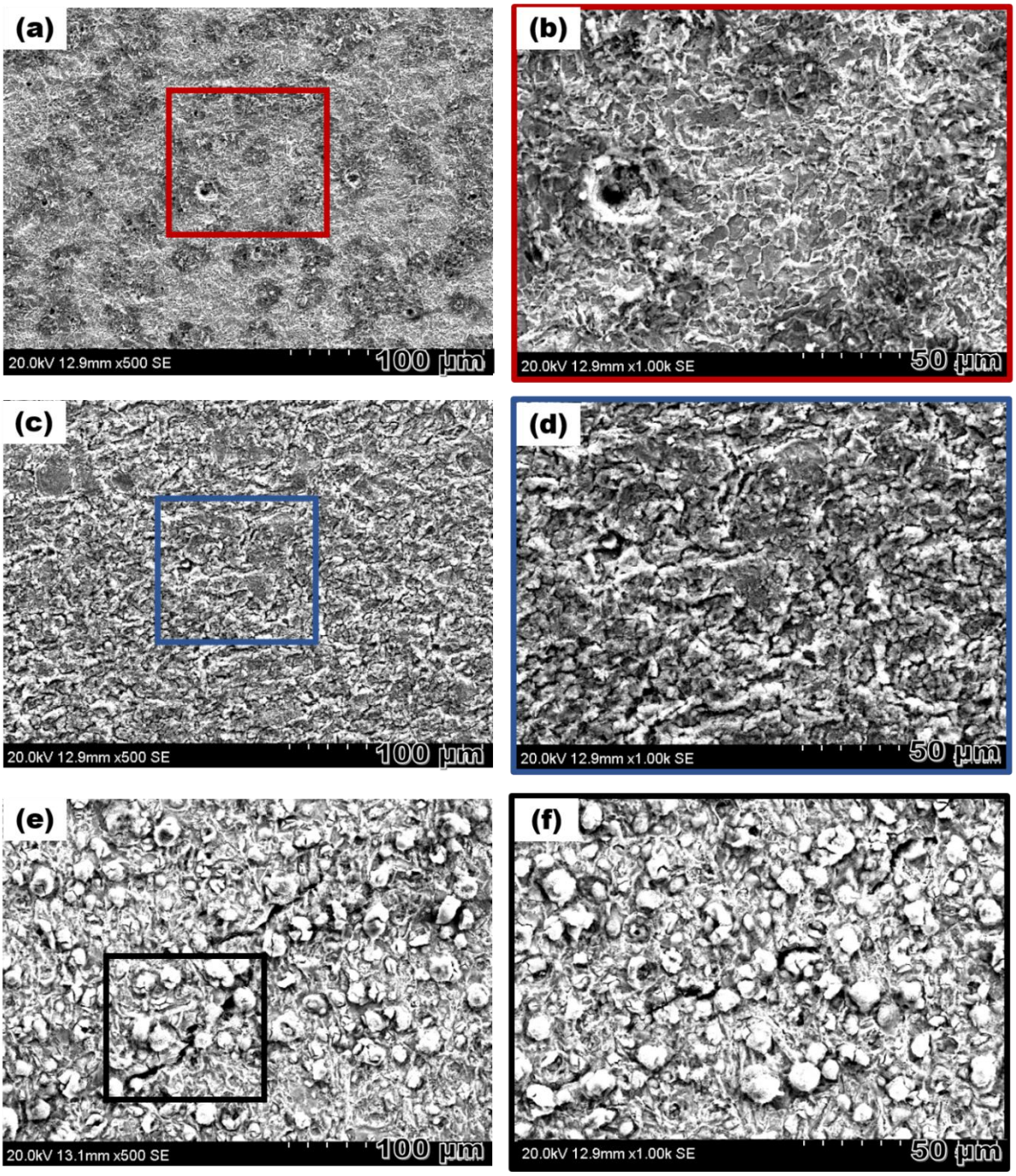

Fig. 5.8 SEM surface morphology after polarization in hydrogen producing media (a-b) 700 ºC, (c-d) 600 ºC, and (e-f) 500 ºC

products on each specimen were comparatively analyzed. The XRD phase identification spectra for corroded surfaces are shown in Figs. 10a-b. Typical ά-ferrite peaks corresponding to (110) and (200) phase are located at 2θ values of approximately 69º and 106º respectively appeared in all

steel specimens. Also, a weak γ-austenite peak belonging to (111) phase is seen at about 2θ equals 65º. Since significant details about the corrosion products were not obtainable by XRD technique, a more robust surface analysis was carried out using XPS. The corresponding X-ray photoelectron wide-scan spectra for tests performed in different corrosive media are displayed in Figs. 5.9c-d. The two spectra show similar adsorption patterns due to the chemistry of the absorbed films, except for the small peaks associated with sulfur at a binding energy of 169 eV. This feature is attributed to the hydrogen producing media (Fig. 5.9c). In literature [390], peaks positioned between 163 and 170 eV were identified as sulfide corrosion-product deposited on API 5L X100 pipeline steel in the hydrogen sulfide environment. The precipitation of protective iron sulfide film (mackinawite) on steel operating in sour environments is widely believed to be a reason for increased passivation, reduced concentration of iron, and leads to decreased corrosion [391–393]. The wide-scan XPS spectra of both media reveal some common elements, mainly Fe, O, and C, as well as Cl due to the electrolyte. O 1s and C 1s are observed in greater amount within both hydrogen producing and non-hydrogen producing media. Table 5.7 shows the composition of the corrosion scales formed on the pipeline steel surface after polarization test.

Table 5.7 Elemental composition of adsorbed layer of corrosion products on warm rolled pipeline steels in hydrogen producing and non-hydrogen producing mediums (wt. %)

Specimens	O 1s	C 1s	N 1s	Na 1s	Fe 2p	Cl 2p	S 2p
Hydrogen producing media							
WR at 700 ℃	19.96	70.68	2.40	-	2.12	2.12	2.05
WR at 600 ℃	36.81	44.59	3.41	0.65	8.28	6.26	-
WR at 500 ℃	41.90	37.65	-	7.47	3.70	7.45	1.84
Non-hydrogen producing media							
WR at 700 ℃	36.33	50.12	3.94	1.16	5.07	1.62	-
WR at 600 ℃	31.47	44.84	1.73	5.91	4.16	-	-
WR at 500 ℃	31.93	29.68	5.48	-	11.60	-	-

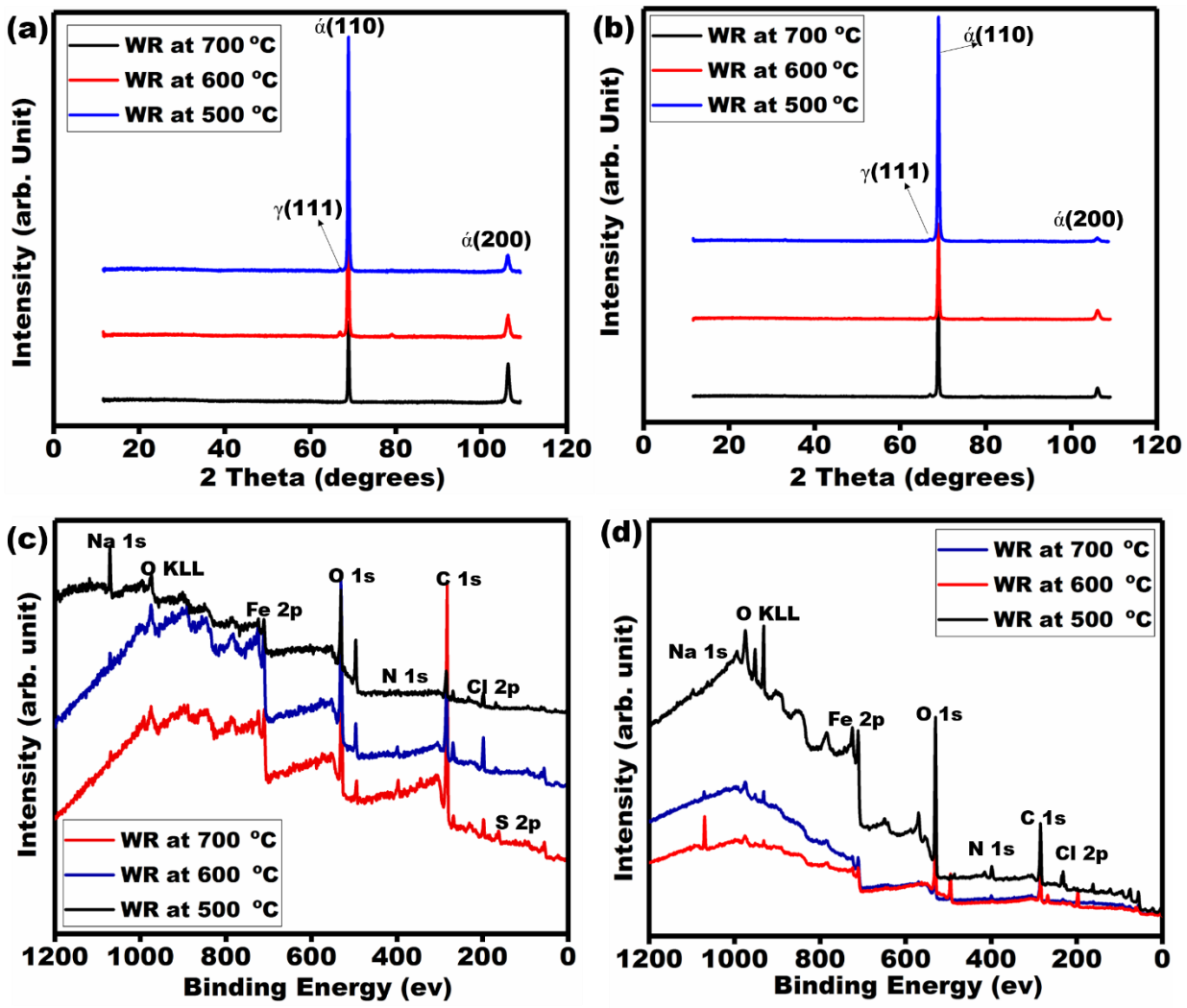

Fig. 5.9 XRD phase identification spectra for corroded surfaces in (a) hydrogen producing and (b) non-hydrogen producing media; XPS spectra of adsorbed corrosion products on specimens in (c) hydrogen producing and (d) non-hydrogen producing media

From the hydrogen producing and non-hydrogen producing media, two distinct doublets peaks (at 710 and 725 eV) are observed on the Fe 2p high-resolution spectra at all rolling temperatures Figs. 5.10-5.11. These peaks could be possibly assigned to Fe_2O_3 (Fe^{2+}) and metallic iron, respectively [394,395]. They also represent a strong indication of the metal surface oxidization as corrosion films spontaneously adsorb. The collection of O 1s spectra for substrates immersed within this medium also reveal a common prominent peak with sharp shoulders around 529 and 531 eV. These could be bonded higher Fe oxides (e.g. Fe_2O_3) and some hydrated ferric oxides (e.g. FeOOH) [394,396]. As observed within Fig. 5.10 and 5.11, the Fe 2p and O 1s XPS spectra show similar

patterns for the adsorbed corrosion products on the warm rolled pipeline steel specimens within both corrosive media. The S 2p spectra was collected for the hydrogen producing medium (Figs. 5.10c), and they reveal two peaks at 161 and 169 eV which are consistent with the expected values of S in sulfide [397] and sulfate [398] phases. In all, the XPS analyses within this study show evidence of corrosion-film adsorption on the surfaces of all warm-rolled specimens exposed to the corrosive media.

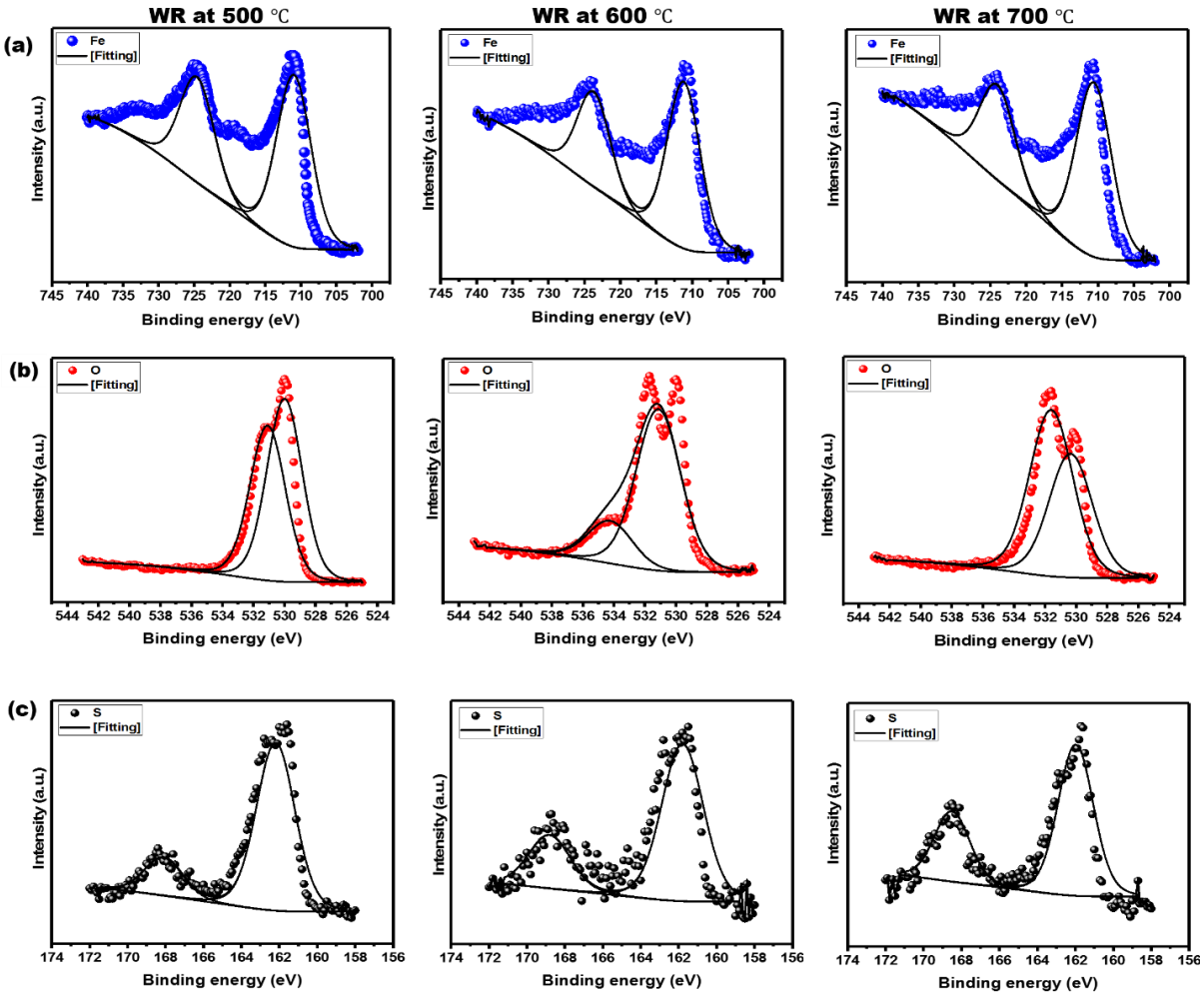

Fig. 5.10 XPS high-resolution scans ((a) Fe 2p, (b) O 1s, and (c) S 2p spectra) for adsorbed corrosion products on pipeline steel substrates warm rolled at various temperatures and exposed to hydrogen producing media

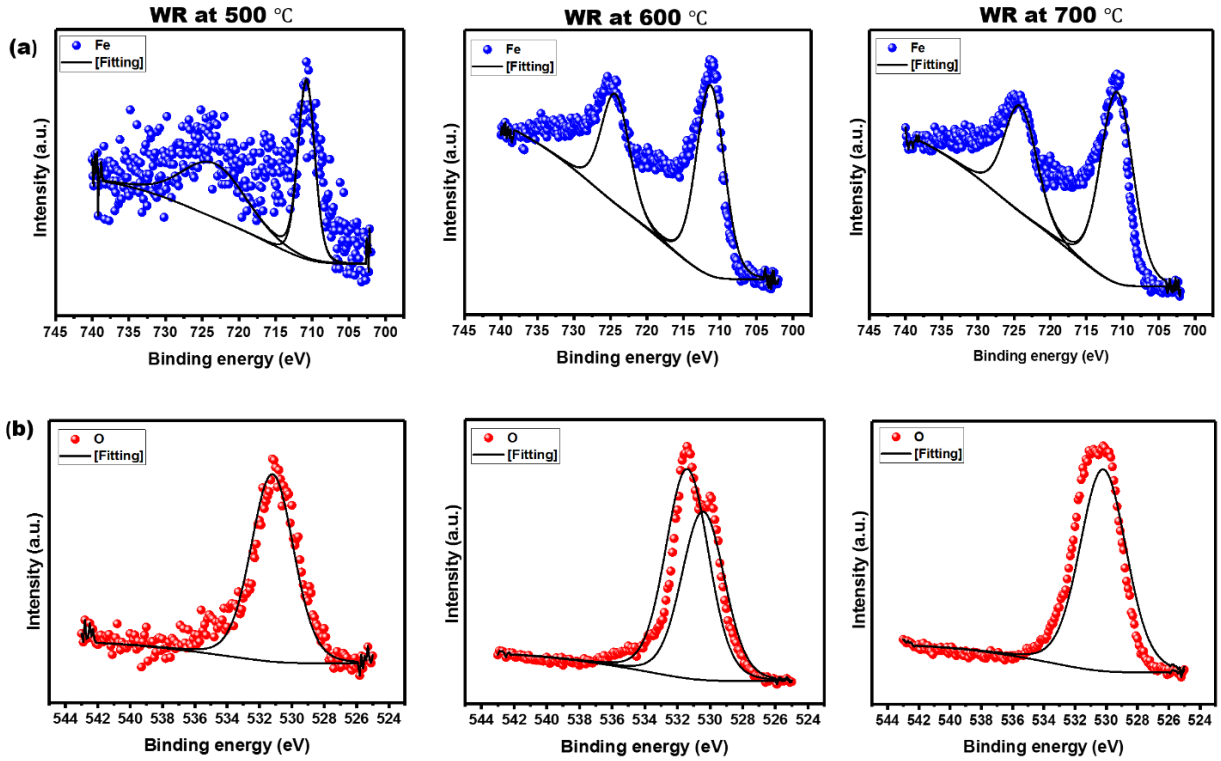

Fig. 5.11 XPS high-resolution scans ((a) Fe 2p, (b) O 1s spectra) for adsorbed corrosion products on pipeline steel substrates warm rolled at various temperatures and exposed to non-hydrogen producing media

5.5 Summary

The role of different warm rolling parameters and resultant microstructural features on the corrosion behavior of API 5L X70 pipeline steel was investigated in both hydrogen producing and non-hydrogen producing media using a combination of experimental and theoretical methods. Detailed microstructure and texture evaluations were carried out by EBSD and XRD techniques, before electrochemical corrosion studies. Thereafter, molecular dynamics simulation was applied in establishing the relationship between selected crystal planes and molecules present in each corrosion media. The following are findings derived from this work:

1. The microstructure of pipeline steel specimen rolled at higher ferritic temperature of 700 ℃ was dominated mainly by finer grains, while specimens rolled at 600 ℃ and 500 ℃ contained a mixture of small and larger chunks of ferrite grains. More shear banding with high dislocation intensity manifested after warm rolling at relatively reduced temperatures, especially at 500 ℃.

2. An increase in hardness was noticed as warm rolled temperature decreased. The measured Vickers micro-hardness values enlarged progressively with rolling temperature in the order of $HV_{700\ ^\circ C} < HV_{600\ ^\circ C} < HV_{500\ ^\circ C}$. The specimen rolled at 500 ℃ displayed the highest deformation area fraction and KAM value. These microstructural features indicate higher dislocation density in 500 ℃ specimen compared to those rolled at 700 ℃ and 600 ℃ respectively.
3. The intensity of texture developed after warm rolling at 700 ℃ showed significant deviation towards $\{111\}||ND$ orientation. The microstructure and texture obtained in the 700 ℃ rolled specimen was associated with the lowest corrosion current. For 600 ℃ and 500 ℃ rolling, the $\{110\}||ND$ and $\{110\}||RD$ texture fibers featured more than in the 700 ℃ specimen. Although the preferred crystallographic orientation was weak across all specimens, it was observed that warm rolling at 500 ℃ resulted in the most random texture.
4. Molecular dynamics simulations indicated that the adsorption energy of corrosive species interacting with the iron surface increased in the order of $E_{interaction\ (111)} < E_{interaction\ (110)} < E_{interaction\ (100)}$ for the hydrogen producing and non-hydrogen producing media. By means of experiments and theoretical approach, a unique correlation was established between corrosion response and crystallographic orientation.
5. Experimental results from electrochemical measurements indicate that resistance to corrosion decreased with steel rolling temperature in the order of 700 ℃ > 600 ℃ > 500 ℃ when polarized in both hydrogen producing and non-hydrogen producing media. It was found that corrosion product film which accumulated on the surfaces of rolled steel promoted passivation, especially on the 700 ℃ rolled specimen. These passive aggregates were identified to be mainly Fe oxides such as Fe_2O_3 and FeOOH

CHAPTER 6 : INFLUENCE OF THERMOMECHANICAL CONTROLLED PROCESSING ON MICROSTRUCTURE AND HYDROGEN INDUCED CRACKING SUSCEPTIBILITY OF API 5L X70 PIPELINE STEEL[5]

6.1 Overview

This chapter addresses the second objective specified earlier in this thesis. The focus is to relate various microstructural characteristics to HIC in pipeline steel. Specifically, the influence of thermomechanically controlled processing on microstructure and texture development in the specimens WE and WD is related to the susceptibility to HIC. The differences between this chapter and the originally published research paper are as follows:

a) The materials and methodology section have been removed to avoid duplication, as this is already described in chapter 3 of this thesis.
b) Detailed texture analysis at both surface and mid-thickness layers has now been added.
c) References in this manuscript has been merged into a single list at the end of the thesis.

The effect of different TMCP routes on the susceptibility of X70 pipeline steel to HIC has been studied. Two X70 pipeline steel labelled WE and WD were investigated. Both pipeline steel specimens have the same chemical composition but processed with different thermomechanical treatments. Microstructural examinations showed that WE consist of mainly acicular ferrite and polygonal ferrite, while WD consist of acicular ferrite and bainitic ferrite. After subjecting both specimens to hydrogen charging for 12 and 16 h in 0.2 M sulphuric acid and 3 g/l ammonium thiocyanate, early onset of HIC occurred in specimen WD. Microstructural evaluation after hydrogen charging resulted in the nucleation of discontinuous cracks in WD after 12 h. of charging. However, extended charging for up to 16 hrs resulted in HIC along the mid-thickness region of both specimens. Hydrogen diffusion across specimen WE was better than that of specimen WD. Therefore, hydrogen trapping at grain boundaries, banded deformed grains, inclusions, and

[5] The results in this chapter are already published, but was used with permission from *Springer* (Appendix F): E. Ohaeri, J. Omale, A. A Tiamiyu, K. M Mostafijur Rahman, J. Szpunar, 'Influence of thermomechanically controlled processing on microstructure and hydrogen induced craking susceptibility of API 5L X70 pipeline steel', *Journal of Materials Engineering and Performance*, 2018, Vol. 27, No 9, pp. 4533-4547

The PhD candidate E. Ohaeri designed all experiments, characterised microstructure and surface morphology of specimens, compiled the report, as well as finalised the manuscript after revision by supervisor and peer-reviewers.

secondary phases such as martensite and cementite aided early crack initiation and propagation. The adverse effect of these features on HIC risks was more prominent in specimen WD compared to specimen WE. The Vickers microhardness values measured in WD (349.6 HV) and WE (307.4 HV) suggest that WD is harder than WE; and higher kennel average misorientation of 0.66º in WD and 0.58º in WE shows higher dislocation density in WD. Results from tensile test confirmed that specimen WD is stronger and more susceptible to HIC than specimen WE. It was concluded that microstructural phases developed during thermomechanical processing improved strength in WD at the expense of its resistance to HIC, while WE with lower strength showed more ductility and higher resistance to HIC.

6.2 Background

Industrialization has greatly affected the world energy demand, and the supply of oil and gas through pipelines is now of major importance. However, the conditions for exploration of oil and gas is becoming harsh and pipelines are more exposed to corrosive environments. There is a need for appropriate selection of materials for pipeline construction. Several failure incidents related to service environments has been recorded in many countries [399]. Most of these failures are attributed to cracking mechanisms. There are serious concerns about pipelines operating in regions that are prone to HIC [400]. The general opinion is that hydrogen ingress can occur under conditions that allow a release of hydrogen around pipelines. This problem has long been recorded in situations where hydrogen is generated as corrosion by-product on pipelines or as a result of uncontrolled cathodic protection. Also, procedures such as welding and heat treatment can predispose pipeline steel to the risk of internal cracking [401,402]. Failures relating to hydrogen entry into pipeline steel has been identified as most often occurring at hydrogen congregation sites, with or without the presence of external stress [403]. The presence of some micro-alloying elements, and improper homogenization during the rolling process can affect microstructure evolution across the thickness of pipeline steel. Another consequence is the segregation and inclusion formation in areas that experience slow cooling during rolling, especially at the mid-thickness region. The segregations of hard secondary phases and inclusions eventually become main trap sites for hydrogen atoms, which leads to exacerbation of cracks at critical levels [114,197,404].

Reports on the mechanism for hydrogen diffusion in steels remain largely inconsistent. Decohesion theory has widely been used to explain cleavage between planes and/or grain boundaries during hydrogen embrittlement, but fractographic analysis elucidates the role of hydrogen on the mobility of dislocations around crack tip under plastic deformation [405]. The localized plasticity theory can also explain the elimination of obstacles to dislocation mobility by hydrogen in order to promote crack propagation. Therefore, a combination of decohesion and localized plasticity models facilitates emission of dislocations from crack tip, and provides a more comprehensive explanation for HIC in steels [116,406]. Moreover, microstructural features increase the risk of hydrogen migration within the structure of pipeline steel. Studies have shown that phases comprising of ferrite-pearlite, bainite, and martensite create high risks of HIC, owing to their hardness and enhanced hydrogen trapping properties [176]. On the other hand, acicular ferrite microstructure offers improved toughness and resistance to HIC [25]. It is noteworthy to mention that a delicate balance exists between alloying elements and mechanical properties of pipeline steel. Therefore, varying chemical composition alone may not provide a reliable route towards achieving an enhanced microstructure for HIC resistance. There are suggestions that deformation induced by TMCP, can offer great potential for generating crack resistant microstructure in pipeline steels. This is based on evidence that TMCP creates sub-grain structure within the microstructure of pipeline steel, which is capable of resisting cracking and improving mechanical properties [407]. Recent investigations indicate that thermomechanical treatment was responsible for developing microstructures with excellent mechanical properties and improved resistance to environmentally assisted cracking in AA7075 alloy [408]. Hence, the aim of this study is to investigate the role of thermomechanical processing on microstructure development and HIC susceptibility of API 5L X70 pipeline steel after two different treatments.

6.3 Experimental procedure

Refer to sections 3.2, 3.3.1 – 3.3.4, and 3.3.8 – 3.3.9 for details about pipeline steel material, microstructural characterization techniques, HIC test procedures, and hydrogen permeation studies.

6.4 Results and discussion

6.4.1 Microstructure evaluation of starting materials (thermomechanically processed)

A wide range of phases are usually present in the microstructure of thermomechanically processed pipeline steel. However, phase mismatch is often a common problem with such grade of steel. This is mainly because of the high internal energy associated with such areas, coupled with the creation of hydrogen traps that could promote HIC susceptibility [409]. To achieve desired microstructure, TMCP parameters for pipeline steel are optimized. Through this means, different volume fractions of acicular ferrite (AF), bainitic ferrite (BF), polygonal ferrite (PF), Widmanstätten ferrite (WF), and martensite/austenite constituents has been achieved in X70 pipeline steel [26,130]. Fig. 6.1 shows the microstructure across the ND – TD planes of as hot rolled WE and WD specimens before hydrogen charging. Both specimens possess non-homogeneous microstructure. Specimen WE comprise of predominantly polygonal ferrite and acicular ferrite, while WD has mainly acicular ferrite and bainitic ferrite. A similar observation has been made and reported elsewhere [139]. In addition, an inclusion is observed in the microstructure of WD along the mid-thickness (Fig. 6.1b). This highlights the presence of segregations around the mid-thickness of pipeline specimens. Other researchers have linked centerline segregation to micro-alloying composition and cooling rate during thermomechanical processing, especially when the composition of carbon and manganese is high [197,410]. For both test specimens, the composition of carbon and manganese fall within the specified maximum chemical requirement of 0.22 wt% for carbon and 1.65 wt% for manganese in X70 pipeline steel [36]. This implies that thermomechanical processing had a greater contribution towards microstructure development in both specimens. It has been noticed that pipeline steel processing often results in martensite nucleation during the transformation of retained austenite in the ferrite-pearlite region [17,206]. It is also known that martensitic phases are strained, with trapped carbon atoms usually accumulating within its lattice. Moreover, carbide and austenite are also distributed inside the martensitic lathes [140]. As a result of dispersed islands of martensite and retained austenite within the grain boundaries of pipeline steels, hydrogen diffusion and HIC susceptibility is enhanced.

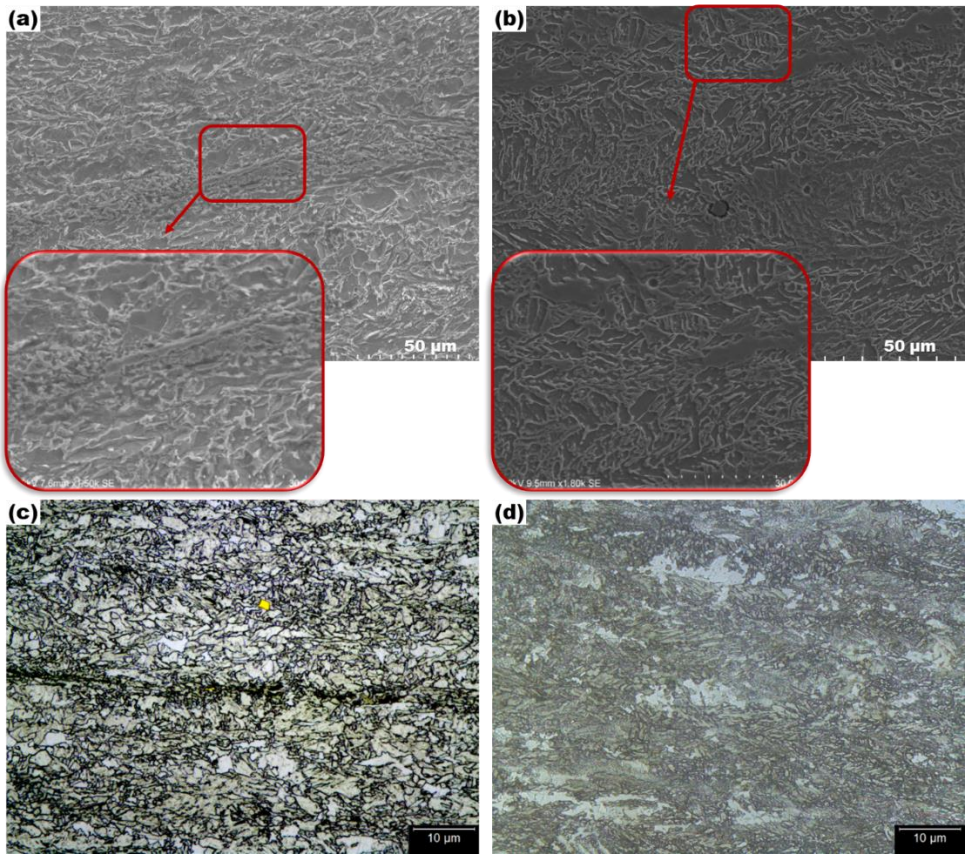

Fig. 6.1 SEM and optical micrographs of as hot rolled pipeline steel specimens WE (a, c), and WD (b, d)

For this study, EBSD analysis was used to identify HIC susceptible phases in pipeline steel specimens. Since ferrite and martensite have body centered cubic structure, the less strained phase in EBSD band contrast map, which is ferrite, will be preferentially indexed. Hence, martensite will appear as unindexed spots. High residual stress and dislocation density are considered the main consequences of martensite formation in a dual-phase steel matrix [411]. Therefore, the authors identified martensite as dark areas corresponding to poor quality patterns in EBSD map. Other microstructural features of test specimens were also established. The maps obtained from EBSD scan across the mid-thickness of WE and WD are presented in Figs. 6.2 and 6.3. In general, the grains noticed in both specimens are consistent with pipeline steel processed with relatively higher cooling rate [295]. The difference in average grain size for WE (2.7 µm) and WD (2.5 µm) after thermomechanical processing was insignificant, because of similar parameters used at the early stages of the treatment process. However, the orientation maps in Figs. 6.2a,f and Figs. 6.3a,f indicate the dominance of ⟨011⟩||RD grains in both specimens, with few grains having ⟨001⟩||RD

orientation. Just like in the case of grain size, similarities in grain orientation for WE and WD is traceable to thermomechanical processing. It may be expected that both specimens will show the same level of susceptibility to HIC considering their similarity in grain orientation. This could not have been the case, because of the presence of other microstructural features that may influence HIC susceptibility. As such, it is also necessary to investigate the grain boundary characteristics, KAM, and recrystallization area fraction. These features can adversely affect HIC susceptibility, even when grain orientation is similar. For instance, a separate study reported that LAGB were more resistant to HIC propagation than HAGB [158]. Considering the grain boundary distribution maps presented in Figs. 6.2b, g and Figs. 6.3b, g, a higher fraction of HAGB is seen in both test specimens compared to LAGB. Table 6.2 shows that the fractions of LAGB and HAGB in WD are more than those measured in WE. This evidence indicate that more grains are present within WD and may have resulted in a higher amount of grain boundaries compared to WE.

Table 6.1 Grain boundary distribution in as hot rolled pipeline steel specimens

Specimens	LAGB fraction (%)	HAGB fraction (%)
WE	6	16
WD	10	18

Also, KAM for WD (0.58º) was slightly more than that of WE (0.56º), but the intensity was higher at the mid-thickness region of both specimens as shown in Figs. 6.2c,h and Figs. 6.3c,h respectively. Similar variation in properties across sample thickness is also observed in the recrystallization area fraction maps, and more deformed grains are seen along the mid-thickness in Figs. 6.2d,i, and Figs. 6.3d,i. However, the area fractions of deformed grains observed in both as hot rolled specimens are relatively the same as presented in Table 6.3.

Table 6.2 Area fraction of recrystallized, recovered and deformed grains in as hot rolled pipeline steel specimens

Specimens	Deformed area fraction (%)	Recovered area fraction (%)	Recrystallized area fraction (%)
WE	18	75	5
WD	18	74	7

The phase maps shown in Figs. 6.2e, j, and Figs. 6.3e, j established the presence of secondary phases consisting of cementite and martensite in both test specimens. Distinctively, austenite phase

featured more along the mid-thickness of specimen WE compared to WD. This can be considered as one of the major microstructural difference between test specimens after thermomechanical processing. For both specimens, formation of cementite is expected to be minimal, owing to low amount of carbon (0.047wt %) used for micro-alloying. Although, pearlite (a mixture of ferrite and cementite), which are more brittle compared to ferrite, may be formed [412]. In pipeline steels containing ferrite, acicular ferrite, and/or bainite microstructure, segregation of martensite and austenite phases often serve as the site for HIC initiation [25]. This study shows that martensite (dark spots) and cementite (yellow spots) phases are present within the mid-thickness of WE and WD. It is possible that the appearance of more retained austenite (red spots) within the microstructure of WE was due to the thermomechanical processing conditions. Nevertheless, a higher presence of martensite is expected in WD compared to WE, given the faster rate of cooling applied during its thermomechanical processing (see Table 3.1). Furthermore, this means that more austenite was transformed into martensite in WD, thereby depleting the fraction of retained austenite within the microstructure of WD. The outcome of this is seen in the intense local misorientation between grains in WD compared to WE. Rapidly cooling steel from dual phase ferrite/austenite temperature often lead to the formation of bainite and martensite phases. Table 3.1 shows that WD experienced a wider temperature difference during hot rolling followed by faster online accelerated cooling. It is possible that these conditions favored evolution of harder microstructural phases and nucleation of smaller sized grains in WD, as shown in Figs 6.1 and 6.3. From Hall-Petch relation [27], smaller grain sized polycrystalline material have more grain boundaries available to obstruct the motion of dislocations, culminating in improved mechanical properties. Also, the Vickers hardness value measured on the ND – TD plane showed 307.4 HV and 349.6 HV for WE and WD, respectively. This means that higher hardness in specimen WD can be attributed to its microstructural composition in comparison with that of WE specimen. A relationship can as well be made between higher hardness values and increased HIC susceptibility in pipeline steels. This can be explained by the role of hard microstructural phases on hydrogen diffusion pattern across pipeline steel microstructure. Harder phases are strong hydrogen trap sites, which limit diffusion of hydrogen atoms through the steel structure [27,109,294]. These findings are in agreement with the view that the optimization of microstructure is necessary for controlling HIC in pipeline steels [15,158].

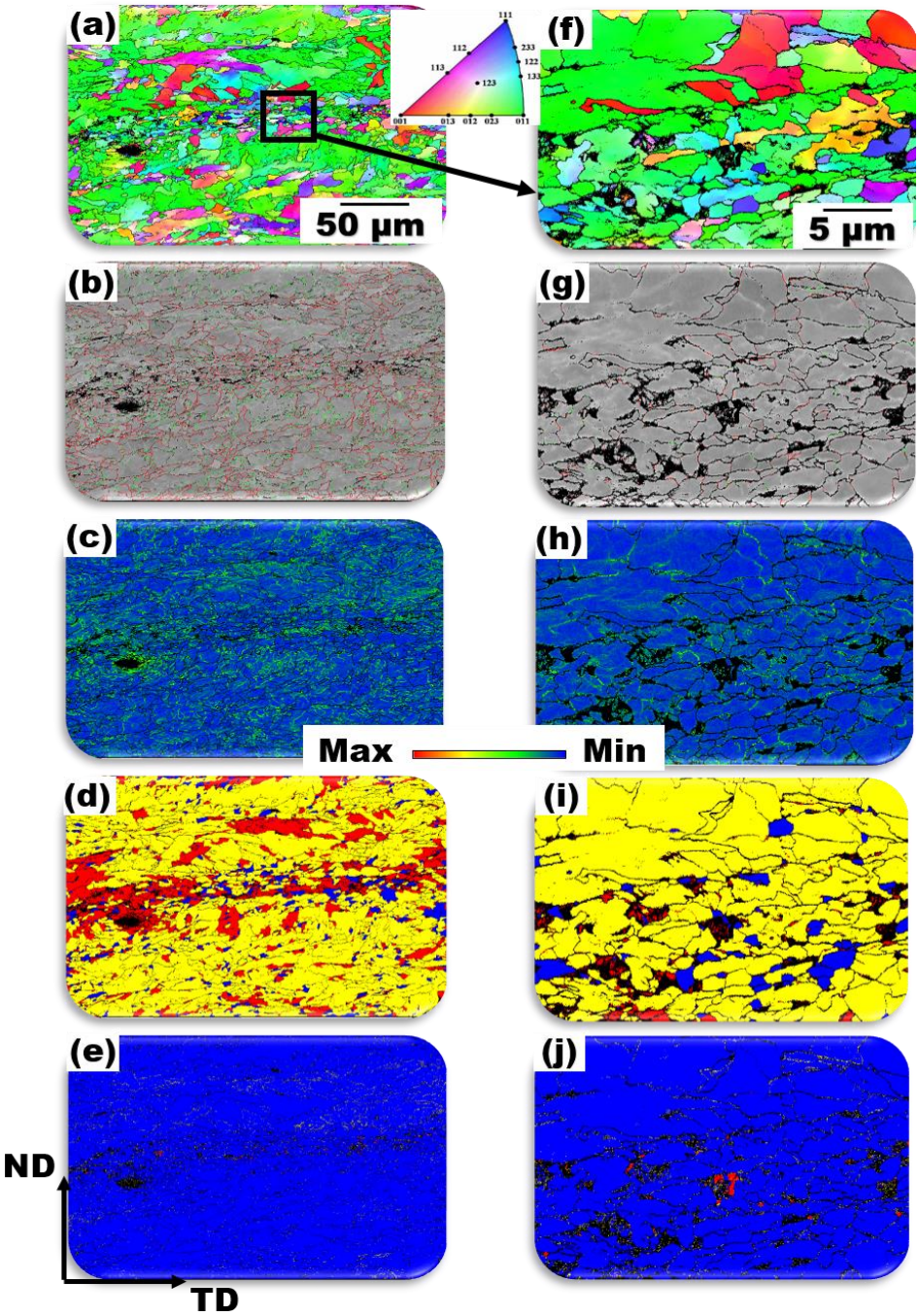

Fig. 6.2 EBSD maps for as hot rolled WE. Orientation maps are a, f. Grain boundary distribution maps are b, g (HAGB = red, LAGB = Green). Kennel average misorientation maps are c, h. Recrystallization maps are d, i, (deformed regions = red, recovered regions = yellow, and recrystallized regions = blue). Phase maps are e, j (blue = ferrite, black = martensite, red = austenite and yellow spots = cementite). (f – j) is the higher magnification of the marked region in (a)

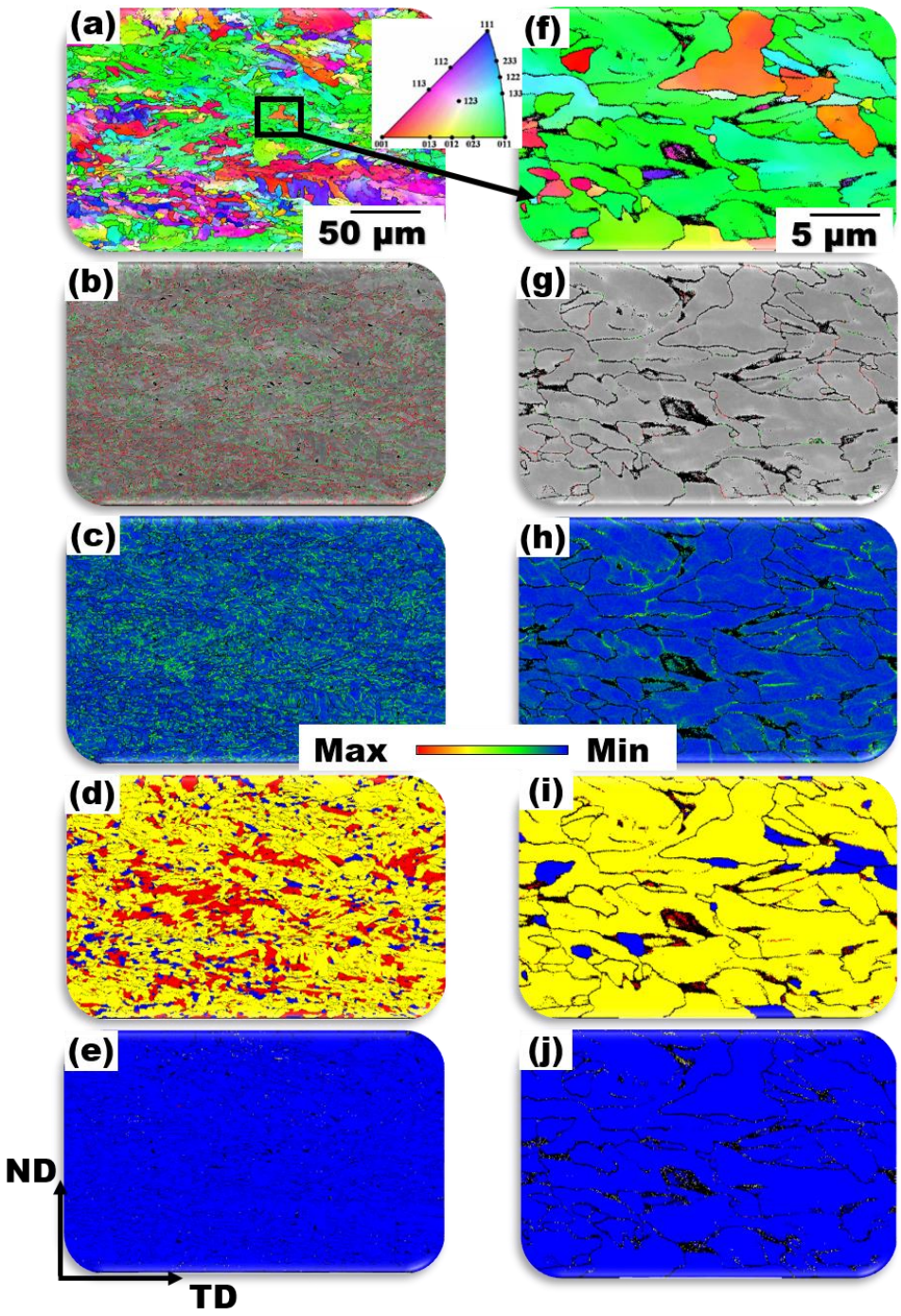

Fig. 6.3 EBSD maps for as hot rolled WD Orientation maps are a, f. Grain boundary distribution maps are b, g (HAGB = red, LAGB = Green). Local misorientation maps are c, h. Recrystallization maps are d, i, (deformed regions = red, recovered regions =yellow, and recrystallized regions = blue). Phase maps are e, j (blue regions = ferrites, black spots = martensite, red spots = austenite and yellow spots = cementite). (f – j) is the higher magnification of the marked region in (a)

6.4.2 Texture variation across thickness

In rolled carbon steel, which is a Body Centered Cubic (BCC) metal, two fiber texture orientation are often seen [413]. These two components categorized as deformation textures include (a) α-fiber i.e. [110] family of directions aligned parallel to the direction of rolling (RD), and (b) γ-fiber i.e. {111} family of planes aligned parallel to the normal direction (ND). Besides, the Goss-component (i.e. [001] oriented grains) can as well be seen. The authors established that γ-fiber formation at the expense of α-fiber was related to increased amount of recrystallization, which manifest the most at the center compared to surface region. It is typical to vary the strain states across steel thickness during the rolling process. Having these in mind, and knowing that pipeline steels are rolled, we cannot overlook the likelihood of texture inhomogeneity.

The texture development in both pipeline steel specimens clearly showed variations across different layers. The inverse pole figures presented in Fig. 6.4 indicate presence of [110]||ND at the surfaces of specimens WE and WD, with some additional manifestation of [001] direction grains in WD (Fig. 6.4b). Within the mid-thickness region, grain orientation displayed a spread covering [111]||ND and [001]||ND (Fig. 6.4c-d) across both specimens. It is common to notice non-uniform microstructural characteristics over rolled steel plates. For instance, Sanchez Mourino *et al.* [414] found a correlation between texture and anisotropy of properties in pipeline steel. They attributed increased volume fraction of {001} planes to the higher tendency for brittle fracture. According to the authors, this idea is based on the principle of crystal plasticity and fracture behavior. Also, TMCP schedule contribute towards the crystallographic effects often seen in steels. In the case of WE and WD, the hot rolling parameters differ, especially at the rolling and cooling stages. Another study showed that rolled steel plates bearing non-uniform structure often comprise of shear textures with $\{011\}\langle 100\rangle$ −Goss orientation and some deviation towards $\{112\}\langle 111\rangle$ at the surface layer; whereas the center region consist of deformation texture such as {111} planes oriented parallel to the plate surface [415]. The dissimilar through- thickness texture evolution in both X70 pipeline steel specimens suggests that sensitivity to cracking in the presence of hydrogen will obviously vary. Besides, such textural changes can alter the failure mode of pipeline steel when subjected to mechanical loading.

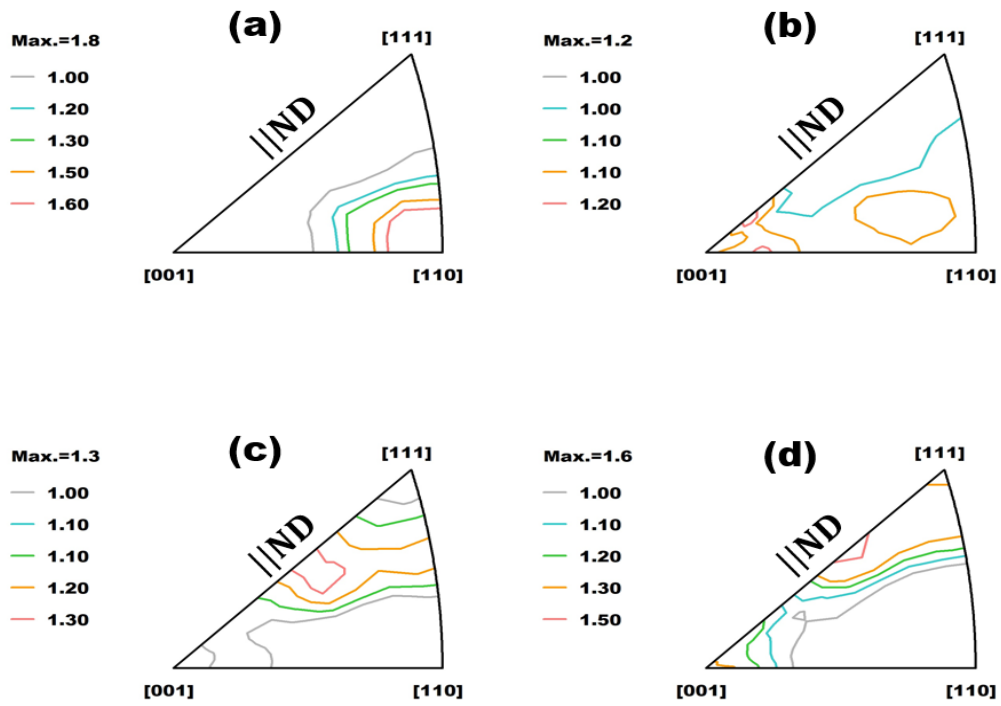

Fig. 6.4 Texture variations across surface layers of specimens (a) WE and (b) WD, as well as the mid-thickness layers of (c) WE and (d) WD

6.4.3 Hydrogen permeation analysis

The hydrogen permeation studies provided a more detailed understanding of the diffusion pattern of hydrogen through pipeline steel specimens. According to Eqs. 3.2-3.4, the important hydrogen permeation parameters were obtained from the current-time polarization curves shown in Fig. 6.5. The results are shown in Table 6.3. Information about the rate at which hydrogen flux passes across the pipeline steel membrane was obtained by the permeability function ($J_{\infty}L$). The apparent solubility (C_{app}) gives the amount of hydrogen trapped within the lattice, while the effective diffusivity (D_{eff}) accounts for the diffusion of hydrogen. During the test, steady state hydrogen permeation current (I_{∞}) was attained at a higher value during the first charging transients for both specimens. It has been established that irreversible trap sites usually attain saturation with hydrogen during the initial charging transient [114]. Mostly reversible hydrogen traps are available to trap hydrogen during the second charging transient. In general, specimen WE had higher I_{∞} values compared to WD. Also, higher amount of hydrogen permeated through specimen WE during first and second charging transients than specimen WD. This translated to higher values for all other hydrogen permeation coefficient in WE. Similarly, Shirband *et al.* [416] established a direct relationship between rate of hydrogen transport through pipeline steel and grain size. The same authors believe that fine granular bainite microstructure with islands of martensite/austenite and inclusions will

offer more sites for hydrogen trapping in comparison to steel with annealed structure. Therefore, lowering dislocation density and relieving stored energy impacted by TMCP can enhance hydrogen diffusivity and reduce the risks of HIC. Notice that specimen WD showed slightly higher KAM value, which suggests that it has more store energy than specimen WE. Lower values of $J_{\infty}L$, D_{eff} and C_{app} indicate difficulty in hydrogen diffusion across specimen WD. It also suggests that there are more defects serving as trap sites for hydrogen in WD. So, there are higher chances of HIC in WD compared to WE. Recall that the hardness value measured in WD was higher than that of WE. In addition, specimen WD possess smaller grains relative to WE. This means that more grain boundaries and dislocations are available as hydrogen trap sites in WD.

Table 6.3 Hydrogen permeation test data for as hot rolled pipeline steel specimens

Hydrogen permeation parameters	WE		WD	
	First charging	Second charging	First charging	Second charging
I_{∞} (A)	3.46×10^{-5}	2.75×10^{-5}	2.45×10^{-5}	1.40×10^{-5}
$J_{\infty}L$ (mol/cm/s)	4.75×10^{-10}	3.79×10^{-10}	3.38×10^{-10}	1.93×10^{-10}
C_{app} (mol/cm^3)	1.88×10^{-5}	4.10×10^{-5}	1.46×10^{-5}	1.57×10^{-5}
D_{eff} (cm^2/s)	5.04×10^{-6}	1.90×10^{-6}	4.63×10^{-6}	2.46×10^{-6}

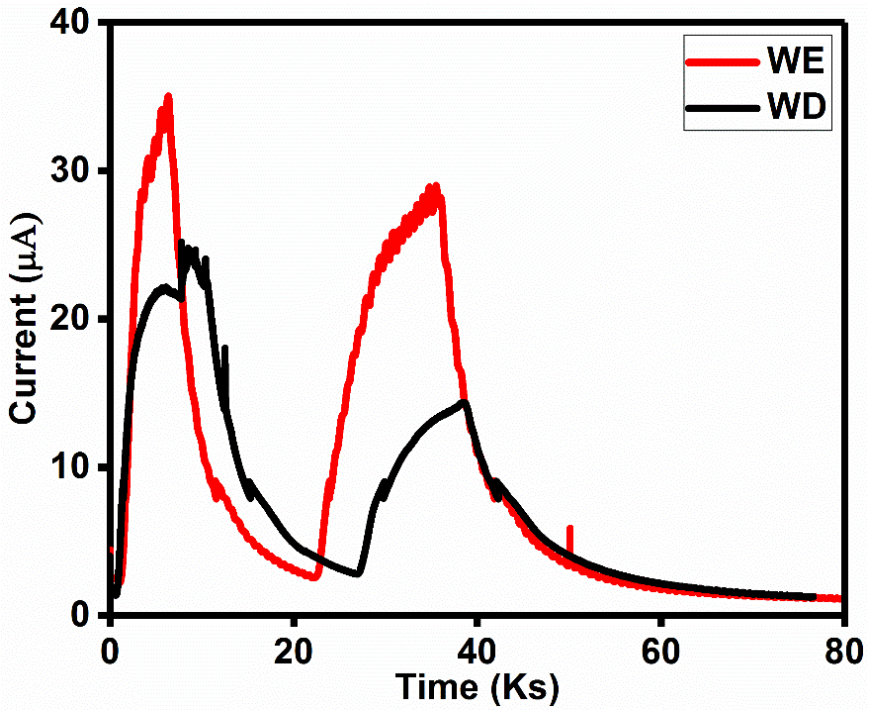

Fig. 6.5 Hydrogen permeation curves for pipeline steel specimens showing first and second hydrogen charging transients

6.4.4 Microstructure evaluation after hydrogen charging

After 12 h of hydrogen charging

The microstructure of both test specimens after hydrogen charging showed similar phases compared to the starting material, except that the onset of HIC along the mid-thickness was different for both specimens as presented in Fig. 6.6. After hydrogen charging for 12 hrs HIC was observed to have nucleated only in WD specimen. This is shown in Fig. 6.6b as discontinuous intergranular microcracks, which propagated along the mid-thickness. The observed crack appeared to be non-orientation dependent in Fig. 6.6c, as crack nucleated at inter-grain boundaries and propagated through boundaries and grains associated with various crystallographic planes. Also, notice in Fig. 6.6d that the crack initiation and propagation path was mainly along the deformed grain regions. This area has been clearly highlighted by the red colored grains aligned according to the crack zone.

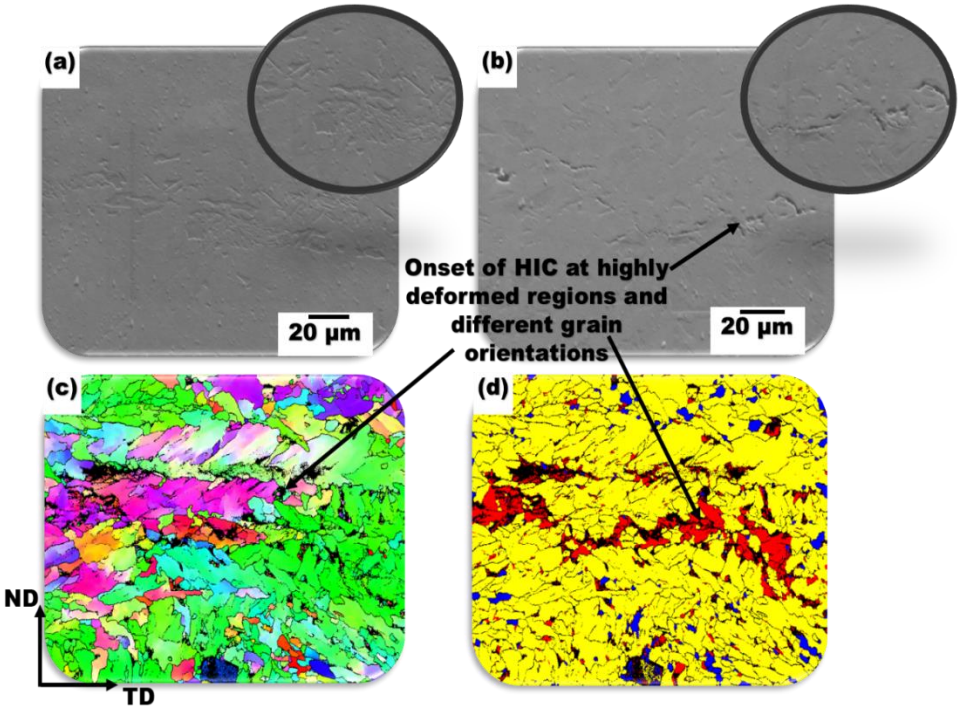

Fig. 6.6 Microstructural images of mid-thickness section after 12 h of hydrogen charging indicating no cracks along banding in WE (a, b), onset of discontinuous cracks in WD (c, d), EBSD orientation map (e) and recrystallization map where deformed regions = red, recovered regions = yellow, and recrystallized regions = blue

After 16 h of hydrogen charging

Hydrogen charging for 16 h showed that more prominent HIC was propagated along the mid-thickness of both specimens. Cracks were aligned parallel to the transverse direction as indicated in Fig. 6.7. It was not clear where exactly the crack started in these specimens. Nevertheless, HIC was clearly formed and propagated through significant portions of both test specimens. In Fig. 6.7a, crack loops can be seen around inclusions in specimen WE. Also, many aggregates of small inclusion are found along crack path in specimen WD (Fig. 6.7b). This suggests that inclusions combined with other microstructural features played a significant role in HIC initiation and propagation across test specimens. A plausible explanation for HIC observed in these steel plates will be that cracks initiated at the mid-thickness as a result of hydrogen attack on inclusions and microstructural phases. Thereafter, crack propagation was stabilized in this region by the presence of susceptible phases and banded deformed grains that were segregated around the mid-thickness following thermomechanical processing.

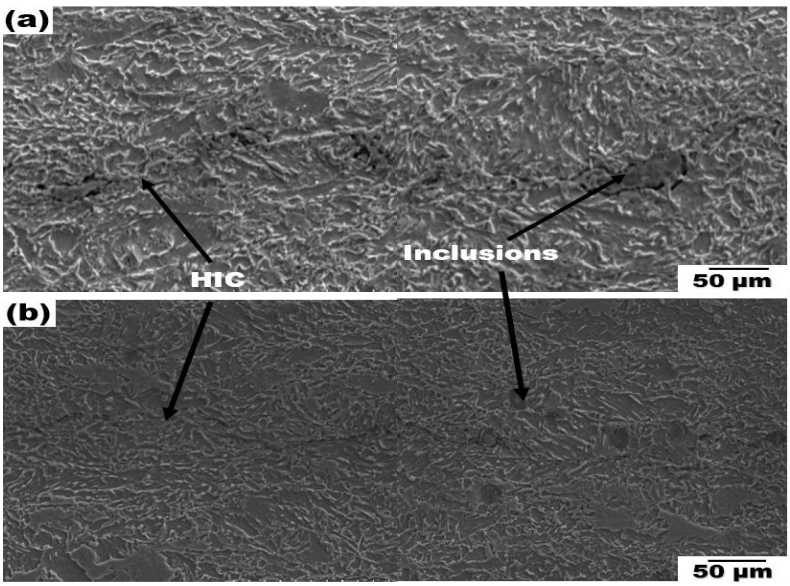

Fig. 6.7 SEM micrographs of mid-thickness section after 16 h of hydrogen charging indicating HIC in (a) WE and (b) WD

Fig. 6.8 shows EBSD maps for both specimens following 16 h of hydrogen charging. It is typical for HIC to propagate in a mixed fracture mode depending on microstructure and grain characteristics [14]. Unlike the nucleation of intergranular hydrogen assisted cracks in WD

specimen after 12 h of hydrogen charging (Fig. 6.6b-d), crack propagation became predominantly trans-granular in both specimens after 16 h The belief is that the nucleated micro-cracks became 'aggressive' at extended charging time. Figs. 6.8a and 6.8f shows similar orientation maps for WE and WD. Again, the same dominance of ⟨011⟩||RD and ⟨001⟩||RD fiber textures in as hot rolled samples were observed after hydrogen charging. In a different study on X65 pipeline steel, grain boundaries of ⟨011⟩||rolling plane (RP) and ⟨111⟩||RP textured grains offered resistance to cracking, while boundaries of ⟨001⟩||RP textured grains were more susceptible to crack propagation [147]. However, there is no evidence in this study that cracks propagated preferentially along grains of specific crystallographic orientation. This confirms the importance of other microstructural features in increasing HIC susceptibility of WE and WD specimens. Most especially, crack susceptible phases, inclusions, and banded deformed grains along the mid-thickness of both specimens will limit the possibility of crack arrest at ⟨011⟩||RD oriented grains. Grain boundary distribution maps in Figs. 6.8b and 6.8g shows a mixture of HAGB and LAGB in the mid-thickness regions of both pipeline steel specimens. In as hot rolled specimens, higher fraction of HAGB was established in WE and WD compared to their LAGB (Table 6.1). Some researchers have associated HAGB with high stored energy, which facilitates initiation and propagation of HIC in steels [15]. However, it is difficult to estimate the exact amount of these boundaries situated along the crack propagation path. Therefore, the predominance of HAGB may not be regarded as the sole driving force for HIC across the mid-thickness of WE and WD, even though more HAGB are observed in WD. Comparing other microstructural features will further elucidate the reasons for early crack initiation in specimen WD and subsequent crack propagation along the mid-thickness region of both test specimens.

Calculating KAM (Kernel Average Misorientation) distribution for both specimen from Figs. 6.8c and 6.8h could be useful in analysis of HIC. Local misorientation values of 0.58° and 0.66° were determined for WE and WD respectively. This also demonstrates that grains in WD have higher number of defects or stored energy, than those in WE. Also, Figs. 6.8c and 6.8h shows that majority of such defects are located along the crack path where local misorientation is higher in both specimens. This finding corroborates earlier observation of high dislocation density and banded deformed grains along the mid-thickness in as hot rolled specimens (Figs. 6.2c,h and Figs. 6.3c,h). In view of this, it is expected that in-grain misorientation and distortions between

neighboring grains in the mid-thickness region will increase cracking susceptibility, especially in WD. Thermomechanical processing impart stored energy in pipeline steel, but recrystallization enables grain recovery. Therefore, recrystallized and recovered grains show less susceptibility to HIC, while deformed grains are highly prone to cracking [417]. Figs. 6.8d and 6.8i shows recrystallization maps for WE and WD respectively after hydrogen charging. When comparing the extent of recrystallization, deformation and recovery in both specimens, higher fraction of deformed grains is found in WD, with less recrystallized and recovered grains as presented in Table 6.4. Considering the cooling rate of 51.5 ℃/ s applied to WD and 42.75 ℃/ s applied to WE, less time will be available for complete recrystallization and recovery to occur in WD. This means that more deformed grains are bound to remain in the structure of WD, whereas less deformed grains, with more recrystallized and recovered grains will develop in WE.

Table 6.4 Area fraction of recrystallized, recovered and deformed grains in pipeline steel specimens after hydrogen charging for 16 h

Specimens	Deformed area fraction (%)	Recovered area fraction (%)	Recrystallized area fraction (%)
WE	16	76	6
WD	30	64	5

The deformed grains in WE are mainly located along the crack path in the mid-thickness, while in WD they are seen both on the crack path and outside. A similar alignment of deformed grains in the mid-thickness region was also seen in as hot rolled specimens (Figs. 6.2d,i and Figs. 6.3d,i), and can be a reason for crack propagation in this area. One can correlate the presence of deformed grains with high local misorientation, and segregation of martensite and cementite along the mid-thickness of specimens. There are more particles of cementite segregated outside the crack path in specimen WE (Fig. 6.8e) in comparison to WD (Fig. 6.8j) which featured more martensite phase. This recalls that diffusion of hydrogen must have been lower in specimen WD when compared to WE. It is possible that higher presence of deformed grains played a significant role in limiting the amount of hydrogen that permeated through specimen WD in relation to specimen WE. The lower fraction of recovered and recrystallized grains within the cracked area of specimen WD supports the idea of lower hydrogen diffusivity and increased tendency for HIC, in contrast to specimen WE with higher fraction of recovered and recrystallized grains.

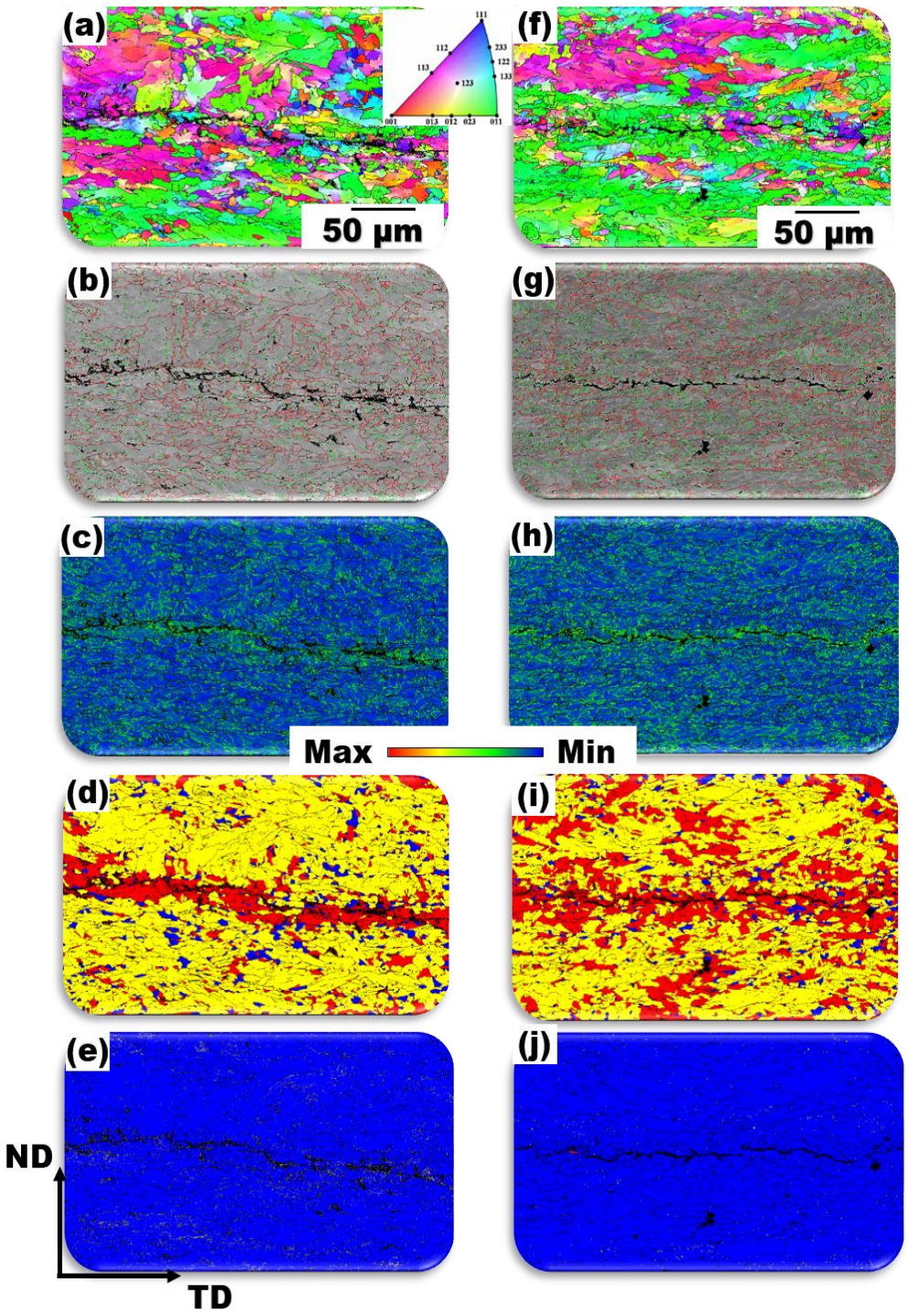

Fig. 6.8 EBSD maps for hydrogen charged pipeline steel specimens WE (a, b, c, d, e), and WD (f, g, h, I, j) after 16 hrs. Orientation maps are a, f. Grain boundary distribution maps are b, g. Local misorientaion maps are c, h. Recrystallization fraction maps d, I, (deformed regions = red, recovered regions = yellow, and recrystallized regions = blue). Phase maps are e, j, (blue = ferrites, black spots = martensite, yellow spots = cementite, red spots = austenite)

6.4.5 EDS inclusion analysis after hydrogen charging

Precipitation of inclusions is detrimental to HIC susceptibility in pipeline steel, due to potential accumulation of atomic hydrogen around them. This phenomenon is related to weakening of bonds between the matrix and inclusion resulting in lack of coherency. The consequence is usually the void creation and hydrogen trapping at matrix-inclusion interface [161]. Many reports have proposed a mechanism for HIC initiation based on pressurization of voids around inclusions due to hydrogen recombination to form molecules, and subsequent straining of the steel structure to create cracks [165]. Inclusion analysis performed by EDS mapping along the crack showed the presence of different elements in test specimens. Majority of the inclusions found are carbonitride, oxides and other precipitates. As shown in Fig. 6.9, specimen WE have mainly oxides and carbonitride inclusions. These are mainly Si-C-N-S-Ca-Mo type inclusions and precipitates of Ti-V-Nb. Interestingly, different kinds of interaction occurred between inclusions and HIC found in specimen WE. In Fig. 6.9a, the most favorable path for crack propagation was the interface between inclusion and matrix. This suggests that the inclusion was non-coherent with the pipeline steel matrix, which made it most favorable for the crack to propagate in form of a loop around it. On the other hand, HIC propagated across the inclusion presented in Fig. 6.9b, indicating a higher degree of interfacial coherence compared to the one shown in Fig. 6.9a. Although both specimens contain similar inclusion types, more particles containing Al-Mg-Mo-Si-Ca-N-S and precipitates of Ti-V-Nb aggregated along the crack path in WD as shown in Fig. 6.10. A more specific study was performed on one of the inclusions identified in WD (Fig. 6.10a) and presented in Fig. 6.10b. The results obtained from this analysis confirm that the inclusion types are quite similar in both pipeline steel samples, but crack propagation pattern across each of them are completely different.

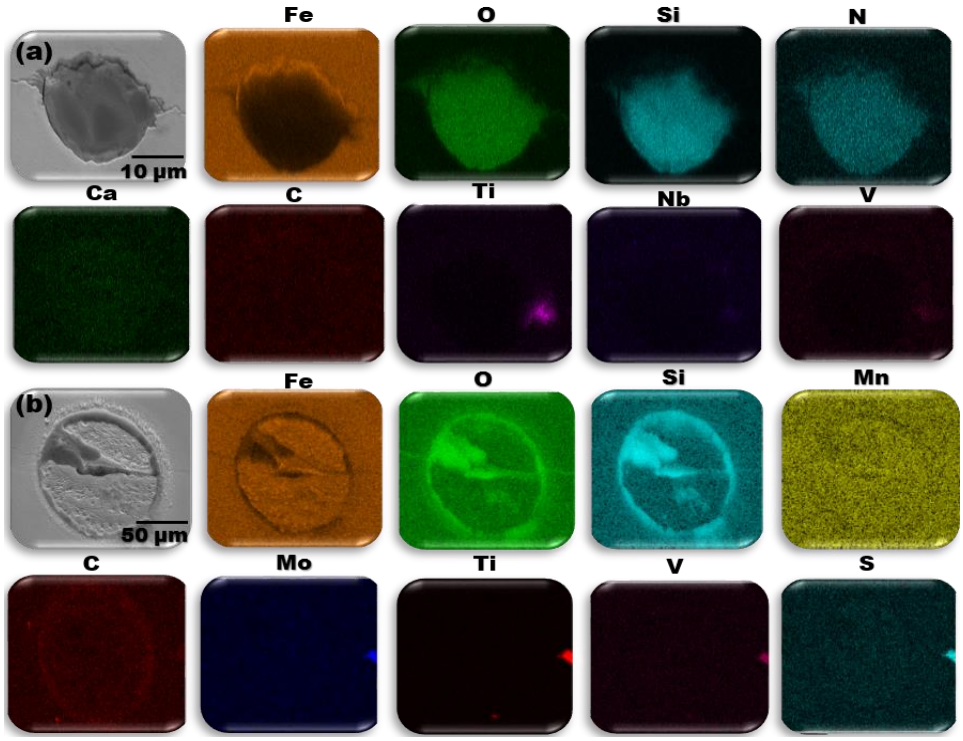

Fig. 6.9 EDS maps for inclusions in pipeline steel specimen WE

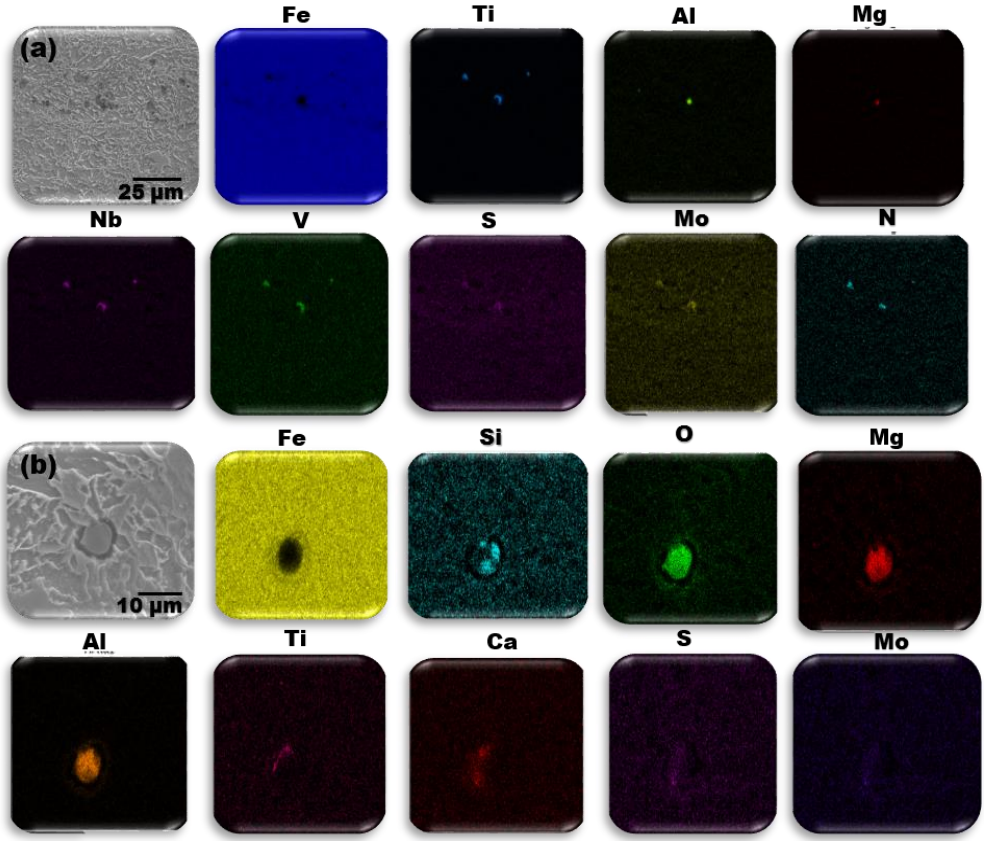

Fig. 6.10 EDS maps for inclusions in pipeline steel specimen WD

Various inclusion types have been identified in pipeline steel. For example, Jin *et al.* [164] documented MnS, Al-Si and Ca-S-Al-O enriched inclusions in X100 pipeline steel but concluded that only Al-Si types were responsible for HIC. Also, inclusions consisting of mainly MnS and carbonitride precipitates comprising of Ti, C, S, N, and V has been observed in X70 pipeline steel [165]. It is worth mentioning that the inclusion types present in both specimens agree with those reported in these literatures. In another study [32], carbonitride precipitates, oxides, and sulfide type inclusions were noticed in X70 pipeline steel. Strikingly, the latter report stated that inclusions of oxide type did not result in HIC. The authors observed oxide type inclusions of Al, Ca, Mn and Mg in greater portion. Yet, they concluded that these inclusions only resulted in reduced fracture toughness of pipeline steel. Their argument was based on the shape of oxide inclusions. Some of the oxide inclusions found in X70 pipeline steel are spherically shaped, which makes it difficult for them to initiate cracks in accordance with stress concentration theory. Also, spherical inclusions lack the edges that are present in the elongated ones. Thus, there is no preferential agglomeration of hydrogen around them. Therefore, it can be implied that inclusion accumulation promoted reduction in fracture toughness of both pipeline steel specimens. The consequence of losing toughness is the stabilization of HIC propagation, especially along the mid-thickness where inclusions are accumulated in specimen WD.

The role of inclusion quantity, shape, size and chemical composition in hydrogen damage on steel has already been studied [168]. Some researchers believe that shape, size and interfacial gap between inclusions and steel matrix are more significant for crack initiation, compared to the composition of inclusion [169]. These authors are of the opinion that Si enriched inclusions and large Ti precipitates were more responsible for reducing fracture toughness and initiating cracks in pipeline steel compared to others. This highlights the importance of precipitate size in improving fracture toughness of pipeline steel. Therefore, changing the morphology of inclusions can potentially help in strengthening pipeline steel and improving crack resistance. Also, micro-alloying with Ca or other rare earth elements helps to achieve shape control and limit hydrogen attack by the formation of CaS precipitates instead of MnS [170,172].

6.4.6 Mechanical response of pipeline steel under tensile loading

The mechanical responses of both pipeline steel specimens under tensile testing condition is shown by the engineering stress – engineering strain curves presented in Fig. 6.11. Initial baseline tensile test without in-situ hydrogen charging indicate that yield and tensile strengths for specimen WE are 567 MPa and 674 MPa respectively; specimen WD showed higher yield and tensile strengths of 620 MPa and 723 MPa respectively. It is necessary to also state that these strength values conform to the tensile requirements stated in API 5L specification for X70 pipeline steel [36]. In addition to higher tensile properties in WD, ductility was observed to be slightly lower than that of WE. This is clearly evident in Fig. 6.11, and the time to failure values recorded for specimen WE was 81 h, while specimen WD failed after a shorter period of 74 h. It is also noticeable on the fracture surfaces of both specimens in Fig. 6.12a-b that dimples occurring due to coalescence of micro-voids in specimen WE are deeper on the shear lip compared to specimen WD. This confirms that specimen WE is more ductile and elongated more when tested without hydrogen charging. The tensile behavior displayed by these specimens can be explained in terms of TMCP parameters used for each specimen and the microstructure developed thereafter. Recent studies on the relationship between processing and mechanical properties of different pipeline steels concluded that cooling at a faster rate and ending at lower temperature results in pipeline steel with higher strength and bainitic microstructure. On the other hand, commencing cooling at a lower temperature will ultimately create a ferritic microstructure and lead to increased deformability [136,418]. These reports are clearly in consensus with the processing schedules, and mechanical properties of specimens WE and WD. Taking into consideration Fig. 6.1, the microstructure of specimen WE is dominated by ferrite compared to specimen WD which contain more bainite. From Table 3.1, cooling started at temperatures of 805 ºC and 815 ºC for WE and WD respectively. After different cooling procedures, the final cooling temperatures for WE and WD were 584 ºC and 500 ºC respectively. These temperature conditions are the main reasons why specimen WD had improved strength and less ductility in contrast to specimen WE.

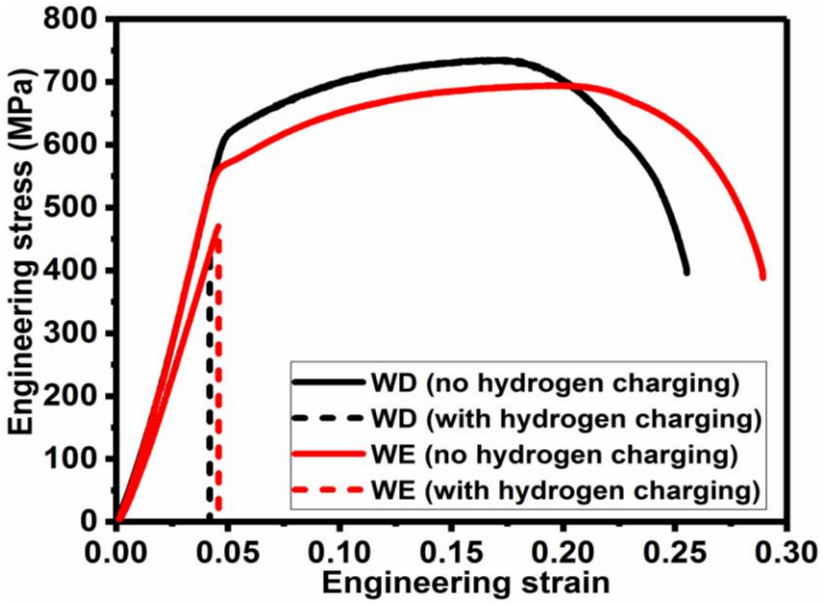

Fig. 6.11 Engineering stress – engineering strain curves for pipeline steel specimens with and without hydrogen charging

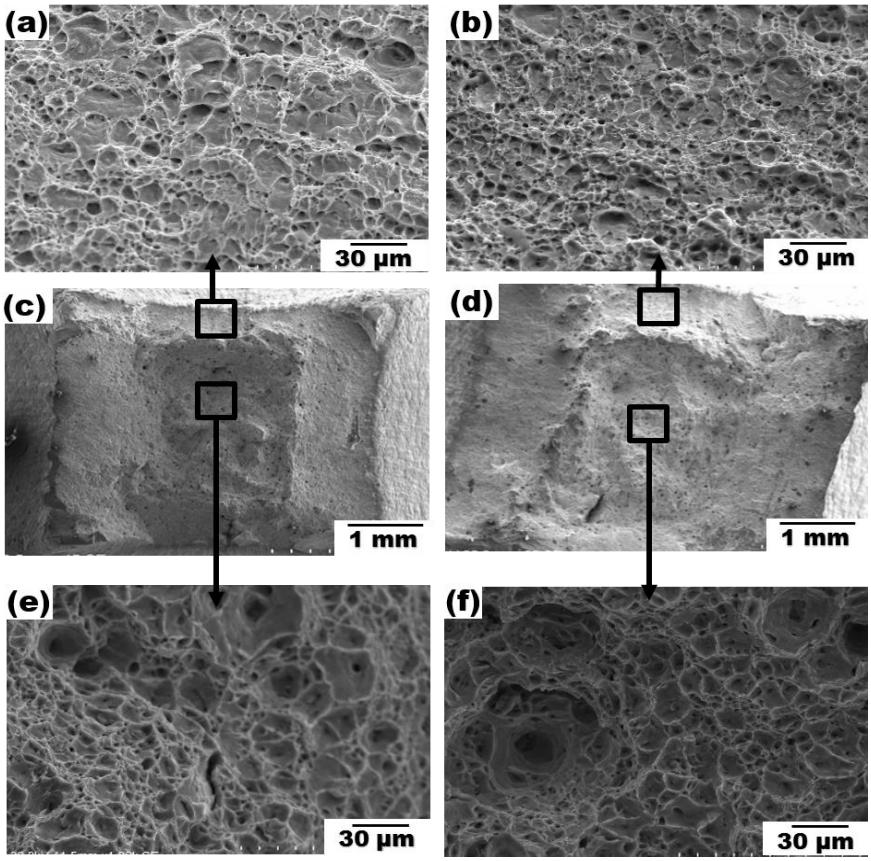

Fig. 6.12 SEM fractographs after slow strain rate tensile testing without hydrogen charging for pipeline steel specimens, WE (a, c, e) and WD (b, d, f)

In the case of tensile test with in-situ hydrogen charging, both pipeline specimens failed below their yield strength in a brittle manner. This is clearly shown by the cleavage fracture surface seen on both specimens in Fig. 6.13. However, specimen WD failed earlier with a time to failure of 11 h. while specimen WE failed after 12 h. Other researchers have shown that applied stress in the elastic range results in instability of passive film formation, and hydrogen permeation into steel is heightened in this region compared to the plastic region [145]. In addition, dislocation motion is absent in the elastic region. This means that reversible hydrogen trap sites are less when the steel is elastically deformed, and dislocations are immobile. Thus, diffusion of atomic hydrogen towards any other defects (irreversible trap sites) that may be present in the pipeline steel structure is more likely during elastic deformation. This phenomenon usually lead to rapid failure, as was seen on both specimens during test with in-situ hydrogen charging. Fig. 6.11 shows that specimen WE resisted higher amount of stress and was strained more within the elastic range prior to failure during hydrogen charging, while failure occurred at lower stress and strain values in specimen WD. The reasoning is that the structure created by thermomechanical treatment on WD was more susceptible to attack by hydrogen. Judging by the differences observed in the structure of both pipeline specimens, and the corresponding influence on mechanical response under tensile loading (with and without in-situ hydrogen charging), it can be said that more atomic hydrogen trapping and recombination to form molecules occurred within the structure of specimen WD compared to specimen WE. Therefore, specimen WD was more susceptible to HIC compared to specimen WE. This ties into the general opinion that stronger materials are more susceptible to HIC.

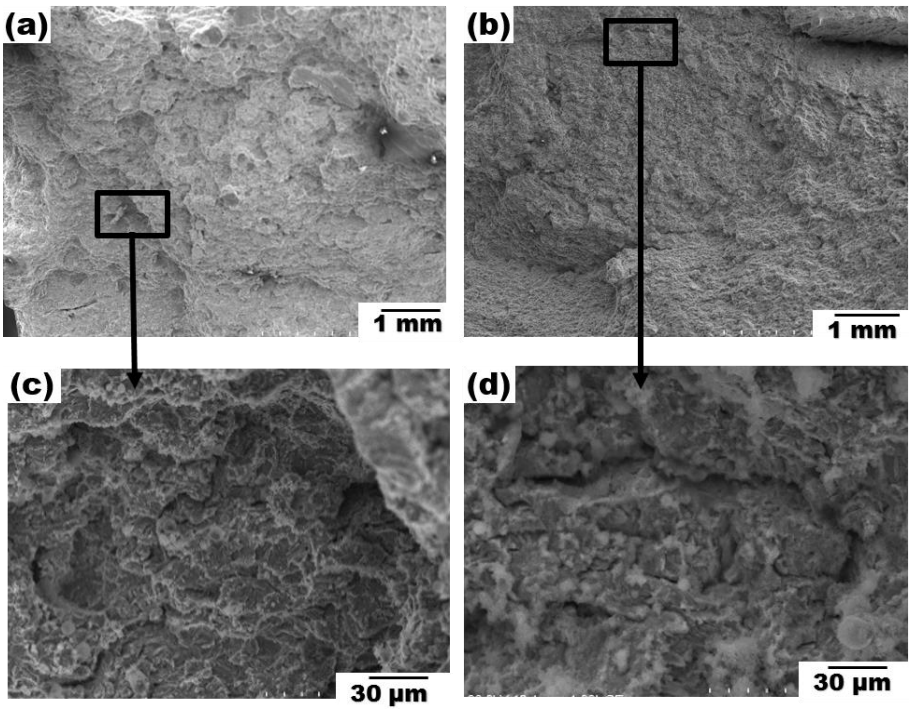

Fig. 6.13 SEM fractographs after slow strain rate tensile testing with in-situ hydrogen charging for pipeline steel specimens WE (a, c) and WD (b, d)

6.5 Summary

Influence of TMCP on microstructure and susceptibility of X70 pipeline steel to HIC was studied by cathodic hydrogen charging with and without tensile loading. The following are key outcomes from this study:

1. The thermomechanical processing routes resulted in similar microstructural phases comprising of polygonal ferrite, acicular ferrite, and some bainitic ferrite which occurred mainly in WD specimen. However, polygonal ferrite and acicular ferrite featured more in WE specimen.
2. Thermomechanical processing resulted in banded deformed grains, segregation of inclusions and secondary phases along the mid-thickness of both pipeline steel specimens. It is these features that promoted HIC propagation in pipeline steel specimens. Although both specimens showed cracks across their mid-thickness after 16 h of hydrogen charging, test performed for 12 h showed early onset of HIC in specimen WD.

3. Hydrogen diffusivity across specimen WE was better than that of specimen WD, which indicates that more hydrogen atoms were trapped within the structure of WD where they recombined into molecules to increase HIC susceptibility compared to WE.
4. Mechanical response of specimen WE without in-situ hydrogen charging was characterized by higher ductility, lower yield strength (567 MPa) and tensile strength (674 MPa), compared to specimen WD with lower ductility, higher yield strength (620 MPa) and tensile strength (723 MPa). Tensile test with in-situ hydrogen charging resulted in failure below yield strength for both test specimens, but WE specimen failed at a higher stress value compared to WD.

CHAPTER 7 : HYDROGEN INDUCED CRACKING SUSCEPTIBILITY OF API 5L X70 PIPELINE STEEL IN RELATION TO MICROSTRUCTURE AND CRYSTALLOGRAPHIC TEXTURE DEVELOPED AFTER DIFFERENT THERMOMECHANICAL TREATMENTS[6]

7.1 Overview

This chapter adds to addressing the second objective specified at the beginning of this thesis. The results which are discussed in this chapter evaluates the influence of thermomechanical treatments on microstructure and texture development across two new X70 specimens labeled WG and WH. Examinations of the microstructural features of steels is correlated with their susceptibility to HIC. Some changes which differentiates this chapter from the published paper are as follows:

a) The materials and methodology section have been removed to avoid duplication, as this aspect is already described in chapter 3 of this thesis.
b) References in this manuscript has been merged into a single list at the end of the thesis.

Thermomechanical treatments offer an innovative means of controlling microstructural development and improving resistance to hydrogen induced cracking (HIC) in pipeline steel. This study was conducted on two X70 pipeline steels labelled WG and WH. Both steel specimens have the same chemical composition but were processed with different thermomechanical parameters. Specimen WG was hot rolled at a higher temperature range of 880 – 820℃, whereas specimen WH was hot rolled between 830 – 760 ℃. Thereafter, the two steels were cooled at the same rate of 25 ℃/ s. Early onset of HIC was observed in specimen WH after electrochemical hydrogen charging for 12 h in a solution of 0.2 molar H_2SO_4 and 3 g/l NH_4SCN, without any applied stress. Also, test pieces from the surface and mid-thickness layers of each pipeline steel were subjected to tensile testing with in-situ hydrogen charging. Characterization techniques such as Optical

[6] The results in this chapter are already been published, but was used with permission from *Elsevier* (Appendix G): E. Ohaeri, J. Szpunar, F. Fazeli, M. Arafin 'Hydrogen induced cracking susceptibility of API 5L X70 pipeline steel in relation to microstructure and crystallographic texture developed after different thermomechanical treatments', *Materials Characterization,* 2018, Vol. 145, pp. 142-156

The PhD candidate E. Ohaeri designed all experiments, characterised microstructure, texture and surface morphology of specimens, compiled the report, as well as finalised the manuscript after revision by supervisor and peer-reviewers.

Microscopy, Scanning Electron Microscopy, Electron Backscattered Diffraction and X-ray Diffraction were used to verify the different microstructures and orientation of grains in pipeline steel specimens. The role of inclusions on HIC was studied by Energy Dispersive X-ray Spectroscopy. Although the microstructures of both specimens were observed to be predominantly ferrite, more martensite/retained austenite (M/A) constituents were featured in WG. Further crystallographic texture analysis indicates that grain orientation at the surfaces of both test specimens were similar with deviations towards ⟨111⟩ on the inverse pole figure (IPF); whereas, pole intensity at the mid-thickness deviated towards the ⟨001⟩ direction. Nevertheless, increased fraction of banded-deformed grains with increased stored energy, determined in terms of higher kernel average misorientation (KAM), justifies the lower HIC resistance of specimen WH in comparison to specimen WG.

7.2 Background

Over the years, manufacturers of pipelines have faced the challenge of producing steel plates with enhanced strength and ability to fail only in ductile manner. The risks of rupture even become worsened in oil and gas pipelines operating in extreme corrosive conditions. Intense loss of materials and/or cracking during the process of corrosion often result in unexpected pipeline failure. Various electrochemical reactions signify the anodic oxidation and cathodic reduction processes that takes place during corrosion. These reactions typically occur on the surface of pipelines where there are anodic sites for metal dissolution (Eq. 7.1), and cathodic sites for the production of hydrogen (Eq. 7.2), and hydroxyl ions (Eq. 7.3) through reduction reactions [11]. However, the proton reduction reaction described in Eq. 7.2 is commonly noticed in acidic environments [419].

Anodic reaction:

$$Fe \rightarrow Fe^{2+} + 2e^{-} \quad (7.1)$$

Cathodic reactions:

$$2H^{+} + 2e \rightarrow H_2 \text{ (Proton reduction)} \quad (7.2)$$

$$O_2 + 2H_2O + 4e^{-} \rightarrow 4OH^{-} \text{ (water reduction)} \quad (7.3)$$

Early studies [420], suggested a mechanism for hydrogen production during cathodic reaction in hydrogen sulfide (H_2S) media (Eq. 7.4). This was the basis for another work detailing different corrosion products formed on iron after exposure to aqueous H_2S [421]. The authors concluded that iron sulfide (FeS), known as *'mackinawite'*, is formed by both precipitation and solid-state reactions (Eq. 7.5).

$$2H_2S + 2e^- \rightarrow 2HS^- + H_2 \quad (7.4)$$

$$Fe + H_2S \rightarrow FeS + H_2 \quad (7.5)$$

Cases of brittle catastrophic failures of in-service pipelines has become common in recent times [324], even in structures originally designed to fail in ductile mode. This highlights the need for better toughness, resistance to hydrogen embrittlement (HE), and other forms of environmentally assisted degradation. It is also important that features like weldability and deformability are not compromised during steel processing. Sour service (H_2S containing environment) is considered the most critical operating environment for pipelines, because of the potential risks of hydrogen uptake and consequent damage by HIC. Atoms of hydrogen released from corrosion reaction in Eq. 7.2, including those from uncontrolled cathodic protection, and dissociation of H_2S can enter pipeline steel, i.e. $H_2 = 2[H]$ at the surface, where $[H]$ denotes the atomic hydrogen dissolved in the iron lattice following absorption at the surface. The small size of these atoms makes it easier for them to diffuse through the lattice spacing within steel, a process that is mainly driven by the concentration gradient of these atoms. The diffusion paths present inside the steel also plays a key role in promoting rapid saturation with atomic hydrogen. For instance, a correlation between diffusivity of hydrogen and crystallographic orientation in austenitic stainless steel showed rapid evolution of hydrogen through $\{110\}$ and $\{100\}$ oriented grains, in comparison to the $\{111\}$ grains [422]. This suggests that the $\{111\}$ oriented grains are relatively more efficient in trapping atomic hydrogen. However, hydrogen atoms which could not make it into the steel structure will simply recombine into molecules and diffuse away according to Eq. 7.6.

$$H_{ads} + H_{ads} \rightarrow H_2 \quad (7.6)$$

Pipeline fluids are usually transported at very high temperature and pressure. Such operating conditions foster the risks of embrittlement by enabling ingress of hydrogen atoms through steel [64,145]. Also, pipeline operation influences the interactions of atomic hydrogen with potential

trap sites inside the steel. A recent study proposed that differences in density of traps affects hydrogen permeation pattern from surface towards the mid-thickness region of rolled steel [114]. Many slow processes, which are often unnoticed, culminate to fracture in steel structures that are exposed to hydrogen [62]. First, evolution of hydrogen either during steel processing and fabrication or from service environment (i.e. corrosion, cathodic protection and chemical species like H_2S). Then, adsorption of atomic hydrogen into steel structure. Finally, internal embrittlement due to hydrogen ingress/trapping within the microstructure.

Atoms of hydrogen accumulate at defects (trap sites) such as dislocations, grain boundaries, inclusions and/or voids. They eventually recombine to form molecules inside the traps, and initiate cracks by internal pressurization at stress concentration regions [423]. This phenomena is common at center line segregation zones, where different types of inclusions accumulate hydrogen and promote failure by HIC [206,424,425]. Consequently, steel casting processes are designed to promote removal of inclusion particles, especially macroscopic oxides and manganese sulfides. The elongated sulfides and stringers of alumina are considered the most detrimental to crack resistance in pipeline steel [138]. Changing elemental composition simply comes to mind as one of the primary means of improving the properties of steel. Lowering the amount of manganese, with the addition of niobium and molybdenum was reported to offer better mechanical properties [130]. Moreover, contemporary steels contain minimal amount of impurities because of continuous advancement in processing technologies; hence, inclusions and segregations are significantly minimized. Apart from using cleaner steel for pipeline production, phase constituents, grain morphology and crystallographic texture are other microstructural features to be considered.

Thermomechanical controlled processing (TMCP) offer an acceptable means of developing the desired microstructure and/or grain orientation in pipeline steel [426]. The amount of plastic deformation impacted during hot rolling significantly affects both mechanical properties and embrittlement behavior of steel [145]. So, it is important to strike a good balance between the key pipeline material properties, which are strength, weldability and toughness. The presence of banded microstructural phases and high precipitate concentration increase the predisposition of steel to cracking, unlike in steels containing mainly acicular ferrite [427]. Furthermore, there are claims that high angle grain boundaries (HAGB) impact strength and less resistance to crack propagation, because of comparatively higher energy in relation to lower energy interfaces like

coincident site lattice (CSL) and low angle grain boundaries (LAGB) [377,428]. Various experimental observations have indicated crack propagation through regions containing mainly high energy boundaries [34,307,429]. Notably, Arafin and Szpunar [147] documented that crack propagation in pipeline steel was primarily through {100}||RP (rolling plane) textured grains; whereas, the crack resistant grains are those textured with {110}||RP and {111}||RP orientation. Similar findings have also been presented elsewhere [149,158]. Another study found that increasing the intensity of crack resistant {110} and {111} planes oriented parallel to the pipeline surface, will indirectly decrease the fraction of HAGB, {100} oriented grains and HIC susceptibility [377]. Therefore, the ease of hydrogen ingress into pipeline steel and subsequent cracking can be linked to TMCP history. It is suggested that HIC resistance can be improved in steel by applying thermomechanical rolling schedule that promotes dominance of {111}||ND, {110}||ND and {112}||ND texture fibers [34,307]. In this regard, recent investigations are aimed at identifying the relationship between hot rolling parameters and susceptibility to different forms of corrosive deterioration in steel [153,160]. Also, a detailed overview on the effect of hydrogen on degradation of pipeline steel has been published [8]. Masoumi *et al.* [160] considered thermomechanical procedures for achieving similar microstructure, but different crystallographic texture in a steel plate with comparable chemical composition to X70 pipeline steel. In a different work [150], the same authors examined the prospects of enhancing HIC resistance in X70 pipeline steel by engineering the distribution of grain boundaries and crystallographic orientation through an isothermal rolling process. They concluded that the prominence of {110}||ND, with minimal {100}||ND textured grains in the rolled samples warranted better HIC resistance; whereas, higher crack susceptibility manifested in samples with dominant {100}||ND textured grains. Till date, studies related to the optimization of desirable texture fibers for crack resistance has been sparsely reported in literature. There is need to find a more reliable processing route to produce pipeline steel plates containing significant fraction of crack resistant grain orientation. The present work contributes towards the overall goal of developing pipeline steel with improved presence of {111}||ND textured grains by TMCP approach. The understanding is that altering the finishing rolling and cooling parameters may increase the intensity of {111} grains and help improve resistance to cracking. The main aim is to investigate the role of different thermomechanical treatments on microstructure and texture evolution in X70 pipeline steel; then relate these properties to HIC susceptibility.

7.3 Experimental procedure

Refer to sections 3.2, 3.3.1 – 3.3.4, and 3.3.9 for details about pipeline steel material, microstructural characterization techniques, and HIC test procedures.

7.4 Result and discussions

7.4.1 Microstructural evaluation of starting materials

Various microstructural features are usually observed in TMCP steel, depending on processing parameters and micro alloying composition [430]. For pipeline steel designated for sour environment, inclusions are usually a great concern. Analysis on specimens WG and WH showed two main categories of inclusion particles. They comprise of the angular precipitates of (Ti-Nb) N with traces of S-Mo, and spherical oxides of Al-Ca-Mg as shown in Fig. 7.1. Observing similar inclusion particles in WG (Figs. 7.1a-b) and WH (Figs. 7.1c-d) was not surprising, since chemical composition is the same for both pipeline steel specimens. Although these kinds of inclusions are widely reported for this grade of pipeline steel [165,169], it is still unclear what their specific roles are with respect to HIC. There are different opinions regarding shape, size, and types of inclusions and how they interact with cracks in steel. These features are of interest in understanding the mechanism of crack initiation and propagation. Properties of steel has strong correlations to the geometry of inclusion particles that may be present in its structure [431]. A study aimed at optimizing X70 pipeline steel production found that more oxides of Al such as Al_2O_3 were present at the initial stages of processing due to deoxidization [171]. However, the authors discovered that the addition of Ca as an alloying element led to the formation of other globular inclusions such as CaS and CaO. The idea is that Ca being an active element easily reacts with oxides of Al, Mg, S impurities and Mo in the molten state to produce spherical inclusions. Some researchers [5,170,171,188] believe that round inclusions are less prone to crack initiation, because they do not possess the sharp edges which constitute zones of stress concentration in the angular ones. Also, the creation of circular CaS helps to diminish MnS inside the pipeline steel structure; thereby depriving atomic hydrogen the opportunity of agglomerating around the characteristic sharp edges of MnS and causing HIC [188]. Moreover, alloying pipeline steel with Ti enables the formation of TiS in the presence of sulfur [187]. This could be a justification for the traces of sulfur found within the multi-component precipitates and oxide particles developed in the two specimens examined in

this work. Subsequently, the current study will explain the relationship between the identified inclusion types and HIC behavior.

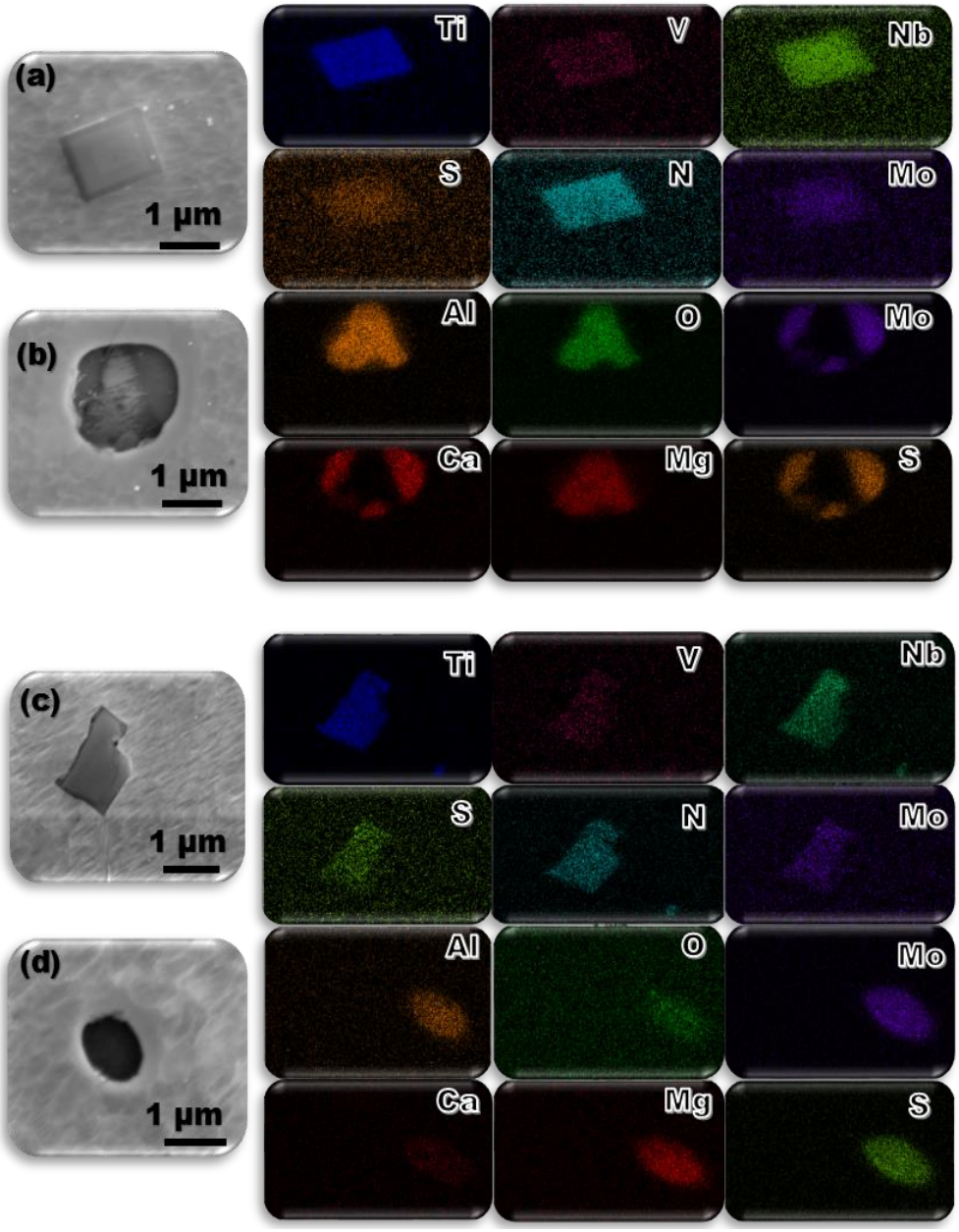

Fig. 7.1 EDX inclusion analysis at the surface of starting pipeline steel materials WG (a, b) and WH (c, d)

In addition to strain-induced precipitates from alloying elements, the resultant microstructure after steel processing also influence properties [432]. The microstructure images corresponding to the RD – TD and ND – TD planes of pipeline steel specimens are presented in Figs. 7.2 – 7.3. Ferrite

grains dominate the microstructure of X70 pipeline steel, as can be seen in the micrographs for both specimens. It is obvious that the grains at the surfaces of WG (Fig. 7.2a and Fig. 7.3a) and WH (Fig. 7.2c and Fig. 7.3c) have irregular shape, with some grains slightly oriented towards the rolling direction, and others are randomly oriented. Grains at the surface appear to be more refined with smaller size than those at the cross-section of the mid-thickness region. Such variations in grain size is known to affect hydrogen diffusivity across pipeline steel thickness [197]. Their study established lower diffusion of hydrogen at the pipeline steel surface because of refined grains with high dislocation density, compared to the center region where less refined grains are present. Since the cooling stop temperature on the run-out table after hot rolling was relatively higher for WG (615°C) than WH (565°C/s), one will expect to find some microstructural differences in these specimens. Microstructural examination across the transverse section (ND – TD plane) clearly indicate higher presence of secondary phases (black spots) in specimen WG (Fig. 7.2b and 7.3b) in comparison to WH (Fig. 7.2d and 7.3d). These are typically martensite grains with some retained austenite (M/A constituents). They are located mainly along the grain boundaries, and inside the grains in few places. We recall that stop cooling temperature and its subsequent air-cooling segment for WG (615°C) was about 50° higher than WH (565°C). Applying such a thermal cycle for WG will encourage decreased fraction of bainite and a higher fraction of untransformed austenite before coiling, in relation to WH. Therefore, more austenite is bound to transform into martensite in WG upon the following stages of coiling and gradual cooling to room temperature. The higher temperature range for bainite formation in WG could also promote formation of some coarse granular bainite, which is expected to be missing in WH. The presence of M/A constituents tends to be associated more with granular bainite morphology. Altogether, both specimens comprise of acicular ferrite, bainitic ferrite and polygonal ferrite; and can be said to be similar in terms of phase constituents.

The microstructural phases in steel are considered important factors in assessing HIC risks. An important characteristic of acicular ferrite phase is that it creates sub-structures that contain highly mobile dislocations, and guarantees a good balance between strength and toughness [169]. It also implies that entanglement of dislocations in steel may constitute sink for hydrogen atoms; thereby causing delayed corrosion and cracking. The presence of hydrogen lowers dislocation interaction, and enhances planar slip [129]. In pipeline steel containing both granular bainite and acicular ferrite, the nucleation of acicular ferrite often occur at the boundaries of deformed austenite grains,

especially at relatively high extent of deformation within the non-recrystallized range [433]. The authors believe this phenomenon indirectly promotes the stabilization of the remaining austenite, which will subsequently transform into M/A constituents. Therefore, they noted that the transformation of acicular ferrite and diffusion of carbon atoms greatly affects the formation of M/A constituents. One may suggest that this was the situation in specimen WG where higher presence of the supposed M/A constituents occurred, compared to specimen WH.

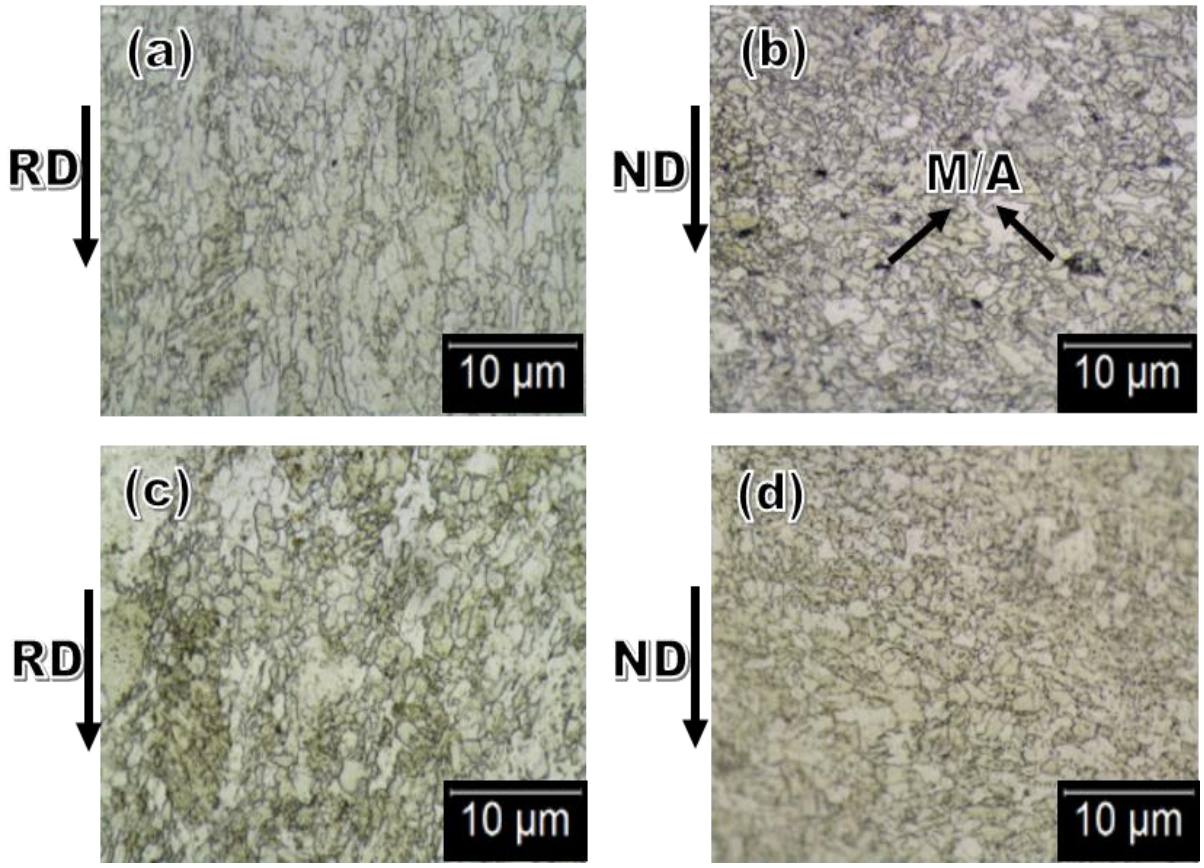

Fig. 7.2 Optical microstructure of specimens at different planes (a) RD – TD for WG (b) ND – TD for WG, (c) RD – TD for WH, and (d) ND – TD for WH (RD: rolling direction, TD: transverse direction, ND: normal direction)

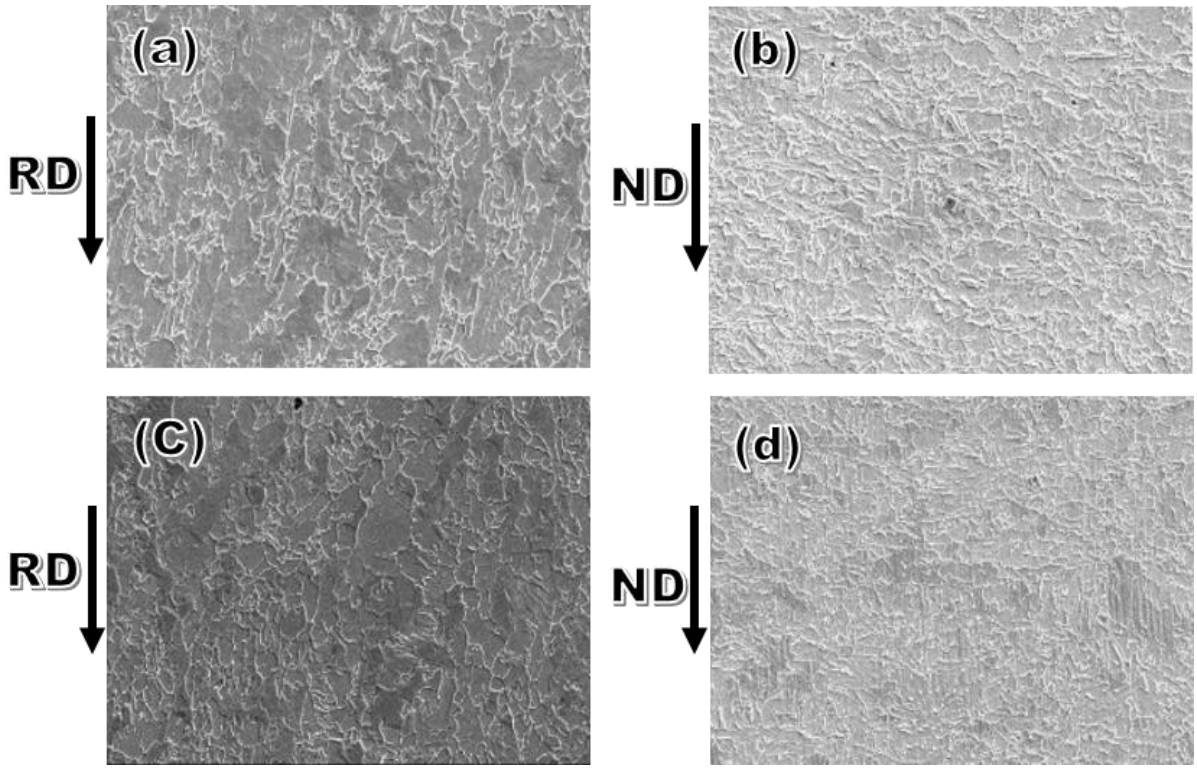

Fig. 7.3 SEM micrograph of specimens at different planes (a) RD – TD for WG (b) ND – TD for WG, (c) RD – TD for WH, and (d) ND – TD for WH (RD: rolling direction, TD: transverse direction, ND: normal direction)

EBSD analyses were performed on pipeline steel specimens at each surface, and mid-thickness RD – TD planes respectively. Despite the non-homogeneous structure of specimens, differences in grain morphology and crystallographic orientation are most significant. Relatively lower grain sizes could be observed at the surfaces of both specimens during microstructure examination might have been related to the pinning effect of secondary phases at grain boundaries. Moreover, the surface region of pipeline steel plate experience extensive shear stresses because of deformation by the rollers. Also, cooling occurs at a faster rate around the surface region in contrast to the mid-thickness. During processing, intense application of pressure at the surface creates more nucleation sites. Subsequently, fast cooling limits the possibility of these sites growing into larger grains. Surface grains do not often undergo full strain recovery. Apart from higher elastic stored energy at the surface, this region also contains harder grains than the mid-thickness. Joodaki *et al*. [434] also observed microstructural variations across the thickness of pipeline steel plates. Nonetheless,

it is less likely that changes in grain size alone will affect HIC susceptibility without contributions from other features.

Phase analysis clearly elucidated the presence of precipitates, which nucleated at different layers of specimens WG and WH. The maps in Fig. 7.4 confirms that the prominent microstructural phase in both pipeline steels is ferrite. In addition, it is noticed that secondary phases of mainly iron carbides and M/A were more in specimen WG, especially at the mid-thickness layer (Fig. 7.4b). Properties of pipelines are often attributed to various form of microstructures, for example ferrite-pearlite, acicular ferrite, and bainitic microstructure [136,435]. The acicular ferrite, granular bainite and quasi-polygonal ferrite microstructure is widely described as having better corrosion resistance [433], especially the acicular ferrite and granular bainite which impart better mechanical properties. In comparison, dual-phase pipeline steel with ferrite and martensite has shown excellent deformability in addition to good strength and toughness [436]. For high grade steels, the formation of M/A constituents depends primarily on the rolling parameters such as finishing rolling temperatures and the extent of holding time for carbon diffusion [295]. The implication is that processing schedule for WG was responsible for higher formation of M/A phase unlike in WH. However, pipeline steel with high presence of martensite are rarely studied. It is believed that martensitic phase will create harder steels and possibly increase the likelihood of cracking. This presumption requires further investigation, as contrary opinions exist in literature [90]. These authors documented improved HIC and sulfide stress corrosion cracking (SSCC) behavior in pipeline steel containing refined microstructure with homogeneously quenched/tempered martensite. In view of these inconsistencies, it is necessary to clearly understand the role of M/A constituents on embrittlement behavior of pipeline steel. That notwithstanding, other microstructural features like texture and grain boundary character also play important roles in crack related failures.

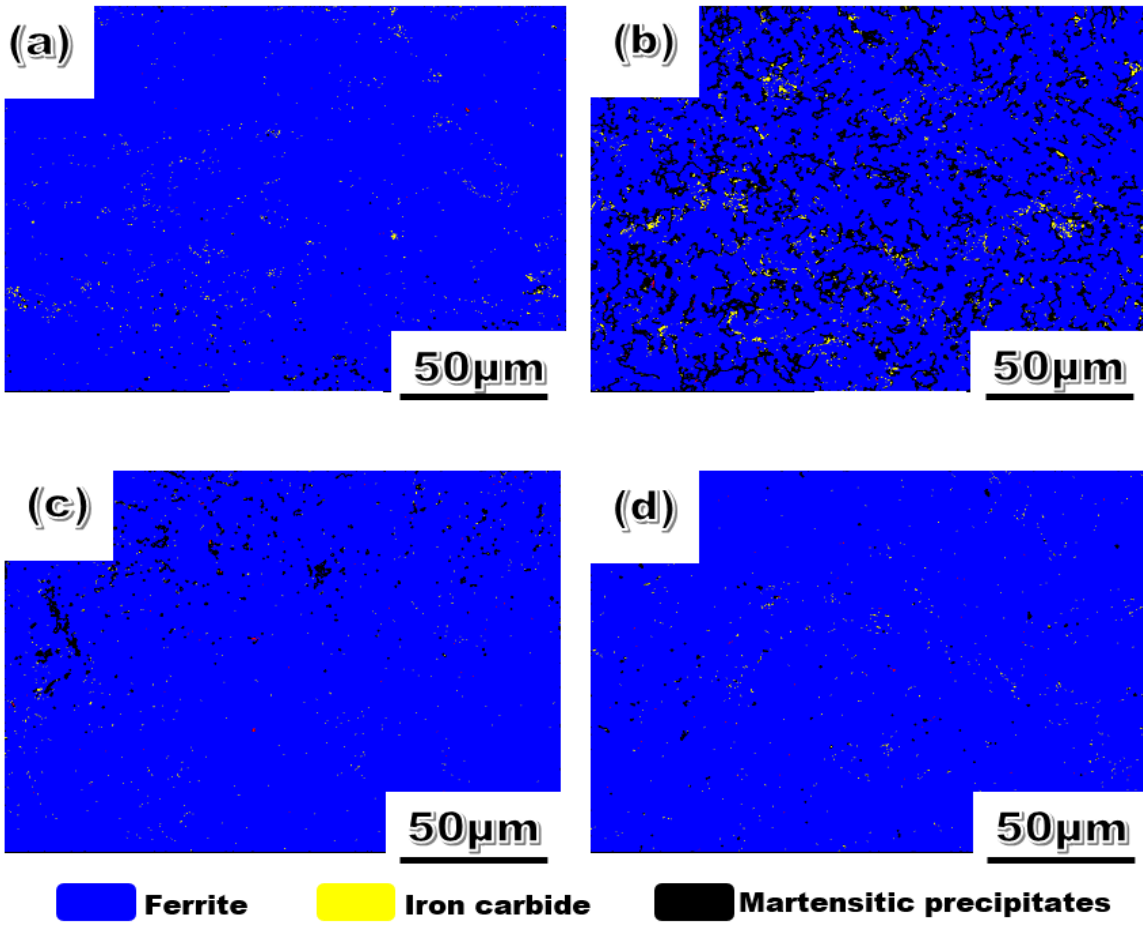

Fig. 7.4 . EBSD phase maps at different layers of specimens (a) WG surface (b) WG mid-thickness (c) WH surface (d) WH mid-thickness

In general, most pipeline steel have randomly oriented grains. According to Raabe [332], the austenite-ferrite transformations that takes place during the hot rolling and cooling processes often produces random textures. So, the following are typical texture fibers that feature prominently in BCC steels; ⟨111⟩||ND (γ fibre), ⟨001⟩||ND (θ fibre), ⟨001⟩||RD (η fibre), ⟨110⟩||RD (α_{bcc} fibre), ⟨011⟩||ND (ζ fibre), and ⟨011⟩||TD (ε fibre). Among these several textures, the gamma fibers which have ⟨111⟩ parallel to normal direction, are believed to be critical for crack arrest [417,437]. Venegas *et al.* [149] already identified {001} planes as the common path for trans-granular cleavage, while the {112}⟨111⟩ and {123}⟨111⟩ texture experience failure by slip. Since {001} planes are prone to cleavage, there is a high possibility that their dominance may cause the alignment of these planes with the fracture surface to cause sudden brittle failure. Nevertheless, the influence all these identified textures in crack susceptibility is not clearly understood.

In the present study, the spread of pole intensity for each specimen shows different orientations to be developed in specimens after processing. The inverse pole figures (IPF) at the surfaces of specimens indicates some increase in intensity at the ⟨111⟩ poles (Figs. 7.5e and g); despite the slight deviation towards ⟨001⟩ pole in WG (Fig. 7.5e), and deviation towards ⟨001⟩ and ⟨011⟩ poles in WH (Fig. 7.5g). At the mid-thickness region, intensities are found deviating towards the ⟨001⟩ pole for both WG (Fig. 7.5f) and WH (Fig. 7.5h). These highlights non-uniformity of microstructure through the two layers of both specimens. Also, Table 7.1 presents the volume fractions of texture components obtained from XRD macro-texture measurements. Considering different textures in the bulk sample, it is obvious that the portion of ⟨111⟩||ND fibres in specimen WG is more than those of specimen WH, especially at the mid-thickness region. On the other hand, evolution of ⟨001⟩||ND fibres, including the cube {001}⟨100⟩ and rotated cube {001}⟨110⟩ texture components featured more in specimen WH in comparison to WG. The {001}⟨110⟩ texture is among the transformation textures known to diminish impact toughness, thereby causing easy crack propagation and delamination [438]. The authors are of the view that such unfavorable {001}⟨110⟩ components are more pronounced in steels that are hot rolled mainly within the recrystallized austenite region; whereas, {112}⟨110⟩, and the {332}⟨113⟩ components are textures from deformed austenite. They also described the later set of textures as beneficial for improved strength, toughness and reduction in anisotropy for X100 pipeline steel. Other fibers such as copper {112}⟨111⟩ and S {123}⟨634⟩ occurred more in specimen WG than WH, except for the Brass {110}⟨112⟩ and Goss {110}⟨001⟩ components that featured more in specimen WH. There is evidence to suggest that more grains in specimen WG are oriented in ways that potentially impede crack propagation; especially because it possesses greater volume fraction of ⟨111⟩||ND compared to WH. This observation is in agreement with already published literatures [159,221]. In another work, [439] it was shown that hot rolling X70 pipeline steel in the recrystallization region promoted the development of $(111)[10\bar{1}]$ and $(112)[\bar{1}\bar{1}1]$ texture components. They claimed that evolution of these components enhanced mechanical properties. They further identified that $(112)[\bar{1}11]$ textures were linked to the predominance of acicular ferrite and polygonal ferrite microstructures, which impacted excellent toughness. The conclusion from their work was that improved mechanical properties in pipeline steel is related to the combined effect of texture and microstructure obtained during hot rolling, coupled with the formation of recrystallized ferrite and dispersed M/A constituents.

Table 7.1 Volume fraction of texture components at different layers of pipeline steel specimens

Texture components	WG surface (%)	WG mid-thickness (%)	WH surface (%)	WH mid-thickness (%)
{**111**}‖ND	9.8	15.2	10.5	12.3
{**110**}‖ND	28.1	14.5	27.3	19.3
{**100**}‖ND	10.7	11.2	11.9	11.3
{**001**}⟨**100**⟩: Cube	3.0	2.1	2.9	2.2
{**001**}⟨**110**⟩: Rotated cube	1.4	2.4	1.9	2.2
{**110**}⟨**112**⟩: Brass	7.7	3.3	6.9	4.3
{**112**}⟨**111**⟩: Copper	6.1	4.2	4.2	4.2
{**123**}⟨**634**⟩: S	12.6	8.2	10.3	8.5
{**110**}⟨**001**⟩: Goss	3.5	1.6	3.4	2.9

Some differences in crystallographic orientation and morphology of grains across the surface and mid-thickness layers of test specimens are presented in Figs. 7.5a-d. The IPF orientation maps shows that grains at the surfaces of both specimens are slightly elongated towards the rolling direction, as was observed during microstructural examination in Figs. 7.2 and 7.3 respectively. In addition, some lathe like bundles of grains were featured at the surface regions of specimens WG and WH. Closer observation indicates stronger appearance of grains with ⟨011⟩||ND and ⟨111⟩||ND orientation at the surfaces of WG (Fig. 7.5a) and WH (Fig. 7.5c). The mid-thickness of both specimens consists of less elongated and more randomly oriented grains compared to the surface. However, ⟨001⟩||ND oriented grains were prominent at the mid-thickness region of the specimens than on their surfaces. Recall that the optical micrographs obtained across the transverse section of specimen WG (Fig. 7.2b) featured lots of dark spot, especially at the grain boundaries; and these features were identified as M/A constituents in Fig. 7.4b. Interestingly, similar observations were made in the mid-thickness orientation map of the same specimen WG (Fig. 7.5a). Besides, the dark spots on IPF map have been correlated to the presence of martensite in the literature [411].

The effect of grain orientation on the susceptibility of steel to cracking has been receiving increasingly more attentions in recent times. Several studies [149,307,429] have demonstrated that controlling HIC in pipeline steel designated for sour service, could be enhanced through crystallographic texture and grain boundary engineering. These authors presented controlled rolling process in the ferritic region (i.e. warm rolling), as a means of developing {111}||ND, {110}||ND and {112}||ND texture fibers. These desired orientations of grains are reported to lower

susceptibility to HIC through the following mechanisms; (1) generating more crack resistant grain boundaries (i.e. LAGB and coincident site lattice boundaries) around {111}||ND oriented grains, (2) lowering the tendency of step-wise crack growth and coalescence, (3) reduce the fraction of cleavage prone {001}||ND textured grains. Their idea is mainly based on the propensity of cracks to propagate preferentially through certain grain orientation. The accumulation of higher lattice strains around {001} crystallographic planes makes them more susceptible to cracking compared to the {111} crystallographic planes [377,440]. Therefore, decreasing the proportion of {001} plane will improve embrittlement resistance of pipeline steel. This emphasizes the need for special TMCP technique to enhance the evolution of predominantly {111} planes parallel to the pipeline steel surface.

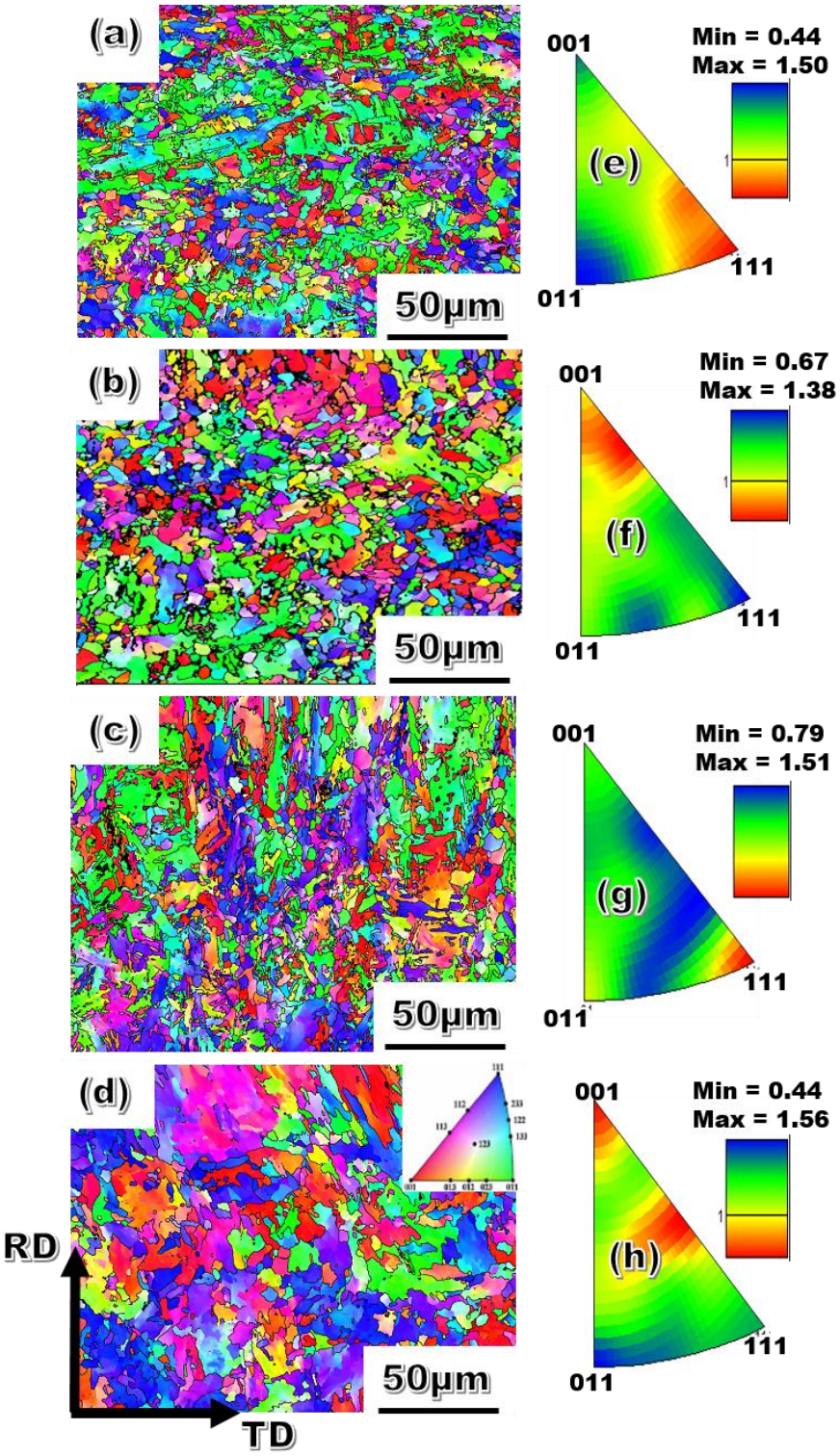

Fig. 7.5 EBSD orientation maps for different layers of specimens (a) WG surface (b) WG mid-thickness (c) WH surface (d) WH mid-thickness, and Inverse pole figures for (e) WG surface (f) WG mid-thickness, (g) WH surface (h) WH mid-thickness

7.4.2 Microstructural evaluation after hydrogen charging

Post-hydrogen charging microstructural examination was necessary to correlate HIC behavior of specimens with features observed in the starting materials. After 12 h of hydrogen charging, no cracking was observed on the ND – TD plane for the specimen WG. Surprisingly, the mid-thickness region of the specimen WG, which featured relatively more segregation, did not experience any cracks as shown in Figs. 7.6a-b. In contrast, specimen WH manifested early onset of cracking. This is evidenced by the crack found along the mid-thickness region of the specimen WH in Fig. 7.6c. The discontinuities observed along the crack propagation path indicate incomplete crack formation after the hydrogen charging. The initial stages of HIC is often characterized by disconnected cracks, and this can be traced back to grain orientation. Scharnweber *et al.* [441] stated that propagation of cracks in steel requires the activation of various slip systems, and the sensitivity of this occurrence to crystallographic orientation of the affected grains cannot be ignored. They also identified stress distribution around crack tip as a factor that determines the direction of crack propagation, as well as the arrangement of slip lines. It suggests that crack disconnection in specimen WG was due to preferential propagation of HIC through the path of least resistance offered by different orientation of grains and their corresponding boundaries. Irrespective of the contributions from grain orientation, the random distribution of grain boundaries with either high or low energy are most likely to cause discontinuity in crack propagation pattern. The reason being that, cracks propagate easily through boundaries with higher energy, but tend to either deflect or arrest at lower energy boundaries [147]. Moreover, there is a chance that cracks in certain areas might have propagated beneath the grain located at regions where disconnection occurred; hence they cannot be seen on the two-dimensional surface being analyzed. Therefore, the apparent discontinuous nature of the cracks could be due to the two-dimensional visualization of a three-dimensional phenomenon, coupled with the crystallographic characteristics of that area.

An inclusion is noted along the path of crack propagation in specimen WH (Fig. 7.6c). From the results presented in Fig. 7.6d, it is evident that the multi-component inclusion particle is comprised of mainly precipitates of (Ti-Nb) N, oxides of Al-Mg-Ca and some traces of Mo-Mn-S. This was not surprising, given that similar inclusion types had already been seen in the starting material (Fig. 7.1). Nevertheless, it is possible that the crack could have initiated at inclusion before

propagating in both directions. The reason being that the crack was noticed to have propagated discontinuously across the mid-thickness of the specimen, even beyond the inclusion. However, one can suggest that the inclusion particle would have offered an easy path for the crack to propagate through. A reasonable explanation for this is the incoherency often associated with interfaces of inclusions and pipeline steel matrix. The voids created at these interfaces can serve as a sink for the accumulation of atomic hydrogen and subsequently lead to the formation of molecular hydrogen and cracking due to pressurization. The interfaces which are incoherent possess higher binding energies compared to both semi-coherent and coherent interfaces [22]. So, incoherent particles are capable of trapping hydrogen irreversibly. Several reports are available on the role of inclusions in promoting HIC in pipeline steel [32,161,165,442]. For instance, increased susceptibility to HIC was attributed to higher fraction of inclusion particles in X120 pipeline steel [443]. The authors identified these particles as Mn-enriched, mixed element and spherical oxide inclusions. Other studies [169,173] already have established the occurrence of oxide rich inclusions, and precipitates of Ti(N,C), and Nb(C,N) in X70 pipeline steel. These inclusions are commonly found in steel and categorized according to their shapes. Oxide type inclusions are generally spherical in shape; whereas, precipitates of Ti, Nb, are cuboidal [444]. They pointed out that MnS inclusions have angular shapes comparable to the cubic shape of TiN. Anyway, the MnS associated with TiN in their study nucleated later to form a shape that seems like a cap on TiN; hence both inclusions coalesced into a more complex one. It is worth mentioning that cubic MnS are not commonly reported. Instead, the MnS particles often occur separately and stretched along the rolling direction in form of stringers.

Pipeline manufacturing involves modification of inclusion shape or morphology to improve coherency. This process is critical in reducing the tendency of either crack initiation or propagation at inclusion sites. According to stress concentration theory, spherical inclusions are less harmful for HIC than other shapes. Mohtadi-Bonab *et al.* [14,114,165] recognized MnS and carbonitride precipitates as the major cause of cracking in X70 pipeline steel. Their conclusion was justified by the incoherency of these particles and the sharp corners of MnS inclusions. They claimed that elongated MnS created areas of stress concentration and increased susceptibility to HIC; whereas spherical oxide inclusions of Al-Ca types are less likely to create crack susceptible zones due to better coherence. On the contrary, other studies on X80 [425] and X100 [164] pipeline steels respectively have documented that crack initiation did not occur at MnS inclusions. Instead, they

found that cracks were mainly related to the Si-Al type inclusions. An interesting work by Peng *et al.* [445] demonstrated that MnS inclusions of sub-micron size are unlikely to promote HIC in X70 pipeline steel. Instead, large amount of these sub-micron inclusion particles aids the dispersion of atomic hydrogen; thereby diminishing the tendency of local agglomeration of hydrogen to cause cracks. Other inclusions of coarse oxides have also been identified as major crack initiation sites in X70 pipeline steel [151,446]. These authors documented groups of oxides including Al-Ca-O or Ca-S as the primary locations for crack nucleation. In the present study, there are evidence to show that HIC propagated through a multi-component inclusion containing carbonitride precipitates, oxides and MnS. Similar findings have been made in a previous work [13]. Although many researchers have different opinions about crack formation at inclusions, a generally accepted view is that lack of coherency between these inclusion particles and pipeline steel matrix create room for accumulation of atomic hydrogen and subsequent HIC [165,425].

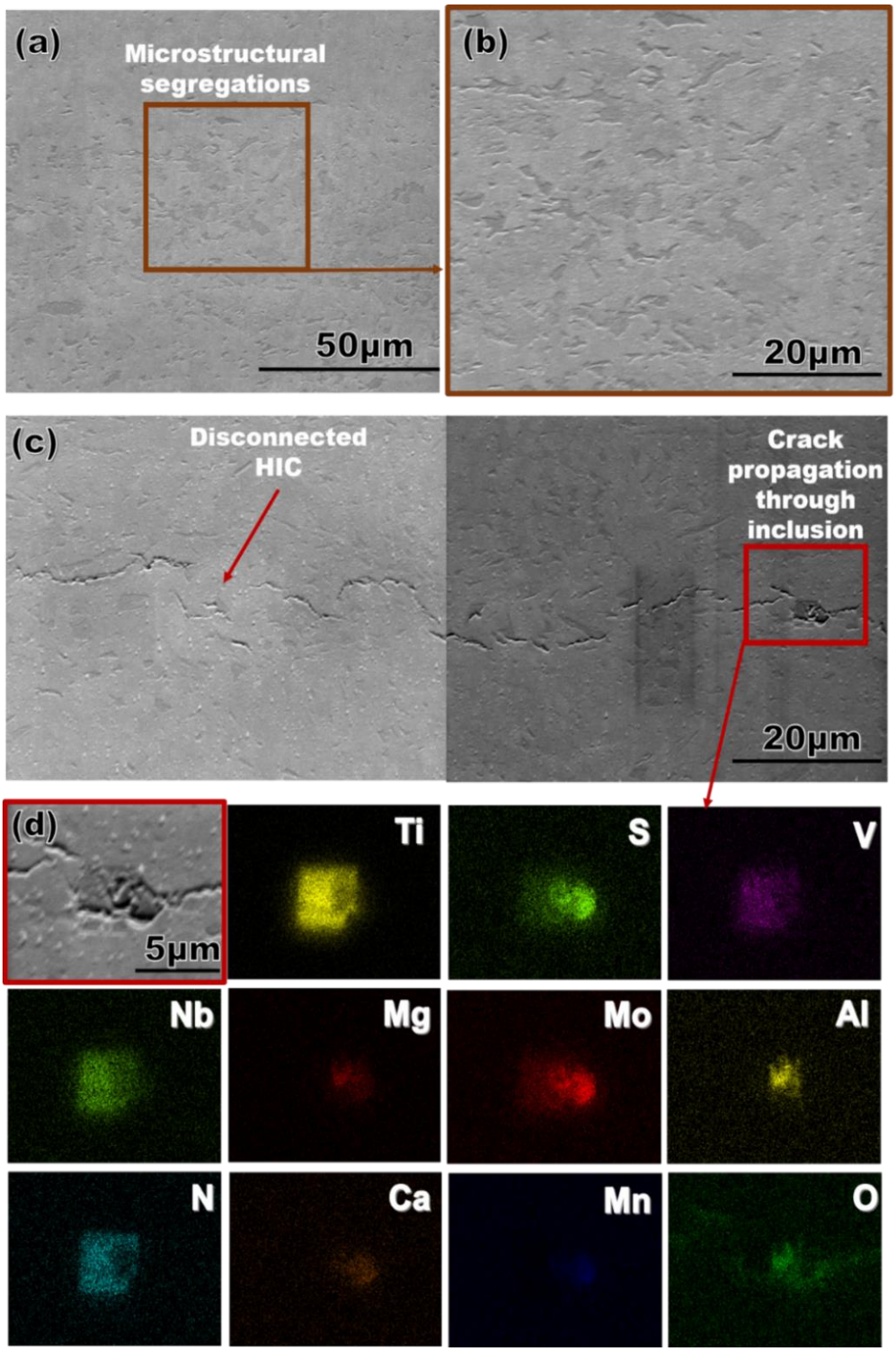

Fig. 7.6 SEM micrographs of mid-thickness ND – TD plane of specimens after 12 h of hydrogen charging (a) WG without crack (b) highlighted region in (a) showing microstructural segregation (c) WH containing disconnected crack which propagated across inclusion (d) EDS maps of inclusion highlighted in (c)

Quantitative evaluation of microstructural features at the mid-thickness cross section (ND – TD plane) was performed using EBSD technique. The orientation maps indicate random texture for both specimens, with slight dominance of ⟨011⟩||RD (greenish colored) oriented grains as shown in Figs. 7.7a and e respectively. Since no cracking was observed in WG, it was of interest to understand the relationship between crystallographic orientation and HIC in WH. Thorough examination of Fig. 7.7e confirmed that crack propagated through grains of different orientations, which demonstrates that HIC did not show orientation dependence. The grains located around the crack consist of ⟨111⟩||RD (blueish colored), ⟨001⟩||RD (reddish colored) and ⟨011⟩||RD (greenish colored) orientation. The implication is that other conditions might have contributed to the early onset of cracking in specimen WH.

Looking at the recrystallization area fraction maps, one can see more banded-deformed grains along the cracked region in WH (Fig. 7.7f) unlike WG (Fig. 7.7b). Variations in microstructure can be explained in terms of amount of recrystallized, recovered and deformed grains that may be present in steel. Moreover, these features are critical for HIC susceptibility of pipeline steel. It is striking in Fig. 7.8 that the area fraction of recrystallized and recovered grains in WG is higher than that of WH, whereas more deformed grains are present in specimen WH. This can be related to the lower finish rolling temperature range deployed on specimen WH, and the subsequent transformation from these heavily pancaked regions. Meanwhile, the phases identified in these specimens during this study are mainly recrystallized ferrite (acicular and polygonal ferrite), which agrees with those reported in the literature [139]. Also, the presence of some ⟨111⟩||ND oriented grains at the surfaces of both test specimens highlights the effect of recrystallization. A different study attributed the dominance of ⟨111⟩||ND fiber texture to recrystallization and subsequent nucleation of strain free grains [434]. Higher fraction of recovered and recrystallized grains manifested itself in specimen WG, in comparison to WH where higher fraction of deformed grains and less of the recovered and recrystallized grains are present. This can as well explain the reason for greater KAM of 0.65° determined from WH, in contrast to 0.48° obtained from WG. The KAM values indirectly show that the specimen WH has higher elastic stored energy for crack propagation because of the increased level of misorientation within its grains compared to the specimen WG. Therefore, a lower number of defects are present within the structure of the specimen WG. Although the stored energy of deformation is lower in the recrystallized and recovered regions,

there is high possibility that cracks could trace their propagation path through regions containing relatively higher fraction of deformed grains like in the case of WH. The result presented in Fig. 7.7f evidently shows that all the grains aligned on the cracked region are deformed. This justifies that deformed grains are more likely to have priority over the recrystallized or recovered ones during HIC propagation.

Considering the phase maps for both specimens, WG is characterized by a lot of unindexed spots (black regions) amidst ferrite (blue regions) and sparse distribution of iron carbide in Fig. 7.7c. These dark spots have earlier been identified in the starting WG material as the martensite phases (Figs. 7.3b, Fig. 7.4b and Fig. 7.5b). However, the specimen WH featured significant amount of iron carbides (yellow regions) along the crack path (Fig 7.7g). Apparently, the high carbon content of M/A constituents in WG prevented the precipitation of such high amount of carbides, in contrast to WH.

Grain boundaries are categorized based on the degree of misorientation between grains. The iron carbide dominated regions in the phase map of WH (Fig. 7.7g) corresponds to the grains with remarkable fraction of HAGB (bunch of red lines) in Fig. 7.7h. One can see a clear relationship between the deformed regions around crack, iron carbide prevalent regions and cluster of HAGB in WH. These features are quite typical of a crack prone structure. Similarly, grain boundary distribution analysis presented in Fig. 7.9 indicate that specimen WH has higher fraction of CSL, LAGB and HAGB than the specimen WG. This implies that grains are more and smaller in WH than in WG. It is reasonable to say that minimal dynamic recovery in WH warranted the increased nucleation of grains and the high KAM values measured. The LAGB and CSL are lower energy boundaries, whereas HAGB possess higher stored energy. There are suggestions that LAGB create good alignment between grains, and impede crack propagation, while HAGB are capable of promoting crack propagation [150]. Also, LAGB are related to formation of sub-grains through interactions of dislocations; thus eliminating pile-ups of dislocations at these boundaries [447]. Although the absence of dislocations reduces boundary strength, it lowers the risks of crack related failures. So, the likelihood of HIC in pipeline steel containing predominantly LAGB is less in comparison to cases where HAGB are more.

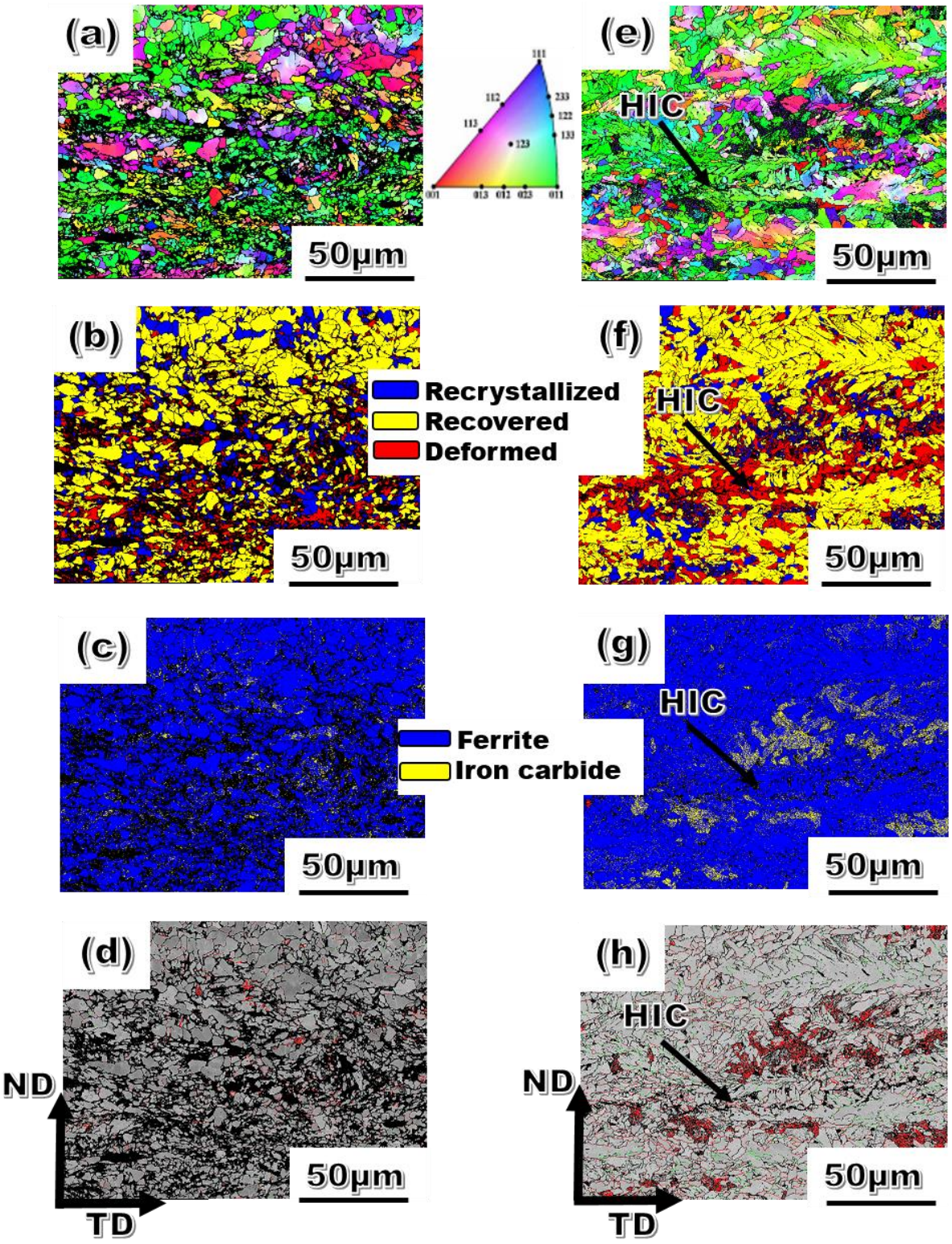

Fig. 7.7 Post-hydrogen charging EBSD images for specimen WG (a) orientation map (b) recrystallization area fraction map (c) phase map (d) grain boundary map, and specimen WH (e) orientation map (f) recrystallization fraction map (g) phase map (h) grain boundary map

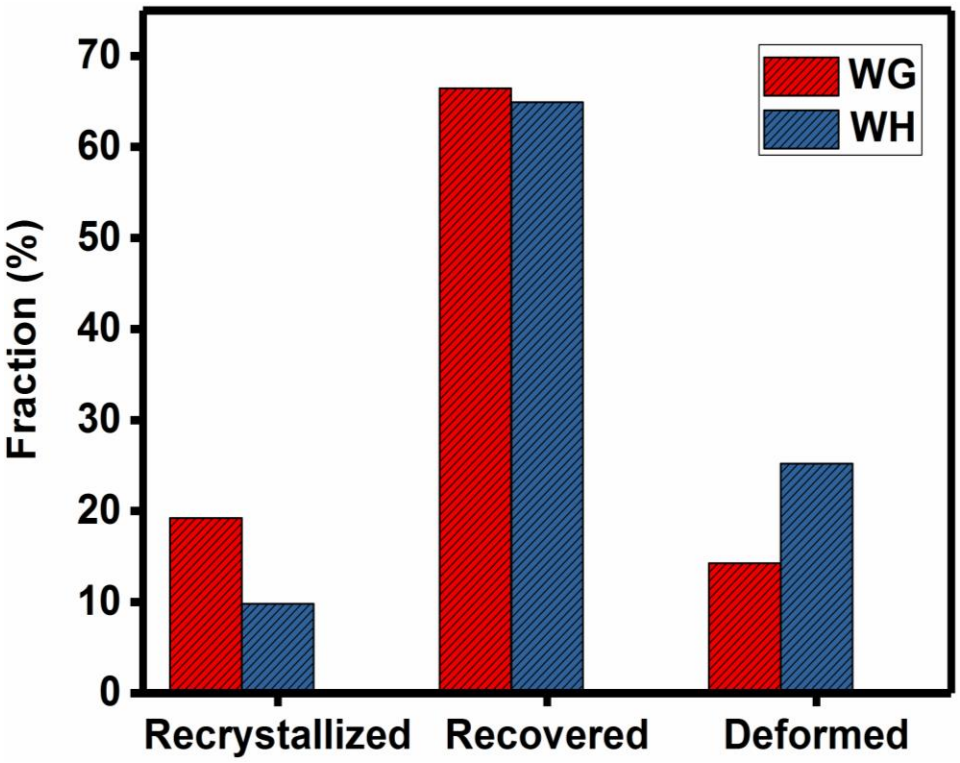

Fig. 7.8 Area fraction of recrystallized, recovered and deformed grains in specimens WG and WH

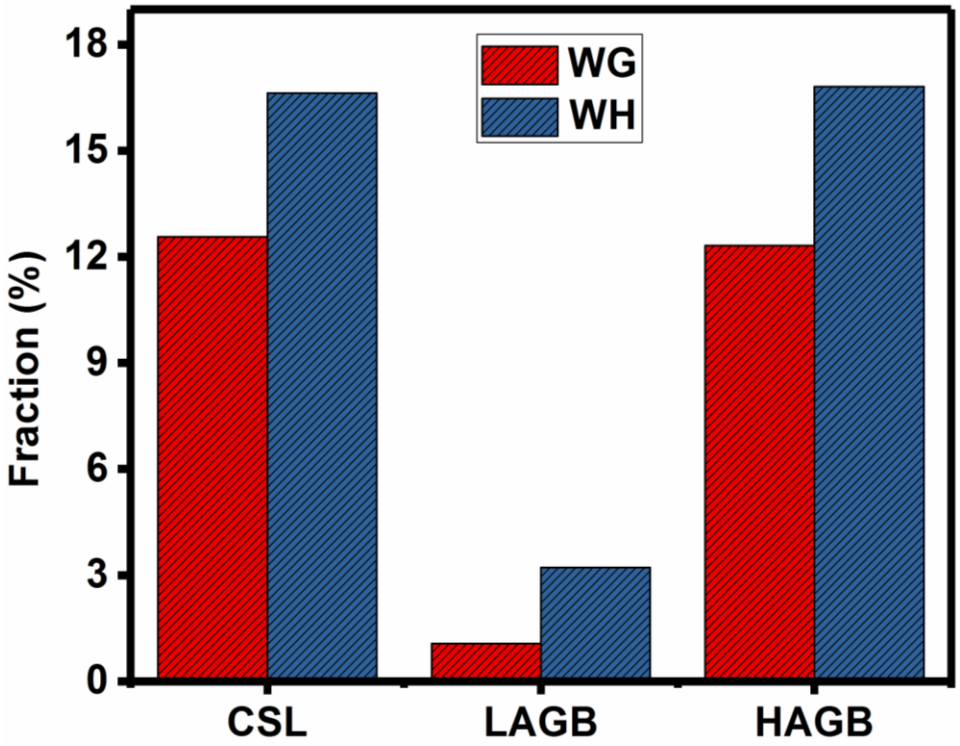

Fig. 7.9 Grain boundary distribution in specimens WG and WH

7.4.3 Effect of mechanical properties and hydrogen trapping on HIC susceptibility

Straining specimens under tensile load will ultimately lead to fracture. As shown in Table 7.2, mechanical properties of test specimens are better when tested without hydrogen charging than after hydrogen charging. Also, the graphs in Fig. 7.10 and Fig. 7.11 shows the engineering stress-engineering strain plots of each sample tested with and without in-situ hydrogen charging respectively. It was interesting to observe that all specimens failed within the elastic region during test with in-situ hydrogen charging; unlike those tested without hydrogen charging that experienced both elastic and plastic deformation. This behaviour is in agreement with other reports that are available in literature [448,449]. As for the specimens tested with hydrogen charging, tensile strength is considered as the failure stress. The results obtained from tensile testing indicate that absence of hydrogen charging allowed specimens to undergo appreciable levels of ductility and strain hardening before failure. This clearly shows that hydrogen eliminated the capability of both test specimens to deform plastically. Considering the lower values for tensile strength and yield strength in specimen WG relative to WH, it can be said that mechanical properties of WG is poorer. However, both pipeline steel specimens possess the required mechanical properties to warrant their classification as API 5L X70 grade [36]. Interestingly, prominent discontinuous yielding was observed in specimen WG (Fig. 7.10). This phenomenon manifested in form of Luders bands in WG (both on surface and mid-thickness specimens). Johnson *et al*. [450] described Luder band formation in steels as a consequence of intense multiplication of dislocation immediately after yielding. In their study, they recorded substantial Luders straining in materials with tempered martensitic structure, while those with mainly upper bainite or ferrite-pearlite microstructure experienced the lower amount of Luders strain. Another study related large instability (luder-like behaviour) associated with tensile deformation of dual-phase (austenite and delta ferrite) steel to strain-induced transformation of austenite into martensite [451]. From the microstructural studies on specimens WG and WH, it is visible that higher amount of martensite was formed in WG. This explains the stronger display of Luders bands in specimen WG compared to WH.

Moreover, reduction in failure stress shows the increasing role of diffusible hydrogen through steel specimens [452]. It is obvious that lower failure strength values obtained with hydrogen charging indicate ductility loss due to embrittlement in test specimens. Nonetheless, hydrogen related

reduction in ductility occurred more at the surface than the mid-thickness. Remember that grains at the surface were observed to be smaller and highly deformed. Therefore, the surface region with higher strength, stored energy and dislocation density becomes easily embrittled compared to the mid-thickness area where strain free grains are dominant. Strength is an indication of HE susceptibility, as steels with relatively high strength are believed to have poorer resistance to embrittlement than the ones with lower strength [162]. However, a good combination of strength and ductility gives rise to excellent toughness and improved resistance to hydrogen damage. Although specimen WG is not as strong as WH, it can be seen to have better ductility, especially at the mid-thickness region (Table 7.2). This may be another justification for the delayed onset of HIC at the mid-thickness of WG.

The migration of hydrogen atoms in steel depends on the kind of traps that are present. Based on the binding energies of different hydrogen traps, they are classified as either reversible or irreversible [10]. The reversible traps possess lower binding energies; as such, they are not considered as permanent traps (e.g. dislocations, micro voids, grain boundaries). Irreversible traps are characterised by high binding energy, which makes them more efficient at trapping hydrogen atoms (e.g. precipitates and interfaces). The typical binding energies for reversible traps are below 60 kJ/mol, above which traps are regarded as irreversible [22]. The same authors recorded the following range of energies for different precipitates often found in steel; TiC: 53-94.5 kJ/mol, and incoherent MnS: 70-90 kJ/Mol. They also documented binding energy for grain boundaries to be within 8.8-58.9 kJ/mol, while energy for dislocations were determined to be slightly higher in the range of 10-60 kJ/mol. In more specific terms, release of hydrogen from dislocations and grain boundaries contained in pure iron was found to occur at activation energies of 26.8 kJ/mol and 17.2 kJ/mol respectively [453]. Considering the differences in binding energies, hydrogen interactions and consequent embrittlement is expected to be more in steel with relatively high dislocation density and incoherent precipitates. According to Lee *et al*. [454], hydrogen related degradation of pipeline steel is affected by hydrogen trapping behaviour and the presence of brittle microstructures. The trap binding energy of retained austenite in steel is in the range of 47-52 KJ/mol, which makes them favourable sites for reversible infusion of hydrogen atoms [455]. Moreover, grain boundaries may either serve as reversible traps or enhance the mobility of hydrogen atoms inside the steel structure. Therefore, an optimum grain size is necessary to achieve good hydrogen diffusion behaviour without increasing the risks of HIC. Based on these results,

higher presence of M/A constituents in the structure of WG will tend to supply more trap sites for hydrogen atoms, especially at the mid-thickness region. Consequently, trapping of hydrogen could have resulted in weakening of bonds and failure at lower stress due to pressurization. Yet, effective trapping of hydrogen within M/A islands in WG will deprive other microstructural features of the much-needed hydrogen to cause cracking; thus, delaying the onset of HIC without the application of tensile loading. This view has already been reported by Bhadeshia [109], who claimed that high presence of irreversible trap sites reduces HE. The author believes that the amount of diffusible hydrogen atoms within the steel lattice is reduced by recombination of atomic hydrogen inside these traps. Even though the increased population of M/A constituents and their high binding energy could be enough to prevent mobility of hydrogen atoms to regions where they activate embrittlement, this study does not show any evidence of hydrogen recombination. However, hydrogen charging was continuous on each test specimen until failure occurred. Our understanding is that despite some similarities in the orientation of grain, other microstructural features influenced hydrogen trapping and embrittlement pattern of both test specimens.

Table 7.2 Tensile properties of X70 pipeline steel specimens tested with and without hydrogen charging

Specimens	Tensile strength (MPa)	Yield strength (MPa)	Elongation (%)	Time to failure (hr)
Without hydrogen charging				
WG surface	703	618	21	77
WH surface	750	665	22	80
With hydrogen charging				
WG surface	429*	-	-	14
WH surface	457*	-	-	15
Without hydrogen charging				
WG mid-thickness	682	596	24	83
WH mid-thickness	740	655	23	80
With hydrogen charging				
WG mid-thickness	511*	-	-	13
WH mid-thickness	551*	-	-	15

* Failure stress under uniaxial tensile loading with in-situ hydrogen charging

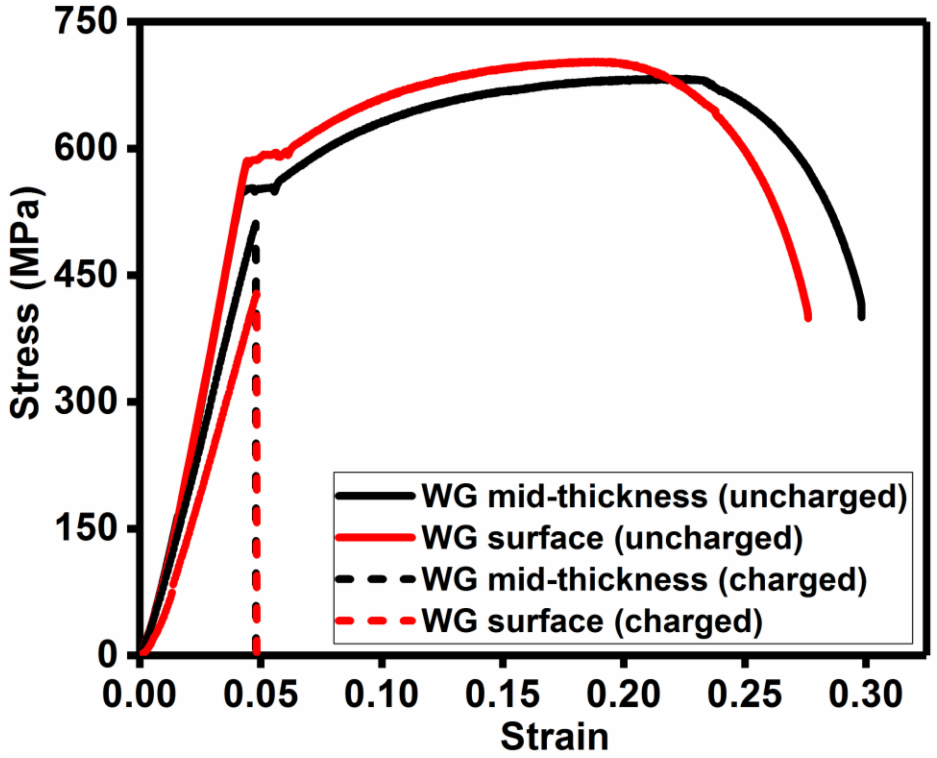

Fig. 7.10 Mechanical response of specimen WG with and without hydrogen charging

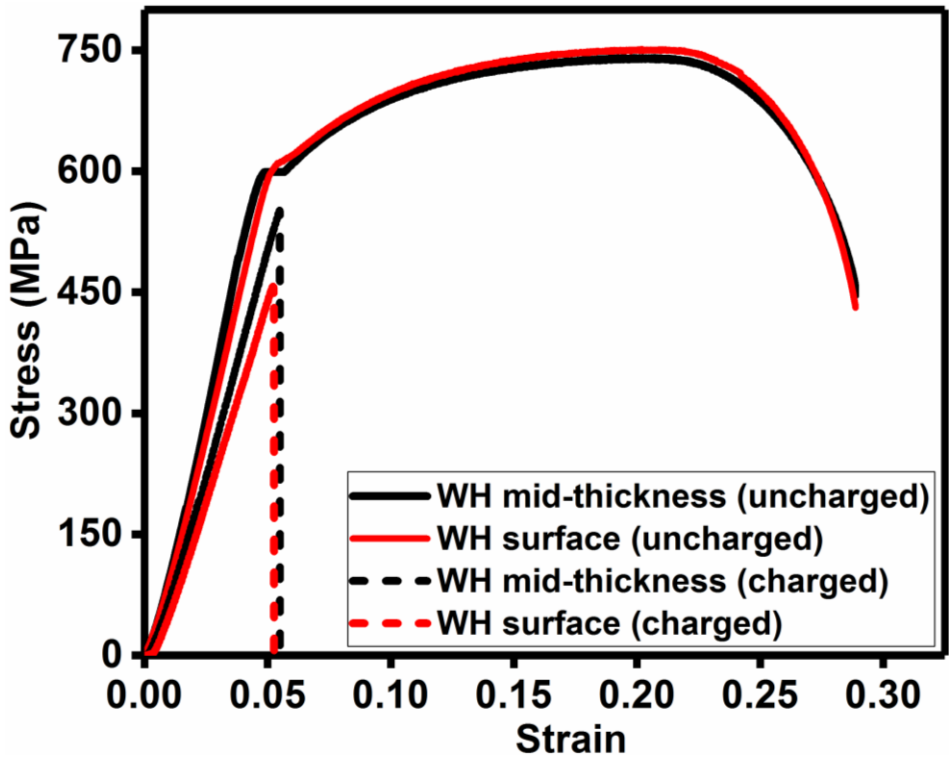

Fig. 7.11 Mechanical response of specimen WH with and without hydrogen charging

7.4.4 Fractography

The fracture surfaces of both specimens after tensile testing with and without hydrogen charging are presented in Fig. 7.12 and 7.13. All specimens tested without hydrogen charging showed the classical ductile fracture surface morphology. This is shown by the characteristic dimpled morphology seen both at the surface and mid-thickness layers of WG (Figs. 7.12b and d) and WH (Figs. 7.13b and d) respectively after testing without hydrogen charging. Dimples occurred more at the center of the fractured surfaces due to micro void coalescence under ductile overload.

For tests conducted under hydrogen charging conditions, the fracture surfaces showed cleavage failure mode. This is quite typical in the case of HE of steel [452]. In this study, simultaneous application of tensile stress and electrochemical hydrogen charging allowed entry of hydrogen into the steel structure at an accelerated rate. The fractured surfaces of both pipeline steel specimens tested with hydrogen charging are presented in Fig. 7.12a and c for WG; then, Fig. 7.13a and c for WH. All surfaces can be seen bearing flat cleavage morphology, which is very consistent with embrittlement [456]. The prominent crack noticed in the mid-thickness of specimen WH corroborates the early onset of the crack observed in the same specimen when tested without tensile loading in Fig 7.6c. This offers clear evidence of increased susceptibility to hydrogen related damage in specimen WH.

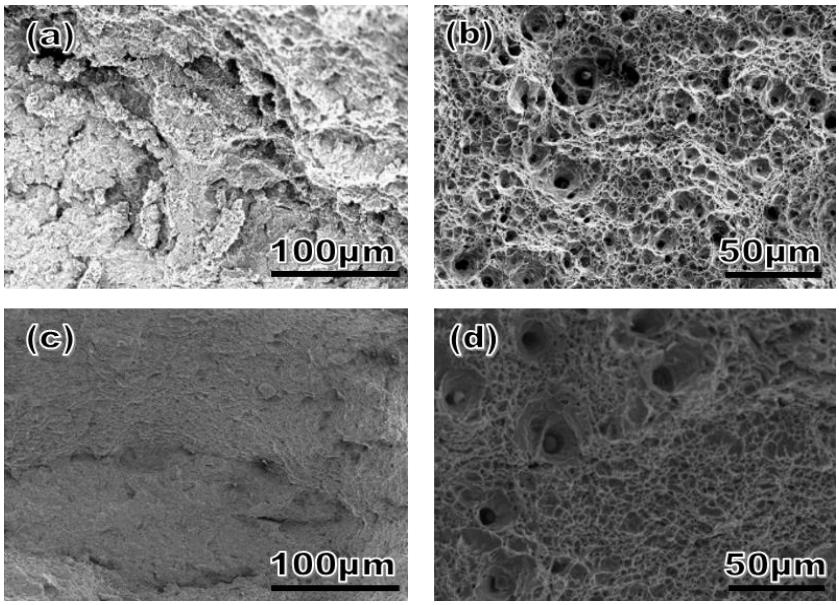

Fig. 7.12 SEM fracture surface morphology of specimen WG with hydrogen charging (a, c), without hydrogen charging (b, d)

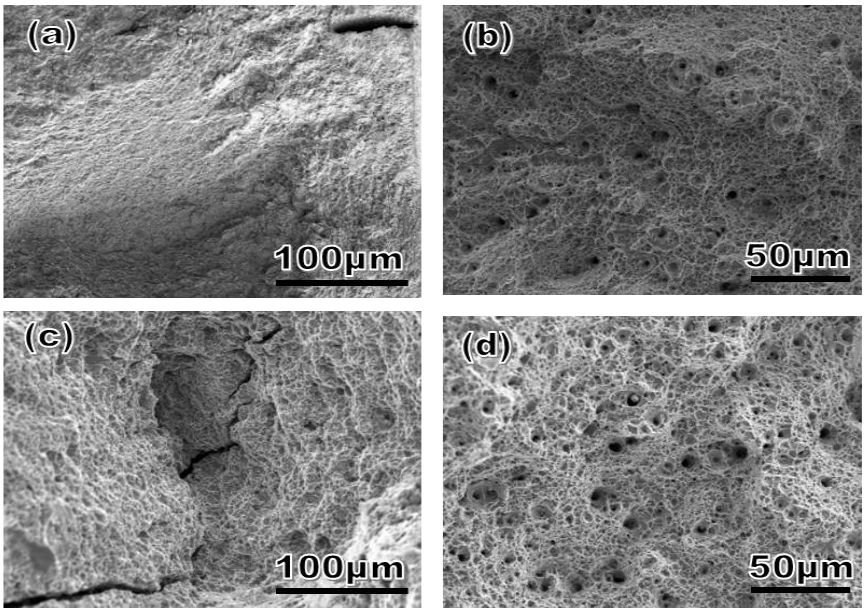

Fig. 7.13 SEM fracture surface morphology of specimen WH with hydrogen charging (a, c), without hydrogen charging (b, d)

7.5 Summary

The role of crystallographic texture, grain size and other microstructural parameters in HIC susceptibility of API X70 pipeline steel was investigated after two different TMCP trials: (a) WG – a higher finishing temperature in the range of 880 – 820°C and a stop cooling temperature at 615°C and (b) WH – a lower finishing at 830 – 760°C and a stop cooling at 565°C. Experimental investigations were carried out by subjecting pipeline steel specimens to electrochemical hydrogen charging with and without the application of tensile loading. The following are important findings made from this study:

1. Early onset of HIC was manifested as disconnected cracks in specimen WH after 12 h of hydrogen charging. Cracks were initiated and propagated through deformed-banded region along the mid-thickness of WH, and was noticed to link with multi-component inclusion particle comprising of (Ti-Nb) N precipitates, Al-Mg-Ca oxide and traces of Mo-Mn-S.
2. More deformed grains with higher KAM were observed in WH specimen; whereas the structure of WG was dominated by higher fraction of recrystallized and recovered grains. Although crystallographic orientation of grains was similar in both specimens, crack propagation at the mid-thickness of specimen WH did not show any orientation

dependence. However, the crack propagation path in WH was mainly along the deformed grains.

3. Comparative examination of tensile properties of pipeline steel specimens at surface and mid-thickness layers showed that WH had higher strength compared to WG. Also, the surface region of each specimen had higher strength compared to their mid-thickness region. However, the specimen WG showed significantly higher ductility at the mid-thickness in comparison to the specimen WH. Failure due to hydrogen attack occurred at a lower stress for specimens obtained from the surface compared to those from the mid-thickness. This is because the surface region experienced more intense deformation and nucleated more small sized grains at elevated processing temperature, and it was cooled rapidly ahead of the mid-thickness region.
4. The increased fraction of M/A constituents in WG was due to a higher stop cooling temperature and austenite decomposition. Also, more recovered microstructure was developed in WG as a result of higher finishing temperature applied during its processing compared to WH. These are considered the main factors for the superior resistance of WG steel to HIC. No tangible differences in terms of texture were noticed due to the different processing routes of WG and WH.

CHAPTER 8 : EFFECT OF POST-PROCESSING ANNEALING TREATMENTS ON MICROSTRUCTURE DEVELOPMENT AND HYDROGEN EMBRITTLEMENT IN API 5L X70 PIPELINE STEEL[7]

8.1 Overview

This chapter addresses the third objective, as identified earlier in this thesis. In order to recommend steel with an improved structure, it was necessary to investigate the specimens with an enhanced resistance to general corrosion and specifically HIC under different heat treatment scenarios. The specimen WG displayed superior resistance to hydrogen embrittlement and was chosen for this study. It was necessary to evaluate the mechanical properties and hydrogen embrittlement behavior of newly developed WG specimen after subjecting it to post-processing annealing treatments.

The mechanical properties of steels are strongly influenced by microstructure and texture developed during thermomechanical processing. Here, different annealing treatments have been performed on pipeline steel at inter-critical temperatures. The aim of this study is to relate hydrogen embrittlement behavior to the microstructural characteristics obtained through one-step, and two-step annealing treatments. Similar grains orientation distributions were observed after the initial hot rolling and the two-step annealing procedures. However, in the later process a dual-phase (i.e. ferrite-martensite) structure was formed; unlike in the starting material where only segregated patches of martensite were observed inside a ferritic microstructure. The one-step treated steel was comprised of relatively large and primarily ferrite grains. As a result, the preliminary processing revealed the highest strength, with reduced ductility. The one-step treatment lowered strength, and ductility. Although the two-step treated steel showed the lowest strength, it was the most ductile with improved resistance to hydrogen embrittlement. The tempering operation introduced in the two-step process created minimal strain and tempered

[7] The results in this chapter are already published, but was used with permission from *Elsevier (*Appendix H): E. Ohaeri, J. Omale, K. M Mostafijur Rahman, J. Szpunar, 'Development of microstructure for improved resistance to hydrogen embrittlement in API 5L X70 pipeline steel', *Materials Characterization*, 2020, Vol. 161, 110124

The PhD candidate E. Ohaeri designed all experiments, characterised microstructure, texture, and examined all of the fracture surface morphology of failed specimens, compiled the report, as well as finalised the manuscript after revision by supervisor and peer-reviewers.

martensite within the steel. This reduced the tendency for hydrogen damage. A direct relationship was established between high tensile strength and increased embrittlement risks. Lowering the strength and hardness through double heat treatment cycles delayed the onset of cracking after pre-hydrogen charging.

8.2 Background

The presence of hydrogen adversely affects the tensile properties of steels. This constitutes a great challenge for the development and installation of pipeline infrastructures. Critical service conditions often result in disastrous failures and have made safety the utmost concern of pipeline operators. Hydrogen facilitate the embrittlement of steel in the form of sulfide stress corrosion cracking (SSCC) [39,64,88,95], stress-oriented hydrogen induced cracking (SOHIC) [97,98], and/or hydrogen induced cracking (HIC) [5]. Current studies are aimed at improving crack resistance in steel by changing elemental composition, controlling microstructures, and texture evolution [89,90]. These measures are targeted at creating steels that are best suited for a wide range of engineering applications. However, a more contemporary technique for pipeline steel production is the thermomechanical processing (TMCP). This process is beneficial in terms of managing the microstructural and mechanical properties of steel. For instance, the homogenization operation performed during TMCP minimizes the segregation of secondary phases and precipitates. Other activities such as desulfurization and inclusion shape control helps to minimize cracking [138]. Previous studies have indicated that a strong presence of {111}||ND grains can lower the risks of corrosion [152,153] and crack related damages [12,114,221,281] in steel. Mohtadi-Bonab *et al.* [417] have shown that cold rolling and annealing treatments conducted on X60 pipeline steel results in a highly deformed structure with increased dislocation density. They noticed a transformation of the weak {110}||ND into {111}||ND and {100}||ND texture fibers afterwards. Their conclusion was that an increase in the fraction of {100}||ND was detrimental to HIC resistance. Similar patterns of texture evolution have also been reported for equiaxed grain structured X70 pipeline steel [457]. Therefore, it is believed that high intensity of {111} grains oriented parallel to the rolling plane can significantly improve the quality of steel. Particularly, such alignment of grains can obstruct crack propagation and lower the tendency for sudden failure. Even though most steel producers adopt TMCP, more is yet to be known in this field. The main problem is how to develop steels that are highly textured with {111} planes directly from the hot

rolling process. Also, what guarantees that such preferred grain orientation can be retained after heat treating rolled plates? These are necessary concerns when thinking about joining steels. Pipeline material should be designed to tolerate highly localized heating from the welding process without undergoing drastic change in properties. It is still unclear how the initial steel structure developed after hot rolling will transform during subsequent hot forming procedures. These activities could potentially affect the final microstructure of pipelines, as well as their hydrogen embrittlement (HE) characteristics. Most pipes are made by pressing a rolled steel plate into a cylindrical shape through the U-ing and O-ing processes. Thereafter, their seams are bonded together by a longitudinal weld. The fabrication and installation stage involve connecting each pipe to the others using a continuous end-to-end welding operation. The implication is that unforeseen variations in microstructure may appear in the fully formed pipes. As such, thermal treatment processes may be deployed to simulate the welded regions in steels. This process can be achieved by heating steel and holding it for a given time at that temperature before cooling to ambient temperature. Other reasons for heat treating steel are stress relief, softening, and enhancement of mechanical properties. Furthermore, annealing at different conditions can affect HE behavior in steel by impeding hydrogen diffusion [458]. The authors found that effective trapping limits the mobility of hydrogen within the microstructure and diminishes the chances of hydrogen assisted failure. They identified the following features as potential trap sites for hydrogen in steel (a) Non-recrystallized grains containing mechanically induced twins, (b) Small recrystallized grains, and (c) Dislocations. However, recent reviews [8,108] have suggested that other factors such as grain boundaries, crystallographic texture, inclusions, and precipitates (e.g. Ti, V, Cr, Mo-Carbide) also contribute in slowing down the diffusion of hydrogen inside the steel. According to Nagao *et al.* [459], precipitates of (Ti, Mo) Carbide increase the risk of HE in steel. They identified nano-sized precipitates as being responsible for promoting hydrogen enhanced plastic failure, because of their trapping characteristics.

Presently, there are a variety of high strength pipeline steel grades available for use in the industry. Based on the important contribution of microstructure towards pipeline integrity certain phases have been identified as superior in terms of improving mechanical properties. Xiao *et al.* [460] used some carefully designed TMCP parameters to achieve the nucleation and growth of acicular ferrite grains. They found that excellent strength and toughness was achieved from microstructure

refinement during processing. In a separate study [17], the HIC characteristics of a typical X80 pipeline steel with ferritic/bainite microstructure was compared with that of an X100 grade having purely bainitic microstructure. It was observed that the bainitic microstructure showed relatively higher vulnerability to HIC. This is because bainite provides more sites for hydrogen accumulation compared to ferrite. Eventually, the prolonged accumulation of hydrogen around the banitic lath boundaries would result in interfacial decohesion. However, these identified microstructures are not the only cause of low yield ratio (i.e. high deformability) in steel. The presence of other phases or precipitates within the microstructure is also important [461]. Another approach is to create a dual-phase structured pipeline steel comprising of relatively uniform dispersion of martensite constituents within the ferrite matrix. Previously [436], enhanced mechanical response was observed in dual phase steel. This was mainly in terms of improved deformability. Moreover, quenched and tempered steel are constituted by microstructural phases (e.g. carbides, martensite and retained austenite) and interfaces which influence their hydrogen permeation behavior [462,463]. There are valid concerns about the ability of pipelines to retain important properties throughout service life. It may be argued that the construction and operating processes could warrant loss of critical attributes in pipelines, due to phase transformation. Therefore, finding out ways of maintaining the steel structure, and/or complement its essential qualities should be of paramount importance. The overall aim of the current study is to explore the influence of post-processing heat treatments on mechanical properties, microstructure and texture evolution in hot rolled pipeline steel. These characteristics are controlled with the view of improving deformability and resistance to HE.

8.3 Experimental procedure

Refer to sections 3.2, 3.3.1 – 3.3.4, and 3.3.9 for details about pipeline steel material/annealing treatments, microstructural evaluation techniques, and mechanical testing conditions for pre-hydrogen charged and uncharged specimens.

8.4 Result and discussions

8.5 Microstructural characteristics

The microstructural transformations across both RD – TD and ND – TD planes after thermal treatments are shown in Figs. 8.1-8.2. The initial structure of TMCP pipeline steel is characterized

by mainly polygonal, acicular, and bainitic ferrite as indicated in Figs. 8.1a, d and 8.2a, d. Other authors [166] have also identified varying fractions of polygonal and acicular ferrite in X70 pipeline steel. After the one-step annealing treatment, dominant presence of relatively larger grains having the polygonal ferrite morphology are seen in Figs. 8.1b, e and 8.2b, e. Also, small whitish particles of cementite are seen nucleated at some grain boundaries in the one-step treated specimen (Fig. 8.1e). However, the micrograph for the two-step annealed steel in Figs. 8.1c, f, and 8.2c, f displayed seemingly duplex microstructure consisting of a distribution of martensite constituents within the ferrite matrix. This observation is most prominent across the ND – TD plane in Fig. 8.2c, f, where martensite particles are seen along almost every grain interface. The high magnification micrograph displayed as inset in Fig. 8.2f clearly shows bulges surrounding flat ferrite grains. Those protruding particles are martensite at the interphases between grains. Such martensite nucleation patterns can be described as a web-like grid covering the entire steel structure. The uniqueness of the two-step annealing treatment lies in the inter-connection of these martensite components. These features are quite typical of a dual-phase (i.e. ferrite-martensite) steel. Moreover, the martensitic phase is responsible for restricting the growth of ferrite grains; thus, developing a refined microstructure. Another investigation by Asrafi *et al.* [270] found the evolution of similar microstructure in low manganese carbon steel after cold rolling and annealing processes.

A uniform spread of one phase in another can significantly diminish the tendency of inhomogeneity within the microstructure. The formation of ferrite-martensite structure after the two-step process is connected to the initial annealing at a slightly elevated inter-critical temperature of 780 ℃. This would have ultimately led to an extensive nucleation of austenite grains within the ferrite phase. There is a very high possibility that most of the austenite will be retained after the initial quenching cycle, leading to further transformation into martensite by subsequent quenching. During the second stage of annealing at a lower inter-critical temperature of 720 ℃, ferrite grains are formed inside the steel structure. Given that the second step in the annealing process is shorter (15 mins), enough time will not be available for the newly formed grains to grow like the one-step case where annealing was performed for a longer duration (1 h). Therefore, the consequence is the formation of small ferrite grains that are encircled in a mesh of tempered martensite. It is obvious that the treatment conditions adopted in the two-step annealing

operation warranted the creation of a dual phase structure comprising of mainly refined ferrite grains and martensite constituents. To better understand the steel microstructure, an extensive EBSD analysis was performed, and the results are displayed in the following section.

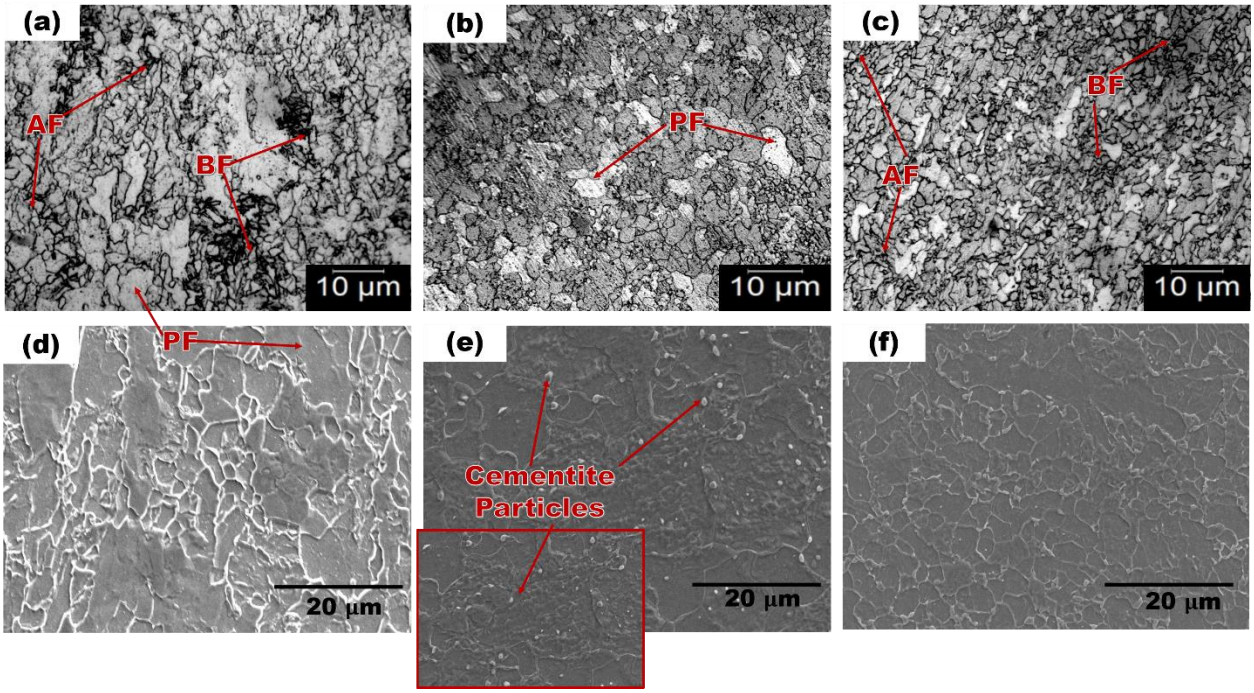

Fig. 8.1 Optical and SEM micrographs for RD – TD plane of pipeline steel after (a, d) initial thermomechanical processing, (b, e) one-step annealing treatment, and (c, f) two-step annealing treatment

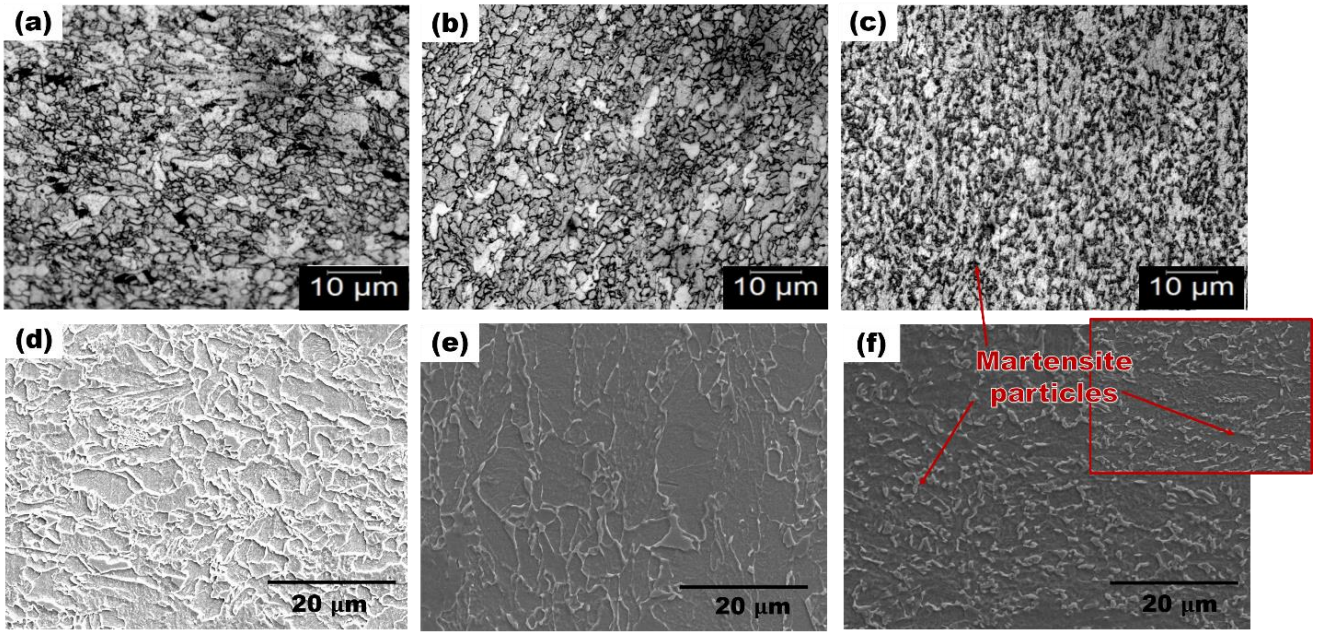

Fig. 8.2 Optical and SEM micrographs for ND – TD plane of pipeline steel after (a, d) initial thermomechanical processing, (b, e) one-step annealing treatment, and (c, f) two-step annealing treatment

8.6 EBSD analysis

The pole figures (PF) obtained from EBSD analysis on the RD – TD and ND – TD planes are presented in Figs 8.3-8.4 respectively. On the RD – TD plane, texture is almost random in the initial TMCP (Fig. 8.3a) and one-step annealed (Fig. 8.3b) steels. Interestingly, the two-step annealed steel showed keen {111}||ND (Fig. 8.3c) and {111}||RD (Fig. 8.4c) texture fibers. Overall, the maximum intensity of measured texture is weak across all specimen. It is noteworthy that the highest intensity of {111}||RD texture seen in Fig. 8.4c corresponds to the ND – TD surface with clear manifestation of duplex (ferrite-martensite) structure (Fig. 8.3f). Although the starting material featured slight deviation from {111}||RD texture in Fig. 8.4a, the intensity is lower than the two-step treated steel. This suggests some form of relationship between texture and microstructure development. One can argue that the evolution of {111} grains in the two-step treated steel is traceable to the increased presence of tempered martensite and subsequent grain refinement. The closeness of both TMCP and two-step treated steels in terms of grain orientation across different sections is striking. Some retained martensite constituents characterize the dark spots featured in the ND – TD plane of the starting steel (Fig. 8.2a), though not as much as is

detected on the same plane in the double step treated steel. Across the two planes that were studied, the one-step annealed steel showed completely random texture.

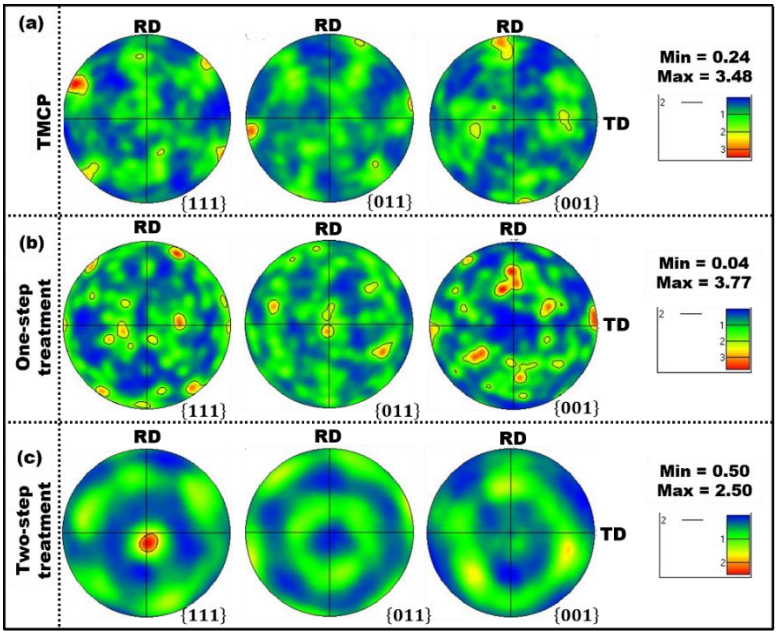

Fig. 8.3 EBSD results showing pole figures from RD – TD planes of (a) TMCP, (b) one-step annealed, and (c) two-step annealed steel

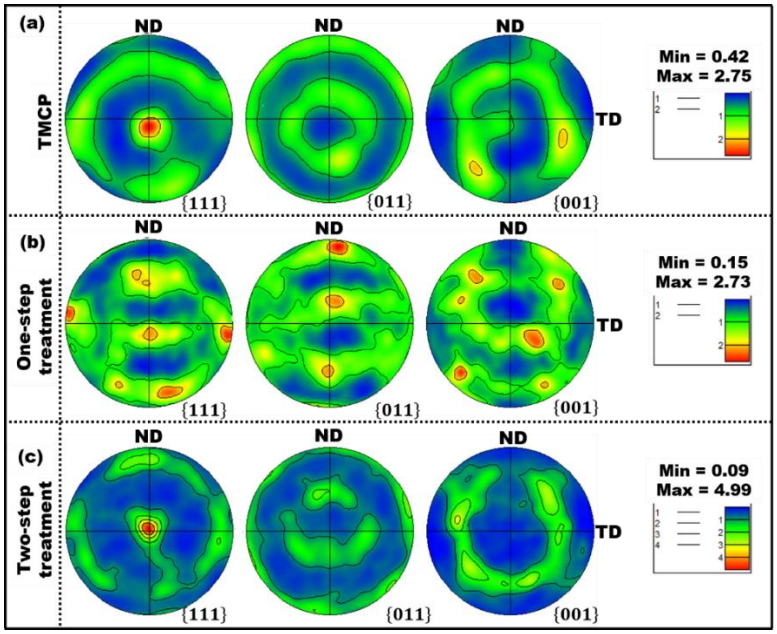

Fig. 8.4 EBSD results showing pole figures from ND – TD planes of (a) TMCP, (b) one-step annealed, and (c) two-step annealed steel

Furthermore, the RD – TD orientation and phase distribution maps for processed steels are displayed in Fig. 6. Like the PF results, some blueish indications of {111}||ND and reddish {001}||ND oriented grains are prominent in the orientation color map (Fig. 8.54a) for initial TMCP steel. In a like manner, the two-step annealing process manifested mainly {111}||ND fibers and fewer {001}||ND fibers as shown in Fig. 8.5c. The one-step annealed steel featured an arbitrary spread of {011}||ND, {111}||ND, and {001}||ND textured grains. It is also important to highlight some of the differences associated with phase distribution after various treatments were performed. The structure of steel is primarily body centered cubic (BCC) as clearly seen by the presence of blueish colored iron (Fe) in Figs. 8.5d-f. Additionally, secondary phase (colored yellow) consisting of iron carbides (Fe_3C) are seen specifically in some ferritic grains and their boundaries. The Fe_3C precipitates are clear in the one-step treated steel (Fig. 8.5e), although smaller particles are sparsely spread around distinct grains in the TMCP and two-step annealed steels. According to Singh and Kumar [464], precipitates of carbides are often found as aggregates inside fine ferrite grains; whereas the coarser particles are formed at the grain boundaries. It can be said that the roughness observed on the inset in the RD – TD plane micrograph for the one-step treated steel in Fig. 8.1e indicates the positioning of carbide sheets across large ferrite grains and their boundaries.

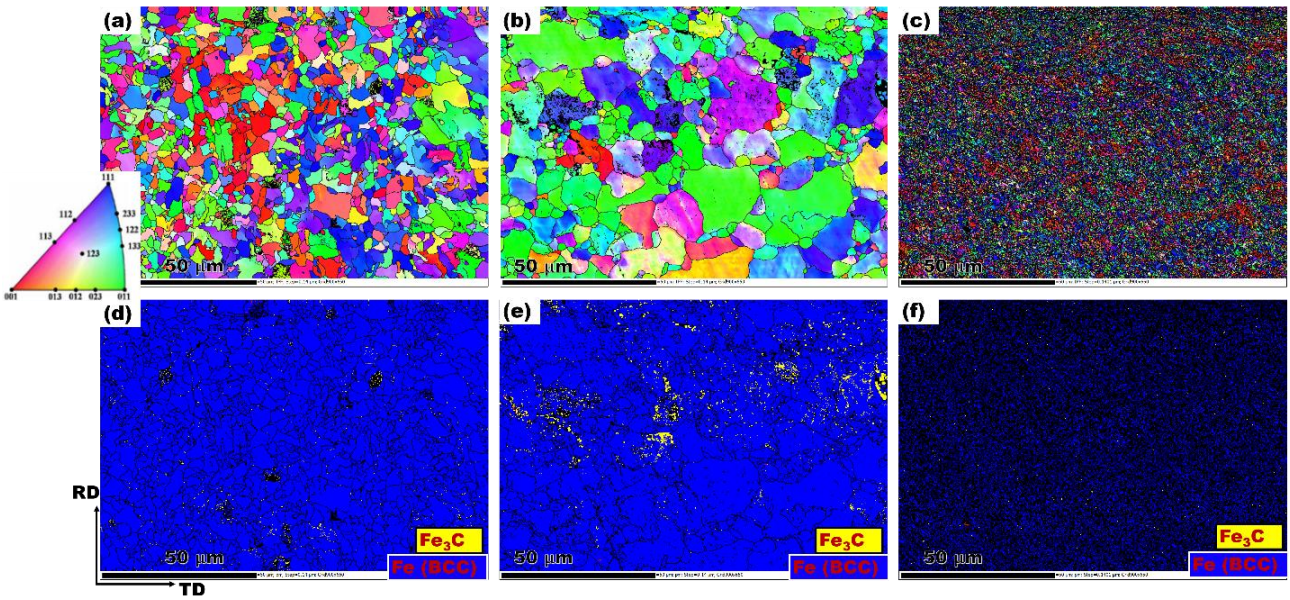

Fig. 8.5 EBSD results showing IPF orientation maps from RD – TD planes for (a) TMCP steel, (b) one-step annealed steel, (c) two-step annealed steel, phase distribution maps for (d) TMCP steel, (e) one-step annealed steel, and (f) two-step annealed steel; grain boundary

Grain boundaries are highlighted in two categories namely the high angle grain boundaries (HAGB) and the low angle grain boundaries (LAGB). The HAGBs are defined as grain boundaries having misorientation angles ranging from 5° to 15°, while the LAGBs are those with misorientation angles above 15°. The spread of these boundary types is non-uniform across pipeline steel specimens. Besides, the annealing treatment produced grain structures with varied boundary character as seen in Fig. 8.6. The highest fraction of grain boundaries occurred in the two-step annealed steel (Fig. 8.6c), while the least number of boundaries featured in the one-step treated steel (Fig. 8.6b). The starting material have intermediate boundary distribution, which comprises of larger amount of HAGB with fewer LAGB (Fig. 8.6a). It has been previously established that areas containing carbides in steel are often prone to the formation of HAGB clusters [12]. This implies that such zones with high accumulation of HAGBs possess highly strained grains. These indications can as well be attributed to the unique heat treatment cycle adopted for each specimen. Recall that the two-step annealing treatment involve subsequent quenching immediately after heating and re-heating (Fig. 3.1). The double quenching approach could have induced thermal strains inside the steel structure at the initial step. Thereafter, the second step in the annealing process (i.e. tempering) promoted the relief of stored energy at grain boundaries. The consequence of such repeated quenching procedures will likely be restricted grain growth. Also, this might have led to possible fragmentation of grains under high strain, impeded growth of new nuclei, and formation of relatively smaller grains with a mixture of high and low stored energy at their interfaces.

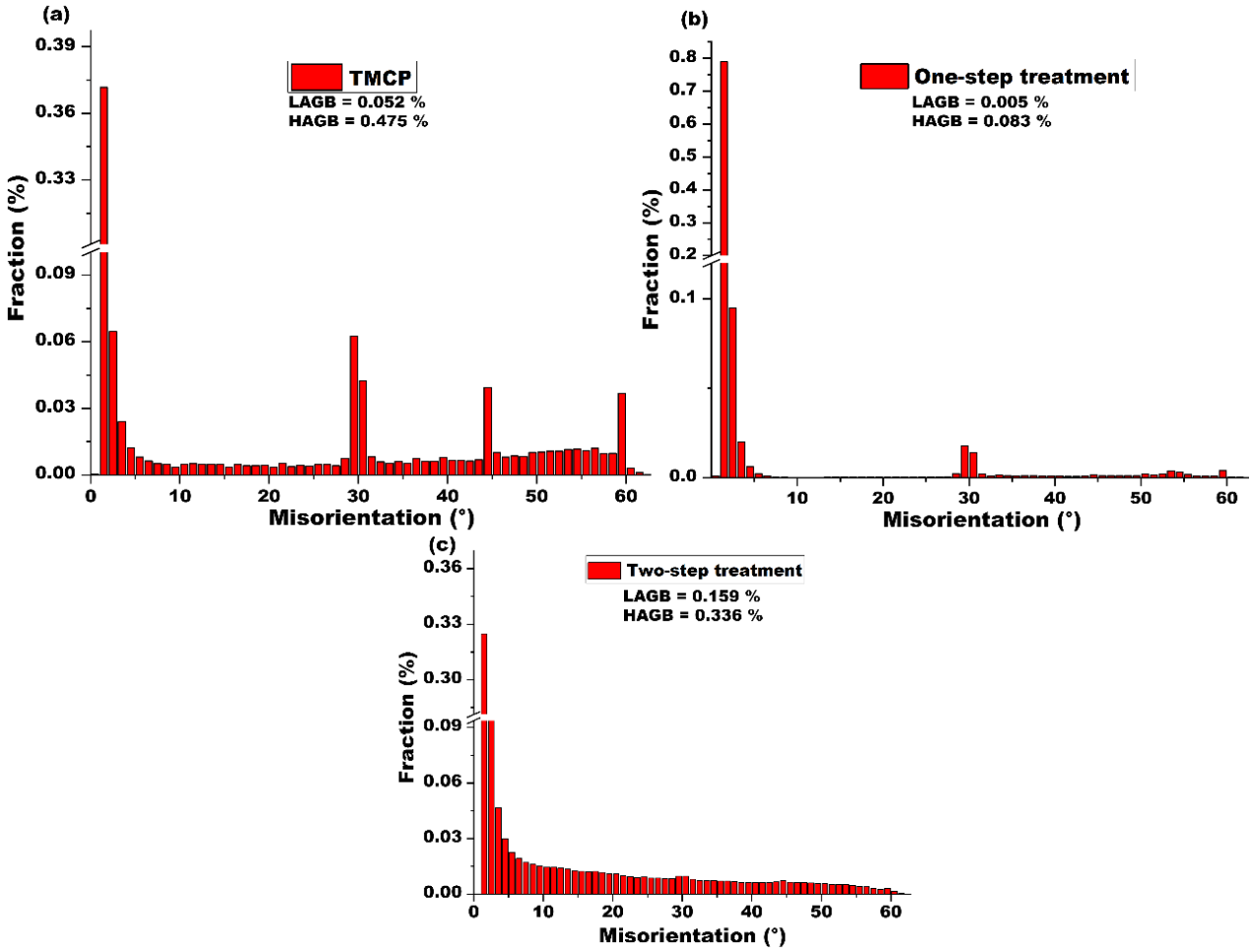

Fig. 8.6 Grain boundary character distribution after (a) initial TMCP, (b) one-step, and (c) two-step annealing treatments

The EBSD band contrast image was overlaid with correlated strain contouring (Figs. 8.7a-c) and local misorientation (Figs. 8.7d-f) maps. There is a consistent increase in micro-strain and misorientation intensity after the double annealing processes as seen in Figs. 8.7c and f. When metals are subjected to deformation, dislocation motions are induced within their lattice [465]. The observed micro-strain distribution patterns are clearly linked with the local average misorientation or kernel average misorientation (KAM) between grains. Also, the degree of misorientation gives an idea about the amount of defects impacted on crystals [466]. It is important to note that there are limitations in the use of EBSD patterns as a variable to determine the extent of deformations or induced strains in a material. This is mainly due to equipment related variations, poor specimen preparation, and relatively small scan areas examined during microstructural characterization. Nevertheless, the KAM is not associated with equipment disparities [467]. Many studies have used

this parameter to established links between misorientation and localized strain due to high density of dislocation (strains) within the microstructure [468,469]. The EBSD results describes the misorientation between each point and its closest neighbor with the aid of color codes. For every point, an average misorientation value is determined with consideration to the adjoining grain. Finally, an overall average of all point-to-point misorientation value is taken. Each scan point possesses a color-coded misorientation value, which is used as an indication of strain distribution. For this study, KAM analysis was conducted only on grain with local misorientation angles (θ) between 0 and 5°. Since misorientation maps are insufficient in this case, quantitative values were extracted and used for explaining the extent of deformation after processing. It is evident in the initial TMCP and one-step treated steel that strain did not initiate uniformly. Instead, localized strains are seen in specific regions marked with relatively high intensity. This agrees with the lower KAM of 0.3° realized from these steels (Figs. 8.7d1-e1). As shown in Fig. 8.7d1, the distribution of local misorientation is concentrated in the range of $\theta \leq 1°$ for the hot rolled steel. The grains developed after one-step annealing experienced local misorientation approximately within the range of $\theta \leq 2°$ (Fig. 8.7e1). An elevation in KAM value to 0.6° is recorded after the one-step treatment. Based on the increased level of micro-strain and misorientation intensity in two-step treated steel, the corresponding KAM was expected to be higher than other specimens. As noted in Fig. 8.7f, the double-step treatment resulted in a KAM value of 1.3°. The aftermath is that local misorientation extended almost completely throughout the $\theta \leq 5°$ range for the two-step annealed steel.

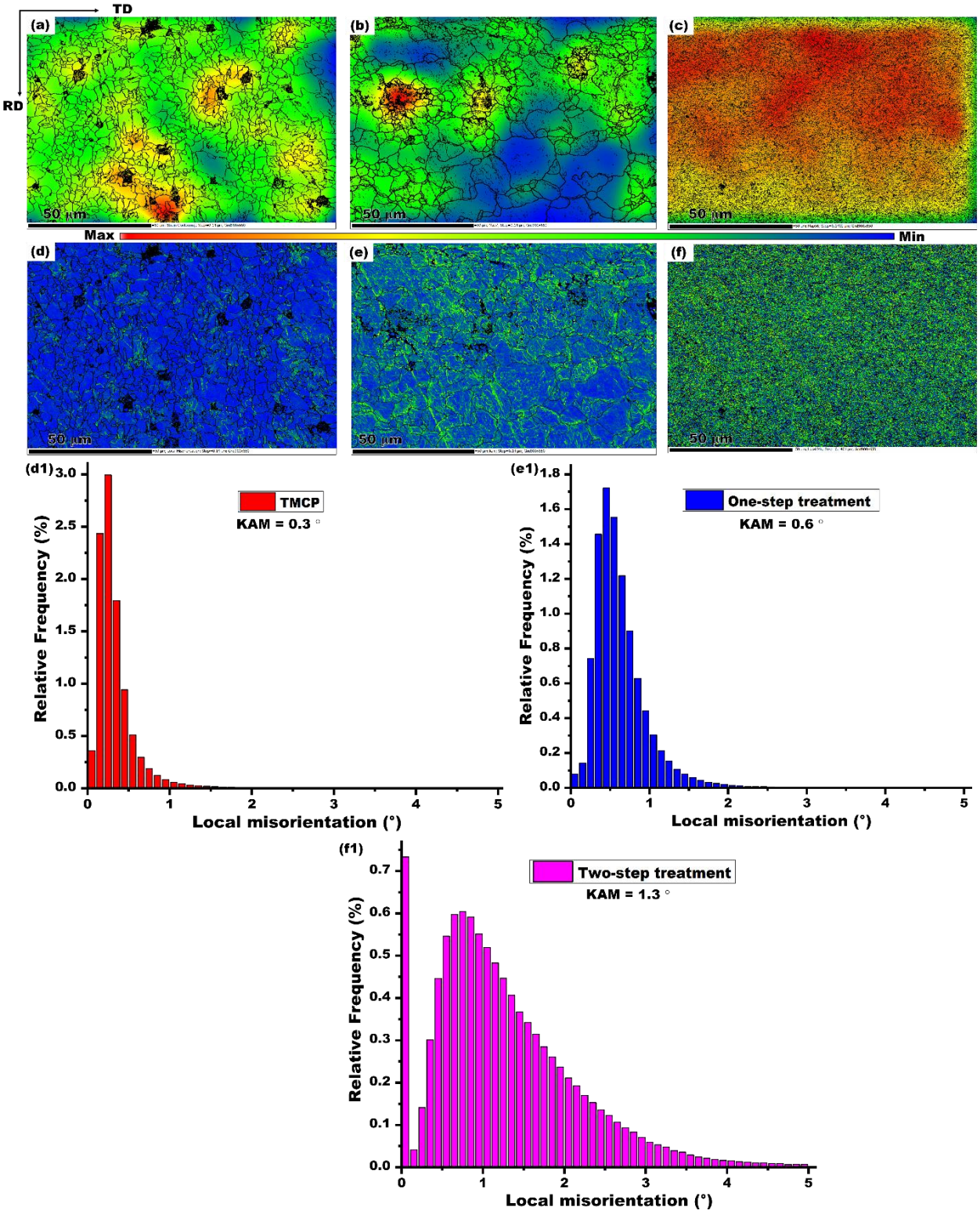

Fig. 8.7 EBSD strain contouring maps for (a) TMCP steel, (b) one-step annealed steel, (c) two-step annealed steel; local average misorientation maps with corresponding plots for (d, d1) TMCP steel, (e, e1) one-step annealed steel, and (f, f1) two-step annealed steel

The maps showing area fractions of recrystallized grains in steel samples after various treatments are shown in Fig. 8.8. Recrystallized regions are identified as sub-grains demarcated by misorientation angle less than 7.5° and grains are separated by misorientation angles above 7.5°. Both recrystallized and non-recrystallized (i.e. recovered and deformed) areas are highlighted by their respective color codes according to the legend. The plot in Fig. 8.8d indicates the distribution of each color field in terms of percentage area fraction. For instance, the blue colored part representing recrystallized portions manifested the most in the TMCP steel (Fig. 8.8a). The same steel sample contain significant proportion of recovered (sub-structured) grains, with very insignificant presence of deformed grains. It is known that dislocation substructures are considerably rearranged during recovery [470]. The consequence of the recovery process will be reduction in the concentration of stored energy leading up to the recrystallization stage. Therefore, one will not be surprised to see that deformed grains are diminished in the TMCP steel. The simple explanation is that the hot rolling conditions and subsequent cooling operations promoted full recovery of deformed grains, and most of the grains will go on to experience complete recrystallization afterwards. Following the one-step treatment, a drastic decrease is seen in the extent of recrystallization (Fig. 8.8b). However, this situation was compensated with the evolution of extensively recovered grains, and some patches of deformed areas. The reasoning is that majority of the deformed grains became recovered during the one-step annealing process, but they did not have enough time to remarkably recrystallize owing to the abrupt quenching. Furthermore, the two-step annealing process resulted in minimal recrystallization with an infinitesimal amount of recovered grains and massively deformed locations (Fig.8.8c). This result confirms that the extensive network of martensite resulted in dominantly deformed structure, while the ferrite matrix progressed through recrystallization. A close observation on Fig. 8.8c indicates a distribution of small recrystallized grains encircled in deformed regions. It is possible that restrictions on the growth of ferrite grains by martensite after the first heat treatment cycle might have created the condition for them to undergo complete recrystallization during the second heat treatment cycle.

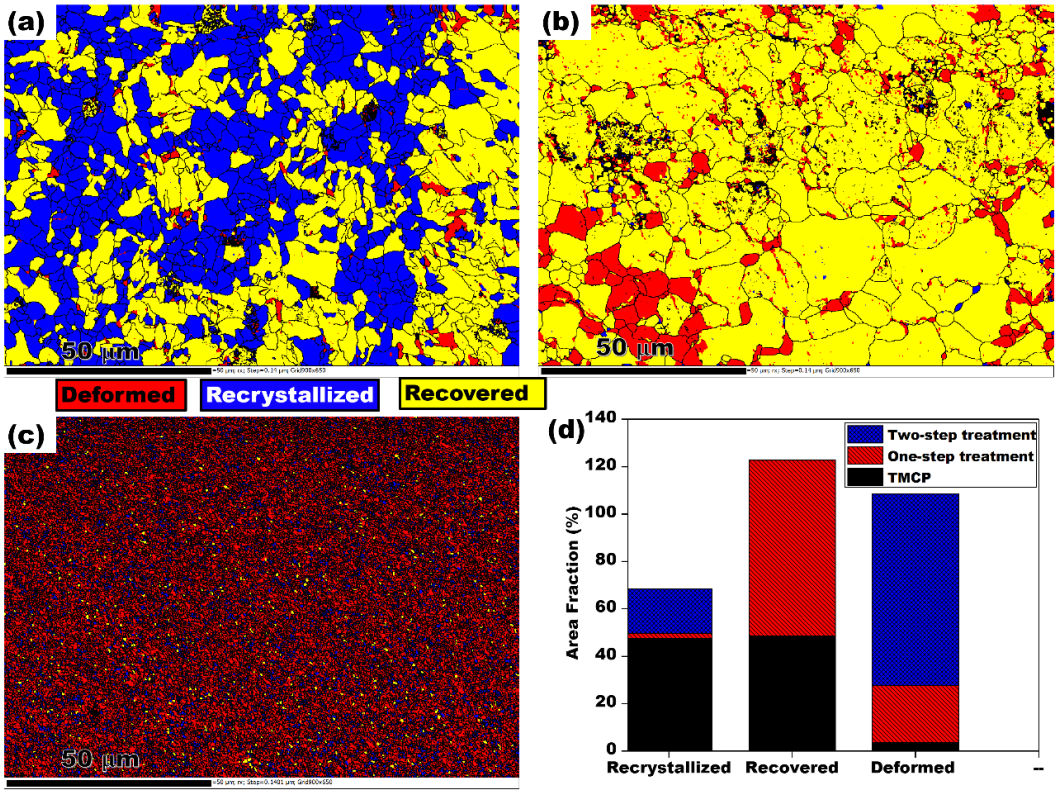

Fig. 8.8 EBSD recrystallization area fraction maps for (a) TMCP steel, (b) one-step annealed steel, (c) two-step annealed steel, and (d) plots of recrystallized, recovered, and deformed regions

The observed differences in grain size with respect to the steel treatment schedules are shown in Fig. 8.9. Since the initial TMCP steel is finished rolled in the austenitic region and rapidly cooled afterwards, the expectation is that austenite grains will undergo transformation into ferrite matrix. Considering the grain size statistics in Figs. 8.9a and c, both starting material and two-step treated steel consist of relatively smaller grains in comparison to the one-step treated steel (Fig. 8.9b). Grains developed from the one-step annealing process are coarser. Such increased measure of grain growth can be linked to the annealing treatment process. Inter-critical annealing at 720 ℃ for a duration of up to 60 mins might have fostered extensive grain growth. Conversely, the double stage annealing offers another opportunity for stepwise grain refinement to be achieved through series of treatments. Similarly, Mondal and Dey [471] realized significant grain refinement in steel through repeated annealing cycles. They modified the structure of dual phase ferrite-martensite steel by performing heat treatment cycles at inter-critical temperatures of 750 ℃ and 800 ℃. Another study [472] also used the inter-critical annealing technique to obtained ultra-fine grained dual-phase microstructure containing a homogeneous spread of martensite particles across ferrite

matrix. Nonetheless, ferrite grains are known to nucleate from austenite during the cooling process. Therefore, the generation of more nuclei during the treatment process will result in the formation of many grains. Subsequent reheating and quenching in a second treatment process could have necessitated the conversion of numerous austenite grains to even smaller grains of ferrite.

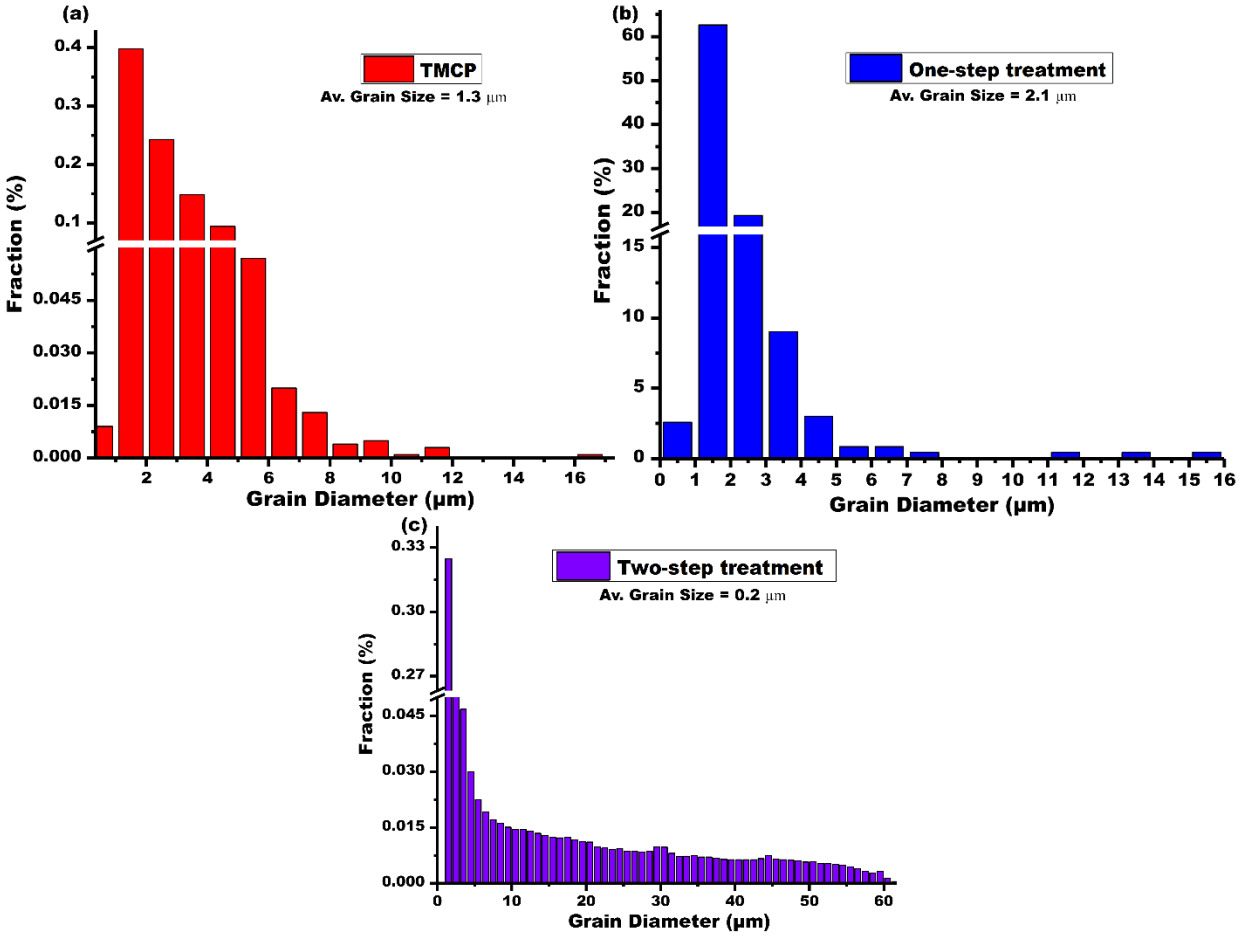

Fig. 8.9 Distribution of grains according to sizes in (a) TMCP steel (b) one-step annealed steel (c) two-step annealed steel

8.7 Texture evolution

The macro-texture results obtained from X-ray diffraction measurements are described in Fig. 8.10 with Orientation Distribution Functions (ODFs) and Inverse Pole Figures (IPFs) of the initial TMCP specimen, including those of the one-step and two-step annealing treatments. It is evident that similarities exist between the initial texture of the rolled plate and the two-step heat treated specimens. As indicated in Figs. 8.10a-c and Figs. 8.10i-k, ideal orientation maxima such as those

belonging to the {100}||ND fibers (specifically $(001)[2-30]$, $(001)[1-10]$, $(010)[101]$), and $(112)[1-10]$ can be seen featuring in both specimens. In a like manner, IPFs corresponding to the initial steel plate (Fig. 8.10d) and that of the two-step treated specimen (Fig. 8.10l) indicate significant deviation of intensity towards [111] and [001] directions. On the contrary, the one-step treated specimen (Figs. 8.10e-g) displayed mainly {011} family of planes aligned in different directions. Some notable orientations include the $\{011\}\langle 2-11\rangle$ in Fig. 8.10e and $\{110\}\langle -112\rangle$ in Fig. 8.10f. There are also manifestations of $(112)[-2-32]$ and $(213)[-2-32]$ texture components after the one-step treatment.

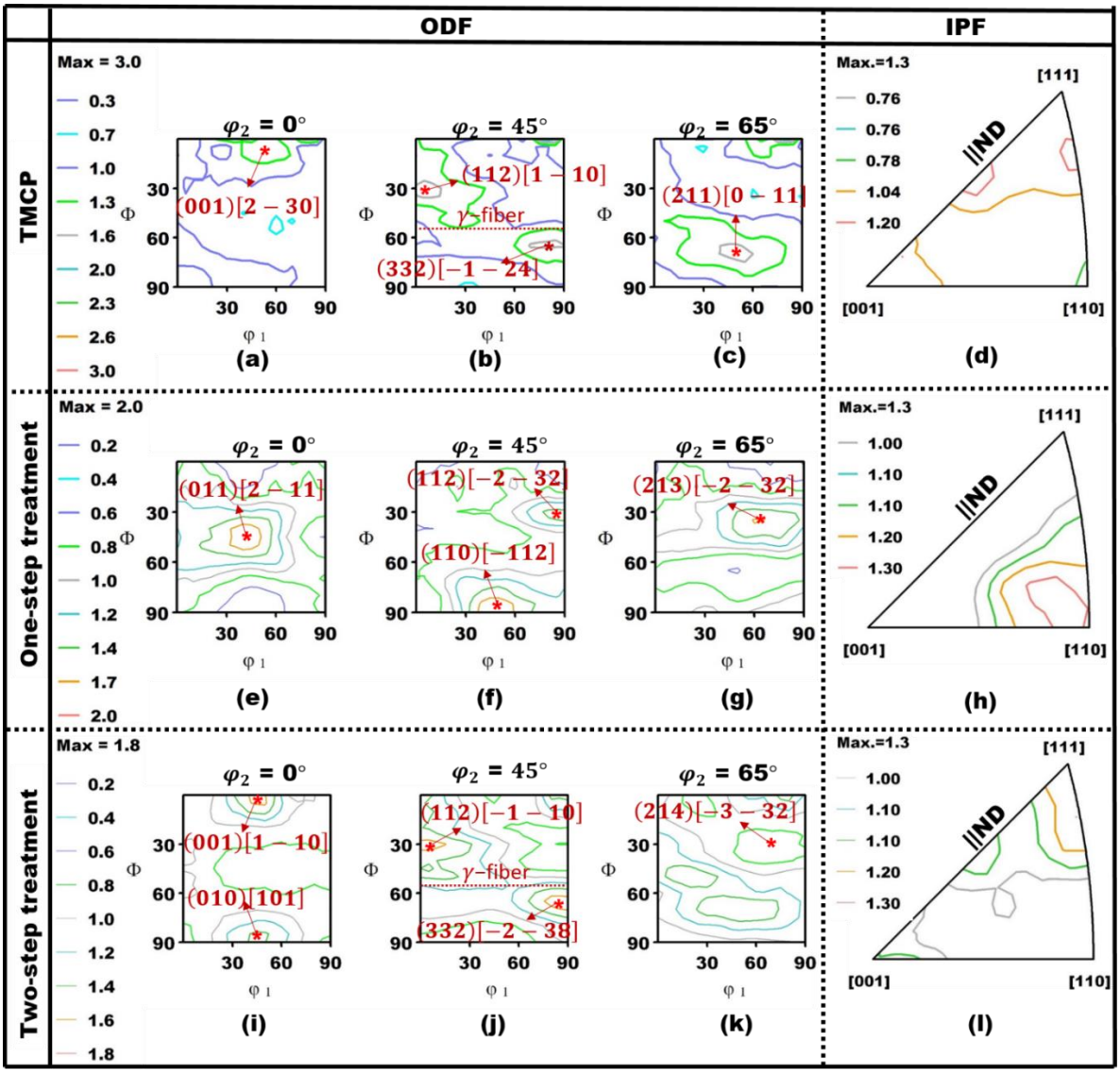

Fig. 8.10 ODF with corresponding IPF for pipeline steel after (a-d) initial TMCP, (e-h) one-step annealing, and (i-l) two-step annealing treatments

The important texture fibers that are often found in a typical BCC steel and their axis of orientation are outlined in the literature [464]. Table 8.1 shows selected texture fibers with their corresponding Euler angles. In the current study, some of these fibers have been identified after different heat treatments. An estimate of the volume fractions of specific orientations and texture fibers are shown in Table 8.2. The proportions of γ – fiber is highest in the two-step treated sample, followed by the starting plate, while the one-step treated steel showed the least amount. Again, θ – fibers (specifically Cube: $\{001\}\langle 100\rangle$ and Rotated cube: $\{001\}\langle 110\rangle$) appeared more in the initial TMCP and two-step treated material compared to the one-step treated steel. This explains the significant deviation of orientation intensity towards those poles (i.e.[111], [001] directions) in Figs. 8.10d and l respectively. In the one-step treated sample, α and ζ – fibers presented the highest volume fraction relative to other specimens (Table 8.2). The single step processing approach produced more ideal orientations belonging to ζ – fibers (specifically Goss $\{110\}\langle 001\rangle$ and Brass $\{110\}\langle 112\rangle$). Additional orientations remarked in significant percentages after the one-step process are Copper $\{112\}\langle 111\rangle$, and S $\{123\}\langle 634\rangle$). These results are agreeable to the microstructural evaluation presented earlier, especially the EBSD analysis. Moreover, the calculated fractions of the main orientations (Table 2) validates the observations made from the ODFs and IPFs in Fig. 8.10.

Table 8.1 Summary of orientation fiber description and corresponding Euler angles

Texture fiber	Ideal orientation description ($\{\mathbf{hkl}\}\langle\mathbf{uvw}\rangle$)	Euler angles $(\boldsymbol{\varphi_1}, \boldsymbol{\Phi}, \boldsymbol{\varphi_2})$
γ – gamma fibers: $\{\mathbf{111}\}\|\|$ND	$\{111\}\langle 112\rangle$, and $\{111\}\langle 110\rangle$	$0-90°$, 55°, 45°
η – eta fibers: $\{\mathbf{100}\}\|\|$RD	$\{001\}\langle 100\rangle$, and $\{011\}\langle 100\rangle$	0°, $0-90°$, 0°
α – alpha fibers: $\langle\mathbf{110}\rangle\|\|$RD	$\{001\}\langle 110\rangle$, $\{112\}\langle 110\rangle$, $\{111\}\langle 110\rangle$, and $\{011\}\langle 110\rangle$	0°, $0-90°$, 45°
ε – epsilon fibers: $\{\mathbf{110}\}\|\|$TD	$\{001\}\langle 110\rangle$, $\{111\}\langle 112\rangle$, and $\{011\}\langle 100\rangle$	90°, $0-90°$, 45°
θ – theta fibers: $\{\mathbf{100}\}\|\|$ND	$\{001\}\langle 110\rangle$, and $\{001\}\langle 100\rangle$	$0-90°$, 0°, 0°
ζ – zeta fibers: $\{\mathbf{110}\}\|\|$ND	$\{011\}\langle 110\rangle$, $\{011\}\langle 100\rangle$, $\{011\}\langle 111\rangle$, and $\{110\}\langle 112\rangle$	$0-90°$, 45°, 0°
β – beta fibers: $\{\mathbf{111}\}\|\|30°$ND	$\{011\}$ close to ND	

Table 8.2 Volume fraction of ideal texture components and some fibers present after each treatment process

Ideal texture components and fibers	Initial thermomechanical treatment (%)	One-step annealing treatment (%)	Two-step annealing treatment (%)
Cube: $\{\mathbf{001}\}\langle\mathbf{100}\rangle$	2.1	1.9	2.0
Goss: $\{\mathbf{110}\}\langle\mathbf{001}\rangle$	2.2	2.9	2.4
Brass: $\{\mathbf{110}\}\langle\mathbf{112}\rangle$	3.6	6.9	3.4
S: $\{\mathbf{123}\}\langle\mathbf{634}\rangle$	7.4	13.0	7.2
Copper: $\{\mathbf{112}\}\langle\mathbf{111}\rangle$:	3.5	5.9	3.4
Rotated cube: $\{\mathbf{001}\}\langle\mathbf{110}\rangle$	2.8	1.4	2.9
γ – fiber: $\{\mathbf{111}\}$‖ND	14.9	11.5	15.6
α – fiber: $\{\mathbf{110}\}$‖RD	7.8	10.9	7.8
θ – fiber: $\{\mathbf{100}\}$‖ND	12.3	8.5	12.1
ζ – fiber: $\{\mathbf{110}\}$‖ND	16.3	24.8	16.5

The orientation density for α, ε, η, ζ, and γ texture fibers are presented as skeleton plots in Fig. 8.11. Interesting correlations are observable when comparing these plots with the ODF results. Apparently, the dual-phase texture obtained after two-step annealing consist of identical fibers seen in the starting steel. For instance, the same pattern of intensity variation for α – fiber lines are noticed in the phi (Φ) range of 0 to 70° of the plots for initial TMCP and two-step treated steel in Fig. 8.11a. The ODFs in Figs. 8.10b and j featured α – fibers in the Φ range of 0 to 40° for $\varphi_2 = 45°$ section. Among the texture components present in the selected range of φ_2 and Φ, the $\{112\}\langle110\rangle$ has the strongest intensity on the α – fiber plots. Other orientations such as the $\{111\}\langle110\rangle$ and $\{011\}\langle110\rangle$ also showed their corresponding peaks in Fig. 8.11a. It was not surprising to see another evidence of $\{111\}$‖RD orientation, given that this has been sighted earlier in Figs. 8.4a and c. Having made a complementary observation from XRD macro-texture evaluations, one can easily confirm the evolution of this peculiar texture in the TMCP and two-step annealed steels. Nevertheless, relatively weaker ideal texture components were identified in the α – fiber plot for one-step annealing treatment (Fig. 8.11a).

The intensity plot for ε – fiber constituents are shown in Fig. 8.11b. Again, the most intense orientation manifested around $\{111\}\langle112\rangle$ in the plots for TMCP and two-step treated steels. The one-step treated steel displayed a drastic rise in ε – fiber intensity in the proximity of the

{112}⟨111⟩ orientation. As for the η – fibers lines in Fig. 8.11c, the graphs showed quite similar trend with an increase towards {011}⟨100⟩ orientation. Overall, the one step processed steel indicated the highest intensity for {011}⟨100⟩ and the lowest for {001}⟨100⟩ orientations. The comparison in ζ – fiber plot (Fig. 8.11d) indicates intense development of {110}||ND texture, especially the {011}⟨211⟩ orientation. Remember that maxima corresponding to the identified orientations also featured in the corresponding ODF presented as Fig. 8.10f. This result is expected, since the IPF for one-step treatment (Fig. 8.10h) contains mainly ζ – fibers. One can say that the processing conditions for the starting material and two-step processed steel did not favor significant evolution of η and ζ – fibers.

The changes in γ – fiber (specifically {111}⟨110⟩ and {111}⟨112⟩) evolution after hot rolling and annealing treatments are shown in Fig. 8.11e. These plots clearly depict a decrease in intensity for all γ – fiber constituents after the one-step annealing treatment; whereas the hot rolled and two-step treated specimens collectively showed an increase in intensity. It can be inferred from these observations that the one-step annealing process eliminated most of the texture fibers developed after the initial processing on the steel. The skeleton plots suggest that the two-step annealing treatment is a potential route to recover most of the initial texture evolved from hot rolling. Notably, the two-step annealing treatment caused the re-emergence of the texture components originally developed during TMCP. This procedure could serve as a way of preserving or modifying important microstructural features in steel. Most especially, the double annealing procedure creates a possibility for retaining the much-desired γ – fiber for improved properties. The trends observed through textural measurements makes it imperative to further examine the effects of these microstructures on mechanical deformability and embrittlement characteristics.

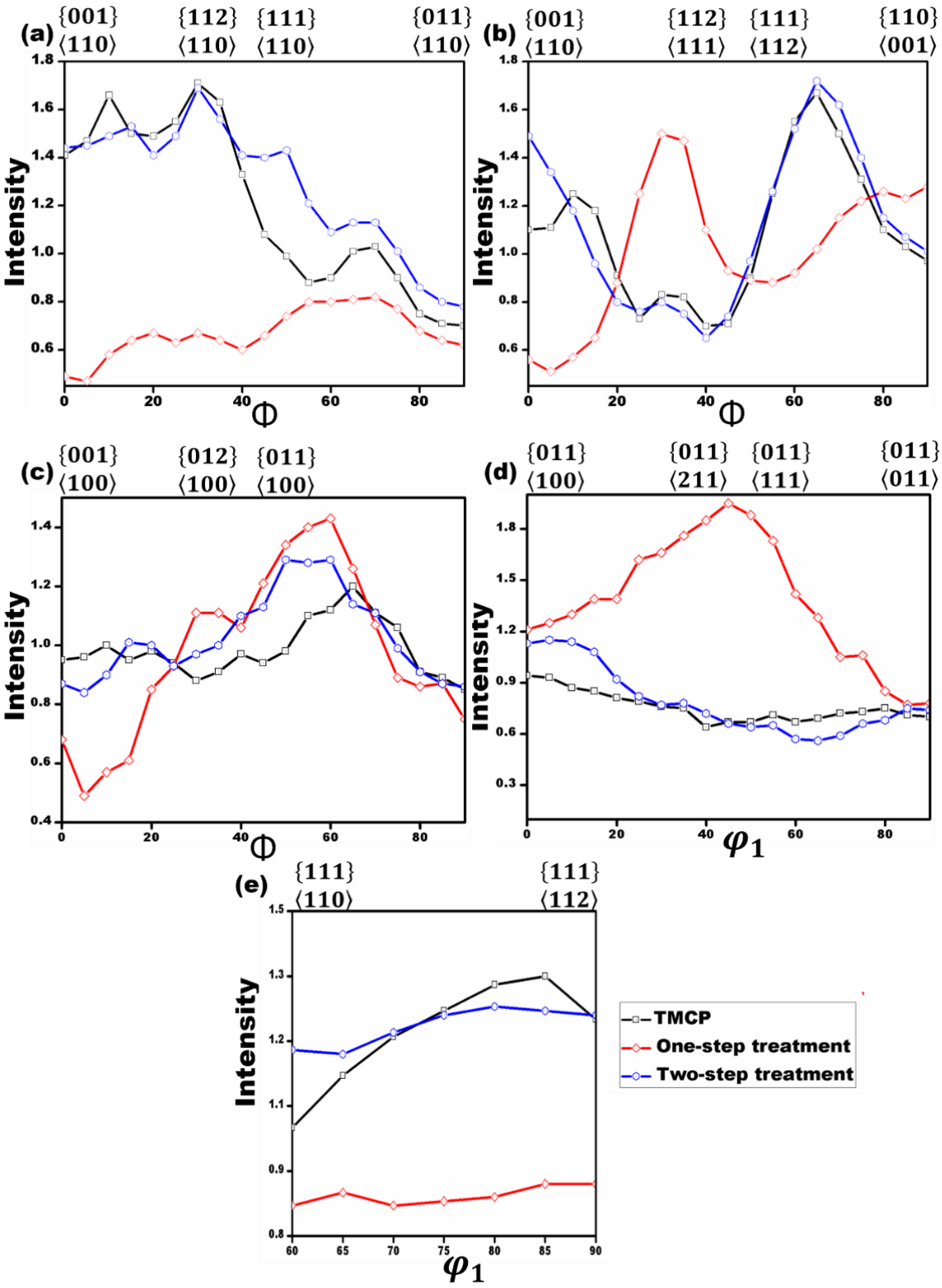

Fig. 8.11 Orientation density plots showing variations in selected texture fibers after treatments on TMCP, one-step annealed, and two-step annealed steels where (a) α, (b) ε, (c) η, (d) ζ, and (e) γ texture fibers

8.8 Mechanical properties

The tensile properties of each specimen before and after pre-hydrogen charging are presented in Table 8.3 and Fig. 8.12. It is obvious that all heat-treated specimens showed lower yield and tensile strengths compared to the starting steel. Also, the hardness value for the hot rolled steel is higher than what was obtained from other specimens. To ascertain that the new steels meet the mechanical property requirements of the initial alloy, they were matched with pipeline grading standards. The API 5L specification for line pipe [36] stipulates tensile strength in the range of 565 – 758 MPa for X70 steel. Considering the results obtained in the current study (Table 8.3), one can say that the unique thermal treatments resulted in steel with acceptable mechanical properties. However, the single annealing operation resulted in the least ductility, whereas the two-step treated steel experienced the highest elongation relative to other processing conditions. Such high amounts of ductility noticed in the double annealed steel could have jeopardized its strength. Also, the expectation is that deformability of the steel will improve following the two-step treatment. An explanation for this observation is linked to microstructure development. Remember that the two-step treated steel was comprised of martensite constituents dispersed in a ductile ferrite matrix. There are suggestions that dual-phase ferrite and martensite structure can foster stress relaxation around crack tip, thus delaying crack nucleation and propagation [473]. This means that low flow stress induced by tempered martensite might have enhanced ductility and toughness. Moreover, a recent study [472] established that dual-phase steel possess higher plasticity in addition to homogeneous strain distribution across networks of ferrite-martensite interfaces. These ideas are attributable to the improved ductility noticed in the two-step annealed steel. Another observation is the continuous yielding experienced in both the initial and two-step processed steel, as shown in Fig. 8.12. Such phenomenon has been widely attributed to the motion of dislocations across obstacles created by Cottrell-Lomer locks [450,474,475]. Tsuchida [475] showed that larger grain with high carbon content impedes Luder band formation. A separate research proposed that Luder band formation results from strain-induced martensite transformation [451]. Given that the one-step annealed steel contains large grains without tempered martensite, the absence of Luder-like deformation in it is justified

Fig. 8.12 contains tensile test results for each processed steel after pre-charging with hydrogen. All hydrogen charged specimens displayed an increase in strength leading to a reduction in their

elongation. Such behavior can be associated with the hydrogen embrittlement effect. Considering these experimental observations, it is evident that hydrogen influenced plasticity in all pipeline steels. The drastic reduction in ductility, implies that the starting material was most affected by hydrogen compared to the newly developed pipeline steels. This could be traced to hydrogen induced plasticity and enhanced dislocation motion [119,476,477]. During tensile loading, trapped hydrogen is forced to move along with dislocation towards other available structural defects. Such situations warrant accumulation of hydrogen in the steel structure, thereby facilitating quicker failure.

Table 8.3 Summary of mechanical properties of pipeline steels before and after pre-hydrogen charging

Sample	Yield stress (MPa)	Tensile strength (MPa)	Total elongation (%)	Hardness (HV)
TMCP	570.4	666.8	26.9	385.1
TMCP (H-charged)	575.7	711.9	13.5	-
One-step treatment	447.4	650.7	23.6	250.1
One-step treatment (H-charged)	501.3	700.2	22.1	-
Two-step treatment	451.7	572.5	32.5	223.4
Two-step treatment (H-charged)	425.9	598.1	26.5	-

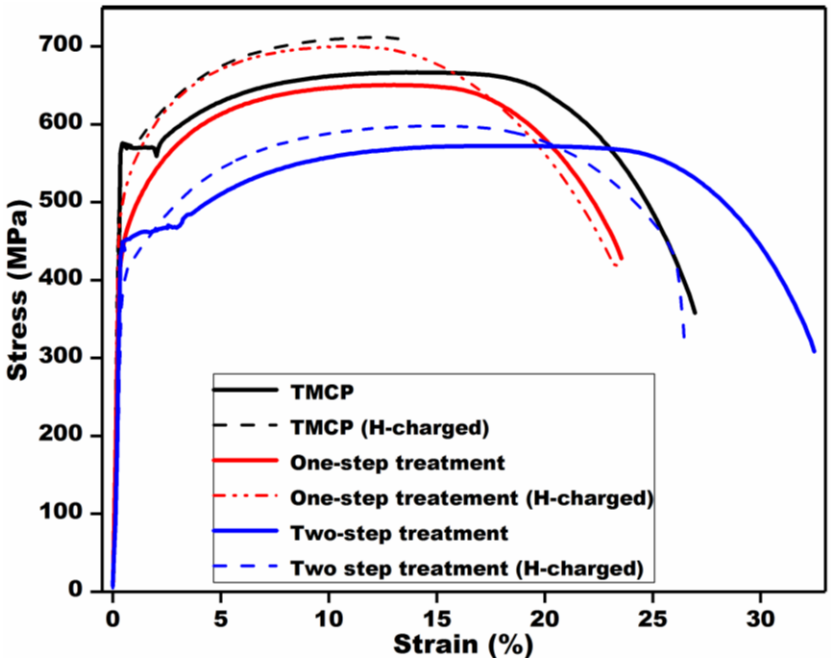

Fig. 8.12 Stress-strain plots for pipeline steels before and after pre-hydrogen charging

8.8.1 Fractography

In steels, HE tends to manifest as a transition from ductile to brittle fracture mode. The ductile mode is characterized by coalescence of micro-voids, while the brittle failure shows cleavage failure facets. Fracture surface examination was conducted on the test specimens from which the engineering stress-engineering strain curves shown in Fig. 8.12 were acquired. The morphology of each failure surface was imaged with SEM and presented in Figs. 8.13-8.14 for uncharged and pre-hydrogen charged specimens respectively. After investigating the fracture mode for all uncharged pipeline steels (Fig. 13), it was found that they displayed the characteristic ductile failure behavior. This is noticeable through the presence of dimples, which are internal microscopic features produced by the combination of different voids during plastic deformation [478]. Dimples are quantified statistically in Table 8.4 and the results indicate higher density for uncharged specimens compared to the embrittled ones. Such evidence confirms that ductility was lowered due to the damaging effect of hydrogen. Overall, more dimples were present in the one-step treated specimen relative to the initial TMCP and two-step annealed steel. Details of dimple morphology is shown in the high magnification micrographs corresponding to each steel (Figs. 8.13b, d, f and 8.14b, d, f). The reasons for this trend are not far-fetched given that the final microstructures are different in all specimens.

Table 8.4 Dimple density estimation on fractured TMCP and annealed specimens

Sample	Average dimple density (dimples/mm^2)
TMCP	2109
TMCP (H-charged)	2061
One-step treatment	3413
One-step treatment (H-charged)	3184
Two-step treatment	2227
Two-step treatment (H-charged)	2054

The dimpled regions are most conspicuous in the starting material and the two-step treated specimens. Enlarged dimples indicate that these two samples displayed the highest ductility compared to the other steels. As seen in Figs. 8.13a-b and e-f, most of the dimples are bigger than the ones presented in Figs. 8.13c-d. The implication is that some sizable dimples may have been formed from the combination of smaller ones during tensile loading. Majority of the large dimples

found in the TMCP and two-step treated steels possess visible voids at their centers, which is an indication of relatively higher extent of plastic deformation. Such wide dimples tend to occupy larger surface areas. This might have resulted in the diminished dimple count recorded for the initial material and double-step annealed steels. Therefore, it can be said that an inverse relationship exists between size and density of dimples. However, many small dimples featured on the one-step treated steel (Figs. 8.13c-d), which validates its reduced ductility. The idea is that the one-step annealed structure defied extensive straining at maximum load, hence the micro-voids formed at the onset of deformation did not sufficiently expand in comparison to other specimens. It is noteworthy that void nucleation in dual-phase steel often starts from either martensite particles or by decohesion at ferrite-martensite interfaces [479]. Since non-homogeneous plastic deformation in dual-phase steel relates to inconsistencies in strain distribution across the two phases, they concluded that the softer ferrite deformed faster than the harder martensite. Considering the possibility of splitting between the ferrite and martensite phases, one can say that fracture occurred by void nucleation at the ferrite regions accompanied by slow shearing at the boundaries.

Various morphological features are noticeable on the fracture surfaces of the pre-hydrogen charged specimens in Figs. 8.14a-f. The fractured specimens are characterized by fewer micro-voids on a quasi-cleavage and inter-granular facets. At lower magnification somewhat flat fracture surfaces are seen (Figs. 8.14a, c, e), but higher resolution micrographs (Figs. 8.14b, d, f) indicate curved undulating features within the center of the fractured region. Few dimples are revealed on the embrittled surface, especially towards the edge of the specimens. This suggests that hydrogen contributed in weakening grain boundaries and reducing cohesion inside the steel structure. Similar appearances have been witnessed on failed X60 and X80 pipeline steels [122]. According to the authors, high dislocation density and slip bands found beneath the undulating fractured surface highlight the effect of microstructural parameters on hydrogen damage.

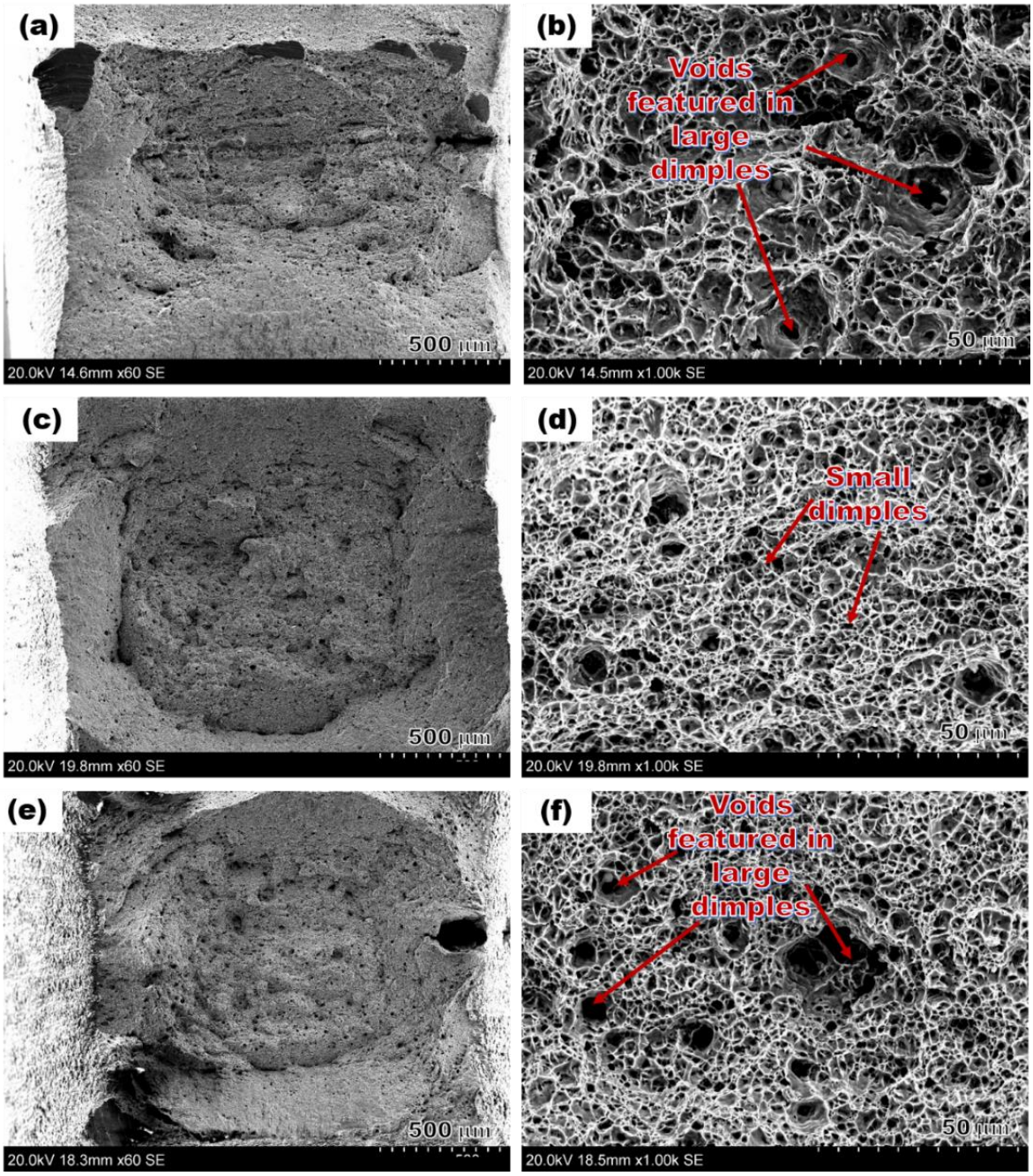

Fig. 8.13 SEM fractographs of tensile specimens tested before hydrogen charging (a, b) initial TMCP, (c, d) one-step annealed, and (e, f) two-step annealed steel

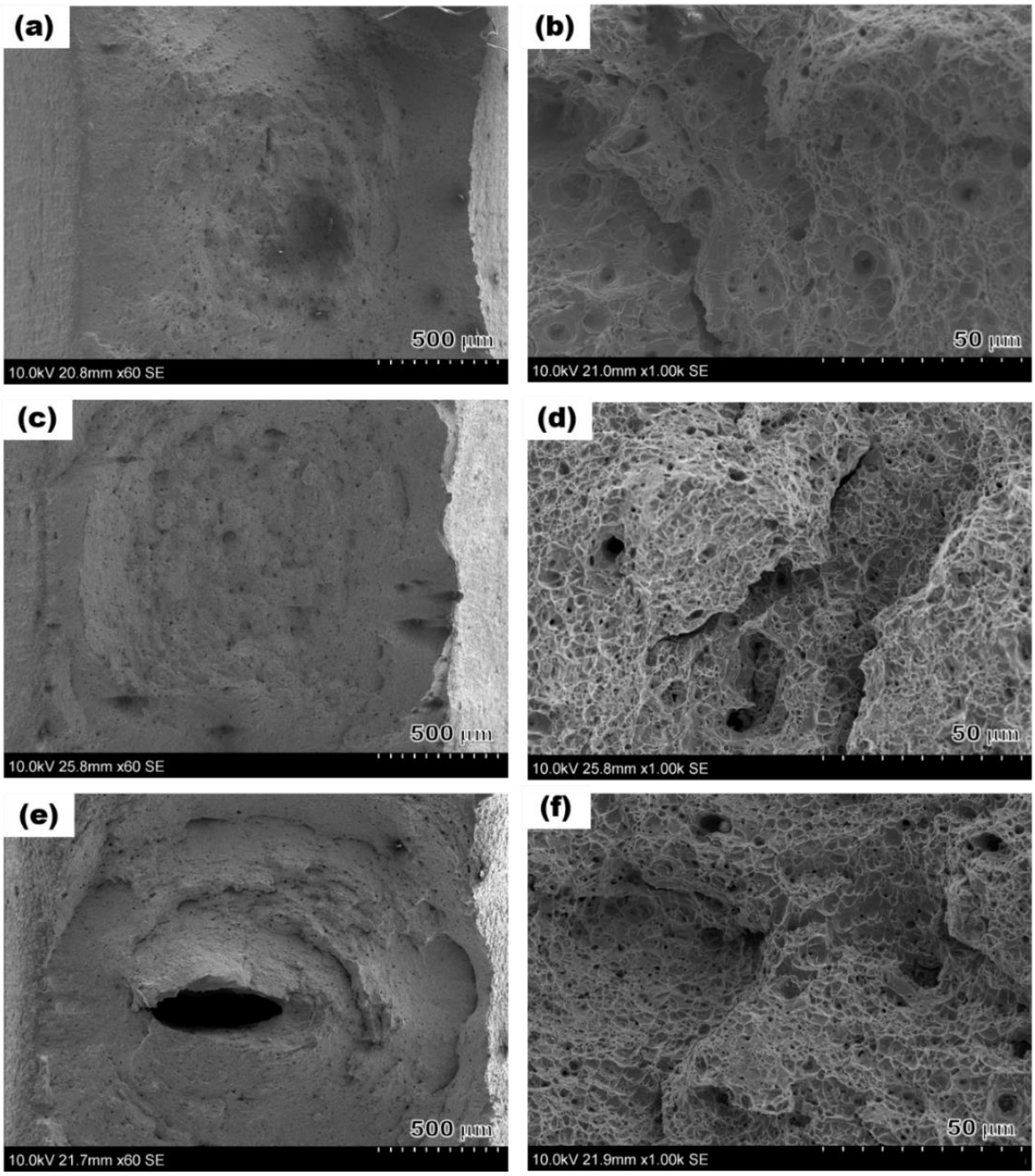

Fig. 8.14 SEM fractographs of tensile specimens tested after pre-hydrogen charging (a, b) initial TMCP, (c, d) one-step annealed, and (e, f) two-step annealed steel

8.9 Discussions

8.9.1 Effect of crystallographic texture on mechanical properties

Some correlations can be made between mechanical behavior and grain orientation. Optimizing texture and microstructure are ways of enhancing mechanical properties in steels. An early work [480] concluded that {111} planes oriented towards the surface of a steel sheet favored increases in deep draw-ability and plastic anisotropy. From other investigations [327,438], the {001} cleavage planes are considered responsible for increased texture anisotropy and delamination. Nonetheless, the evolution of ideal texture components belonging to {001}||ND fibers can be minimized through properly controlled rolling. It is valid to say that the unique texture noticed in the TMCP and the two-step treated specimens contributed to their improved deformability in relation to the one-step treated specimen. Also, the increased presence of {111}||ND texture at the surface of both steels may have contributed to better resistance to hydrogen attack in comparison to the one-step treated specimen (Table 8.3). In summary, the results indicate that the hot rolled steel has the best combination of strength and ductility. The one-step treated specimen showed better strength then the two-step treated specimen, but its ductility was the poorest. Although the two-step treated specimen had the lowest strength, it revealed the highest ductility compared all other specimens.

8.9.2 Effect of hydrogen on yielding and flow stress behavior

There are controversies on whether steel becomes stronger or softer under the influence of hydrogen. This has resulted in a debate on what happens to yielding and flow stress after hydrogen charging. Some studies [12,13,17,378] have shown that hydrogen degradation susceptibility increases with strength due to strain hardening. Others [481] have either reported completely eliminated, or decreased yielding in the form of material softening. The possible explanation proposed by the authors is that hydrogen promotes dislocation motion. This further interferes with the work hardening process and lowers flow stress. In their opinion, accumulation of hydrogen around dislocations relaxes the elastic interaction. Since the authors studied high purity single crystals and bi-crystals of iron, it is expected that hydrogen mediated deformation mechanisms in alloyed polycrystalline materials will differ. Considering the relative increase in strength values obtained after testing hydrogen charged steels, the belief is that hydrogen induced hardening may

have occurred. Another evidence is seen in the disappearance of discontinuous yielding for the initial TMCP steel after pre-hydrogen charging. The pipeline steels investigated in this study contain microstructural features that could potentially create a solute atmosphere around dislocations. Therefore, continuous tensile loading after yielding means that solution hardening will lead to viscous drag through hydrogen atmosphere [482]. Therefore, the presence of hydrogen inside the steel could potentially interfere with dislocation motion during tensile loading. Furthermore, Oguri and Kimura [483] suggested that hardening in hydrogen charged iron proceeds according to the following systems synergy between hydrogen and impurities to diminish solution softening, and formation of hydrogen-impurity complexes to aid solution hardening.

8.9.3 Some related hydrogen embrittlement mechanisms

The evidence of HE in the fractured steels suggest that adsorbed hydrogen atoms influenced crack initiation and propagation. There is no doubt that hydrogen may have concentrated ahead of the crack tip inside the lattice, hence generating intense hydrostatic stresses as they are conveyed by dislocation motion. The contention about the exact embrittlement behavior in steel has remained unsolved. Some researchers [123,484] have argued that HE in non-hydride producing materials is either because of hydrogen enhanced localized plasticity (HELP) or hydrogen induced decohesion (HEDE) mechanism. The HELP system of fracture involves hydrogen interference with dislocation activities and enhancing crack formation due to planar slip whereas the HEDE is associated with inter-granular cleavage caused by reduced plasticity. Early fractographic investigation [118] on embrittled steels showed that hydrogen promoted dislocation motion. An increase in dislocation density will indirectly produce more trap sites for hydrogen. Also, the mobility of dislocations enhances the spread of atomic hydrogen inside the material. This is most prominent in areas of relatively high plastic deformation. In addition, various ideas have been proposed in many reviews [121,405]. Lynch [485] is of the opinion that HE does not necessarily have to occur based on localized slip and/or decohesion. Other studies [116,319] have found that the adsorption induced dislocation emission (AIDE) model is a mixture of hydrogen mediated bond softening (i.e. HEDE) and localized slip induced cracking (i.e. HELP). Despite numerous contradicting opinions on this subject, it is necessary to develop an experimental approach that clearly demonstrates these mechanisms. Currently, there is inadequate evidence to strongly justify the occurrence of a form of embrittlement. The HELP mechanism has gained wide attention mainly

due to microscopy-based studies that allow visualization of cracks and microstructural features such as dislocations. However, these techniques are often performed on very small portions on thin pieces of materials. Apart from these common mechanisms, Robertson *et al.* [484] outlined alternative forms of embrittlement that are noticeable in materials.

Nevertheless, it is not enough to solely attribute the HE phenomena to any of these mechanisms alone. Understanding the damaging effects of hydrogen on pipeline steel requires probing into the microstructural aspects. There are possibilities of having a combination of various embrittlement mechanisms depending on the mechanical testing conditions, hydrogen charging concentration, and type of material. These parameters create the enabling circumstances for revealing the connection between hydrogen permeation and embrittlement patterns. Luppo and Ovejero-Garcia [486] already established a direct relationship between embrittlement and amount of adsorbed hydrogen. They are of the view that diffusion and distribution of hydrogen across the steel structure is of utmost importance. Their idea can be linked to the HELP mechanism, since the mobility of hydrogen is required to advance plastic failure.

8.9.4 Effect of microstructure on hydrogen diffusion and trapping behavior

Variations in the fraction of recrystallized areas within each processed steel contributes towards HE behavior. Mohtadi-Bonab *et al.* [457] reported that the formation of recrystallized grains reduces strain induced defects that accumulate hydrogen and cause HIC. The understanding is that fewer obstacles are present in the recrystallized steel structure to interfere with hydrogen diffusion. However, embrittlement is not only determined by the permeation of hydrogen. Other considerations should include hydrogen solubility and trapping properties. Some important hydrogen trap sites seen within a deformed steel lattice are already established [79,487]. These traps are generally categorized based on their physical nature and ability to either hold hydrogen temporarily (reversible traps) or permanently (irreversible traps). The energy at which hydrogen is released from each type of trap vary depending on the energy of interaction between hydrogen and that particular trap site [94]. Strongly trapped hydrogen are believed to be less damaging owing to inadequate distribution of hydrogen across the steel. However, it is worth mentioning that permanently trapped hydrogen can lead to localized bond weakening and decohesion (i.e. HEDE) at critical levels. Reversible hydrogen traps such as vacancies, dislocations, grain boundaries and

substitutional solute atoms tend to have lower interaction energy with hydrogen compared with irreversible traps. Therefore, hydrogen atoms held at reversible traps can desorb after some time, but hydrogen trapped at irreversible sites cannot leave except at elevated temperatures. For instance, metallic inclusions such as incoherent precipitates of TiC combine actively with hydrogen because of a high interaction energy of up to 95 kJ/mol [488]. Pressouyre and Bernstein [489] developed a kinetic model for the prediction of HIC. They found that Fe-Ti alloy made up of fine reversible traps distributed uniformly will eventually circulate hydrogen harmlessly within the microstructure leading to a reduced extent of hydrogen damage. The presence of calcium and aluminum oxide inclusions where found to be responsible for HE in X60 pipeline steel designed for sour for service [490,491]. This implies that numerous inclusion particles can serve as permanent trapping location for hydrogen inside the steel. Also, they diminish mechanical properties, and potentially increasing the risks of embrittlement. On the other hand, fine particles of uniformly distributed irreversible traps result in prolonged onset of cracking.

Based on the hydrogen desorption activation energy, the change in hydrogen trapping energy with respect to tempering temperature can be determined [105]. According to the authors, two main microstructural factors that are responsible for hydrogen content in tempered martensitic steel include inherited dislocations and ferrite boundaries. They disregarded the hydrogen trapping contributions of carbide precipitates (i.e. cementite and ε-carbide). Despite some reports [492–494] establishing diverse precipitates of carbide as potential hydrogen traps in steel, there are indications that dislocations have greater effects. The disorderliness of these defects enables crack propagation. Consequently, the recovery process is necessary to lower stored energy through the rearrangement of dislocations [495]. They also established that minimal hydrogen charging time was required for cracking to occur in a deformed steel. This is due to the presence of many deformation induced defects that favor hydrogen related blister formation, crack initiation and propagation. Moreover, recovered materials are expected to show intermediated embrittlement characteristics that closely resemble those seen in highly recrystallized microstructures. The embrittlement pattern observed in this study suggest that the steel which experienced minimal recrystallization has relatively higher sensitivity to hydrogen assisted failure. In the one-step treated steel, an insignificant fraction of recrystallization is achieved (Fig. 8.8). This indirectly supports its poor HE resistance. The starting material was found to be more recrystallized and

recovered; whereas, the two-step treated steel showed some degree of recrystallization with negligible fraction of recovery in a mostly deformed structure. Yet, the highest embrittlement resistance occurred in the double-step processed steel. The implication is that HE mechanism must have been influenced by a combination of different circumstances.

Even highly recrystallized steels can still experience trans-granular cracking. Sometimes the main factor that determine failure may not just be hydrogen diffusivity. Different embrittlement systems manifest depending on the prevailing conditions. One could argue that the initial TMCP steel with the highest amount of recrystallization should be the most resistant to cracking. However, the results from this study did not show that. The starting material with higher recrystallization area fraction failed earlier than the two-step treated specimen after pre-hydrogen charging. It is possible that internal pressurization played a vital role in crack propagation. Rather than rely completely on texture and microstructural features to understand embrittlement behaviors, considerations should also be given to the risk of cracks being driven by internal stresses at defected regions. Recent findings [76] have suggested that neither HEDE nor HELP alone may be responsible for HE, instead crystal decohesion (i.e. decrease in inter-atomic bonding energy) and formation of structural defects should be considered. They are of the opinion that the current form of those models is unable to account for embrittlement down to the nanoscale. The idea is that microstructure may have a crucial influence at the initiation stage of cracking, but propagation is accelerated through the path of least resistance depending on various crack driving parameters.

The delayed failure observed in the two-step treated steel is unique due to its microstructure. Similar investigation by Davies [496] established that tempering dual-phase steel at temperatures above 350 °C results in less significant effect of hydrogen charging. The reason being that tempering lowers the strength of the evolved martensite and decreases embrittlement sensitivity. Elsewhere, phase transformations during heat treatments such as quenching, partitioning, and tempering have also been linked to enhanced resistance to HE [497]. This suggests that microstructure obtained after tempering the two-step treated specimen influenced its hydrogen degradation pattern. In addition, the evolution of refined grain structure creates more hydrogen traps in the form of ferrite-martensite interfaces and grain boundaries in dual-phase structured steels [498]. The current study indicates that hydrogen may have diffused easily through the starting material and the one-step treated steel compared to the two-step treated sample. The reason

being that the network of inter-connecting martensite particles (Fig. 8.2c and f) found across the quenched and tempered steel could have minimized the mobility of hydrogen. This will indirectly lower the susceptibility to HE in the two-step annealed steel. Carneiro *et al* [90] reported similar findings in pipeline steels with different alloying compositions and microstructures. They confirmed that refined quenched and tempered bainite-martensite microstructure showed better resistance to HIC/SSCC compared to as-rolled or normalized steels. Hence, the drastic reduction in ductility observed in the TMCP and one-step annealed steel can be related to diffusible hydrogen across their susceptible microstructure. Similar improvement in the trapping capacity of steel have been reported previously [492]. The authors also established that steel having martensitic microstructures can trap hydrogen effectively relative to other microstructures. Therefore, the localized agglomeration of atomic hydrogen will be minimized, leading to suppressed embrittlement tendencies. Finally, it is believed that the tempering process decomposed most retained austenite, reduce grains size, and lowered the density of dislocation within the martensite constituents in the dual-phase steel.

8.10 Summary

The effect of microstructure and texture developed through thermomechanical treatment followed by different annealing processes at inter-critical temperatures has been investigated. Two annealing treatments were adopted for this study namely a) one-step annealing process, and b) two-step annealing process. The following conclusions were made:

1. The microstructure of the starting material obtained after the initial hot rolling showed mainly acicular/bainitic ferrite, with few segregated martensite. For the one-step annealed specimen, martensite was sparsely seen, whereas the two-step treated specimen possessed a dual-phase (ferrite-martensite) structure.
2. Crystallographic texture analysis indicates that the starting material and two-step annealed steel comprise mainly of γ – fibers (specifically $\{111\}\langle 110\rangle$and $\{111\}\langle 112\rangle$), and θ – fibers (specifically $\{001\}\langle 110\rangle$, and $\{001\}\langle 100\rangle$), while the one-step annealed steel contain mainly ζ – fibers (specifically $\{110\}\langle 112\rangle$ and $\{110\}\langle 111\rangle$).
3. Tensile deformation of the initial treated steel resulted in a good combination of strength and ductility. The one-step annealed specimen displayed strength, which is next to that of the starting steel, but its ductility was the poorest. Despite having the lowest strength, the

two-step annealed steel showed the largest degree of ductility. The double annealing schedule resulted in significant reduction in grains size and the formation of tempered martensite, which made it the preferred route for improving deformability.

4. The microstructure and texture properties influenced the embrittlement behavior of pipeline steel. It was found that the two-step treated steel showed the highest embrittlement resistance compared to the one-step treated sample with is the most susceptible structure. The starting steel possessed intermediate HE characteristics. Therefore, the two-step annealing technique holds great promise in the development of highly deformable pipeline steel with enhanced resistance to hydrogen embrittlement.

CHAPTER 9 : SUMMARY, CONCLUSIONS, AND RECOMMENDATIONS FOR FUTURE WORKS

9.1 Overall summary and conclusions

The use of pipelines remains one of the most important methods for industrial transportation of fluids. However, limited research is currently available on their failure behavior in hydrogen related environments. The steel manufacturing industry has traditionally used strength as a means of categorizing pipeline steel. The present study confirms that microstructures can be used to assess the suitability of pipelines for applications in hydrogen producing environments. Irrespective of mechanical properties, other features such as secondary microstructural phases, inclusions, precipitates, grain orientation, grain boundary distribution, and grain size can potentially increase the risk of HIC even in supposedly high strength steels. This thesis is centered on the use of a thermomechanical processing approach to improve failure resistance of API 5L X70 pipeline steel. Different treatments were applied with the view of changing microstructure and enhancing the steel quality. Also, the evolution of microstructure, crystallographic texture, and mechanical properties were discussed. These features were investigated in relation to hydrogen induced failure mechanisms. This study is aimed at the following: 1) establishing the effects of microstructural characteristics on the electrochemical corrosion response of pipeline steels; 2) determining the role of microstructural features on hydrogen assisted cracking behavior in pipeline steels; and finally, 3) evaluating the effect of heat treatments on microstructure evolution and hydrogen embrittlement behavior of pipeline steel.

In line with the first objective of this study, the outcome of the investigation into corrosion behavior of newly developed pipeline steels is presented in Chapter 4 and 5. It is evident that among the four hot rolled specimens compared with commercially available X70, in Chapter 4, the specimen labelled WG showed better resistance to anodic dissolution relative to the others. The results from warm rolling (in Chapter 5) indicates that the steel rolled at a slightly elevated ferritic temperature of 700 °C performed better than those processed at 600 °C and 500 °C when exposed to both hydrogen producing and non-hydrogen producing media.

The results of HIC studies, which addresses the second objective of this research, are presented in Chapters 6 and 7. It was confirmed that the hot rolled steels labelled WH and WD displayed early

onset of cracking after 12 h of static hydrogen. A combination of in-situ hydrogen charging, and tensile loading led to a drastic loss of ductility in all the specimens. Consequently, fractures occurred below the yield strength. Although the strength is slightly lower in WG, it was observed to be the most resistant to cracking compared to the other hot rolled steels.

Based on the improved resistance to hydrogen assisted failure in specimen WG, its microstructure was identified for further inter-critical annealing procedures in view of the third objective. In order to recommend the microstructure developed in WG steel specimens, heat treatments were used to simulate microstructural changes that may occur during welding or high temperature applications. The results from this investigation are presented in Chapter 8. It was found that the microstructure achieved from the double step annealing treatment imparted a significant increase in ductility compared to the starting material and the single step annealed steel. In addition, the double step annealing treatment reduced hydrogen embrittlement susceptibility compared to both the hot rolled WG specimen and the single step treated steel.

The overall conclusions made from the entire project are as follows:

1. The electrochemical corrosion response of processed steels suggests that sensitivity to anodic dissolution depends on microstructures. Pipeline steel specimens such as WG and WD displayed stronger presence of finer ferrite grains at their surface layer relative to the other hot rolled steel. However, specimen WG showed decreased corrosion behavior in a hydrogen producing corrosive medium. This observation was attributed to relatively higher fraction of surface grains oriented towards both ⟨111⟩ and ⟨011⟩ directions, and the presence of finer bainitic and acicular ferrite grains. Corrosion response was found to increase in other steels containing higher fraction of ⟨001⟩ direction grains.
2. Warm rolling processing parameters affects microstructure development, which indirectly determines the corrosion behavior of rolled steel. The results from electrochemical corrosion measurements indicate a relationship between corrosion resistance and rolling temperature in the order of 700 ℃ > 600 ℃ > 500 ℃. Again, the Vickers hardness values increased with warm rolling temperature according to the following trend, $HV_{700\ ^\circ C} < HV_{600\ ^\circ C} < HV_{500\ ^\circ C}$. The associated texture measurement suggests that the largest proportion of ⟨111⟩ direction grains featured after rolling at 700 ℃. Moreover, the grains at the surface of the specimen warm rolled at 700 ℃ are mostly refined compared to the

other specimens. Molecular dynamics simulation of the interactions between corrosive species and specific crystal planes in steel shows an adsorption energy decrease in the order of $E_{interaction\ (111)} < E_{interaction\ (110)} < E_{interaction\ (100)}$ for the hydrogen producing and non-hydrogen producing media. Therefore, the low surface corrosion measured in specimens with high volume fraction of (111) crystals is justified.

3. The resultant microstructure obtained in specimen WG was primarily ferrite with many of martensite/austenite constituents. It was observed that a combination of grain refinement and secondary microstructural phases provided trap sites, which limited hydrogen diffusivity across steel, thus lowering susceptibility to cracking after hydrogen charging. The processing schedule adopted in producing specimens WG imparted the best resistance to hydrogen related degradation relative to the others.
4. Hydrogen induced cracking patterns in pipeline steel showed strong dependence on microstructures developed after processing, but crack propagation paths did not clearly show orientation dependence after static hydrogen charging. The ability of pipeline steel to deform plastically was eliminated by in-situ hydrogen attacks during tensile loading. Cracks initiated and propagated along the mid-thickness regions, which were banded with microstructural segregations. Also, the accumulation of secondary phases like iron carbide containing high angle grain boundaries aided crack initiation and propagation along the mid thickness region.
5. Inclusions and precipitates are important contributors in terms of promoting crack nucleation and propagation. Early onset of HIC in pipeline steel specimens, especially WH, was linked with multi-component inclusion particles containing precipitates of angular (Ti-Nb) N, spherical oxides of Al-Mg-Ca, and traces of Mo-Mn-S. The coherency between the inclusions and the steel matrix also affected crack behavior. Crack was noticed to have passed through spherical oxide inclusion in some instances and looped around them in other situations. This finding suggests that the property of inclusion particles affects crack initiation and propagation mechanisms.
6. Post-processing annealing treatments performed in two different cycles on WG pipeline steel resulted in the development of a dual-phase (ferrite-martensite) structure. The evolution of the tempered martensite network across the steel structure impeded growth and led to significant grain refinement. Also, the double-step annealed steel displayed

increased resistance to hydrogen embrittlement and enhanced deformability. Although strength was slightly reduced after the annealing treatment, similarities were observed in terms of textural properties in the two-step treated steel and that of the starting material.

9.2 Future perspectives on hydrogen related corrosion mechanisms

Generally, interpretations of HE studies are based on results obtained from very small sample of test materials. A lot of information regarding various microstructural parameters that affect hydrogen damage and degradation mechanisms reflect existing inconsistencies. In many aspects, hydrogen related corrosion patterns are yet to be well established in pipeline steel. This is because of the significant microstructural variations in TMCP steels, and limited data from EBSD as well as other characterization techniques. It has become necessary to develop safer pipelines that can last for longer periods of time. TMCP is expected to be further optimized to improve properties and reliability of steels in various service conditions. Such enhancements should be possible at a reasonable cost without jeopardizing weldability and machinability. Advanced metallurgical processes could be useful in controlling microstructure and texture evolution during steel manufacturing. Although descent amount of work has been done in this field, there is need for further exploration of methods for optimizing structure.

9.2.1 The complexity behind low embrittlement for low hydrogen concentration at interfaces

It is documented that without external stress application, the concentration of hydrogen at the interfaces and grain boundaries is low [125]. However, this rather complex phenomenon needs more research attention. More studies are needed on the mechanics of crack propagation and the decohesion thermodynamics at various interfaces. A better understanding of these problems could also address decohesion issues in the presence of impurity atoms, if experiments are conducted for stress-driven diffusion along interfaces. A few earlier works [9,499] on segregated interfaces have already addressed uniform separation under the influence of the tensile stress that was applied perpendicular to the interfacial plane. Future works should focus beyond ‘slow and fast separations’ of diffused impurities towards interfaces relative to the separation or the impurity sources.

9.2.2 Role of microstructural features in hydrogen embrittlement

It is widely reported that higher strength pipeline steels are more susceptible to HE compared to lower grades. However, earlier reports have demonstrated embrittlement exist in iron that has much lower strengths [500]. There is a lot of contradiction when it comes to different microstructures and their susceptibility to cracking. Some argue that acicular and bainitic ferrite are more resistant to HIC as opposed to ferritic pearlite or martensite microstructure, but evidence for this in the literature has remained either inconsistent or not fully proven [17,142,426]. This is questionable because different forms of hydrogen damage have been observed in pipeline steel having different microstructures. An in-depth investigation is necessary to clarify the role of each microstructural phase in HE. It is suggested that crystallographic texture and grain boundary engineering can be used to influence susceptibility to HIC in pipeline steels [14,114,150,206,281]. Most of the results show that $\{111\}$, $\{110\}$, and $\{332\}$ planes which are oriented parallel to the steel surface have the capacity to resist crack propagation, unlike $\{001\}$ planes that facilitate the crack propagation. The cracks have also been observed across $\{110\}||$ND textured grains. Further, research is required to properly understand the contributions of texture in HIC resistance of pipeline steels.

9.2.3 Binding energy of hydrogen trap sites

The classification of hydrogen trap sites as either reversible or irreversible is made using the binding energies of different traps [22]. Also, coherency of the inclusion or precipitates with steel may decide if trap is irreversible or reversible [163]. Although traps are categorized using thermal desorption experiments [109], emphasis should be on the fact that the hydrogen release rate is a function of time and temperature. Therefore, changes in pipeline operating temperatures can potentially alter the hydrogen trapping behavior. The role of the hydrogen binding energies of inclusions often found in pipeline steel is yet to be fully studied. There are still controversies surrounding the belief that some inclusions trap hydrogen irreversibly and improve resistance to HIC failure. We must remember that steel manufacturers often depend on precipitation strengthening to improve mechanical properties, and for this reason understanding the relationship between hydrogen trapping and precipitate characteristics is of importance. The role of composition, coherency, and number of precipitates on the susceptibility for hydrogen degradation should be investigated using experimental techniques and analyzed through theoretical modelling.

9.2.4 Standpoint on mechanism of hydrogen embrittlement

The exact mechanism of hydrogen damage in non-hydride forming materials such as pipeline steel remain largely unreliable. Lynch [319,405] argued that hydrogen weakens the interatomic bonds within the pipeline steel and allows for emission of dislocations along slip planes a mechanism known as adsorption-induced dislocation emission (AIDE). The author further stated that discounting hydrogen enhanced decohesion (HEDE) and AIDE while considering the hydrogen enhanced localized plasticity (HELP) mechanism as a single contributor to hydrogen-assisted cracking in pipeline steel may not be justified. The reason for this could be that AIDE considers the combination of bond weakening/decohesion and localized plasticity around mobile dislocations due to hydrogen as important. Koyama *et al.* [476] claimed that both HELP and HEDE synergistically induced hydrogen damage in dual-phase steel samples, an opinion which is largely consistent with the AIDE mechanism. In other words, both mechanisms can occur concurrently while factors such as temperature, environment, and stress intensity will determine their contribution to failure. Also, hydrogen diffusion in pipeline steel may be affected by accumulated strain, surface crystallography, roughness, steel structure and surface coverage [116]. It is necessary to point out that despite decades of research on the mechanism of hydrogen attack, controversy still exist concerning the failure mechanism and hydrogen embrittlement in different materials. This is partly due to the difficulties encountered in collecting evidences at the atomic level and limited capabilities of the current characterization techniques. An opinion expressed in most recent studies is that HELP and HEDE mechanisms are unable to explain hydrogen damage in their current form [76]. The authors of this study proposed a model based on decrease in defect formation energy and inter atomic bonding energy. Since the hydrogen embrittlement starts at the nano/micro scale, this has prompted further investigation into the micro-mechanisms of damage progression on oil and gas pipelines operating in hydrogen environment. Profoundly, Nagumo [501] observed that hydrogen related damage is a function of vacancy accumulation instead of just hydrogen. This mechanism has been accepted by many researchers. Another study argued that enhanced plasticity is followed by the accumulation of vacancies by nano-void coalescence [322].

REFERENCES

[1] K. Nishioka, K. Ichikawa, Progress in thermomechanical control of steel plates and their commercialization, Science and Technology of Advanced Materials. 13 (2012) 023001.

[2] S. Endo, N. Nakata, Development of Thermo-Mechanical Control Process (TMCP) and high performance steel in JFE Steel, JFE Technical Report. 20 (2015) 1–7.

[3] D. Mizuno, K. Yasuda, N. Ishikawa, M. Kimura, K. Kobayashi, T. Fujishiro, E. Tada, T. Hara, Recent activities in ISIJ HLP research committee corrosion working group: Proposal of pH buffer test solution for fitness-for-purpose HIC evaluations, ISIJ International. 56 (2016) 498–503.

[4] A. Yoshie, M. Fujioka, Y. Watanabe, K. Nishioka, H. Morikawa, Modelling of microstructural evolution and mechanical properties of steel plates produced by thermo-mechanical control process., ISIJ International. 32 (2008) 395–404.

[5] M. Elboujdaini, R. W. Revie, Metallurgical factors in stress corrosion cracking (SCC) and hydrogen-induced cracking (HIC), Journal of Solid State Electrochemistry. 13 (2009) 1091–1099.

[6] T. Hara, H. Asahi, H. Ogawa, Conditions of hydrogen-induced corrosion occurence of X65 grade line pipe steels in sour environments, Corrosion. 60 (2004) 1113–1121.

[7] Q. Liu, A. Atrens, A critical review of the influence of hydrogen on the mechanical properties of medium-strength steels, Corrosion Reviews. 31 (2013) 85–103.

[8] E. Ohaeri, U. Eduok, J. Szpunar, Hydrogen related degradation in pipeline steel: A review, International Journal of Hydrogen Energy. 43 (2018) 14584–14617.

[9] J. P. Hirth, Effects of hydrogen on the properties of iron and steel, Metallurgical Transactions A. 11 (1980) 861–890.

[10] G. Ghosh, P. Rostron, R. Garg, A. Panday, Hydrogen induced cracking of pipeline and pressure vessel steels: A review, Engineering Fracture Mechanics. 199 (2018) 609–618.

[11] A. Charles, Corrosion mechanisms in theory and practice, 2nd Edition, Hardback, Electrochimica Acta. 48 (2003) 1081.

[12] E. Ohaeri, J. Szpunar, F. Fazeli, M. Arafin, Hydrogen induced cracking susceptibility of API 5L X70 pipeline steel in relation to microstructure and crystallographic texture developed after different thermomechanical treatments, Materials Characterization. 145

(2018) 142–156.

[13] E. Ohaeri, J. Omale, A. Tiamiyu, K. M. M. Rahaman, J. Szpunar, Influence of thermomechanically controlled processing on microstructure and hydrogen induced cracking susceptibility of API 5L X70 pipeline steel, Journal of Materials Engineering and Performance. 27 (2018) 4533–4547.

[14] M. A. Mohtadi-Bonab, J. A. Szpunar, R. Basu, M. Eskandari, The mechanism of failure by hydrogen induced cracking in an acidic environment for API 5L X70 pipeline steel, International Journal of Hydrogen Energy. 40 (2015) 1096–1107.

[15] M. Masoumi, L. Flavio, G. Herculano, H. Ferreira, G. De Abreu, Study of texture and microstructure evaluation of steel API 5L X70 under various thermomechanical cycles, Materials Science & Engineering A. 639 (2015) 550–558.

[16] T. P. Perng, J. K. Wu, A brief review note on mechanisms of hydrogen entry into metals, Materials Letters. 57 (2003) 3437–3438.

[17] M. A. Arafin, J. A. Szpunar, Effect of bainitic microstructure on the susceptibility of pipeline steels to hydrogen induced cracking, Materials Science and Engineering A. 528 (2011) 4927–4940.

[18] D. Bai, L. Collins, F. Hamad, X. Chen, R. Klein, Microstructure and mechanical properties of high strength linepipes steels, Proceedings of the Materials Science & Technology Congress; AIST/ASM: Warrendale, PA, USA, (2007) 355–366.

[19] S. Vervynckt, K. Verbeken, B. Lopez, J. J. Jonas, Modern HSLA steels and role of non-recrystallisation temperature, International Materials Reviews. 57 (2012) 187–207.

[20] S. Ghosh, S. Mula, Thermomechanical processing of low carbon Nb-Ti stabilized microalloyed steel: Microstructure and mechanical properties, Material Science & Engineering A. 646 (2015) 218–233.

[21] P. Valles, M. Gómez, S. F. Medina, A. Pastor, O. Vilanova, Evolution of microstructure and precipitation state during thermomechanical processing of a low carbon microalloyed steel, Microscopy and Microanalysis. 18 (2012) 119–120.

[22] K. O. Findley, M. K. O'Brien, H. Nako, Critical assessment 17: Mechanisms of hydrogen induced cracking in pipeline steels, Materials Science and Technology (United Kingdom). 31 (2015) 1673–1680.

[23] A. Brown, C. L. Jones, Hydrogen induced cracking in pieline steels, Corrosion. 40 (1984)

330–336.

[24] A. K. Nieto, J. Elias, T. Lopez, G. Campos, G. Lopez, F. Garcia, R. De, Development of technology for the production of HIC resistant slabs for sour service applications at Arcelormittal Lazaro Cardenas, Materials Science and Technology. (2012) 1044–1053.

[25] G. T. Park, S. U. Koh, G. H. Jung, Y. K. Kim, Effect of microstructure on the hydrogen trapping efficiency and hydrogen induced cracking of linepipe steel, Corrosion Science. 50 (2008) 1865–1871.

[26] B. Hwang, Y. M. Kim, S. Lee, N. J. Kim, J. Y. Yoo, Correlation of rolling condition, microstructure, and low-temperature toughness of X70 pipeline steels, Metallurgical and Materials Transactions A. 36 (2005) 1793–1805.

[27] N. Hansen, Hall – Petch relation and boundary strengthening, 51 (2004) 801–806.

[28] Y. I. Matrosov, E .O. Tskitishvili, E. S. Popov, G. N. Konovalov, A. A. Kholodnyi, Accelerated cooling after controlled rolling during heavy plate pipe steel manufacture in 3600 mill at the azovstal metallurgical combine, Metallurgist. 57 (2014) 837–844.

[29] DNVGL-Report, Assessment of global cost of corrosion, (2015).

[30] C. I. Ossai, B. Boswell, I. J. Davies, Pipeline failures in corrosive environments - A conceptual analysis of trends and effects, Engineering Failure Analysis. 53 (2015) 36–58.

[31] M. A. Mohtadi-bonab, M. Eskandari, K. M. M. Rahman, R. Ouellet, An extensive study of hydrogen-induced cracking susceptibility in an API X60 sour service pipeline steel, International Journal of Hydrogen Energy. 41 (2016) 4185–4197.

[32] M. A. Mohtadi-Bonab, M. Eskandari, R. Karimdadashi, J. A. Szpunar, Effect of different microstructural parameters on hydrogen induced cracking in an API X70 pipeline steel, Metals and Materials International. 23 (2017) 726–735.

[33] V. Venegas, F. Caleyo, T. Baudin, J. M. Hallen, R. Penelle, Role of microtexture in the interaction and coalescence of hydrogen-induced cracks, Corrosion Science. 51 (2009) 1140–1145.

[34] V. Venegas, F. Caleyo, T. Baudin, J. H. Espina-hernández, J. M. Hallen, On the role of crystallographic texture in mitigating hydrogen-induced cracking in pipeline steels, Corrosion Science. 53 (2011) 4204–4212.

[35] J. Bauer, P. Flu¨ss, E. Amoris, V. Schwinn, Microstructure and properties of thermomechanical controlled processing steels for linepipe applications, Ironmaking &

Steelmaking. 32 (2005) 325–330.

[36] API 5L, Specification for line pipe, 2000.

[37] B. D. B. Tiu, R. C. Advincula, Polymeric corrosion inhibitors for the oil and gas industry: Design principles and mechanism, Reactive and Functional Polymers. 95 (2015) 25–45.

[38] W. Beck, J. O. Bockris, J. McBreen, L. Nanis, Hydrogen permeation in metals as a function of stress, temperature and dissolved hydrogen concentration, Proceedings of the Royal Society A: Mathematical, Physical and Engineering Sciences. 290 (1966) 220–235.

[39] M. Al-Mansour, A. M. Alfantazi, M. El-boujdaini, Sulfide stress cracking resistance of API-X100 high strength low alloy steel, Materials and Design. 30 (2009) 4088–4094.

[40] T. Wenman, J. Dim, Pipeline integrity management, SPE International Petroleum Exhibition & Conference, (2012) 11–14.

[41] R. Palmer-jones, S. Turner, P. Hopkins, A new approach to risk based pipeline integrity management, International Pipeline Conference, Calgary, Alberta, Canada. 44 (2006) 811–823.

[42] G. Schreier, D. Hausamann, I. Lingenfelder, U. Benz, W. Zirnig, Test cases and prospects of pipeline management using space borne earth observation, Proceedings, 31st International Symposium on Remote Sensing of Environment, ISRSE 2005: Global Monitoring for Sustainability and Security. (2005)1-7.

[43] C. V. Tao, Y. Hu, Assessment of airborne lidar and imaging technology for pipeline mapping and safety applications, Pecora 15/Land Satellite Information IV/ISPRS Commission I/FIEOS 2002 Conference Proceedings, (2002) 1-11.

[44] C. I. Ossai, Advances in asset management techniques: An overview of corrosion mechanisms and mitigation strategies for oil and gas pipelines, ISRN Corrosion. 2012 (2012) 1–10.

[45] H. R. Vanaei, A. Eslami, A. Egbewande, A review on pipeline corrosion, in-line inspection (ILI), and corrosion growth rate models, International Journal of Pressure Vessels and Piping. 149 (2017) 43–54.

[46] T. Beuker, B. Stephan, H. Lindner, Overcoming the specific issues associated with the in-line inspection of gas pipelines, Pipeline & Gas Journal. 238 (2011) 28–40.

[47] E. Bini, L. Di Biase, D. Scrocchi, G. Zonta, Cost-saving strategies for pipeline integrity, Onshore Pipeline Cost Reduction Conference Organised by Pipes and Pipelines

International, Amsterdam, (2000) 5–13.

[48] O. Barrera, D. Bombac, Y. Chen, T. Daff, E. Galindo-nava, D. Haley, R. Horton, I. Katzarov, Understanding and mitigating hydrogen embrittlement of steels atomistic to continuum review of experimental , modelling and design progress, Journal of Materials Science. 53 (2018) 1–44.

[49] Y. F. Cheng, Analysis of electrochemical hydrogen permeation through X-65 pipeline steel and its implications on pipeline stress corrosion cracking, International Journal of Hydrogen Energy. 32 (2007) 1269–1276.

[50] Y. F. Cheng, Fundamentals of hydrogen evolution reaction and its implications on near-neutral pH stress corrosion cracking of pipelines, Electrochimica Acta. 52 (2007) 2661–2667.

[51] O. J. Van Der Schijff, R. M. Latanision, Pipeline condition sssessment - locating, diagnosing, and mitigating corrosion damage, NACE Corrosion Conference & Expo. (2011) 1–9.

[52] I. Thompson, J. R. Saithala, Review of pipeline coating systems from an operator's perspective, Corrosion Engineering, Science and Technology. 51 (2015) 118–135.

[53] C. J. Townend, R. D. Worthington, N. M. Munro, A comparative review of some modern pipeline coatings and experience gained applying a polyurethane-tar coating, Anti-Corrosion Methods and Materials. 27 (1980) 5–11.

[54] L. Fan, F. Tang, S. T. Reis, G. Chen, M. L. Koenigstein, Corrosion resistance of transmission pipeline steel coated with five types of enamels, Acta Metallurgica Sinica (English Letters). 30 (2017) 390–398.

[55] S. Papavinasam, M. Attard, W. R. Revie, Evolution of external pipeline coatings for corrosion protection – A review, Corrosion Reviews. 26 (2008) 2–4.

[56] U. Angst, M. Büchler, B. Martin, H.G. Schöneich, G. Haynes, S. Leeds, F. Kajiyama, Cathodic protection of soil buried steel pipelines – a critical discussion of protection criteria and threshold values, Materials and Corrosion. 67 (2016) 1135–1142.

[57] V. A. Ojeda, L. Lázaro, J. J. Benito, J. M. Bastidas, Assessment of cathodic protection by close interval survey incorporating the instant off potential method, Corrosion Engineering, Science and Technology. 51 (2016) 241–247.

[58] L. P. Djukic, W. S. Sum, K. H. Leong, W. D. Hillier, T. W. Eccleshall, A. Y. L. Leong,

Development of a fibre reinforced polymer composite clamp for metallic pipeline repairs, Materials and Design. 70 (2015) 68–80.

[59] K. C. Bendall, Corrosion resistant alloys - an industry-wide overview of applications, Anti-Corrosion Methods and Materials. 42 (1995) 12–15.

[60] S. Hasan, L. Sweet, J. Hults, G. Valbuena, B. Singh, M. Carlo, Corrosion risk-based subsea pipeline design, International Journal of Pressure Vessels and PIping. 159 (2018) 1–14.

[61] A. A. Olajire, Corrosion inhibition of offshore oil and gas production facilities using organic compound inhibitors - A review, Journal of Molecular Liquids. 248 (2017) 775–808.

[62] G. P. Tiwari, A. Bose, J.K. Chakravartty, S.L. Wadekar, M.K. Totlani, A study of internal hydrogen embrittlement of steels, Materials Science & Engineering A. 286 (2000) 269–281.

[63] P. Kentish, Stress corrosion cracking of gas pipelines - Effect of surface roughness, orientations and flattening, Corrosion Science. 49 (2007) 2521–2533.

[64] W. K. Kim, H. G. Jung, G. T. Park, S. U. Koh, K. Y. Kim, Relationship between hydrogen-induced cracking and type I sulfide stress cracking of high-strength linepipe steel, Scripta Materialia. 62 (2010) 195–198.

[65] A. R. Troiano, The role of hydrogen and other interstitials in the mechanical behavior of metals: (1959 Edward De Mille Campbell Memorial Lecture), Metallography, Microstructure, and Analysis. 5 (2016) 557–569.

[66] R. A. Oriani, A mechanistic theory of hydrogen embrittlement of steels, Berichte Der Bunsengesellschaft Für Physikalische Chemie. 76 (1972) 848–857.

[67] R. A. Oriani, P.H. Josephic, Equilibrium and kinetic studies of the hydrogen-assisted cracking of steel, Acta Metallurgica. 25 (1977) 979–988.

[68] C. Lam, W. Zhou, Statistical analyses of incidents on onshore gas transmission pipelines based on PHMSA database, International Journal of Pressure Vessels and Piping. 145 (2016) 29–40.

[69] G. Rosenberg, I. Sinaiova, Evaluation of hydrogen induced damage of steels by different test methods, Materials Science and Engineering A. 682 (2017) 410–422.

[70] N. Shohoji, Comparative study of solubilities of hydrogen, nitrogen and carbon in iron, Journal of Materials Science. 21 (1986) 2147–2152.

[71] L. R. Botvina, I. M. Petrova, I. V Gadolina, V. P. Levin, A. P. Soldatenkov, High cycle fatigue failure of low carbon steel after long term aging, Inorganic Materials. 46 (2010)

1570–1577.

[72] B. Vargas-Arista, A. Albiter, F. García-Vázquez, Ó. Mendoza-Camargo, J. M. Hallen, Effect of natural aging on the microstructural regions, mechanical properties, corrosion resistance and fracture in welded joints on API5L X52 steel pipeline, Revista de Metalurgia. 50 (2014) 1-11.

[73] H. Matsui, H. Kimura, S. Moriya, The effect of hydrogen on the mechanical properties of high purity iron I. Softening and hardening of high purity iron by hydrogen charging during tensile deformation, Material Science & Engineering. 40 (1979) 207–216.

[74] M. Smialowski, Softening vs. hardening effects produced in iron by charging with high fugacity hydrogen, Scripta Metallurgica. 13 (1979) 393–395.

[75] X. Li, J. Zhang, Y. Wang, B. Li, P. Zhang, X. Song, Effect of cathodic hydrogen-charging current density on mechanical properties of prestrained high strength steels, Materials Science and Engineering A. 641 (2015) 45–53.

[76] A. Barnoush, H. Vehoff, Recent developments in the study of hydrogen embrittlement: Hydrogen effect on dislocation nucleation, Acta Materialia. 58 (2010) 5274–5285.

[77] E. Villalba, A. Atrens, Hydrogen embrittlement and rock bolt stress corrosion cracking, Engineering Failure Analysis. 16 (2009) 164–175.

[78] M. Loidl, O. Kolk, Hydrogen embrittlement in HSSs limits use in lightweight body in white design, Advanced Materials and Processes. 169 (2011) 22–25.

[79] G. Pressouyre, I. Bernstein, A quantitative analysis of hydrogen trapping, Metallurgical Transactions A. 9A (1978) 1571–1580.

[80] P. Roffey, E. H. Davies, The generation of corrosion under insulation and stress corrosion cracking due to sulphide stress cracking in an austenitic stainless steel hydrocarbon gas pipeline, Engineering Failure Analysis. 44 (2014) 148–157.

[81] Y. S. Chen, D. Haley, S. S. A. Gerstl, A. J. London, F. Sweeney, R. A. Wepf, W. M. Rainforth, P. A. J. Bagot, M. P. Moody, Direct observation of individual hydrogen atoms at trapping sites in a ferritic steel, Science. 355 (2017) 1196–1199.

[82] M. Javidi, S. Bahalaou Horeh, Investigating the mechanism of stress corrosion cracking in near-neutral and high pH environments for API 5L X52 steel, Corrosion Science. 80 (2014) 213–220.

[83] X. Chen, X. G. Li, C. W. Du, Y. F. Cheng, Effect of cathodic protection on corrosion of

pipeline steel under disbonded coating, Corrosion Science. 51 (2009) 2242–2245.

[84] B. Fang, E. H. Han, J. Wang, Z. Zhu, W. Ke, Hydrogen in stress corrosion cracking of X-70 pipeline steels in near-neutral pH solutions, Journal of Materials Science. 41 (2006) 1797–1803.

[85] B. Y. Fang, A. Atrens, J. Q. Wang, E. H. Han, Z. Y. Zhu, W. Ke, Review of stress corrosion cracking of pipeline steels in “low” and “high” pH solutions, Journal of Materials Science. 38 (2003) 127–132.

[86] D. Kuang, Y. F. Cheng, Study of cathodic protection shielding under coating disbondment on pipelines, Corrosion Science. 99 (2015) 249–257.

[87] M. Gojić, L. Kosec, L. Vehovar, The susceptibility to sulphide stress cracking of low alloy steels, Materials and Corrosion - Werkstoffe Und Korrosion. 49 (1998) 27–33.

[88] Z. H. Zhang, M. Liu, Y. H. Liu, M. Luo, C. X. Zhang, C. H. Wang, G. H. Cao, A systematical analysis with respect to multiple hydrogen traps influencing sulfide stress cracking behavior of API-5CT-C110 casing steel, Materials Science and Engineering A. 721 (2018) 81–88.

[89] B. Beidokhti, A. Dolati, A. H. Koukabi, Effects of alloying elements and microstructure on the susceptibility of the welded HSLA steel to hydrogen-induced cracking and sulfide stress cracking, Materials Science and Engineering A. 507 (2009) 167–173.

[90] R. A. Carneiro, R. C. Ratnapuli, V. de Freitas Cunha Lins, The influence of chemical composition and microstructure of API linepipe steels on hydrogen induced cracking and sulfide stress corrosion cracking, Materials Science and Engineering A. 357 (2003) 104–110.

[91] M. A. Lucio-Garcia, J. G. Gonzalez-Rodriguez, M. Casales, L. Martinez, J. G. Chacon-Nava, M. A. Neri-Flores, A. Martinez-Villafañe, Effect of heat treatment on H_2S corrosion of a micro-alloyed C-Mn steel, Corrosion Science. 51 (2009) 2380–2386.

[92] J. L. Gonzalez, R. Ramirez, J. M. Hallen, R. A. Guzman, Hydrogen-induced crack growth rate in steel plates exposed to sour environments, Corrosion (Houston). 53 (1997) 935–943.

[93] A. Kawashima, K. Hashimoto, S. Shimodaira, Hydrogen electrode reaction and hydrogen embrittlement of mild steel in hydrogen sulfide solutions, Corrosion. 32 (1976) 321–331.

[94] M. Liu, C.H. Wang, Y. C. Dai, X. Li, G. H. Cao, A. M. Russell, Y. H. Liu, X. M. Dong, Effect of quenching and tempering process on sulfide stress cracking susceptibility in API-

5CT-C110 casing steel, Material Science & Engineering A. 688 (2017) 378–387.

[95] M. A. Al-Anezi, G. S. Frankel, A. K. Agrawal, Susceptibility of conventional pressure vessel steel to HIC and SOHIC in H_2S d iglycolamine solutions, Corrosion. 55 (1999) 1101–1109.

[96] H. Huang, W. J. D. Shaw, Cold work effects on sulfide stress cracking of pipeline steel exposed to sour environments, Corrosion Science. 34 (1993) 61–78.

[97] R. J. Pargeter, Susceptibility to SOHIC for linepipe and pressure vessel- Review of current knowledge, NACE Corrosion. (2007) 1–27.

[98] M. S. Cayard, R. D. Kane, R. J. Horvath, SOHIC resistance of C-Mn plate steels used in refinery service, Corrosion. (2002) 1–12.

[99] D. Li, R. P. Gangloff, J. R. Scully, Hydrogen trap states in ultrahigh-strength AERMET 100 steel, Metallurgical and Materials Transactions A. 35 (2004) 25–27.

[100] P. Castaño Rivera, V. P. Ramunni, P. Bruzzoni, Hydrogen trapping in an API 5L X60 steel, Corrosion Science. 54 (2012) 106–118.

[101] W. Y. Choo, J. Y. Lee, Effect of cold working on the hydrogen trapping phenomena in pure iron, Metallurgical Transactions A. 14 (1983) 1299–1305.

[102] H. Wu, A. V. Skripov, T. J. Udovic, J. J. Rush, S. Derakhshan, H. Kleinke, Hydrogen in Ti_3Sb and Ti_2Sb: Neutron vibrational spectroscopy and neutron diffraction studies, Journal of Alloys and Compounds. 496 (2010) 1–6.

[103] J. G. Roquefere, J. Lang, A. Yonkeu, J. Dufour, J. Huot, Effect of iron on the hydriding properties of the Mg6Pd hydrogen storage system, International Journal of Hydrogen Energy. 36 (2011) 2165–2169.

[104] B. Beidokhti, P. He, A. H. Kokabi, A. Dolati, Control of hydrogen cracking in the welded steel using microstructural traps, Materials Science and Technology (United Kingdom). 33 (2017) 408–414.

[105] F. G. Wei, K. Tsuzaki, Response of hydrogen trapping capability to microstructural change in tempered Fe-0.2C martensite, Scripta Materialia. 52 (2005) 467–472.

[106] T. Yamaguchi, M. Nagumo, Simulation of hydrogen thermal desorption under reversible trapping by lattice defects, ISIJ International. 43 (2008) 514–519.

[107] T. Ohmisawa, S. Uchiyama, M. Nagumo, Detection of hydrogen trap distribution in steel using a microprint technique, Journal of Alloys and Compounds. 356–357 (2003) 290–294.

[108] M. A. Mohtadi-Bonab, H. Ghesmati-Kucheki, Important factors on the failure of pipeline steels with focus on hydrogen induced cracks and improvement of their resistance: review paper, Metals and Materials International. 25 (2019) 1109-1134.

[109] H. K. D. H. Bhadeshia, Prevention of Hydrogen Embrittlement in Steels, ISIJ International. 56 (2016) 24–36.

[110] H. M. Ha, J. H. Ai, J. R. Scully, Effects of prior cold work on hydrogen trapping and diffusion in API X-70 line pipe steel during electrochemical charging, Corrosion. 70 (2014) 166–184.

[111] V. P. Ramunni, T. D. P. Coelho, P. E. V de Miranda, Interaction of hydrogen with the microstructure of low-carbon steel, Materials Science and Engineering A. 435–436 (2006) 504–514.

[112] H. J. Grabke, F. Gehrmann, E. Riecke, Hydrogen in microalloyed steels, Steel Research. 72 (2001) 225–235.

[113] M. Dadfarnia, P. Sofronis, T. Neeraj, Hydrogen interaction with multiple traps: Can it be used to mitigate embrittlement?, International Journal of Hydrogen Energy. 36 (2011) 10141–10148.

[114] M. A. Mohtadi-Bonab, J. A. Szpunar, S. S. Razavi-Tousi, Hydrogen induced cracking susceptibility in different layers of a hot rolled X70 pipeline steel, International Journal of Hydrogen Energy. 38 (2013) 13831–13841.

[115] L. Jemblie, V. Olden, P. Mainçon, O.M. Akselsen, Cohesive zone modelling of hydrogen induced cracking on the interface of clad steel pipes, International Journal of Hydrogen Energy. 42 (2017) 28622–28634.

[116] S. P. Lynch, Progress towards understanding mechanisms of hydrogen embrittlement and stress corrosion cracking, NACE Corrosion, (2007), 1–10.

[117] W. W. Gerberich, P. G. Marsh, J. W. Hoehn, Hydrogen induced cracking mechanisms - are there critical experiments?, Hydrogen Effects in Materials, (1996) 539–551.

[118] C. D. Beachem, A new model for hydrogen-assited crcaking (hydrogen “embrittlement”), Metallurgical and Materials Transactions B. 3 (1972), 441-455.

[119] H. K. Birnbaum, P. Sofronis, Hydrogen-enhanced localized plasticity-a mechanism for hydrogen-related fracture, Materials Science and Engineering A. 176 (1994) 191–202.

[120] I. M. Robertson, H. K. Birnbaum, P. Sofronis, Chapter 91 Hydrogen Effects on Plasticity,

Dislocations in Solids. 15 (2009) 249–293.

[121] S. P. Lynch, Mechanisms of hydrogen assisted cracking - A review, Proceedings of the International Conference on Hydrogen Effects on Material Behaviour and Corrosion Deformation Interactions. (2003) 449–466.

[122] P. Martin, M. L. Robertson, I. M. Sofronis, Interpreting hydrogen-induced fracture surfaces in terms of deformation processes: A new approach, Acta Materialia. 59 (2011) 3680–3687.

[123] P. Sofronis, I. M. Robertson, Viable mechanisms of hydrogen embrittlement - A review, AIP Conference Proceedings. 837 (2006) 64–70.

[124] F. F. Dear, G. C. G. Skinner, Mechanisms of hydrogen embrittlement in steels: discussion Subject Areas, Philosophical Transactions A. 375 (2017).

[125] I. H. Katzarov, A. T. Paxton, Hydrogen embrittlement II. Analysis of hydrogen-enhanced decohesion across (111) planes in α-Fe, Physical Review Materials. 1 (2017) 033603.

[126] H. K. Birnbaum, Hydrogen effects on deformation - Relation between dislocation behavior and the macroscopic stress-strain behavior, Scripta Metallurgica et Materiala. 31 (1994) 149–153.

[127] I. M. Robertson, H. K. Birnbaum, An HVEM study of hydrogen effects on the deformation and fracture of nickel, Acta Metallurgica. 34 (1986) 353–366.

[128] P. Rozenak, I. M. Robertson, H. K. Birnbaum, HVEM studies of the effects of hydrogen on the deformation and fracture of AISI type 316 austenitic stainless steel, Acta Metallurgica Et Materialia. 38 (1990) 2031–2040.

[129] J. Song, W. A. Curtin, Mechanisms of hydrogen-enhanced localized plasticity: An atomistic study using α-Fe as a model system, Acta Materialia. 68 (2014) 61–69.

[130] S. S. Nayak, R. D. K. Misra, J. Hartmann, F. Siciliano, J. M. Gray, Microstructure and properties of low manganese and niobium containing HIC pipeline steel, Materials Science and Engineering A. 494 (2008) 456–463.

[131] J. H. Bae, Y. J. Ro, S. H. Chon, H. K. Sung, S. Lee, C. S. Lee, Development of X60 and X100 linepipe steels with high deformation capacity for strain-based design, Proceedings of the International Offshore and Polar Engineering Conference, (2015) 657–662.

[132] W. Wang, Y. Shan, K. Yang, Study of high strength pipeline steels with different microstructures, Materials Science and Engineering A. 502 (2009) 38–44.

[133] G. Mori, J. Feyerl, H. Zitter, On the influence of hydrogen content and stress level on

hydrogen embrittlement of bainitic carbon steel fasteners, NACE Corrosion, (2002) 1–10.

[134] H. K. D. H. Bhadeshia, Lower bainite transformation and the significance of carbide precipitation., Acta Metallurgica. 28 (1980) 1103–1114.

[135] H. K. D. H. Bhadeshia, D. V. Edmonds, Mechanism of bainite formation in steels., Acta Metallurgica. 28 (1980) 1265–1273.

[136] J. Xu, R. D. K. Misra, B. Guo, Z. Jia, L. Zheng, Understanding variability in mechanical properties of hot rolled microalloyed pipeline steels : Process – structure – property relationship, Material Science & Engineering A. 574 (2013) 94–103.

[137] D. P. Dunne, D. Hejazi, A. A. Saleh, A. J. Haq, A. Calka, E. V. Pereloma, Investigation of the effect of electrolytic hydrogen charging of X70 steel: I. The effect of microstructure on hydrogen-induced cold cracking and blistering, International Journal of Hydrogen Energy. 41 (2016) 12411–12423.

[138] G. Domizzi, G. Anteri, J. Ovejero-García, Influence of sulphur content and inclusion distribution on the hydrogen induced blister cracking in pressure vessel and pipeline steels, Corrosion Science. 43 (2001) 325–339.

[139] J. I. Omale, E. G. Ohaeri, A. A. Tiamiyu, M. Eskandari, K. M. Mostafijur, J. A. Szpunar, Microstructure, texture evolution and mechanical properties of X70 pipeline steel after different thermomechanical treatments, Materials Science and Engineering: A. 703 (2017) 477–485.

[140] E. Ramírez, J. G. González-Rodriguez, A. Torres-Islas, S. Serna, B. Campillo, G. Dominguez-Patiño, J. A. Juárez-Islas, Effect of microstructure on the sulphide stress cracking susceptibility of a high strength pipeline steel, Corrosion Science. 50 (2008) 3534–3541.

[141] L. Lan, C. Qiu, D. Zhao, X. Gao, Microstructural Evolution and Mechanical Properties of Nb-Ti Microalloyed Pipeline Steel, Journal of Iron and Steel Research, International. 18 (2011) 57–63.

[142] D. Hardie, E. A. Charles, A. H. Lopez, Hydrogen embrittlement of high strength pipeline steels, Corrosion Science. 48 (2006) 4378–4385.

[143] T. Depover, D. Pérez Escobar, E. Wallaert, Z. Zermout, K. Verbeken, Effect of hydrogen charging on the mechanical properties of advanced high strength steels, International Journal of Hydrogen Energy. 39 (2014) 4647–4656.

[144] S. J. Kim, Effect of the elastic tensile load on the electrochemical corrosion behavior and diffusible hydrogen content of ferritic steel in acidic environment, International Journal of Hydrogen Energy. 42 (2017) 19367–19375.

[145] S. J. Kim, H. G. Jung, K. Y. Kim, Effect of tensile stress in elastic and plastic range on hydrogen permeation of high-strength steel in sour environment, Electrochimica Acta. 78 (2012) 139–146.

[146] A. Telang, A. S. Gill, K. Zweiacker, C. Liu, J. M. K. Wiezorek, V. K. Vasudevan, Effect of thermo-mechanical processing on sensitization and corrosion in alloy 600 studied by SEM- and TEM-Based diffraction and orientation imaging techniques, Journal of Nuclear Materials. (2017) 1–13.

[147] M. A. Arafin, J. A. Szpunar, A new understanding of intergranular stress corrosion cracking resistance of pipeline steel through grain boundary character and crystallographic texture studies, Corrosion Science. 51 (2009) 119–128.

[148] M. Eskandari, M. R. Yadegari-Dehnavi, A. Zarei-Hanzaki, M. A. Mohtadi-Bonab, R. Basu, J. A. Szpunar, In-situ strain localization analysis in low density transformation-twinning induced plasticity steel using digital image correlation, Optics and Lasers in Engineering. 67 (2015) 1–16.

[149] V. Venegas, F. Caleyo, J. L. González, T. Baudin, J. M. Hallen, R. Penelle, EBSD study of hydrogen-induced cracking in API-5L-X46 pipeline steel, Scripta Materialia. 52 (2005) 147–152.

[150] M. Masoumi, C. C. Silva, M. Béreš, D. H. Ladino, H. F. G. de Abreu, Role of crystallographic texture on the improvement of hydrogen-induced crack resistance in API 5L X70 pipeline steel, International Journal of Hydrogen Energy. 42 (2017) 1318–1326.

[151] A. A. Saleh, D. Hejazi, A. A. Gazder, D. P. Dunne, E. V. Pereloma, Investigation of the effect of electrolytic hydrogen charging of X70 steel: II. Microstructural and crystallographic analyses of the formation of hydrogen induced cracks and blisters, International Journal of Hydrogen Energy. 41 (2016) 12424–12435.

[152] S. I. Wright, D. P. Field, Recent studies of local texture and its influence on failure, Materials Science and Engineering A. 257 (1998) 165–170.

[153] E. Ohaeri, J. Omale, U. Eduok, J. Szpunar, Effect of thermomechanical processing and crystallographic orientation on the corrosion behavior of API 5L X70 pipeline steel,

Metallurgical and Materials Transactions A: Physical Metallurgy and Materials Science. 49 (2018) 2269–2280.

[154] N. Ishikawa, H. Sueyoshi, A. Nagao, Hydrogen Microprint Analysis on the Effect of Dislocations on Grain Boundary Hydrogen Distribution in Steels, ISIJ International. 56 (2016) 413–417.

[155] M. Koyama, E. Akiyama, K. Tsuzaki, D. Raabe, Hydrogen-assisted failure in a twinning-induced plasticity steel studied under in situ hydrogen charging by electron channeling contrast imaging, Acta Materialia. 61 (2013) 4607–4618.

[156] D. Dwivedi, K.R. Lepko, T. Becker, Carbon steel corrosion: a review of key surface properties and characterization methods, RSC Adv. 7 (2017) 4580–4610.

[157] O. Lavigne, E. Gamboa, J. Griggs, V. Luzin, M. Law, A. Roccisano, High-pH inclined stress corrosion cracking in Australian and Canadian gas pipeline X65 steels, Materials Science and Technology. 32 (2016) 684–690.

[158] M. A. Mohtadi-Bonab, M. Eskandari, J. A. Szpunar, Texture, local misorientation, grain boundary and recrystallization fraction in pipeline steels related to hydrogen induced cracking, Materials Science and Engineering A. 620 (2015) 97–106.

[159] O. Lavigne, E. Gamboa, V. Luzin, M. Law, M. Giuliani, W. Costin, The effect of the crystallographic texture on intergranular stress corrosion crack paths, Materials Science and Engineering A. 618 (2014) 305–309.

[160] M. Masoumi, C. C. Silva, H. F. G. de Abreu, Effect of crystallographic orientations on the hydrogen-induced cracking resistance improvement of API 5L X70 pipeline steel under various thermomechanical processing, Corrosion Science. 111 (2016) 121–131.

[161] W. Qin, J.A. Szpunar, A general model for hydrogen trapping at the inclusion-matrix interface and its relation to crack initiation, Philosophical Magazine. 97 (2017) 3296–3316.

[162] T. Depover, O. Monbaliu, E. Wallaert, K. Verbeken, Effect of Ti , Mo and Cr based precipitates on the hydrogen trapping and embrittlement of Fe-C-X Q&T alloys, International Journal of Hydrogen Energy. 40 (2015) 16977–16984.

[163] F. G. Wei, K. Tsuzaki, Quantitative analysis on hydrogen trapping of TiC particles in steel, Metallurgical and Materials Transactions A: Physical Metallurgy and Materials Science. 37 (2006) 331–353.

[164] T.Y. Jin, Z.Y. Liu, Y.F. Cheng, Effect of non-metallic inclusions on hydrogen-induced

cracking of API5L X100 steel, International Journal of Hydrogen Energy. 35 (2010) 8014–8021.

[165] M. A. Mohtadi-Bonab, M. Eskandari, A focus on different factors affecting hydrogen induced cracking in oil and natural gas pipeline steel, Engineering Failure Analysis. 79 (2017) 351–360.

[166] C. F. Dong, X. G. Li, Z. Y. Liu, Y. R. Zhang, Hydrogen-induced cracking and healing behaviour of X70 steel, Journal of Alloys and Compounds. 484 (2009) 966–972.

[167] H. R. Hajibagheri, A. Heidari, R. Amini, An experimental investigation of the nature of longitudinal cracks in oil and gas transmission pipelines, Journal of Alloys and Compounds. 741 (2018) 1121-1129.

[168] O. M. I. Todoshchenko, Y. Yagodzinskyy, T. Saukkonen, H. Hänninen, Role of nonmetallic inclusions in hydrogen embrittlement of high-strength carbon steels with different microalloying, Metallurgical and Materials Transactions A. 45 (2014) 4742–4747.

[169] M. W. Zhou, H. Yu, Effects of precipitates and inclusions on the fracture toughness of hot rolling X70 pipeline steel plates, International Journal of Minerals, Metallurgy and Materials. 19 (2012) 805–811.

[170] J. Nieto, T. Elías, G. Lopez, G. Campos, F. Lopez, R. Garcia, A.K. De, Effective process design for the production of HIC-resistant linepipe steels, Journal of Materials Engineering and Performance. 22 (2013) 2493–2499.

[171] J. H. Liu, H. J. Wu, Y. P. Bao, M. Wang, Inclusion variations and calcium treatment optimization in pipeline steel production, International Journal of Minerals, Metallurgy and Materials. 18 (2011) 527–534.

[172] Z. Lv, H.-W. Ni, H. Zhang, C. Liu, Evolution of MnS inclusions in Ti-bearing X80 pipeline steel, Journal of Iron and Steel Research, International. 24 (2017) 654–660.

[173] Z. Y. Liu, X. G. Li, C.W. Du, L. Lu, Y. R. Zhang, Y.F. Cheng, Effect of inclusions on initiation of stress corrosion cracks in X70 pipeline steel in an acidic soil environment, Corrosion Science. 51 (2009) 895–900.

[174] Y. Li, J. Liu, Y. Deng, X. Han, W. Hu, C. Zhong, Ex situ characterization of metallurgical inclusions in X100 pipeline steel before and after immersion in a neutral pH bicarbonate solution, Journal of Alloys and Compounds. 673 (2016) 28–37.

[175] H. B. Xue, Y. F. Cheng, Hydrogen permeation and electrochemical corrosion behavior of

the X80 pipeline steel weld, Journal of Materials Engineering and Performance. 22 (2013) 170–175.

[176] F. Huang, J. Liu, Z. J. Deng, J. H. Cheng, Z. H. Lu, X. G. Li, Effect of microstructure and inclusions on hydrogen induced cracking susceptibility and hydrogen trapping efficiency of X120 pipeline steel, Material Science & Engineering A. 527 (2010) 6997–7001.

[177] S. C. Hong, S. H. Lim, H. S. Hong, K. J. Lee, D. H. Shin, K. S. Lee, Effects of Nb on strain induced ferrite transformation in C-Mn steel, Materials Science and Engineering A. 355 (2003) 241–248.

[178] C. P. Reip, S. Shanmugam, R. D. K. Misra, High strength microalloyed CMn(V-Nb-Ti) and CMn(V-Nb) pipeline steels processed through CSP thin-slab technology: Microstructure, precipitation and mechanical properties, Materials Science and Engineering A. 424 (2006) 307–317.

[179] P. Ghosh, R. K. Ray, Effects of composition and coiling temperature on precipitation and texture formation in a few interstitial free high strength steels, Ceramic Transactions. 200 (2008) 151–159.

[180] C. Capdevila, V. Amigó, F. G. Caballero, C. G. de Andrés, M. D. Salvador, Influence of microalloying elements on recrystallization texture of warm-rolled interstitial free steels, Materials Transactions. 51 (2010) 625–634.

[181] F. Haddadi, J. W. Cho, S. Y. Lee, The effect of chemical composition on grain structure and texture evolution of hot rough rolled carbon steels, Materials Science and Engineering A. 607 (2014) 102–112.

[182] G. Chen, W. Yang, S. Guo, Z. Sun, Characteristics of microstructural evolution during deformation-enhanced ferrite transformation in Nb-microalloyed HSLA steel, Journal of University of Science and Technology Beijing. 14 (2007) 36–40.

[183] Z. Shirband, M. R. Shishesaz, A. Ashrafi, Hydrogen degradation of steels and its related parameters, a review, Phase Transitions. 84 (2011) 924–943.

[184] C. Mendibide, T. Sourmail, Composition optimization of high-strength steels for sulfide stress cracking resistance improvement, Corrosion Science. 51 (2009) 2878–2884.

[185] A. Graux, S. Cazottes, D. De Castro, D. San Martín, C. Capdevila, J.M. Cabrera, S. Molas, S. Schreiber, D. Mirković, F. Danoix, M. Bugnet, D. Fabrègue, M. Perez, Precipitation and grain growth modelling in Ti-Nb microalloyed steels, Materialia. 5 (2019) 100233.

[186] S. Vervynckt, P. Thibaux, K. Verbeken, Effect of niobium on the microstructure and mechanical properties of hot rolled microalloyed steels after recrystallization-controlled rolling, Metals and Materials International. 18 (2012) 37–46.

[187] H. Y. Liou, R. I. Shieh, F. I. Wei, S. C. Wang, Roles of microalloying elements in hydrogen induced cracking resistant property HSLA steel, Corrosion. 49 (1993) 389–398.

[188] J. Moon, S. J. Kim, C. Lee, Role of Ca treatment in hydrogen induced cracking of hot rolled API pipeline steel in acid sour media, Metals and Materials International. 19 (2013) 45–48.

[189] A. J. Deardo, Niobium in modern steels, International Materials Reviews. 48 (2003) 371–402.

[190] W. B. Morrison, Microalloy steels – the beginning, Materials Science and Technology. 25 (2009) 1066–1073.

[191] J. Villalobos, A. Del-Pozo, B. Campillo, J. Mayen, S. Serna, Microalloyed Steels through History until 2018: Review of Chemical Composition, Processing and Hydrogen Service, Metals. 8 (2018) 351.

[192] T. N. Baker, Titanium microalloyed steels, Ironmaking and Steelmaking. 46 (2019) 1–55.

[193] T. N. Baker, Microalloyed steels, Ironmaking & Steelmaking. 43 (2016) 264–307.

[194] T. I. Ramjaun, S. W. Ooi, R. Morana, H. K. D. H. Bhadeshia, Designing steel to resist hydrogen embrittlement: Part 1-trapping capacity Designing steel to resist hydrogen embrittlement: Part 1-trapping capacity, Materials Science and Technology. 34 (2018) 1737–1746.

[195] K. Baba, D. Mizuno, K. Yasuda, H. Nakamichi, N. Ishikawa, Effect of Cu addition in pipeline steels on prevention of hydrogen permeation in mildly sour environments, Corrosion. 72 (2016) 1107–1115.

[196] X. Shi, W. Yan, W. Wang, Y. Shan, K. Yang, Novel Cu-bearing high-strength pipeline steels with excellent resistance to hydrogen-induced cracking, Materials and Design. 92 (2016) 300–305.

[197] A. J. Haq, K. Muzaka, D. P. Dunne, A. Calka, E. V Pereloma, Effect of microstructure and composition on hydrogen permeation in X70 pipeline steels, International Journal of Hydrogen Energy. 38 (2013) 2544–2556.

[198] M. N. Nazarova, R. R. Akhmetov, S. A. Krainov, Temperature factors effect on occurrence of stress corrosion cracking of main gas pipeline, IOP Conference Series: Earth and

Environmen Science, (2017) 062011.

[199] F. Xie, D. Wang, M. Wu, C. Yu, D. Sun, X. Yang, C. Xu, Effect of applied potentials on stress corrosion cracking of X80 pipeline steel in simulated Yingtan soil solution, Metallurgical and Materials Transactions A. 49 (2018) 1372–1382.

[200] P. C. Okonkwo, M. H. Sliem, R. A. Shakoor, A. M. A. Mohamed, A. M. Abdullah, Effect of temperature on the corrosion behavior of API X120 pipeline steel in H_2S environment, Journal of Materials Engineering and Performance. 26 (2017) 3775–3783.

[201] NACE TM 0284-2016, Standard Test Method: Evaluation of pipeline and pressure vessel steels for resistance to hydrogen-induced cracking.

[202] ANSI/NACE TM0177-2016, Standard Test Method: Laboratory testing of metals for resistance to sulfide stress cracking and stress corrosion cracking in H_2S environments.

[203] NACE TM198-2016, Slow strain rate test method for screening corrosion-resistant alloys (CRAs) for stress corrosion cracking in sour oilfield service.

[204] F. Thebault, S. Frappart, L. Delattre, H. Marchebois, L.A. Rochelle, Hydrogen diffusion in model molybdenum containing steel: A comparison between hydrogen ingress promoted by H_2S or cathodic charging, NACE Corrosion Conference & Expo, (2011) 1–14.

[205] J. A. Ronevich, J .G. Speer, G. Krauss, D. K. Matlock, Improvement of the hydrogen microprint technique on AHSS steels, Metallography, Microstructure, and Analysis. 1 (2012) 79–84.

[206] M. A. Mohtadi-Bonab, J. A. Szpunar, S. S. Razavi-Tousi, A comparative study of hydrogen induced cracking behavior in API 5L X60 and X70 pipeline steels, Engineering Failure Analysis. 33 (2013) 163–175.

[207] M. Koyama, D. Yamasaki, K. Tsuzaki, In situ observations of silver-decoration evolution under hydrogen permeation: Effects of grain boundary misorientation on hydrogen flux in pure iron, Scripta Materialia. 140 (2017) 91–92.

[208] M. I. Luppo, J. Ovejero-García, New application of the hydrogen microprint technique for the study of hydrogen behaviour in steels, Journal of Materials Science Letters. 14 (1995) 682–684.

[209] J. Ovejero-García, Hydrogen microprint technique in the study of hydrogen in steels, Journal of Materials Science. 20 (1985) 2623–2629.

[210] P. Kappen, B. D. Arhatari, M. B. Luu, E. Balaur, T. Caradoc-Davies, Combined synchrotron

X-ray tomography and X-ray powder diffraction using a fluorescing metal foil, Review of Scientific Instruments. 84 (2013) 063703.

[211] N. Kardjilov, I. Manke, A. Hilger, M. Strobl, J. Banhart, Neutron imaging in materials science, Materials Today. 14 (2011) 248–256.

[212] A. Griesche, E. Dabah, T. Kannengiesser, N. Kardjilov, A. Hilger, I. Manke, Three-dimensional imaging of hydrogen blister in iron with neutron tomography, Acta Materialia. 78 (2014) 14–22.

[213] A. Griesche, E. Dabah, T. Kannengiesser, A. Hilger, N. Kardjilov, I. Manke, B. Schillinger, Measuring Hydrogen Distributions in Iron and Steel Using Neutrons, Physics Procedia. 69 (2015) 445–450.

[214] Y. Zhao, M. Seok, I. Choi, Y. Lee, S. Park, U. Ramamurty, J. Suh, J. Jang, The role of hydrogen in hardening / softening steel : Influence of the charging process, Scripta Materialia. 107 (2015) 46–49.

[215] C. V. Tapia-Bastidas, A. Atrens, E. M. A. Gray, Thermal desorption spectrometer for measuring ppm concentrations of trapped hydrogen, International Journal of Hydrogen Energy. 43 (2018) 7600–7617.

[216] A. Turnbull, R.B. Hutchings, D.H. Ferriss, Modelling of thermal desorption of hydrogen from metals, Materials Science and Engineering A. 238 (1997) 317–328.

[217] E. V. Chatzidouros, A. Traidia, R. S. Devarapalli, D. I. Pantelis, T. A. Steriotis, M. Jouiad, Effect of hydrogen on fracture toughness properties of a pipeline steel under simulated sour service conditions, International Journal of Hydrogen Energy. 43 (2018) 5747–5759.

[218] L. Zhang, H. Shen, K. Lu, W. Cao, Y. Sun, Y. Fang, Y. Xing, Y. Du, M. Lu, Investigation of hydrogen concentration and hydrogen damage on API X80 steel surface under cathodic overprotection, International Journal of Hydrogen Energy. 42 (2017) 29888–29896.

[219] S. Evers, C. Senöz, M. Rohwerder, Hydrogen detection in metals: A review and introduction of a Kelvin probe approach, Science and Technology of Advanced Materials. 14 (2013) 014201.

[220] L. Dapeng, H. Wenhui, L. Yingkun, Z. Lei, L. Minxu, W. Jiejun, Effect of H_2S content on corrosion behaviour and hydrogen permeation of pipeline steel, NACE Corrosion, (2014) 1–11.

[221] M. A. Mohtadi-Bonab, R. Karimdadashi, M. Eskandari, J. A. Szpunar, Hydrogen-induced

cracking assessment in pipeline steels through permeation and crystallographic texture measurements, Journal of Materials Engineering and Performance. 25 (2016) 1781–1793.

[222] L. Niu, Y. F. Cheng, Development of innovative coating technology for pipeline operation crossing the permafrost terrain, Construction and Building Materials. 22 (2008) 417–422.

[223] T. C. Bayram, N. Orbey, R. Y. Adhikari, M. Tuominen, FP-based formulations as protective coatings in oil/gas pipelines, Progress in Organic Coatings. 88 (2015) 54–63.

[224] B. Y. Chang, S. M. Park, Electrochemical impedance spectroscopy, Annual Review of Analytical Chemistry. 3 (2010) 207–229.

[225] W. Reitz, A Review of: "Impedance spectroscopy, theory, experiment, and applications, E. Barsoukov and J. R. Macdonald, (editors)," Materials and Manufacturing Processes. 22 (2007) 294–294.

[226] D. D. MacDonald, Reflections on the history of electrochemical impedance spectroscopy, Electrochimica Acta. 51 (2006) 1376–1388.

[227] E. S. Ivanov, P. P. Stepanov, Y. V. Ryabov, D. V. Kudashov, A. L. Klyuev, Use of impedance spectroscopy for evaluating pipe steel susceptibility towards hydrogenation and hydrogen cracking, Metallurgist. 56 (2012) 597–603.

[228] A. Aballe, A. Bautista, U. Bertocci, F. Huet, Measurement of the noise resistance for corrosion applications, Corrosion. 57 (2001) 35–42.

[229] R. Galván-Martínez, R. Orozco-Cruz, J. Mendoza-Flores, J. Genesca-Llongueras, A. Contreras-Cuevas, Electrochemical noise study on corrosion of low carbon pipeline steel in sour solutions, Materials Science Forum. 793 (2014) 67–76.

[230] F. Mansfeld, The electrochemical noise technique - Applications in corrosion research, AIP Conference Proceedings. 780 (2005) 625–630.

[231] R. E. Ricker, U. Bertocci, A review of electrochemical noise and its application to the study of stress corrosion cracking, The Metals & Materials Society. (1996) 235–245.

[232] Y. Zhao, P. Liang, Y. Shi, Y. Zhang, T. Yang, The pitting susceptibility investigation of passive films formed on X70, X80, and X100 pipeline steels by electrochemical noise and Mott-Schottky measurements, International Journal of Corrosion. 2015 (2015) 12–14.

[233] D. Örnek, T. K. Wood, C. H. Hsu, Z. Sun, F. Mansfeld, Pitting corrosion control of aluminum 2024 using protective biofilms that secrete corrosion inhibitors, Corrosion. 58 (2002) 761–767.

[234] F. M. Alabbas, C. Williamson, S. M. Bhola, J. R. Spear, D. L. Olson, B. Mishra, A.E. Kakpovbia, Influence of sulfate reducing bacterial biofilm on corrosion behavior of low-alloy, high-strength steel (API-5L X80), International Biodeterioration & Biodegradation. 78 (2013) 34–42.

[235] H. Castaneda, X. D. Benetton, SRB-biofilm influence in active corrosion sites formed at the steel-electrolyte interface when exposed to artificial seawater conditions, Corrosion Science. 50 (2008) 1169–1183.

[236] J. W. Costerton, Bacterial bofilms: a common cause of persistent infections, Science. 284 (1999) 1318–1322.

[237] F. K. Sahrani, Z. Ibrahim, A. Yahya, A. Madzlan, Isolation and Identification of Marine Sulphate-Reducing Bacteria, Desulfovibrio sp and Citrobacter freundii from Pasir Gudang, Malaysia, Sains Malaysiana. 37 (2008) 365–371.

[238] M. V. V. Biezma, The role of hydrogen in microbiologically influenced corrosion and stress corrosion cracking, International Journal of Hydrogen Energy. 26 (2001) 515–520.

[239] T. Wu, M. Yan, D. Zeng, J. Xu, C. Sun, C. Yu, W. Ke, Hydrogen permeation of X80 steel with superficial stress in the presence of sulfate-reducing bacteria, Corrosion Science. 91 (2015) 86–94.

[240] M. Stipaničev, O. Rosas, R. Basseguy, F. Turcu, Electrochemical and fractographic analysis of Microbiologically Assisted Stress Corrosion Cracking of carbon steel, Corrosion Science. 80 (2014) 60–70.

[241] U. Eduok, O. Faye, J. Szpunar, Recent developments and applications of protective silicone coatings: A review of PDMS functional materials, Progress in Organic Coatings. 111 (2017) 124–163.

[242] M. Yan, J. Wang, E. Han, W. Ke, Local environment under simulated disbonded coating on steel pipelines in soil solution, Corrosion Science. 50 (2008) 1331–1339.

[243] I. B. Obot, I. B. Onyeachu, A. M. Kumar, Sodium alginate: A promising biopolymer for corrosion protection of API X60 high strength carbon steel in saline medium, Carbohydrate Polymers. 178 (2017) 200–208.

[244] S. A. Umoren, A. Madhankumar, Effect of addition of CeO_2 nanoparticles to pectin as inhibitor of X60 steel corrosion in HCl medium, Journal of Molecular Liquids. 224 (2016) 72–82.

[245] I. B. Obot, N.K. Ankah, A. Sorour, Z. M. Gasem, K. Haruna, 8-Hydroxyquinoline as an alternative green and sustainable acidizing oilfield corrosion inhibitor, Sustainable Materials and Technologies. 14 (2017) 1–10.

[246] J. A. Calderón, F. A. Vásquez, J. A. Carreño, Adsorption and performance of the 2-mercaptobenzimidazole as a carbon steel corrosion inhibitor in EDTA solutions, Materials Chemistry and Physics. 185 (2017) 218–226.

[247] N. C. Ngobiri, E. E. Oguzie, N. C. Oforka, O. Akaranta, Comparative study on the inhibitive effect of Sulfadoxine-Pyrimethamine and an industrial inhibitor on the corrosion of pipeline steel in petroleum pipeline water, Arabian Journal of Chemistry. 12 (2019) 1024-1034.

[248] T. Wu, J. Xu, C. Sun, M. Yan, C. Yu, W. Ke, Microbiological corrosion of pipeline steel under yield stress in soil environment, Corrosion Science. 88 (2014) 291–305.

[249] T. Wu, M. Yan, D. Zeng, J. Xu, C. Sun, C. Yu, W. Ke, Stress Corrosion Cracking of X80 Steel in the Presence of Sulfate-reducing Bacteria, Journal of Materials Science & Technology. 31 (2015) 413–422.

[250] K. M. Al-Nabulsi, F. M. Al-Abbas, T. Y. Rizk, A. E. M. Salameh, Microbiologically assisted stress corrosion cracking in the presence of nitrate reducing bacteria, Engineering Failure Analysis. 58 (2015) 165–172.

[251] T. Liu, Y. F. Cheng, The influence of cathodic protection potential on the biofilm formation and corrosion behaviour of an X70 steel pipeline in sulfate reducing bacteria media, Journal of Alloys and Compounds. 729 (2017) 180–188.

[252] H. Liu, Y. Frank Cheng, Mechanism of microbiologically influenced corrosion of X52 pipeline steel in a wet soil containing sulfate-reduced bacteria, Electrochimica Acta. 253 (2017) 368–378.

[253] X. Chen, G. Wang, F. Gao, Y. Wang, C. He, Effects of sulphate-reducing bacteria on crevice corrosion in X70 pipeline steel under disbonded coatings, Corrosion Science. 101 (2015) 1–11.

[254] T. Liu, Y. F. Cheng, M. Sharma, G. Voordouw, Effect of fluid flow on biofilm formation and microbiologically influenced corrosion of pipelines in oilfield produced water, Journal of Petroleum Science and Engineering. 156 (2017) 451–459.

[255] H. Wan, D. Song, D. Zhang, C. Du, Z. Liu, D. Ding, X. Li, D. Song, D. Zhang, C. Du, Z. Liu, D. Ding, X. Li, Corrosion effect of Bacillus cereus on X80 pipeline steel in a Beijing

soil environment, Bioelectrochemistry. 121 (2018) 18–26.

[256] A. Bahgat Radwan, M.H. Sliem, P.C. Okonkwo, M.F. Shibl, A.M. Abdullah, Corrosion inhibition of API X120 steel in a highly aggressive medium using stearamidopropyl dimethylamine, Journal of Molecular Liquids. 236 (2017) 220–231.

[257] N. Muthukumar, A. Ilangovan, S. Maruthamuthu, N. Palaniswamy, A. Kimura, 1-Aminoanthraquinone derivatives as a novel corrosion inhibitor for carbon steel API 5L-X60 in white petrol-water mixtures, Materials Chemistry and Physics. 115 (2009) 444–452.

[258] K. Hu, J. Zhuang, C. Zheng, Z. Ma, L. Yan, H. Gu, X. Zeng, J. Ding, Effect of novel cytosine- L -alanine derivative based corrosion inhibitor on steel surface in acidic solution, 222 (2016) 109–117.

[259] G. Xia, X. Jiang, L. Zhou, Y. Liao, M. Duan, H. Wang, Q. Pu, J. Zhou, Enhanced anticorrosion of methyl acrylate by covalent bonded N-alkylpyridinium bromide for X70 steel in 5M HCl, Journal of Industrial and Engineering Chemistry. 27 (2015) 133–148.

[260] U. Eduok, E. Jossou, J. Szpunar, Enhanced surface protective performance of chitosanic hydrogel by nano-CeO_2 dispersion for API 5L X70 alloy: Experimental and theoretical examination of the contributions of CeO_2, Journal of Molecular Liquids. 241 (2017) 684–693.

[261] A. S. Fouda, M. A. Elmorsi, S. M. Shaban, T. Fayed, O. Azazy, Evaluation of N-(3-(dimethyl hexadecyl ammonio)propyl) palmitamide bromide as cationic surfactant corrosion inhibitor for API N80 steel in acidic environment, Egyptian Journal of Petroleum. 27 (2018) 683-694.

[262] Y. Z. Li, N. Xu, X. P. Guo, G. A. Zhang, Inhibition effect of imidazoline inhibitor on the crevice corrosion of N80 carbon steel in the CO_2-saturated NaCl solution containing acetic acid, Corrosion Science. 126 (2017) 127–141.

[263] E. B. Ituen, J. E. Asuquo, Inhibition of X80 steel corrosion in oilfield acidizing environment using 3-(2-chloro-5,6-dihydrobenzo[b][1]benzazepin-11-yl)-N,N-dimethylpropan-1-amine and its blends, Journal of King Saud University - Science. 31 (2017) 127-135.

[264] M. Yadav, D. Behera, U. Sharma, Nontoxic corrosion inhibitors for N80 steel in hydrochloric acid, Arabian Journal of Chemistry. 61 (2016) 1487–1495.

[265] S. A. Umoren, I. B. Obot, A. Madhankumar, Z. M. Gasem, Performance evaluation of pectin as ecofriendly corrosion inhibitor for X60 pipeline steel in acid medium: Experimental and

theoretical approaches, Carbohydrate Polymers. 124 (2015) 280–291.

[266] S. A. Umoren, Polypropylene glycol: A novel corrosion inhibitor for X60 pipeline steel in 15% HCl solution, Journal of Molecular Liquids. 219 (2016) 946–958.

[267] Y. Zhu, J. Zhuang, Y. Yu, X. Zeng, Research on anti-corrosion property of rare earth inhibitor for X70 steel, Journal of Rare Earths. 31 (2013) 734–740.

[268] G. Xia, X. Jiang, L. Zhou, Y. Liao, M. duan, H. Wang, Q. Pu, J. Zhou, Synergic effect of methyl acrylate and N-cetylpyridinium bromide in N-cetyl-3-(2-methoxycarbonylvinyl)pyridinium bromide molecule for X70 steel protection, Corrosion Science. 94 (2015) 224–236.

[269] Y. Zuo, L. Yang, Y. Tan, Y. Wang, J. Zhao, The effects of thioureido imidazoline and $NaNO_2$ on passivation and pitting corrosion of X70 steel in acidic NaCl solution, Corrosion Science. 120 (2017) 99–106.

[270] H. Ashrafi, M. Shamanian, R. Emadi, N. Saeidi, A novel and simple technique for developement of dual phase steels with excellent ductility, Material Science & Engineering A. 680 (2017) 197–202.

[271] S. I. Wright, M. M. Nowell, S. P. Lindeman, P. P. Camus, M. De Graef, M. A. Jackson, Introduction and comparison of new EBSD post-processing methodologies, Ultramicroscopy. 159 (2015) 81–94.

[272] T. Maitland, Electron backscattered diffraction, Advanced Materials & Processes. (2004) 34–36.

[273] A. H. King, S. Shekhar, What does it mean to be special? The significance and application of the Brandon criterion, Journal of Materials Science. 41 (2006) 7675–7682.

[274] A. A. Kovalev, L. A. Tishchenko, V. D. Shashurin, A. L. Galinovskii, Application of X-ray diffraction methods to studying materials, Russian Metallurgy (Metally). 2017 (2017) 1186–1193.

[275] NACE International Task Group (TG) 070, Field monitoring of corrosion rates in oil and gas production environments using electrochemical techniques, (2014).

[276] H.A. Masayuki Sagara, Yusaku Tomio, Yohei Otome, Naoki Sawawatari, Tomohiko Omura, Evaluation of susceptibility of hydrogen embrittlement of high strength corrosion resistant alloys, NACE Corrosion Conference & Expo, (2016) 1–15.

[277] K. O. Sulaiman, A. T. Onawole, O. Faye, D. T. Shuaib, Understanding the corrosion

inhibition of mild steel by selected green compounds using chemical quantum based assessments and molecular dynamics simulations, Journal of Molecular Liquids. 279 (2019) 342–350.

[278] M. A. V Devanathan, Z. Stachurski, The adsorption and diffusion of electrolytic hydrogen in palladium, in: Proceedings of the Royal Society of London. Series A, Mathematical and Physical Sciences, (1962) 90–102.

[279] J. P. D. Carvalho, E. O. Vilar, B. A. Araújo, A critical review and experimental analysis of the equation recommended by ASTM G148-97 and ISO 17081: 2004 for the calculation of the hydrogen diffusivity in metals and alloys, International Journal of Hydrogen Energy. 42 (2017) 681–688.

[280] G. Biggiero, A. Borruto, I. Taraschi, Effects of hydrogen charging methods on ductility and fracture characteristics of AISI 9840 steel, International Journal of Hydrogen Energy. 20 (1995) 465–470.

[281] M. A. Mohtadi-Bonab, J. A. Szpunar, L. Collins, R. Stankievech, Evaluation of hydrogen induced cracking behavior of API X70 pipeline steel at different heat treatments, International Journal of Hydrogen Energy. 39 (2014) 6076–6088.

[282] G. Koch, J. Varney, N. Thompson, O. Moghissi, M. Gould, J. Payer, International measures of prevention, application, and economics of corrosion technologies study, NACE International. (2016) 1–3.

[283] A. W. Peabody, R. L. Bianchetti, Control of Pipeline Corrosion Second Edition, 2000.

[284] E. Klechka, S. F. Daily, K. C. Garrity, Practical consideration for upper limits of cathodic protection, Concrete. (2007) 1–11.

[285] V. Ashworth, Principles of cathodic protection, Shreir's Corrosion. 2 (2010) 2747–2762.

[286] H. B. Xue, Y. F. Cheng, Passivity and pitting corrosion of X80 pipeline steel in carbonate/bicarbonate solution studied by electrochemical measurements, Journal of Materials Engineering and Performance. 19 (2010) 1311–1317.

[287] D. L. Miller, K. D. Efird, N. Davis, Rate measurements in the presence of hydrogen sulphide: electrochemical activity of solution species, NACE Corrosion Conference & Expo, (2008) 1–21.

[288] M. Tjelta, J. Kvarekval, Electrochemistry of iron sulfide and its galvanic coupling to carbon steel in sour aqueous solutions, NACE Corrosion Conference & Expo, (2016) 1–14.

[289] F. F. Eliyan, A. Alfantazi, Electrochemical investigations on the corrosion behavior and corrosion natural inhibition of API-X100 pipeline steel in acetic acid and chloride-containing CO_2-saturated media, Journal of Applied Electrochemistry. 42 (2012) 233–248.

[290] A. Shahryari, J. A. Szpunar, S. Omanovic, The influence of crystallographic orientation distribution on 316LVM stainless steel pitting behavior, Corrosion Science. 51 (2009) 677–682.

[291] M. Hoseini, A. Shahryari, S. Omanovic, J. A. Szpunar, Comparative effect of grain size and texture on the corrosion behaviour of commercially pure titanium processed by equal channel angular pressing, Corrosion Science. 51 (2009) 3064–3067.

[292] M. Jiang, L. N. Chen, J. He, G. Y. Chen, C. H. Li, X. G. Lu, Effect of controlled rolling/controlled cooling parameters on microstructure and mechanical properties of the novel pipeline steel, Advances in Manufacturing. 2 (2014) 265–274.

[293] X. L. Wan, K. M. Wu, Z. H. Xia, The Effect of microstructure on properties of high deformation pipeline steel X70, Advanced Materials Research. 690 (2013) 182–185.

[294] D. Hejazi, A. J. Haq, N. Yazdipour, D. P. Dunne, F. J. Barbaro, E. V. Pereloma, Role of microstructure in susceptibility of X70 pipeline steel to hydrogen embrittlement, Materials Science Forum. 654–656 (2010) 162–165.

[295] X.H. Gao, J. Li, C. Li, Y. Liang, L.X. Du, Z.G. Liu, Research of high grade HIC-resistant pipeline steel, Advanced Materials Research. 900 (2014) 730–733.

[296] M. Zhu, C. Du, X. Li, Z. Liu, S. Wang, T. Zhao, J. Jia, Effect of strength and microstructure on stress corrosion cracking behavior and mechanism of X80 pipeline steel in high pH carbonate/bicarbonate solution, Journal of Materials Engineering and Performance. 23 (2014) 1358–1365.

[297] F. Castro Cerda, L. Kestens, A. Monsalve, R. Petrov, The effect of ultrafast heating in cold-rolled low carbon steel: Recrystallization and texture evolution, Metals. 6 (2016) 288.

[298] S. A. Park, J. G. Kim, Y. S. He, K. S. Shin, J. B. Yoon, Comparative study on the corrosion behavior of the cold rolled and hot rolled low-alloy steels containing copper and antimony in flue gas desulfurization environment, The Physics of Metals and Metallography. 115 (2014) 1285–1294.

[299] N. M. Shkatulyak, O. M. Tkachuk, A role played by the crystallographic texture in the process of corrosion of hot-rolled rods made of carbon steel, Materials Science. 48 (2012)

153–161.

[300] S. Qu, X. Pang, Y. Wang, K. Gao, Corrosion behavior of each phase in low carbon microalloyed ferrite – bainite dual-phase steel : Experiments and modeling, Corrosion Science. 75 (2013) 67–77.

[301] A. H. Bott, D. S. Dos Santos, P. E. V De Miranda, Influence of cementite morphology on the hydrogen permeation parameters of low carbon steel, Journal of Material Science Letters. 12 (1993) 390–393.

[302] G. W. Hong, J. Y. Lee, The interaction of hydrogen and the cementite-ferrite interface in carbon steel, Journal of Materials Science. 18 (1983) 271–277.

[303] A. Telang, A. S. Gill, M. Kumar, S. Teysseyre, D. Qian, S. R. Mannava, V. K. Vasudevan, Iterative thermomechanical processing of alloy 600 for improved resistance to corrosion and stress corrosion cracking, Acta Materialia. 113 (2016) 180–193.

[304] J. Zuo, L. Hou, J. Shi, H. Cui, L. Zhuang, J. Zhang, Enhanced plasticity and corrosion resistance of high strength Al-Zn-Mg-Cu alloy processed by an improved thermomechanical processing, Journal of Alloys and Compounds. 716 (2017) 220–230.

[305] V. Randle, R. Jones, Grain boundary plane distributions and single-step versus multiple-step grain boundary engineering, Materials Science and Engineering A. 524 (2009) 134–142.

[306] M. A. Mohtadi-Bonab, M. Eskandari, J. A. Szpunar, Role of cold rolled followed by annealing on improvement of hydrogen induced cracking resistance in pipeline steel, Engineering Failure Analysis. 91 (2018) 172–181.

[307] V. Venegas, F. Caleyo, J. M. Hallen, T. Baudin, R. Penelle, Role of crystallographic texture in hydrogen-induced cracking of low carbon steels for sour service piping, Metallurgical and Materials Transactions A: Physical Metallurgy and Materials Science. 38 (2007) 1022–1031.

[308] E. E. Oguzie, Y. Li, F. H. Wang, Effect of 2-amino-3-mercaptopropanoic acid (cysteine) on the corrosion behaviour of low carbon steel in sulphuric acid, Electrochimica Acta. 53 (2007) 909–914.

[309] S. Choudhary, A. Garg, K. Mondal, Relation between open circuit potential and polarization resistance with rust and corrosion monitoring of mild steel, Journal of Materials Engineering and Performance. 25 (2016) 2969–2976.

[310] U. Eduok, E. Jossou, A. Tiamiyu, J. Omale, J. Szpunar, Ceria/acrylic polymer microgel composite: synthesis, characterization, and anticorrosion application for API 5L X70 substrate in chloride-enriched medium, Industrial and Engineering Chemistry Research. 56 (2017) 5586–5597.

[311] U. Eduok, O. Faye, J. Szpunar, Corrosion inhibition of X70 sheets by a film-forming imidazole derivative at acidic pH, RSC Adv. 6 (2016) 108777–108790.

[312] G. R. Argade, S. K. Panigrahi, R. S. Mishra, Effects of grain size on the corrosion resistance of wrought magnesium alloys containing neodymium, Corrosion Science. 58 (2012) 145–151.

[313] X. Zhang, K. Xiao, C. Dong, J. Wu, X. Li, Y. Huang, In situ Raman spectroscopy study of corrosion products on the surface of carbon steel in solution containing Cl^- and SO_4, Engineering Failure Analysis. 18 (2011) 1981–1989.

[314] S. N. Smith, Disscussion of the history and relevance of the CO_2/H_2S ratio, NACE Corrosion, (2011) 1–13.

[315] S. N. Smith, M. W. Joosten, Corrosion of carbon steel by H_2S in CO_2 containing oil field environments, NACE Corrosion, (2006) 1–26.

[316] P. C. Pistorius, Final Technical Report on Accelerated corrosion of stainless steel in thiocyanate - containing solutions, (2012).

[317] M. E. Mitzithra, S. Paul, Scaling investigation of API 5L X65 steel in a ‘sweet’ followed by a ‘ sour ’ environment, NACE Corrosion Conference & Expo, (2016) 1–14.

[318] Y. Wang, W. Zhao, H. Ai, X. Zhou, T. Zhang, Effects of strain on the corrosion behaviour of X80 steel, Corrosion Science. 53 (2011) 2761–2766.

[319] S. P. Lynch, Interpreting hydrogen-induced fracture surfaces in terms of deformation processes: A new approach, Scripta Materialia. 65 (2011) 851–854.

[320] T. E. Perez, Corrosion in the oil and gas industry: An increasing challenge for materials, Jom. 65 (2013) 1033–1042.

[321] X. J. Shen, S. Tang, Y. J. Wu, X. L. Yang, J. Chen, Z. Y. Liu, R. D. K. Misra, G. D. Wang, Evolution of microstructure and crystallographic texture of microalloyed steel during warm rolling in dual phase region and their influence on mechanical properties, Materials Science and Engineering A. 685 (2017) 194–204.

[322] R. Srinivasan, T. Neeraj, Hydrogen embrittlement of ferritic steels: Deformation and failure

mechanisms and challenges in the oil and gas industry, Jom. 66 (2014) 1377–1382.

[323] T. Alp, B. Dogan, T. J. Davies, The effect of microstructure in the hydrogen embrittlement of a gas pipeline steel, Journal of Materials Science. 22 (1987) 2105–2112.

[324] L. Dai, D. Wang, T. Wang, Q. Feng, X. Yang, Analysis and comparison of long-distance pipeline failures, Journal of Petroleum Engineering. (2017) 1–7.

[325] T. Wen, H. Bin, W. Shui-ze, Y. Yi, Z. Chao, Z. Yong-kun, Effects of TMCP parameters on microstructure and mechanical properties of hot rolled economical dual phase steel in CSP, Journal of Iron and Steel Research. 19 (2012) 37–41.

[326] V. Carretero Olalla, V. Bliznuk, N. Sanchez, P. Thibaux, L.A.I. Kestens, R.H. Petrov, Analysis of the strengthening mechanisms in pipeline steels as a function of the hot rolling parameters, Materials Science and Engineering A. 604 (2014) 46–56.

[327] S. Nafisi, M. A. Arafin, L. Collins, J. Szpunar, Texture and mechanical properties of API X100 steel manufactured under various thermomechanical cycles, Materials Science and Engineering A. 531 (2012) 2–11.

[328] P. Siahpour, R. Miresmaeili, A. Sabour Rouhaghdam, Temperature effect of hot rolling process on microstructure, strength and fracture toughness of X65 pipeline steel, Transactions of the Indian Institute of Metals. 71 (2018) 1531–1541.

[329] G. H. Akbari, C. M. Sellars, J. A. Whiteman, Microstructural development during warm rolling of an IF steel, Acta Materialia. 45 (1997) 5047–5058.

[330] S. H. Sun, Y. Xiong, J. Zhao, Z. Q. Lv, Y. Li, D. L. Zhao, W. T. Fu, Microstructure characteristics in high carbon steel rod after warm cross-wedge rolling, Scripta Materialia. 53 (2005) 137–140.

[331] M. Sánchez-Araiza, S. Godet, P. J. Jacques, J. J. Jonas, Texture evolution during the recrystallization of a warm-rolled low-carbon steel, Acta Materialia. 54 (2006) 3085–3093.

[332] D. Raabe, Overview on basic types of hot rolling textures of steels, Steel Research International. 74 (2003) 327–337.

[333] J. Hu, L.X. Du, H. Xie, P. Yu, R. D. K. Misra, A nanograined/ultrafine-grained low-carbon microalloyed steel processed by warm rolling, Materials Science and Engineering A. 605 (2014) 186–191.

[334] F. Gao, Z. Liu, H. Liu, G. Wang, Toughness under different rolling processes in ultra purified Fe-17 wt% Cr alloy steels, Journal of Alloys and Compounds. 567 (2013) 141–

147.

[335] A. A. Gazder, M. Sánchez-Araiza, J. J. Jonas, E. V. Pereloma, Evolution of recrystallization texture in a 0.78 wt.% Cr extra-low-carbon steel after warm and cold rolling, Acta Materialia. 59 (2011) 4847–4865.

[336] K. Handa, Y. Kimura, Y. Yasumoto, T. Kamioka, Y. Mishima, Effect of deformation and annealing temperatures on ultrafine microstructure development and yield strength of pearlitic steel through continuous recrystallization, Materials Science and Engineering A. 527 (2010) 1926–1932.

[337] T. Schambron, A. Dehghan-Manshadi, L. Chen, T. Gooch, C. Killmore, E. Pereloma, Effect of Mo on dynamic recrystallization and microstructure development of microalloyed steels, Metals and Materials International. 23 (2017) 778–787.

[338] S. H. Cho, K. B. Kang, J. J. Jonas, Effect of manganese on recrystallisation kinetics of niobium microalloyed steel, Materials Science and Technology. 18 (2002) 389–395.

[339] C. de A. Martins, E. Poliak, L. B. Godefroid, N. Fonstein, Determining the conditions for dynamic recrystallization in hot deformation of C–Mn–V steels and the effects of Cr and Mo additions, ISIJ International. 54 (2014) 227–234.

[340] M. Sanchez-Ariza, S. Godet, J. J. Jonas, Effect of rolling temperature, reduction and alloying additions on the texture of warm rolled steels, Materials Science Forum. 495–497 (2005) 501–506.

[341] E. V. Pereloma, I. B. Timokhina, J. J. Jonas, M. K. Miller, Fine-scale microstructural investigations of warm rolled low-carbon steels with and without Cr, P, and B additions, Acta Materialia. 54 (2006) 4539–4551.

[342] M. S. Araïza, Texture evolution in warm rolled low-carbon steels, McGill University, Canada (2005).

[343] R. Riastuti, R. Bastian M., D. Priadi, E.S. Siradj, Grain refinement through warm rolling of wedge-shaped low carbon steel, Advanced Materials Research. 383–390 (2011) 5869–5873.

[344] H. Wang, C. Yu, Effect of grain size on corrosion properties of low alloy steel under H_2S/CO_2 environment, International Journal of Electrochemical Science. 12 (2017) 4327–4340.

[345] R. Pandi, S. Yue, Dynamic transformation of austenite to ferrite in low carbon steel., ISIJ

International. 34 (1994) 270–279.

[346] D. B. Santos, R. K. Bruzszek, P. C. M. Rodrigues, E. V. Pereloma, Formation of ultra-fine ferrite microstructure in warm rolled and annealed C-Mn steel, Materials Science and Engineering A. 346 (2003) 189–195.

[347] C. Medrea-Bichtas, I. Chicinas, S. Domsa, Study on warm rolling of AISI 1015 carbon steel, Z. Metallkunde. 93 (2002) 554–558.

[348] A. Haldar, R.K. Ray, Microstructural and textural development in an extra low carbon steel during warm rolling, Materials Science and Engineering A. 391 (2005) 402–407.

[349] A. Belyakov, R. Kaibyshev, V. Torganchuk, Microstructure and Mechanical Properties of 18%Mn TWIP/TRIP Steels Processed by Warm or Hot Rolling, Steel Research International. 88 (2017) 171–175.

[350] B. Hu, H. Luo, A strong and ductile 7Mn steel manufactured by warm rolling and exhibiting both transformation and twinning induced plasticity, Journal of Alloys and Compounds. 725 (2017) 684–693.

[351] S. Serajzadeh, Modelling the warm rolling of a low carbon steel, Materials Science and Engineering A. 371 (2004) 318–323.

[352] B. Koohbor, D. Ohadi, S. Serajzadeh, J.M. Akhgar, Effect of rolling speed on the occurrence of strain aging during and after warm rolling of a low-carbon steel, Journal of Materials Science. 45 (2010) 3405–3412.

[353] W.B. Hutchinson, Developement and control of annealing textures in low-carbon steels, International Metals Reviews. 29 (1984) 25–42.

[354] J. I. Omale, E.G. Ohaeri, J.A. Szpunar, M. Arafin, F. Fateh, Microstructure and texture evolution in warm rolled API 5L X70 pipeline steel for sour service application, Materials Characterization. 147 (2019) 453–463.

[355] A. S. Magalhães, C. E. dos Santos, A. O. V. Ferreira, D. S. Alves, D. B. Santos, Analysis of medium manganese steel through cold-rolling and intercritical annealing or warm-rolling, Materials Science and Technology. 0836 (2018) 1–14.

[356] S. Gollapudi, Grain size distribution effects on the corrosion behaviour of materials, Corrosion Science. 62 (2012) 90–94.

[357] C. D. Terwilliger, Y. M. Chiang, Size-dependent solute segregation and total solubility in ultrafine polycrystals: Ca in TiO2, Acta Metallurgica Et Materialia. 43 (1995) 319–328.

[358] H. Yu, Influences of microstructure and texture on crack propagation path of X70 acicular ferrite pipeline steel, Journal of University of Science and Technology Beijing: Mineral Metallurgy Materials (Eng Ed). 15 (2008) 683–687.

[359] M. R. Toroghinejad, A.O. Humphreys, F. Ashrafizadeh, A. Najafizadeh, J.J. Jonas, Effect of rolling temperature on the recrystallization texture of warm rolled steels, Material Science Forum. 426–432 (2003) 3691–3696.

[360] M. R. Barnett, J. J. Jonas, Influence of ferritic rolling temperature on grain size and texture in annealed low C and IF steels, ISIJ International. 37 (1997) 706–714.

[361] K. D. Ralston, N. Birbilis, Grain size effects on alloy corrosion, Materials Forum. 34 (2008) 54–63.

[362] J. W. Schultze, B. Davepon, F. Karman, C. Rosenkranz, A. Schreiber, O. Voigt, Corrosion and passivation in nanoscopic and microscopic dimensions: the influence of grains and grain boundaries, Corrosion Engineering, Science and Technology. 39 (2004) 45–52.

[363] A. A. Tiamiyu, V. Tari, J. A. Szpunar, A. G. Odeshi, A. K. Khan, Effects of grain refinement on the quasi-static compressive behavior of AISI 321 austenitic stainless steel: EBSD, TEM, and XRD studies, International Journal of Plasticity. 107 (2018) 79–99.

[364] C. K. Syn, D. R. Lesuer, O. D. Sherby, Microstructure in adiabatic shear bands in a pearlitic ultrahigh carbon steel, Materials Science and Technology. 21 (2005) 317–324.

[365] S. Boakye Yiadom, A. Khaliq Khan, N. Bassim, Effect of microstructure on the nucleation and initiation of adiabatic shear bands (ASBs) during impact, Materials Science and Engineering A. 615 (2014) 373–394.

[366] S. Lee, B.C. De Cooman, Effect of warm rolling on the rolling and recrystallization textures of non-oriented 3% si steel, ISIJ International . 51 (2011) 1545–1552.

[367] R. Khatirkar, L. Kestens, R. Petrov, I. Samajdar, Controlled warm working: possible tool for optimizing stored energy advantage in deformed gamma-fiber (ND//<111>), Isij International. 49 (2009) 78–85.

[368] A. O. Humphreys, D. Liu, M. R. Toroghinejad, E. Essadiqi, J. J. Jonas, Warm rolling behaviour of low carbon steels, Materials Science and Technology. 19 (2003) 709–714.

[369] H. Inagaki, Fundamental Aspect of Texture Formation in Low-Carbon Steel, Isij International. 34 (1994) 313–321.

[370] S. Matsuoka, M. Morita, O. Furukimi, T. Obara, Effect of lubrication condition on

recrystallization texture of ultra low C sheet steel hot-rolled in ferrite region, ISIJ International. 38 (1998) 633–639.

[371] M. R. Barnett, J. J. Jonas, Distinctive aspects of the physical metallurgy of warm rolling, ISIJ International. 39 (1999) 856–873.

[372] K. Ushioda, W.B. Hutchinson, J. Agren, U. Von Schlippenbach, Investigation of structure and texture developement during annealing of low carbon steel, Material Science and Technology. 2 (1986) 807–815.

[373] D. R. Gabe, The centenary of Tafel's equation, Transactions of the IMF. 83 (2005) 121–124.

[374] K. Morshed-Behbahani, P. Najafisayar, M. Pakshir, N. Zakerin, The effect of surface modification on the corrosion protection ability of the passive films of sensitized UNS S31803 duplex stainless steel, Corrosion Engineering Science and Technology. 54 (2019) 174–183.

[375] A. A. Tiamiyu, U. Eduok, J. A. Szpunar, A. G. Odeshi, Corrosion behavior of metastable AISI 321 austenitic stainless steel: Investigating the effect of grain size and prior plastic deformation on its degradation pattern in saline media, Scientific Reports. 9 (2019) 1–18.

[376] K. D. Ralston, N. Birbilis, C. H. J. Davies, Revealing the relationship between grain size and corrosion rate of metals, Scripta Materialia. 63 (2010) 1201–1204.

[377] M. Masoumi, H. L. F. Coelho, S. S. M. Tavares, C. C. Silva, H. F. G. de Abreu, Effect of Grain Orientation and Boundary Distributions on Hydrogen-Induced Cracking in Low-Carbon-Content Steels, Jom. 69 (2017) 1368–1374.

[378] E. Ohaeri, U. Eduok, J. Szpunar, Relationship between microstructural features in pipeline steel and hydrogen assisted degradation, Engineering Failure Analysis. 96 (2019) 496–507.

[379] A. Schreiber, J. W. Schultze, M. M. Lohrengel, F. Kármán, E. Kálmán, Grain dependent electrochemical investigations on pure iron in acetate buffer pH 6.0, Electrochimica Acta. 51 (2006) 2625–2630.

[380] M. Seo, M. Chiba, Nano-mechano-electrochemistry of passive metal surfaces, Electrochimica Acta. 47 (2001) 319–325.

[381] M. Chiba, M. Seo, Mechanoelectrochemical properties of passive iron surfaces evaluated by an in situ nanoscratching test, Journal of the Electrochemical Society. 150 (2003) 525-529.

[382] J. W. Schultze, M. M. Lohrengel, Stability, reactivity and breakdown of passive films. Problems of recent and future research, Electrochimica Acta. 45 (2000) 2499–2513.

[383] K. Fushimi, M. Seo, An SECM observation of dissolution distribution of ferrous or ferric ion from a polycrystalline iron electrode, Electrochimica Acta. 47 (2001) 121–127.

[384] A. J. Davenport, L. J. Oblonsky, M. P. Ryan, M. F. Toney, Structure of the passive film that forms on iron in aqueous environments, Journal of the Electrochemical Society. 147 (2000) 2162–2173.

[385] W. R. Buck, H. Leidheiser, The corrosion of single crystals and recrystallized single crystals of iron and steel in citric acid, Journal of the Electrochemical Society. 104 (1957) 474–481.

[386] G. P. Cammarota, L. Felloni, G. Palombarini, S. S. Traverso, Optical microscopy studies of anodic dissolution of iron in sulfuric and hydrochloric acid solutions: influence of metal purity, structure, heat treatment, Corrosion. 26 (1970) 129–140.

[387] I. M. Gadala, A. Alfantazi, Low Alloy X100 Pipeline Steel Corrosion and Passivation Behavior in Bicarbonate-Based Solutions of pH 6.7 to 8.9 with Groundwater Anions: An Electrochemical Study, Metallurgical and Materials Transactions A: Physical Metallurgy and Materials Science. 46 (2015) 3104–3116.

[388] Y. Lv, H. Luo, J. Tang, J. Guo, J. Pi, K. Ye, Corrosion properties of phase reversion induced nano/ultrafine grained AISI 304 metastable austenite stainless steel, Materials Research Bulletin. 107 (2018) 421–429.

[389] L. Jinlong, L. Hongyun, L. Tongxiang, G. Wenli, The effects of grain refinement and deformation on corrosion resistance of passive film formed on the surface of 304 stainless steels, Materials Research Bulletin. 70 (2015) 896–907.

[390] P. Okonkwo, R. Shakoor, A. Benamor, A. Amer Mohamed, M. Al-Marri, Corrosion behavior of API X100 steel material in a hydrogen sulfide environment, Metals. 7 (2017) 109.

[391] J. L. Crolet, N. Thevenot, S. Nesic, Role of Conductive Corrosion Products in the Protectiveness of Corrosion Layers, Corrosion. 54 (1998) 194–203.

[392] J. Banaś, U. Lelek-Borkowska, B. Mazurkiewicz, W. Solarski, Effect of CO_2 and H_2S on the composition and stability of passive film on iron alloys in geothermal water, Electrochimica Acta. 52 (2007) 5704–5714.

[393] Y. El Mendili, A. Abdelouas, J. F. Bardeau, Impact of a sulphidogenic environment on the

corrosion behavior of carbon steel at 90°C, RSC Advances. 3 (2013) 15148–15156.

[394] U. Eduok, E. Ohaeri, J. Szpunar, Electrochemical and surface analyses of X70 steel corrosion in simulated acid pickling medium: Effect of poly (N-vinyl imidazole) grafted carboxymethyl chitosan additive, Electrochimica Acta. 278 (2018) 302–312.

[395] N. Nakayama, A. Obuchi, Inhibitory effects of 5-aminouracil on cathodic reactions of steels in saturated $Ca(OH)_2$ solutions, Corrosion Science. 45 (2003) 2075–2092.

[396] S. B. Jiang, L. H. Jiang, Z. Y. Wang, M. Jin, S. Bai, S. Song, X. Yan, Deoxyribonucleic acid as an inhibitor for chloride-induced corrosion of reinforcing steel in simulated concrete pore solutions, Construction and Building Materials. 150 (2017) 238–247.

[397] H. Huang, G. Shuai, X. Wei, C. Yin, Effects of sulfur addition on the wettability and corrosion resistance of Sn-0.7Cu lead-free solder, Microelectronics Reliability. 74 (2017) 15–21.

[398] L. Qiu, K. Zou, G. Xu, Investigation on the sulfur state and phase transformation of spent and regenerated S zorb sorbents using XPS and XRD, Applied Surface Science. 266 (2013) 230–234.

[399] E. Sadeghi Meresht, T. Shahrabi Farahani, J. Neshati, Failure analysis of stress corrosion cracking occurred in a gas transmission steel pipeline, Engineering Failure Analysis. 18 (2011) 963–970.

[400] Y. Baik, Y. Choi, The effects of crystallographic texture and hydrogen on sulfide stress corrosion cracking behavior of a steel using slow strain rate test method, The Physics of Metals and Metallography. 115 (2014) 1318–1325.

[401] J. Capelle, J. Gilgert, I. Dmytrakh, G. Pluvinage, The effect of hydrogen concentration on fracture of pipeline steels in presence of a notch, Engineering Fracture Mechanics. 78 (2011) 364–373.

[402] J. Capelle, J. Gilgert, I. Dmytrakh, G. Pluvinage, Sensitivity of pipelines with steel API X52 to hydrogen embrittlement, International Journal of Hydrogen Energy. 33 (2008) 7630–7641.

[403] C. Bosch, T. Haase, S. Mannesmann, F. Gmbh, Effect of NACE TM0284 test modifications on the HIC performance of large diameter pipes, NACE Corrosion Conference & Expo, (2008) 1–13.

[404] C. F. Dong, Z. Y. Liu, X. G. Li, Y. F. Cheng, Effects of hydrogen-charging on the

susceptibility of X100 pipeline steel to hydrogen-induced cracking, International Journal of Hydrogen Energy. 34 (2009) 9879–9884.

[405] S. Lynch, Hydrogen embrittlement phenomena and mechanisms, Corrosion Reviews. 30 (2012) 105–123.

[406] R. Srinivasan, T. Neeraj, Hydrogen embrittlement of ferritic steels: deformation and failure mechanisms and challenges in the oil and gas industry, The Minerals, Metals & Materials Society. 66 (2014) 1377–1382.

[407] V. P. Afanas'ev, T. S. Dolotova, V. V Galtykhina, V. M. Yankovskii, E. A. Solomadina, E. D. Mokhova, The influence of thermomechanical working conditions on the resistance of low carbon steel to sulfide cracking, Soviet Material Science: Translated from Fiziko-Khimiches-Kaya Mekhanika Materialov. 16 (1981) 45–48.

[408] R. Ghosh, A. Venugopal, P. Sankaravelayudham, R. Panda, S. C. Sharma, K. M. George, V. S. Raja, Effect of Thermomechanical Treatment on the Environmentally Induced Cracking Behavior of AA7075 Alloy, Journal of Materials Engineering and Performance. 24 (2014) 545–555.

[409] D. G. Stalheim, B. Hoh, Guidelines for Production of API Pipelines Steels Suitable for Hydrogen Induced, Proceedings of the 8th International Pipeline Conference, Calgary, Alberta, Canada, (2010) 1–11.

[410] R. Mendoza, M. Alanis, R. Perez, O. Alvarez, C. Gonzalez, J. A. Juarez-Islas, On the processing of Fe-C-Mn-Nb steels to produce plates for pipelines with sour gas resistance, Materials Science and Engineering A. 337 (2002) 115–120.

[411] B. Jeong, R. Gauvin, S. Yue, EBSD study of martensite in a dual phase steel, Metals and Materials. 8 (2002) 700–701.

[412] T. Teshima, M. Kosaka, K. Ushioda, N. Koga, N. Nakada, Local cementite cracking induced by heterogeneous plastic deformation in lamellar pearlite, Materials Science and Engineering A. 679 (2017) 223–229.

[413] M. Y. Huh, Y. Cho, J. S. Kim, O. Engler, Effect of lubrication on the evolution of through-thickness texture gradinets in cold rolled and recrystalized low carbon steel, Z. Metallkunde. 90 (1999) 124–131.

[414] N. S. Mouriño, R. Petrov, J. H. Bae, K. Kim, L. A. I. Kestens, Texture dependent mechanical anisotropy of X80 pipeline steel, Advanced Engineering Materials. 12 (2010) 973–980.

[415] M. Y. Huh, Y. S. Cho, J. S. Kim, O. Engler, Influence of a solution treatment on the evolution of through-thickness texture gradients in dry cold rolled and recrystalized low carbon steel, Zeitschrift Fuer Metallkunde. 90 (1999) 124–131.

[416] Z. Shirband, M. R. Shishesaz, A. Ashrafi, Investigating the effect of heat treatment on hydrogen permeation behavior of API X-70 steel, Phase Transitions. 85 (2012) 503–511.

[417] M. A. Mohtadi-Bonab, M. Eskandari, J. A. Szpunar, Effect of arisen dislocation density and texture components during cold rolling and annealing treatments on hydrogen induced cracking susceptibility in pipeline steel, Journal of Material Research. 31 (2016) 3390–3400.

[418] L. Lan, Z. Chang, X. Kong, C. Qiu, D. Zhao, Phase transformation, microstructure, and mechanical properties of X100 pipeline steels based on TMCP and HTP concepts, Journal of Materials Science. 52 (2017) 1661–1678.

[419] J. Kittel, F. Ropital, F. Grosjean, E. M. M. Sutter, B. Tribollet, Corrosion mechanisms in aqueous solutions containing dissolved H_2S. Part 1: characterisation of H_2S reduction on 316 rotating disc electrode, Corrosion Science. 66 (2013) 324–329.

[420] P. W. Bolmer, Polarization of Iron in H_2S-NaHS Buffers, Corrosion. 21 (1965) 69–75.

[421] D. W. Shoesmith, The Formation of Ferrous Monosulfide Polymorphs during the Corrosion of Iron by Aqueous Hydrogen Sulfide at 21°C, Journal of The Electrochemical Society. 127 (1980) 1007.

[422] Z. Hua, B. An, T. Iijima, C. Gu, J. Zheng, The finding of crystallographic orientation dependence of hydrogen diffusion in austenitic stainless steel by scanning Kelvin probe force microscopy, Scripta Materialia. 131 (2017) 47–50.

[423] A. Duval, M. Robinson, Measurement and prediction of hydrogen embrittlement in high strength carbon steel Measurement and prediction of hydrogen embrittlement in high strength carbon steel, Corrosion Engineering, Science and Technology. 44 (2009) 340–346.

[424] J. Cappel, R. Flender, R. Höffken, G. Kemper, K. Wünnenberg, Centre segregation, soft reduction and oxide cleanness for large diameter line pipe with highest demands on HIC, Steel Research International. 76 (2005) 588–594.

[425] H. B. Xue, Y. F. Cheng, Characterization of inclusions of X80 pipeline steel and its correlation with hydrogen-induced cracking, Corrosion Science. 53 (2011) 1201–1208.

[426] J. I. Verdeja, J. Asensio, J. A. Pero-Sanz, Texture, formability, lamellar tearing and HIC

susceptibility of ferritic and low-carbon HSLA steels, Materials Characterization. 50 (2003) 81–86.

[427] S. Serna, B. Campillo, J. L. Albarrán, Crack Growth in Microalloyed Pipeline Steels for Sour Gas Transport, Journal of Materials Engineering and Performance. 14 (2005) 224–228.

[428] L. Li, B. Song, J. Cheng, Y. Yang, Z. Liu, Effects of cooling processes on microstructure and susceptibility of hydrogen-induced cracking of X80 pipeline steel, Materials and Corrosion. (2017) 590–600.

[429] V. Venegas, O. Herrera, F. Caleyo, J.M. Hallen, T. Baudin, Crystallographic texture control helps improve pipeline steel resistance to hydrogen induced cracking, Proceedings of the 8th International Pipeline Conference, IPC2010, Calgary, Alberta, Canada, (2010) 1–7.

[430] S. Shanmugam, R. D. K. Misra, J. Hartmann, S. G. Jansto, Microstructure of high strength niobium-containing pipeline steel, Materials Science and Engineering A. 441 (2006) 215–229.

[431] M. Sozańska, J. Sojka, P. Beťáková, C. Dagbert, L. Hyspecká, J. Galland, M. Tvrdý, Examination of hydrogen interaction in carbon steel by means of quantitative microstructural and fracture descriptions, Materials Characterization. 46 (2001) 239–243.

[432] M. Gomez, P. Valles, S. F. Medina, Evolution of microstructure and precipitation state during thermomechanical processing of a X80 microalloyed steel, Materials Science and Engineering A. 528 (2011) 4761–4773.

[433] J. Li, X. Gao, L. Du, Z. Liu, Relationship between microstructure and hydrogen induced cracking behavior in a low alloy pipeline steel, Journal of Materials Science & Technology. 33 (2017) 1504–1512.

[434] R. Joodaki, S. R. Alavi Zaree, K. Gheisari, M. Eskandari, Effect of annealing treatments on the microstructure and texture development in API 5L X60 microalloyed pipeline steel, Journal of Materials Engineering and Performance. 26 (2017) 2003–2013.

[435] H. Nykyforchyn, E. Lunarska, O. Tsyrulnyk, K. Nikiforov, G. Gabetta, Effect of the long-term service of the gas pipeline on the properties of the ferrite-pearlite steel, Materials and Corrosion. 60 (2009) 716–725.

[436] R. Li, X. Zuo, Y. Hu, Z. Wang, D. Hu, Microstructure and properties of pipeline steel with a ferrite/martensite dual-phase microstructure, Materials Characterization. 62 (2011) 801–

806.

[437] M. Béreš, L. Wu, L. P. M. Santos, M. Masoumi, F. A. M. da Rocha Filho, C. C. da Silva, H. F. G. de Abreu, M. J. Gomes da Silva, Role of lattice strain and texture in hydrogen embrittlement of 18Ni (300) maraging steel, International Journal of Hydrogen Energy. 42 (2017) 14786–14793.

[438] X. L. Yang, Y. B. Xu, X. D. Tan, D. Wu, Relationships among crystallographic texture, fracture behavior and Charpy impact toughness in API X100 pipeline steel, Materials Science and Engineering A. 641 (2015) 96–106.

[439] M. Masoumi, C. C. Silva, H. Ferreira, G. De Abreu, Effect of rolling in the recrystallization temperature region associated with a post-heat treatment on the microstructure , crystal orientation, and mechanical properties of API 5L X70 pipeline steel, Materials Research. 20 (2017) 151–160.

[440] G. Yuan, W. Hu, X. Wang, J. Kang, J. Zhao, H. Di, R. D. K. Misra, G. Wang, The relationship between microstructure , crystallographic orientation , and fracture behavior in a high strength ferrous alloy, Journal of Alloys and Compounds. 695 (2017) 526–539.

[441] M. Scharnweber, W. Tirschler, C. Oertel, W. Skrotzki, Mechanisms of short crack propagation in austenitic – ferritic duplex steel, Materials Science & Engineering A. 595 (2014) 269–283.

[442] W. Kim, S. Koh, Y. Kim, B. Yang, The effect of metallurgical factors on HIC of high strength linepipe steel, Corrosion 2007. (2007) 1–9.

[443] F. Huang, X. G. Li, J. Liu, Y. M. Qu, C.W. Du, Effects of alloying elements, microstructure, and inclusions on hydrogen induced cracking of X120 pipeline steel in wet H_2S sour environment, Materials and Corrosion. 63 (2012) 59–66.

[444] Y. Liu, L. Zhang, H. Duan, Y. Zhang, Y. Luo, A. N. Conejo, Extraction, thermodynamic analysis, and precipitation mechanism of MnS-TiN complex inclusions in low-sulfur steels, Metallurgical and Materials Transactions A: Physical Metallurgy and Materials Science. 47 (2016) 3015–3025.

[445] Z. Peng, J. Liu, F. Huang, Q. Hu, Z. Cheng, S. Liu, Y. Cheng, Effect of submicron-scale MnS inclusions on hydrogen trapping and HIC susceptibility of X70 pipeline steels, Steel Research International. 1700566 (2018) 1–8.

[446] W. K. Kim, J. H. Bae, K. M. Noh, K. S. Kim, Sour properties of API X70 / 80 grade hot

rolled steel, 18th International Corrosion Congress, (2011) 4–7.

[447] M. Masoumi, L. P. M. Santos, I. N. Bastos, S. S. M. Tavares, M. J. G. da Silva, H. F. G. de Abreu, Texture and grain boundary study in high strength Fe-18Ni-Co steel related to hydrogen embrittlement, Materials and Design. 91 (2016) 90–97.

[448] T. E. Garcia, C. Rodriguez, F. J. Belzunce, I. I. Cuesta, Effect of hydrogen embrittlement on the tensile properties of CrMoV steels by means of the small punch test, Materials Science and Engineering A. 664 (2016) 165–176.

[449] Z. Kapel', Y. G. Matvienko, G. Pluvinage, Fracture toughness and hydrogen embrittlement of pipes with notches, Inorganic Materials. 46 (2010) 1558–1563.

[450] D. H. Johnson, M. R. Edwards, P. Chard-Tuckey, Microstructural effects on the magnitude of Lüders strains in a low alloy steel, Materials Science and Engineering A. 625 (2015) 36–45.

[451] L. Fu, Z. Li, H. Wang, A. Shan, Luders-like deformation induced by delta-ferrite-assisted martensitic transformation in dual-phaes high manganease steel, Scripta Materialia. 67 (2012) 297–300.

[452] S. Li, Z. Zhang, E. Akiyama, K. Tsuzaki, B. Zhang, Evaluation of susceptibility of high strength steels to delayed fracture by using cyclic corrosion test and slow strain rate test, Corrosion Science. 52 (2010) 1660–1667.

[453] W. Y. Choo, J. Y. Lee, Thermal analysis of trapped hydrogen in pure iron, Metallurgical Transactions. A, Physical Metallurgy and Materials Science. 13 (1982) 135-140.

[454] J. A. Lee, D. H. Lee, M. Y. Seok, U. B. Baek, Y. H. Lee, S. H. Nahm, J. I Jang, Hydrogen-induced toughness drop in weld coarse-grained heat-affected zones of linepipe steel, Materials Characterization. 82 (2013) 17–22.

[455] A. B. Cota, S. W. Ooi, W. Solano-Alvarez, H. K. D. H. Bhadeshia, Infusion of hydrogen into nanostructured bainitic steel, Materials Characterization. 134 (2017) 96–102.

[456] Q. Liu, B. Irwanto, A. Atrens, Influence of hydrogen on the mechanical properties of some medium-strength Ni-Cr-Mo steels, Materials Science & Engineering A. 617 (2014) 200–210.

[457] M. Eskandari, M. A. Mohtadi-bonab, J. A. Szpunar, Evolution of the microstructure and texture of X70 pipeline steel during cold-rolling and annealing treatments, JMADE. 90 (2016) 618–627.

[458] T. M. Park, M. T. Kim, K. H. Baik, M. Koyama, J. Han, Enhancement of hydrogen embrittlement resistance of Fe-Mn-C twinning-induced plasticity steel by partial recrystallization technique, Materials Characterization. 151 (2019) 221–226.

[459] A. Nagao, M. L. Martin, M. Dadfarnia, P. Sofronis, I. M. Robertson, The effect of nanosized (Ti,Mo)C precipitates on hydrogen embrittlement of tempered lath martensitic steel, Acta Materialia. 74 (2014) 244–254.

[460] F. R. Xiao, B. Liao, Y. Y. Shan, G. Y. Qiao, Y. Zhong, C. Zhang, K. Yang, Challenge of mechanical properties of an acicular ferrite pipeline steel, Materials Science and Engineering A. 431 (2006) 41–52.

[461] A. Guo, R. D. K. Misra, J. Xu, B. Guo, S. G. Jansto, Ultrahigh strength and low yield ratio of niobium-microalloyed 900MPa pipeline steel with nano/ultrafine bainitic lath, Materials Science and Engineering A. 527 (2010) 3886–3892.

[462] S. S. Nayak, R. Anumolu, R. D. K. Misra, K. H. Kim, D. L. Lee, Microstructure-hardness relationship in quenched and partitioned medium-carbon and high-carbon steels containing silicon, Materials Science and Engineering A. 498 (2008) 442–456.

[463] Y. Toji, G. Miyamoto, D. Raabe, Carbon partitioning during quenching and partitioning heat treatment accompanied by carbide precipitation, Acta Materialia. 86 (2015) 137–147.

[464] C. D. Singh, S. Kumar, Texture evolution in hot band and annealed hot bands of low alloyed ferritic stainless steel, Materials Science and Technology. 19 (2003) 1037–1044.

[465] M. Kamaya, Assessment of local deformation using EBSD: Quantification of accuracy of measurement and definition of local gradient, Ultramicroscopy. 111 (2011) 1189–1199.

[466] P.O. Guglielmi, M. Ziehmer, E.T. Lilleodden, On a novel strain indicator based on uncorrelated misorientation angles for correlating dislocation density to local strength, Acta Materialia. 150 (2018) 195–205.

[467] G. Roberts, R. M. Ward, M. Strangwood, C. L. Davis, Use of misorientation values to further understand deformation in rail steels, Ironmaking & Steelmaking. 40 (2012) 92–97.

[468] S. H. Choi, Y. S. Jin, Evaluation of stored energy in cold-rolled steels from EBSD data, Materials Science and Engineering A. 371 (2004) 149–159.

[469] L. Lan, W. Zhou, R. D. K. Misra, Effect of hot deformation parameters on flow stress and microstructure in a low carbon microalloyed steel, Materials Science and Engineering A. 756 (2019) 18–26.

[470] A. A. Saleh, A. A. Gazder, E. V. Pereloma, EBSD observations of recrystallisation and tensile deformation in twinning induced plasticity steel, Transactions of the Indian Institute of Metals. 66 (2013) 621–629.

[471] D. K. Mondal, R. M. Dey, Effect of grain size on the microstructure and mechanical properties of a CMnV dual-phase steel, Materials Science and Engineering A. 149 (1992) 173–181.

[472] N. Saeidi, F. Ashrafizadeh, B. Niroumand, Development of a new ultrafine grained dual phase steel and examination of the effect of grain size on tensile deformation behavior, Materials Science and Engineering A. 599 (2014) 145–149.

[473] E. Fereiduni, S. S. Ghasemi Banadkouki, Improvement of mechanical properties in a dual-phase ferrite-martensite AISI4140 steel under tough-strong ferrite formation, Materials and Design. 56 (2014) 232–240.

[474] G. Schoeck, Interaction of Lomer-Cottrell locks with screw dislocations, Philosophical Magazine. 90 (2010) 629–636.

[475] N. Tsuchida, Y. Tomota, K. Nagai, K. Fukaura, A simple relationship between Lüders elongation and work-hardening rate at lower yield stress, Scripta Materialia. 54 (2006) 57–60.

[476] M. Koyama, C.C. Tasan, E. Akiyama, K. Tsuzaki, D. Raabe, Hydrogen-assisted decohesion and localized plasticity in dual-phase steel, Acta Materialia. 70 (2014) 174–187.

[477] A. Laureys, T. Depover, R.H. Petrov, K. Verbeken, Microstructural characterization of hydrogen induced cracking in TRIP steels by EBSD, Materials Characterization. 112 (2016) 169–179.

[478] Z. Li, Y. Zhou, S. Wang, Influence of strain and stress triaxiality on the fracture behavior of GB 35CrMo steel during hot tensile testing, Advances in Materials Science and Engineering. 2018 (2018) 1–11.

[479] J. Kadkhodapour, A. Butz, S. Ziaei Rad, Mechanisms of void formation during tensile testing in a commercial, dual-phase steel, Acta Materialia. 59 (2011) 2575–2588.

[480] N.. G. Shul'ga, M.F. Zamora, Y.N. Nikiforchin, Dependence of the deformability of chromium steel Kh17 on texture, Material Science and Heat Treatment. 14 (1972) 805–808.

[481] E. Lunarska, V. Novak, N. Zarubova, S. Kadeckova, Effect of electrolytic hydrogen charging on flow stress and slip line pattern in iron single crystals, Scripta Metallurgica. 17

(1983) 705–710.

[482] Y. Tobe, W.R. Tyson, Effect of hydrogen on yield of iron, Scripta Metallurgica. 11 (1977) 849–852.

[483] K. Oguri, H. Kimura, Effect of hydrogen on the flow stress of iron with various purities, Scripta Metallurgica. 14 (1980) 1017–1022.

[484] I. M. Robertson, P. Sofronis, A. Nagao, M. L. Martin, S. Wang, D. W. Gross, K. E. Nygren, Hydrogen embrittlement understood, Metallurgical and Materials Transactions A: Physical Metallurgy and Materials Science. 46 (2015) 2323–2341.

[485] S. P. Lynch, Mechanisms and kinetics of environmentally assisted cracking: Current status, issues, and suggestions for further work, Metallurgical and Materials Transactions A: Physical Metallurgy and Materials Science. 44 (2013) 1209–1229.

[486] M. I. Luppo, J. Ovejero-Garcia, The influence of microstructure on the trapping and diffusion of hydrogen in a low carbon steel, Corrosion Science. 32 (1991) 1125–1136.

[487] A. H. M. Krom, A. D. Bakker, Hydrogen trapping models in steel, Metallurgical and Materials Transactions B: Process Metallurgy and Materials Processing Science. 31 (2000) 1475–1482.

[488] F. G. Wei, T. Hara, T. Tsuchida, K. Tsuzaki, Hydrogen trapping in quenched and tempered 0.42C-0.30Ti steel containing bimodally dispersed TiC particles, ISIJ International. 43 (2003) 539–547.

[489] M. Pressouyre, I. M. Bernstein, A kinetic trapping model for hydrogen-induced cracking, Acta Metallurgica. 27 (1978) 89–100.

[490] K. M. M. Rahman, M. A. Mohtadi-Bonab, R. Ouellet, J. Szpunar, A comparative study of the role of hydrogen on degradation of the mechanical properties of API X60, X60SS, and X70 pipeline steels, Steel Research International. 1900078 (2019) 1–9.

[491] K. M. Mostafijur Rahman, M. A. Mohtadi-Bonab, R. Ouellet, J. Szpunar, N. Zhu, Effect of electrochemical hydrogen charging on an API X70 pipeline steel with focus on characterization of inclusions, International Journal of Pressure Vessels and Piping. 173 (2019) 147–155.

[492] T. I. Ramjaun, S. W. Ooi, R. Morana, H. K. D. H. Bhadeshia, Designing steel to resist hydrogen embrittlement: Part 1–trapping capacity, Materials Science and Technology (United Kingdom). 34 (2018) 1737–1746.

[493] S. M. Lee, J. Y. Lee, The effect of the interface character of TiC particles on hydrogen trapping in steel, Acta Metallurgica. 35 (1987) 2695–2700.

[494] J. Takahashi, K. Kawakami, Y. Kobayashi, T. Tarui, The first direct observation of hydrogen trapping sites in TiC precipitation-hardening steel through atom probe tomography, Scripta Materialia. 63 (2010) 261-264.

[495] A. Laureys, E. Van den Eeckhout, R. Petrov, K. Verbeken, Effect of deformation and charging conditions on crack and blister formation during electrochemical hydrogen charging, Acta Materialia. 127 (2017) 192–202.

[496] R. G. Davies, Hydrogen Embrittlement of Dual-Phase Steels, (1981) 1667–1668.

[497] X. Zhu, W. Li, T. Y. Hsu, S. Zhou, L. Wang, X. Jin, Improved resistance to hydrogen embrittlement in a high-strength steel by quenching-partitioning-tempering treatment, Scripta Materialia. 97 (2015) 21–24.

[498] J. Sun, T. Jiang, Y. Sun, Y. Wang, Y. Liu, A lamellar structured ultrafine grain ferrite-martensite dual-phase steel and its resistance to hydrogen embrittlement, Journal of Alloys and Compounds. 698 (2017) 390–399.

[499] J. R. Rice, J. S. Wang, Embrittlement of interfaces by solute segregation, Materials Science and Engineering A. 107 (1989) 23–40.

[500] L.B. Pfeil, The effect of occluded hydrogen on the tensile strength of iron, Proceeding of the Royal Society of London Series A, Containing Papers of a Mathematical and Physical Character. 112 (1926) 182–195.

[501] M. Nagumo, Hydrogen related failure of steels – a new aspect, Materials Science and Technology. 20 (2004) 940–950.

APPENDIX A

LIST OF PUBLISHED ARTICLES

1. **E. Ohaeri,** J. Omale, J. Szpunar, U. Eduok, F. Fazeli, M. Arafin, 'Effect of microstructure and texture evolution on the electrochemical corrosion behavior of warm rolled API 5l x70 pipeline steel' *Metallurgical and Materials Transactions,* 2020, Vol 51, pp. 2255-2275.
2. **E. Ohaeri,** J. Omale, K. M. Mostafijur Rahman, J. Szpunar, 'Effect of post-processing annealing treatments on microstructure development and hydrogen embrittlement in API 5L X70 pipeline steel' *Materials Characterization*, 2020, Vol 161, 110124.
3. **E. Ohaeri,** U. Eduok, J. Szpunar, 'Relationship between microstructural features in pipeline steel and hydrogen assisted degradation' *Engineering Failure Analysis*, 2019, Vol. 96, pp. 496-507.
4. **E. Ohaeri,** J. Omale, U. Eduok, J. Szpunar, 'Effect of thermomechanical processing and crystallogrphic orientation on the corrosion behavior of API 5L X70 pipeline steel' *Metallurgical and Materials Transactions A,* 2018, Vol. 49, No 6, pp. 2269-2280.
5. **E. Ohaeri,** U. Eduok, J. Szpunar, 'Hydrogen related degradation in pipeline steel: A review' *International Journal of Hydrogen Energy,* 2018, Vol. 43, No 31, pp. 14584-14617.
6. **E. Ohaeri,** J. Omale, A. Tiamiyu, K. M. Mostafijur Rahman, J. Szpunar, 'Influence of thermomechanically controlled processing on microstructure and hydrogen induced cracking susceptibility of API 5L X70 pipeline steel' *Journal of Materials Engineering and Performance,* 2018, Vol. 27, No 9, pp. 4533-4547.
7. **E. Ohaeri,** J. Szpunar, F. Fazeli, M. Arafin, 'Hydrogen induced cracking susceptibility of API 5L X70 pipeline steel in relation to microstructure and crystallographic texture developed after different thermomechanical treatments' *Materials Characterization,* 2018, Vol 145, pp. 142-156.

LIST OF CONFERENCES ATTENDED

1. **E. Ohaeri**, U. Eduok, and J. Szpunar, 'Understanding the electrochemical corrosion response of API 5l X70 pipeline steel after different thermomechanical treatments' *NACE International Northern Area Western Conference,* Delta Hotels, Regina, Saskatchewan, Canada, February 5-6, 2020
2. **E. Ohaeri,** and J. Szpunar, 'Hydrogen embrittlement susceptibility of API 5L X70 pipeline steel after different thermomechanical treatments' *Canadian Material Science Conference (CMSC),* University of Alberta, Edmonton, Canada, June 19-22, 2018.
3. **E. Ohaeri**, and J. Szpunar, 'Microstructural variation at different layers of API 5L X80 pipeline steel thickness and its relation to hydrogen degradation' *Proceedings of Materials Science and Technology Conference, (MS&T),* Columbus Convention Centre, Ohio, October 14-18, 2018, pp. 762-769.

APPENDIX B

COPYRIGHT PERMISSION FOR CHAPTER 2

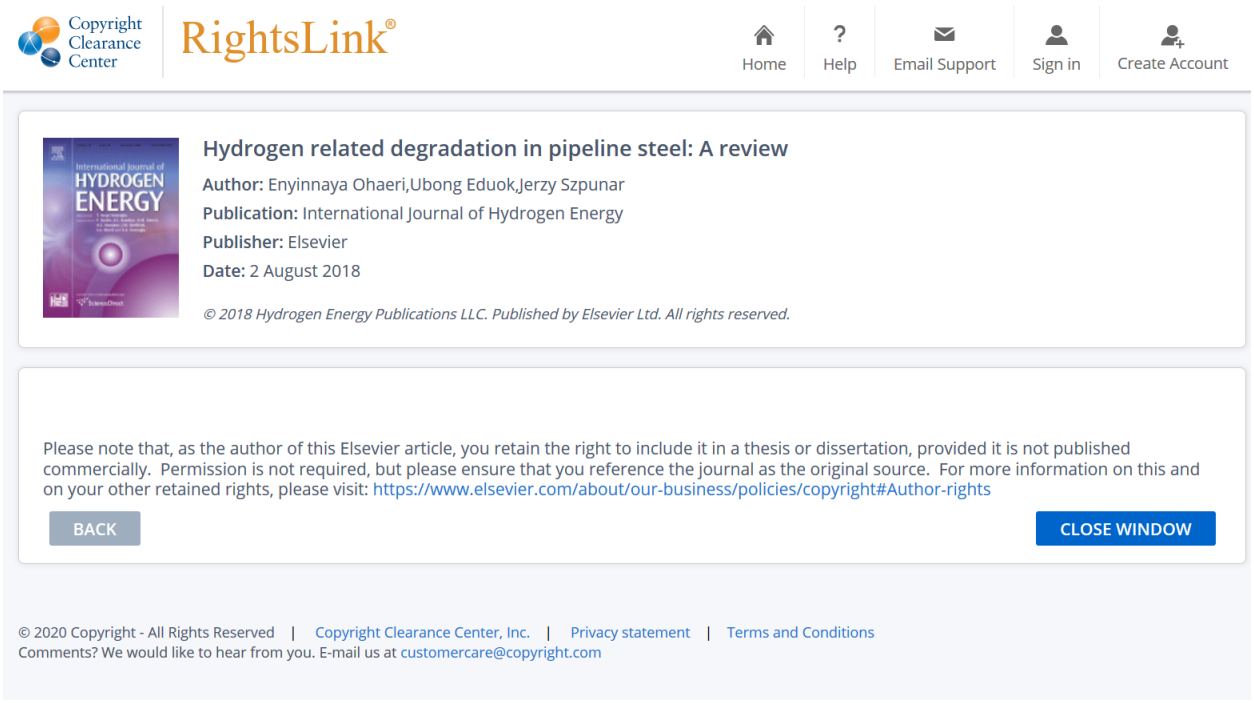

Copyright Clearance Center | RightsLink®

Home | Help | Email Support | Sign in | Create Account

Hydrogen related degradation in pipeline steel: A review

Author: Enyinnaya Ohaeri,Ubong Eduok,Jerzy Szpunar

Publication: International Journal of Hydrogen Energy

Publisher: Elsevier

Date: 2 August 2018

© 2018 Hydrogen Energy Publications LLC. Published by Elsevier Ltd. All rights reserved.

Please note that, as the author of this Elsevier article, you retain the right to include it in a thesis or dissertation, provided it is not published commercially. Permission is not required, but please ensure that you reference the journal as the original source. For more information on this and on your other retained rights, please visit: https://www.elsevier.com/about/our-business/policies/copyright#Author-rights

BACK | CLOSE WINDOW

© 2020 Copyright - All Rights Reserved | Copyright Clearance Center, Inc. | Privacy statement | Terms and Conditions

Comments? We would like to hear from you. E-mail us at customercare@copyright.com

APPENDIX C

COPYRIGHT PERMISSION FOR CHAPTER 2, FIG. 2.12

This Agreement between Enyinnaya Ohaeri ("You") and Elsevier ("Elsevier") consists of your license details and the terms and conditions provided by Elsevier and Copyright Clearance Center.

License Number	4722700772451
License date	Dec 05, 2019
Licensed Content	Elsevier
Publisher	Elsevier
Licensed Content	
Publication	Acta Materialia
Licensed Content Title	Three-dimensional imaging of hydrogen blister in iron with neutron tomography
Licensed Content Author	Axel Griesche,Eitan Dabah,Thomas Kannengiesser,Nikolay Kardjilov,André Hilger,Ingo Manke
Licensed Content Date	Oct 1, 2014
Licensed Content Volume	78
Licensed Content Issue	n/a
Licensed Content Pages	9
Start Page	14
End Page	22
Type of Use	reuse in a thesis/dissertation
Portion	figures/tables/illustrations
Number of figures/tables/illustrations	3
Format	both print and electronic
Are you the author of this Elsevier article?	No
Will you be translating?	No
Title	Enhancing the corrosion resistance of API 5L X70 pipeline steel through thermomechanically controlled processing
Institution name	University of Saskatchewan
Expected presentation date	Feb 2020
Portions	Fig. 3, Fig. 4 and Fig 5
Requestor Location	Enyinnaya Ohaeri Department of Mechanical Engineering University of Saskatchewan

Saskatoon, SK S7N 5A9
Canada
Attn: Enyinnaya Ohaeri
Publisher Tax ID GB 494 6272 12
Total 0.00 CAD

Terms and Conditions

INTRODUCTION

1. The publisher for this copyrighted material is Elsevier. By clicking "accept" in connection with completing this licensing transaction, you agree that the following terms and conditions apply to this transaction (along with the Billing and Payment terms and conditions established by Copyright Clearance Center, Inc. ("CCC"), at the time that you opened your Rightslink account and that are available at any time at http://myaccount.copyright.com).

GENERAL TERMS

2. Elsevier hereby grants you permission to reproduce the aforementioned material subject to the terms and conditions indicated.

3. Acknowledgement: If any part of the material to be used (for example, figures) has appeared in our publication with credit or acknowledgement to another source, permission must also be sought from that source. If such permission is not obtained then that material may not be included in your publication/copies. Suitable acknowledgement to the source must be made, either as a footnote or in a reference list at the end of your publication, as follows:

"Reprinted from Publication title, Vol /edition number, Author(s), Title of article / title of chapter, Pages No., Copyright (Year), with permission from Elsevier [OR APPLICABLE SOCIETY COPYRIGHT OWNER]." Also Lancet special credit - "Reprinted from The Lancet, Vol. number, Author(s), Title of article, Pages No., Copyright (Year), with permission from Elsevier."

4. Reproduction of this material is confined to the purpose and/or media for which permission is hereby given.

5. Altering/Modifying Material: Not Permitted. However figures and illustrations may be altered/adapted minimally to serve your work. Any other abbreviations, additions, deletions and/or any other alterations shall be made only with prior written authorization of Elsevier Ltd. (Please contact Elsevier at permissions@elsevier.com). No modifications can be made to any Lancet figures/tables and they must be reproduced in full.

6. If the permission fee for the requested use of our material is waived in this instance, please be advised that your future requests for Elsevier materials may attract a fee.

7. Reservation of Rights: Publisher reserves all rights not specifically granted in the combination of (i) the license details provided by you and accepted in the course of this licensing transaction, (ii) these terms and conditions and (iii) CCC's Billing and Payment

terms and conditions.

8. License Contingent Upon Payment: While you may exercise the rights licensed immediately upon issuance of the license at the end of the licensing process for the transaction, provided that you have disclosed complete and accurate details of your proposed use, no license is finally effective unless and until full payment is received from you (either by publisher or by CCC) as provided in CCC's Billing and Payment terms and conditions. If full payment is not received on a timely basis, then any license preliminarily granted shall be deemed automatically revoked and shall be void as if never granted. Further, in the event that you breach any of these terms and conditions or any of CCC's Billing and Payment terms and conditions, the license is automatically revoked and shall be void as if never granted. Use of materials as described in a revoked license, as well as any use of the materials beyond the scope of an unrevoked license, may constitute copyright infringement and publisher reserves the right to take any and all action to protect its copyright in the materials.

9. Warranties: Publisher makes no representations or warranties with respect to the licensed material.

10. Indemnity: You hereby indemnify and agree to hold harmless publisher and CCC, and their respective officers, directors, employees and agents, from and against any and all
claims arising out of your use of the licensed material other than as specifically authorized pursuant to this license.

11. No Transfer of License: This license is personal to you and may not be sublicensed, assigned, or transferred by you to any other person without publisher's written permission.

12. No Amendment Except in Writing: This license may not be amended except in a writing signed by both parties (or, in the case of publisher, by CCC on publisher's behalf).

13. Objection to Contrary Terms: Publisher hereby objects to any terms contained in any purchase order, acknowledgment, check endorsement or other writing prepared by you, which terms are inconsistent with these terms and conditions or CCC's Billing and Payment terms and conditions. These terms and conditions, together with CCC's Billing and Payment terms and conditions (which are incorporated herein), comprise the entire agreement between you and publisher (and CCC)

concerning this licensing transaction. In the event of any conflict between your obligations established by these terms and conditions and those established by CCC's Billing and Payment terms and conditions, these terms and conditions shall control.

14. Revocation: Elsevier or Copyright Clearance Center may deny the permissions described in this License at their sole discretion, for any reason or no reason, with a full refund payable to you. Notice of such denial will be made using the contact information provided by you. Failure to receive such notice will not alter or invalidate the denial. In no event will Elsevier or Copyright Clearance Center be responsible or liable for any costs, expenses or damage incurred by you as a result of a denial of your permission request, other than a refund of the amount(s) paid by you to Elsevier and/or Copyright Clearance Center for denied permissions.

LIMITED LICENSE

The following terms and conditions apply only to specific license types:
15. **Translation**: This permission is granted for non-exclusive world **English** rights only unless your license was granted for translation rights. If you licensed translation rights you may only translate this content into the languages you requested. A professional translator must perform all translations and reproduce the content word for word preserving the integrity of the article.

16. **Posting licensed content on any Website**: The following terms and conditions apply as follows: Licensing material from an Elsevier journal: All content posted to the web site must maintain the copyright information line on the bottom of each image; A hyper-text must be included to the Homepage of the journal from which you are licensing at http://www.sciencedirect.com/science/journal/xxxxx or the Elsevier homepage for books at http://www.elsevier.com; Central Storage: This license does not include permission for a scanned version of the material to be stored in a central repository such as that provided by Heron/XanEdu.

Licensing material from an Elsevier book: A hyper-text link must be included to the Elsevier homepage at http://www.elsevier.com . All content posted to the web site must maintain the copyright information line on the bottom of each image.

Posting licensed content on Electronic reserve: In addition to the above the following clauses are applicable: The web site must be password-protected and made available only to bona fide students registered on a relevant course. This permission is granted for 1 year only. You may obtain a new license for future website posting.

17. **For journal authors:** the following clauses are applicable in addition to the above:

Preprints:
A preprint is an author's own write-up of research results and analysis, it has not been peer reviewed, nor has it had any other value added to it by a publisher (such as formatting, copyright, technical enhancement etc.).

Authors can share their preprints anywhere at any time. Preprints should not be added to or enhanced in any way in order to appear more like, or to substitute for, the final versions of articles however authors can update their preprints on arXiv or RePEc with their Accepted Author Manuscript (see below). If accepted for publication, we encourage authors to link from the preprint to their formal publication via its DOI. Millions of researchers have access to the formal publications on ScienceDirect, and so links will help users to find, access, cite and use the best available version. Please note that Cell Press, The Lancet and some society-owned have different preprint policies. Information on these policies is available on the journal homepage.

Accepted Author Manuscripts: An accepted author manuscript is the manuscript of an article that has been accepted for publication and which typically includes author incorporated changes suggested during submission, peer review and editor-author communications.

Authors can share their accepted author manuscript:

- immediately
    - via their non-commercial person homepage or blog
    - by updating a preprint in arXiv or RePEc with the accepted manuscript
    - via their research institute or institutional repository for internal institutional uses or as part of an invitation-only research collaboration work-group
    - directly by providing copies to their students or to research collaborators for their personal use
    - for private scholarly sharing as part of an invitation-only work group on commercial sites with which Elsevier has an agreement
- After the embargo period
    - via non-commercial hosting platforms such as their institutional repository
    - via commercial sites with which Elsevier has an agreement

In all cases accepted manuscripts should:

- link to the formal publication via its DOI
- bear a CC-BY-NC-ND license - this is easy to do
- if aggregated with other manuscripts, for example in a repository or other site, be shared in alignment with our hosting policy not be added to or enhanced in any way to appear more like, or to substitute for, the published journal article.

Published journal article (JPA): A published journal article (PJA) is the definitive final record of published research that appears or will appear in the journal and embodies all value-adding

publishing activities including peer review co-ordination, copy-editing, formatting, (if relevant) pagination and online enrichment. Policies for sharing publishing journal articles differ for subscription and gold open access articles:

Subscription Articles: If you are an author, please share a link to your article rather than the full-text. Millions of researchers have access to the formal publications on ScienceDirect, and so links will help your users to find, access, cite, and use the best available version.

Theses and dissertations which contain embedded PJAs as part of the formal submission can be posted publicly by the awarding institution with DOI links back to the formal publications on ScienceDirect.

If you are affiliated with a library that subscribes to ScienceDirect you have additional private sharing rights for others' research accessed under that agreement. This includes use for classroom teaching and internal training at the institution (including use in course packs and courseware programs), and inclusion of the article for grant funding purposes.

Gold Open Access Articles: May be shared according to the author-selected end-user license and should contain a CrossMark logo, the end user license, and a DOI link to the formal publication on ScienceDirect. Please refer to Elsevier's posting policy for further information.

18. **For book authors** the following clauses are applicable in addition to the above: Authors are permitted to place a brief summary of their work online only. You are not allowed to download and post the published electronic version of your chapter, nor may you scan the printed edition to create an electronic version. **Posting to a repository:** Authors are permitted to post a summary of their chapter only in their institution's repository.

19. **Thesis/Dissertation**: If your license is for use in a thesis/dissertation your thesis may be submitted to your institution in either print or electronic form. Should your thesis be published commercially, please reapply for permission. These requirements include permission for the Library and Archives of Canada to supply single copies, on demand, of the complete thesis and include permission for Proquest/UMI to supply single copies, on demand, of the complete thesis. Should your thesis be published commercially, please reapply for permission. Theses and dissertations which contain embedded PJAs as part of the formal submission can be posted publicly by the awarding institution with DOI links back to the formal publications on ScienceDirect.

APPENDIX D

COPYRIGHT PERMISSION FOR CHAPTER 4

SPRINGER NATURE LICENSE
TERMS AND CONDITIONS

Nov 26, 2019

This Agreement between Enyinnaya Ohaeri ("You") and Springer Nature ("Springer Nature") consists of your license details and the terms and conditions provided by Springer

Nature and Copyright Clearance Center.

License Number	4716680416342
License date	Nov 26, 2019
Licensed Content Publisher	Springer Nature
Licensed Content Publication	Metallurgical and Materials Transactions A
Licensed Content Title	Effect of Thermomechanical Processing and Crystallographic Orientation on the Corrosion Behavior of API 5L X70 Pipeline Steel
Licensed Content Author	Enyinnaya Ohaeri, Joseph Omale, Ubong Eduok et al
Licensed Content Date	Jan 1, 2018
Licensed Content Volume	49
Licensed Content Issue	6
Type of Use	Thesis/Dissertation
Requestor type	Academic/university or research institute
Format	Print and electronic
Portion	Full article/chapter
Will you be translating?	no
Circulation/distribution	50000 or greater
Author of this Springer Nature content	yes
Title	Enhancing the corrosion resistance of API 5L X70 pipeline steel through thermomechanically controlled processing
Institution name	University of Saskatchewan
Expected presentation date	Feb 2020
Requestor Location	Enyinnaya Ohaeri Department of Mechanical Engineering University of Saskatchewan Saskatoon, SK S7N 5A9

	Canada Attn: Enyinnaya Ohaeri
Total	0.00 CAD

Terms and Conditions

Springer Nature Customer Service Centre GmbH
Terms and Conditions

This agreement sets out the terms and conditions of the licence (the **Licence**) between you and **Springer Nature Customer Service Centre GmbH** (the **Licensor**). By clicking 'accept' and completing the transaction for the material (**Licensed Material**), you also confirm your acceptance of these terms and conditions.

1. Grant of License

1. 1. The Licensor grants you a personal, non-exclusive, non-transferable, world-wide licence to reproduce the Licensed Material for the purpose specified in your order only. Licences are granted for the specific use requested in the order and for no other use, subject to the conditions below.

1. 2. The Licensor warrants that it has, to the best of its knowledge, the rights to license reuse of the Licensed Material. However, you should ensure that the material you are requesting is original to the Licensor and does not carry the copyright of another entity (as credited in the published version).

1. 3. If the credit line on any part of the material you have requested indicates that it was reprinted or adapted with permission from another source, then you should also seek permission from that source to reuse the material.

2. Scope of Licence

2. 1. You may only use the Licensed Content in the manner and to the extent permitted by these Ts&Cs and any applicable laws.

2. 2. A separate licence may be required for any additional use of the Licensed Material, e.g. where a licence has been purchased for print only use, separate permission must be obtained for electronic re-use. Similarly, a licence is only valid in the language selected and does not apply for editions in other languages unless additional translation rights have been granted separately in the licence. Any content owned by third parties are expressly excluded from the licence.

2. 3. Similarly, rights for additional components such as custom editions and derivatives require additional permission and may be subject to an additional fee. Please apply to

Journalpermissions@springernature.com/bookpermissions@springernature.com for these rights.

2. 4. Where permission has been granted **free of charge** for material in print, permission may also be granted for any electronic version of that work, provided that the material is incidental to your work as a whole and that the electronic version is essentially equivalent to, or substitutes for, the print version.

2. 5. An alternative scope of licence may apply to signatories of the STM Permissions Guidelines, as amended from time to time.

3. Duration of Licence

3. 1. A licence for is valid from the date of purchase ('Licence Date') at the end of the relevant period in the below table:

Scope of Licence	Duration of Licence
Post on a website	12 months
Presentations	12 months
Books and journals	Lifetime of the edition in the language purchased

4. Acknowledgement

4. 1. The Licensor's permission must be acknowledged next to the Licenced Material in print. In electronic form, this acknowledgement must be visible at the same time as the figures/tables/illustrations or abstract and must be hyperlinked to the journal/book's homepage. Our required acknowledgement format is in the Appendix below.

5. Restrictions on use

5. 1. Use of the Licensed Material may be permitted for incidental promotional use and minor editing privileges e.g. minor adaptations of single figures, changes of format, colour and/or style where the adaptation is credited as set out in Appendix 1 below. Any other changes including but not limited to, cropping, adapting, omitting material that affect the meaning, intention or moral rights of the author are strictly prohibited.

5. 2. You must not use any Licensed Material as part of any design or trademark.

5. 3. Licensed Material may be used in Open Access Publications (OAP) before publication by Springer Nature, but any Licensed Material must be removed from OAP sites prior to final publication.

6. Ownership of Rights

6. 1. Licensed Material remains the property of either Licensor or the relevant third party and any rights not explicitly granted herein are expressly reserved.

7. Warranty

IN NO EVENT SHALL LICENSOR BE LIABLE TO YOU OR ANY OTHER PARTY OR ANY OTHER PERSON OR FOR ANY SPECIAL, CONSEQUENTIAL, INCIDENTAL OR INDIRECT DAMAGES, HOWEVER CAUSED, ARISING OUT OF OR IN CONNECTION WITH THE DOWNLOADING, VIEWING OR USE OF THE MATERIALS REGARDLESS OF THE FORM OF ACTION, WHETHER FOR BREACH OF CONTRACT, BREACH OF WARRANTY, TORT, NEGLIGENCE, INFRINGEMENT OR OTHERWISE (INCLUDING, WITHOUT LIMITATION, DAMAGES BASED ON LOSS OF PROFITS, DATA, FILES, USE, BUSINESS OPPORTUNITY OR CLAIMS OF THIRD PARTIES), AND WHETHER OR NOT THE PARTY HAS BEEN ADVISED OF THE POSSIBILITY OF SUCH DAMAGES. THIS LIMITATION SHALL APPLY NOTWITHSTANDING ANY FAILURE OF ESSENTIAL PURPOSE OF ANY LIMITED REMEDY PROVIDED HEREIN.

8. Limitations

8. 1. ***BOOKS ONLY:*** Where **'reuse in a dissertation/thesis'** has been selected the following terms apply: Print rights of the final author's accepted manuscript (for clarity, NOT the published version) for up to 100 copies, electronic rights for use only on a personal website or institutional repository as defined by the Sherpa guideline (www.sherpa.ac.uk/romeo/).

9. Termination and Cancellation

9. 1. Licences will expire after the period shown in Clause 3 (above).

9. 2. Licensee reserves the right to terminate the Licence in the event that payment is not received in full or if there has been a breach of this agreement by you.

Appendix 1 — Acknowledgements:

For Journal Content:
Reprinted by permission from [**the Licensor**]: [**Journal Publisher** (e.g. Nature/Springer/Palgrave)] [**JOURNAL NAME**] [**REFERENCE CITATION** (Article name, Author(s) Name), [**COPYRIGHT**] (year of publication)

For **Advance Online Publication papers:**
Reprinted by permission from [**the Licensor**]: [**Journal Publisher** (e.g. Nature/Springer/Palgrave)] [**JOURNAL NAME**] [**REFERENCE CITATION** (Article name,

Author(s) Name), [**COPYRIGHT**] (year of publication), advance online publication, day month year (doi: 10.1038/sj.[JOURNAL ACRONYM].)

For Adaptations/Translations:
Adapted/Translated by permission from [**the Licensor**]: [**Journal Publisher** (e.g. Nature/Springer/Palgrave)] [**JOURNAL NAME**] [**REFERENCE CITATION** (Article name, Author(s) Name), [**COPYRIGHT**] (year of publication)

Note: For any republication from the British Journal of Cancer, the following credit line style applies:

Reprinted/adapted/translated by permission from [**the Licensor**]: on behalf of Cancer Research UK: : [**Journal Publisher** (e.g. Nature/Springer/Palgrave)] [**JOURNAL NAME**] [**REFERENCE CITATION** (Article name, Author(s) Name), [**COPYRIGHT]** (year of publication)

For **Advance Online Publication** papers:
Reprinted by permission from The [**the Licensor**]: on behalf of Cancer Research UK: [**Journal Publisher** (e.g. Nature/Springer/Palgrave)] [**JOURNAL NAME**] [**REFERENCE CITATION** (Article name, Author(s) Name), [**COPYRIGHT**] (year of publication), advance online publication, day month year (doi: 10.1038/sj. [JOURNAL ACRONYM])

For Book content:
Reprinted/adapted by permission from [**the Licensor**]: [**Book Publisher** (e.g. Palgrave Macmillan, Springer etc) [**Book Title**] by [**Book author**(s)] [**COPYRIGHT**] (year of publication)

Other Conditions:
Version 1.2
Questions? customercare@copyright.com or +1-855-239-3415 (toll free in the US) or +1-978-646-2777.

APPENDIX E

COPYRIGHT PERMISSION FOR CHAPTER 5

SPRINGER NATURE LICENSE
TERMS AND CONDITIONS

This Agreement between Enyinnaya Ohaeri ("You") and Springer Nature ("Springer Nature") consists of your license details and the terms and conditions provided by Springer Nature and Copyright Clearance Center.

License Number	4803860460576
License date	Apr 07, 2020
Licensed Content Publisher	Springer Nature
Licensed Content Publication	Metallurgical and Materials Transactions A
Licensed Content Title	Effect of Microstructure and Texture Evolution on the Electrochemical Corrosion Behavior of Warm-Rolled API 5L X70 Pipeline Steel
Licensed Content Author	Enyinnaya Ohaeri et al
Licensed Content Date	Feb 22, 2020
Type of Use	Thesis/Dissertation
Requestor type	academic/university or research institute
Format	print and electronic
Portion	full article/chapter
Will you be translating?	no
Circulation/distribution	50000 or greater
Author of this Springer Nature content	yes
Title	Enhancing the corrosion resistance of API 5L X70 pipeline steel through thermomechanically controlled processing
Institution name	University of Saskatchewan
Expected presentation date	Apr 2020
Requestor Location	Enyinnaya Ohaeri Department of Mechanical Engineering University of Saskatchewan Saskatoon, SK S7N 5A9 Canada Attn: Enyinnaya Ohaeri
Total	0.00 CAD

APPENDIX F

COPYRIGHT PERMISSION FOR CHAPTER 6

SPRINGER NATURE LICENSE
TERMS AND CONDITIONS

This Agreement between Enyinnaya Ohaeri ("You") and Springer Nature ("Springer Nature") consists of your license details and the terms and conditions provided by Springer Nature and Copyright Clearance Center.

License Number	4716680861568
License date	Nov 26, 2019
Licensed Content Publisher	Springer Nature
Licensed Content Publication	Journal of Materials Engineering and Performance
Licensed Content Title	Influence of Thermomechanically Controlled Processing on Microstructure and Hydrogen Induced Cracking Susceptibility of API 5L X70 Pipeline Steel
Licensed Content Author	Enyinnaya Ohaeri, Joseph Omale, Ahmed Tiamiyu et al
Licensed Content Date	Jan 1, 2018
Licensed Content Volume	27
Licensed Content Issue	9
Type of Use	Thesis/Dissertation
Requestor type	Academic/university or research institute
Format	Print and electronic
Portion	Full article/chapter
Will you be translating?	no
Circulation/distribution	50000 or greater
Author of this Springer Nature content	yes
Title	Enhancing the corrosion resistance of API 5L X70 pipeline steel through thermomechanically controlled processing
Institution name	University of Saskatchewan
Expected presentation date	Feb 2020
Requestor Location	Enyinnaya Ohaeri Department of Mechanical Engineering University of Saskatchewan Saskatoon, SK S7N 5A9 Canada Attn: Enyinnaya Ohaeri
	Total 0.00 CAD

APPENDIX G

COPYRIGHT PERMISSION FOR CHAPTER 7

Copyright Clearance Center | RightsLink®

Home | Help | Email Support | Sign in | Create Account

Hydrogen induced cracking susceptibility of API 5L X70 pipeline steel in relation to microstructure and crystallographic texture developed after different thermomechanical treatments

Author: Enyinnaya Ohaeri,Jerzy Szpunar,Fateh Fazeli,Muhammad Arafin

Publication: Materials Characterization

Publisher: Elsevier

Date: November 2018

Please note that, as the author of this Elsevier article, you retain the right to include it in a thesis or dissertation, provided it is not published commercially. Permission is not required, but please ensure that you reference the journal as the original source. For more information on this and on your other retained rights, please visit: https://www.elsevier.com/about/our-business/policies/copyright#Author-rights

BACK | CLOSE WINDOW

APPENDIX H

COPYRIGHT PERMISSION FOR CHAPTER 8

Copyright Clearance Center | RightsLink®

Home | Help | Email Support | Sign in | Create Account

Effect of post-processing annealing treatments on microstructure development and hydrogen embrittlement in API 5L X70 pipeline steel

Author: Enyinnaya Ohaeri,Joseph Omale,K.M. Mostafijur Rahman,Jerzy Szpunar

Publication: Materials Characterization

Publisher: Elsevier

Date: March 2020

© 2020 Elsevier Inc. All rights reserved.

Please note that, as the author of this Elsevier article, you retain the right to include it in a thesis or dissertation, provided it is not published commercially. Permission is not required, but please ensure that you reference the journal as the original source. For more information on this and on your other retained rights, please visit: https://www.elsevier.com/about/our-business/policies/copyright#Author-rights

BACK | CLOSE WINDOW